DOES MORPHOLOGICAL ADJUSTMENT DURING TSUNAMI INUNDATION INCREASE LEVELS OF HAZARD?

BY

BABAK TEHRANIRAD, JAMES T. KIRBY AND FENGYAN SHI

RESEARCH REPORT NO. CACR-16-02
NOVEMBER 2016

SUPPORTED BY THE NATIONAL TSUNAMI HAZARD MITIGATION PROGRAM
NATIONAL WEATHER SERVICE GRANT NOS.
NA10NWS4670010; NA13NWS4670014;
NA14NWS4670041; NA15NWS4670029
AND NA16NWS4670034

CENTER FOR APPLIED COASTAL RESEARCH

Ocean Engineering Laboratory
University of Delaware
Newark, Delaware 19716

TABLE OF CONTENTS

LIST OF FIGURES

ABSTRACT

Previous tsunami inundation mapping for the US East Coast(USEC) have shown that barrier islands would potentially be highly impacted during a possible tsunami. Many of these barrier islands along USEC are home to populated cities like Atlantic City, NJ and Ocean City, MD. Inundation mapping results showed insignificant inundation for many regions on the mainland behind these barriers. However, we know that a tsunami can significantly change coastal morphology, and post-tsunami surveys have confirmed that during tsunami inundation, large amounts of sediment have been eroded from sandy coasts and deposited further onshore. In some cases, sand dunes were completely eroded, and the sediment got deposited either onshore behind the dunes, or offshore during the rundown process. Thus, it seems essential to consider barrier island topographic changes during the inundation mapping process for assessing tsunami hazard. In this thesis, we considered tsunami-induced bathymetric changes to study whether morphological adjustment during tsunami inundation increases levels of hazard. For this purpose, we coupled the FUNWAVE-TVD model with an advection-diffusion depth-averaged sediment transport model and a morphology module to capture bed evolution in tsunami conditions. Then, we used the model to simulated two laboratory experiments. First, bed changes under breaking solitary waves were modeled. Then, we simulated sediment transport of a dam-break wave. Moreover, we simulated tsunami-induced morphological changes inside Crescent City harbor during the 2011 Tohoku-oki tsunami. The results indicated that the model can locate erosion and deposition regions correctly for laboratory and field tests. Finally, we applied our model to study barrier island topographic changes for four different tsunamis: 1) A cone collapse of Cumbre Vieja volcano in the Canary Islands, 2) A tsunami generated by an earthquake in the Puerto Rico subduction zone, 3) Another

earthquake-generated tsunami in Azores-Gibraltar convergence zone, and 4) A tsunami caused by a landslide on the USEC shelf break. We studied two different locations on the USEC, Assateague Island as an area without infrastructures, and Ocean City, MD to investigate the effect of complexities such as pavements, buildings, and jetties on tsunami-induced morphological changes. Our results suggest that a tsunami can cause significant bathymetric changes on a barrier island. Due to the erosion on top of the barrier, it is shown that the mainland behind can experience higher levels of tsunami hazard compared to the condition with fixed bathymetry.

Chapter 1

MOTIVATION AND BACKGROUND

1.1 Motivation

A tsunami can change coastal morphology significantly (Gelfenbaum and Jaffe, 2003; Goto et al., 2011). During recent events, there were numerous examples of tsunamis completely eroding barrier islands, sand dunes and coastal protection systems (Choowong el al., 2008; Fritz et al., 2011; Goto et al.,2011, 2012a-b; Haraguchi et al., 2012; Wilson et al., 2012; Sugawara et al., 2014). However, none of the previous tsunami hazard assessments performed using numerical simulations has considered morphological changes during tsunami inundation as a possible contribution to the overall hazard assessment. The main goal of this thesis is to capture morphological adjustments during tsunami inundation and to study whether hazard levels change with consideration of dynamic bathymetry conditions. As part of the NTHMP project, we have studied tsunami inundation impacts for several locations on the US East Coast (USEC), including Ocean City, MD, Atlantic City, NJ, New York City, NY, Montauk, NY, Nantucket, MA, Savannah, GA, Cape Hatteras, NC, Virginia Beach, VA and Myrtle Beach, SC (Tehranirad et al., 2014, 2015b-j). Various sources such as volcanic collapses (Tehranirad et al., 2015), submarine landslides (Grilli et al., 2015), and coseismic tsunami types (Grilli et al., 2010) were simulated throughout this work. Numerical simulations were performed with FUNWAVE-TVD (Tehranirad et al., 2011; Shi et al., 2012; Kirby et al., 2013) and NHWAVE (Ma et al., 2012) models. More than 50 hazard maps have been generated for populated areas along USEC (Tehranirad et al., 2014, 2015b-j). Our results showed that almost all of the barrier islands on the USEC would be completely overtopped during a possible tsunami, with maximum velocities as large as 10 m/s on top of barriers. This observation suggests that significant

sediment transport and possible morphology adjustments could occur on top of these barriers during a tsunami inundation.

Tsunami wave trains usually have more than one significant wave. For example, during the 2009 South Pacific tsunami in Samoa and Tonga, tide gauge data showed that the tsunami signal lasted for more than an hour, and was composed of five major waves with a dominant period of about 10 minutes (Fritz et al., 2011). Thus, it is possible that the first wave of the tsunami erodes the barrier island such that later tsunami waves experience a different bathymetry, possibly a flatter barrier. Therefore, the later wave characteristics, such as inundation depth and runup might be altered. Hazard assessments based on a fixed bathymetry might be inaccurate, especially on the mainland located behind barrier islands. Previously obtained inundation lines might extend further onshore when considering morphological changes during tsunami inundation modeling.

In this study, FUNWAVE-TVD was coupled with appropriate sediment transport and morphology modules to study the impact of morphology adjustments during tsunami inundation on levels of hazard. In the next section of this chapter, a review of existing field observations is provided. These observations help us understand the phenomenon we are trying to simulate, and help us choose the right model to capture the physics of tsunami-induced sediment action correctly. Next, a review of previous works on modeling tsunami-induced morphological changes is provided in the final section of this chapter.

1.2 Field Observations

Extensive sediment movement has been reported in many areas exposed to tsunamis, such as bays, estuaries, coastal dunes and around coastal structures (Tanaka et al., 2012; Goto et al., 2012a; Udo et al., 2012; Szczuciński et al., 2012; Haraguchi et al., 2013). Post-tsunami measurements suggest that, during tsunami inundation, large amounts of sand get eroded from sandy coasts and deposited further onshore

(Wilson et al., 2012). In many cases, on shorelines with sand dune protection systems, dunes were completely eroded, and the eroded sediment was deposited onshore behind the dunes (Haraguchi et al., 2013). After the 2004 Indian Ocean Tsunami on the western coasts of Thailand, tsunami deposits were found extending 1 km onshore, covering the low-lying coastal areas, while field surveys show that coastal dunes close to the shoreline were the source of sand deposits further onshore (Choowong et al., 2008; Hori et al., 2007). More recently, the Tohoku-Oki tsunami, which devastated the most tsunami-prepared coastline in the world, revealed the potential for tsunami flow to change coastal morphology (Udu et al., 2012, Goto et al., 2012a-b). Figure 1.1 depicts an example of dune breaching that occurred at the Arahma Coast, Japan, after the 2011 tsunami. The picture is provided by New York Times (2011) magazine from satellite images, taken by GeoEye/EyeQ, from before and after the disaster. As shown in this figure, this coastal community was strongly protected by detached breakwaters, a dune system as well as vegetation. Despite the existence of several coastal protection systems, the sandy coast behind the breakwaters was eroded significantly, and vegetation was completely washed away after the tsunami. Although about 0.2 to 0.3 m subsidence was reported in this area, the main changes in the topography were caused by erosive tsunami flows (Udu et al., 2012). Thus, even protected coastal areas are exposed to morphological damage from tsunamis. Similar to sandy beaches, large morphological changes were observed on coasts with intermittent coastal protection, where severe damage and erosion in less protected areas were noticed (Tanaka et al., 2012, Goto et al., 2012a).

In addition to barrier islands or dunes, tsunami morphological impacts are expected to be significant in other coastal areas. For example, sand spits at mouths of rivers are among the most vulnerable areas to tsunami-induced morphological impacts. During 2011 Tohoku-Oki tsunami, in most cases where the tsunami directly inundated the estuarine environment, sand spits around river mouths were completely eroded (Udo et al., 2012; Tanaka et al., 2012). Figure 1.2 depicts the morphological changes at Kitakami River mouth in Japan before and after 2011 tsunami. As shown

Figure 1.1: Satellite picture of Arahma Coast, Japan, before and after the 2011 Tohoku-Oki tsunami (Picture provided by New York Times (2011).

in Figure 1.2, the two sand spits were completely eroded, and severe breaching and erosion happened on the mainland behind the river mouth area. Udu et al. (2012) reported that between 20 to 50 cm subsidence occurred on Japan coasts. However, the observed large erosion on the shoreface, dunes, and sand spits of the order of several meters (Tanaka et al., 2012; Sugawara et al., 2014), suggest that tsunami flow caused them rather than the subsidence.

Significant tsunami-induced erosion and deposition inside harbors have also been recorded. During the 1960 Chilean tsunami, sediment up to 4 meters thick was deposited in parts of Crescent City harbor in California, while significant scouring around coastal structures occurred (Lander et al., 1993). A similar amount of deposition was reported by Goto et al. (2011) for Kirinda Harbor in Sri Lanka after the 2004 Indian Ocean tsunami. After the 2011 Tohoku-Oki tsunami, although there is no record of any significant inundation on the west coast of the US, Wilson et al. (2012) reported that the tsunami generated strong currents inside Crescent City (Figure 1.3) and Santa Cruz harbors, and caused considerable morphological changes. Inside Crescent City harbor, scour of 289,400 m^3 was observed in an area of 0.67 km^2. In Santa Cruz, because of the limited width in some areas such as the entrance, and shallow bathymetry of the harbor, current velocity increased in the narrower areas, causing strong scour and depositing large volumes of the sand at the docks.

Tsunami sediment action can also impact coastal structure stability due to scour caused by strong flows (Goto et al., 2012a). Yeh et al. (2005) mentioned that tsunami scouring around structures happens during runup. Afterward, during the drawdown, water levels decrease, and pore pressure adjacent to the structure would decrease as well (Tonkin et al., 2003). This drop in the effective stress around the structure can lead to serious instability issues (Goto et al., 2012b). In addition to the damages caused by tsunami runup impact, there are plenty of examples of scour and sedimentation around structures resulting in the destruction of the structure, especially during the rundown (Goto et al., 2012a).

Researchers have conducted several surveys and post-tsunami assessments to

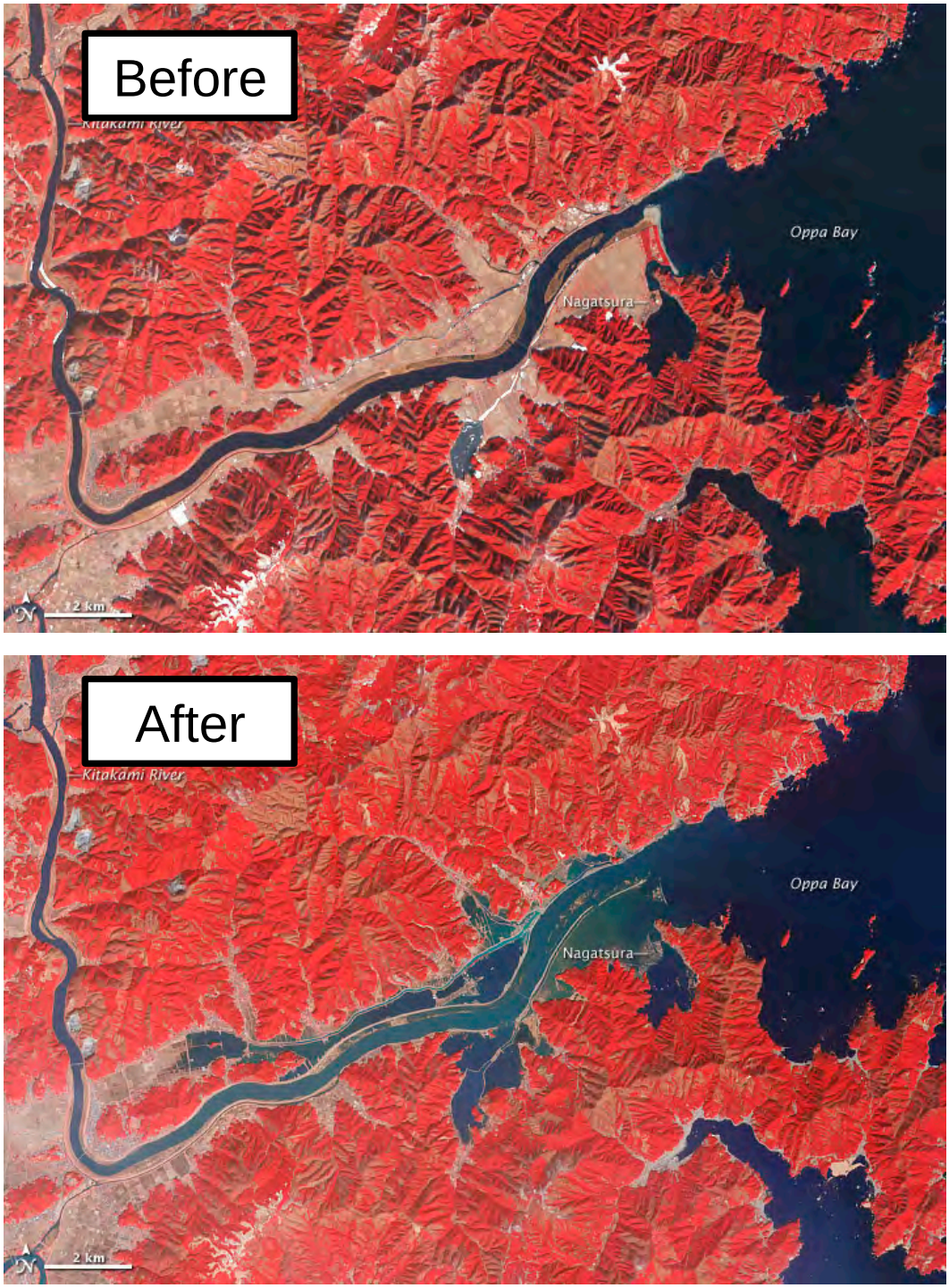

Figure 1.2: Satellite picture of Kitakami River mouth before and after the 2011 Tohoku-Oki tsunami. It should be noted that 28 cm subsidence was reported for this area in addition to tsunami erosion. Pictures are taken from NASA Earth Observatory (http://earthobservatory.nasa.gov/IOTD/view.php?id=77379).

Figure 1.3: Tsunami flow-regime map for Crescent City Harbor. Current directions and velocities, and areas of sediment erosion and deposition are based on observations of the various ground-level and aerial video, pre- and post-tsunami bathymetry, and sediment analyses (Wilson et al., 2012, Figure 5)

locate the origin of sediment deposition sources. These surveys were conducted from deep water offshore, to the inundation line inland to determine the role of offshore deposits as well as onshore sand sources. Evaluations after the 1993 Hokkaido Nansei-Oki tsunami demonstrated that the volume of sediment eroded from the beach and dunes was approximately equal to the deposited amount (Sato et al., 1995). Goto et al. (2012a,b) have also concluded that, for the Tohoku-Oki tsunami, most of the sediment deposits inland originated from dune erosion. Although a few observations (Gelfenbaum and Jaffe, 2003) suggest that deep-water (depths of 20-800 m) sediments were the main tsunami deposition sources inland, for most scenarios sandy deposits onshore originated primarily from beach and sand dune erosion nearshore (e.g. Szczuciński et al., 2012). Accordingly, the simulations of tsunami-induced morphological changes could be focused on the nearshore area, since field observations suggest that tsunami sediment action is mainly limited to shallow water and onshore.

Choowong et al. (2008) reconstructed the hydraulic conditions of the 2004 Indian Ocean tsunami at Bagtao, Thailand, using eyewitness evidence, photographs, surface bedforms and particle-size analysis (Figure 1.4). They concluded that after the initial withdrawal of water from the shoreline, the first inflow eroded the beach surface but only carried the sediment 30 meters inland. Then, the second inflow deposited the sediment volume denoted Unit 1 (shown in Figure 1.4) further onshore. Minutes later, the third inflow (also the largest one), eroded Unit 2 from the beach face and covered Unit 1 with the thicker and more extensive Unit 2. Finally, bedforms were shaped at the surface of Unit 2 during rundown of the tsunami. Other researchers have also pointed out that large sediment action occurs during the rundown process (Goto et al., 2011a,b; Tanaka et al., 2012; Udo et al., 2012).

1.3 Modeling Background

Increased computational power and development of higher order numerical schemes during recent decades have paved the path for significant developments in utilizing complex models which can model tsunami hydrodynamics accurately (e.g. Lynett and

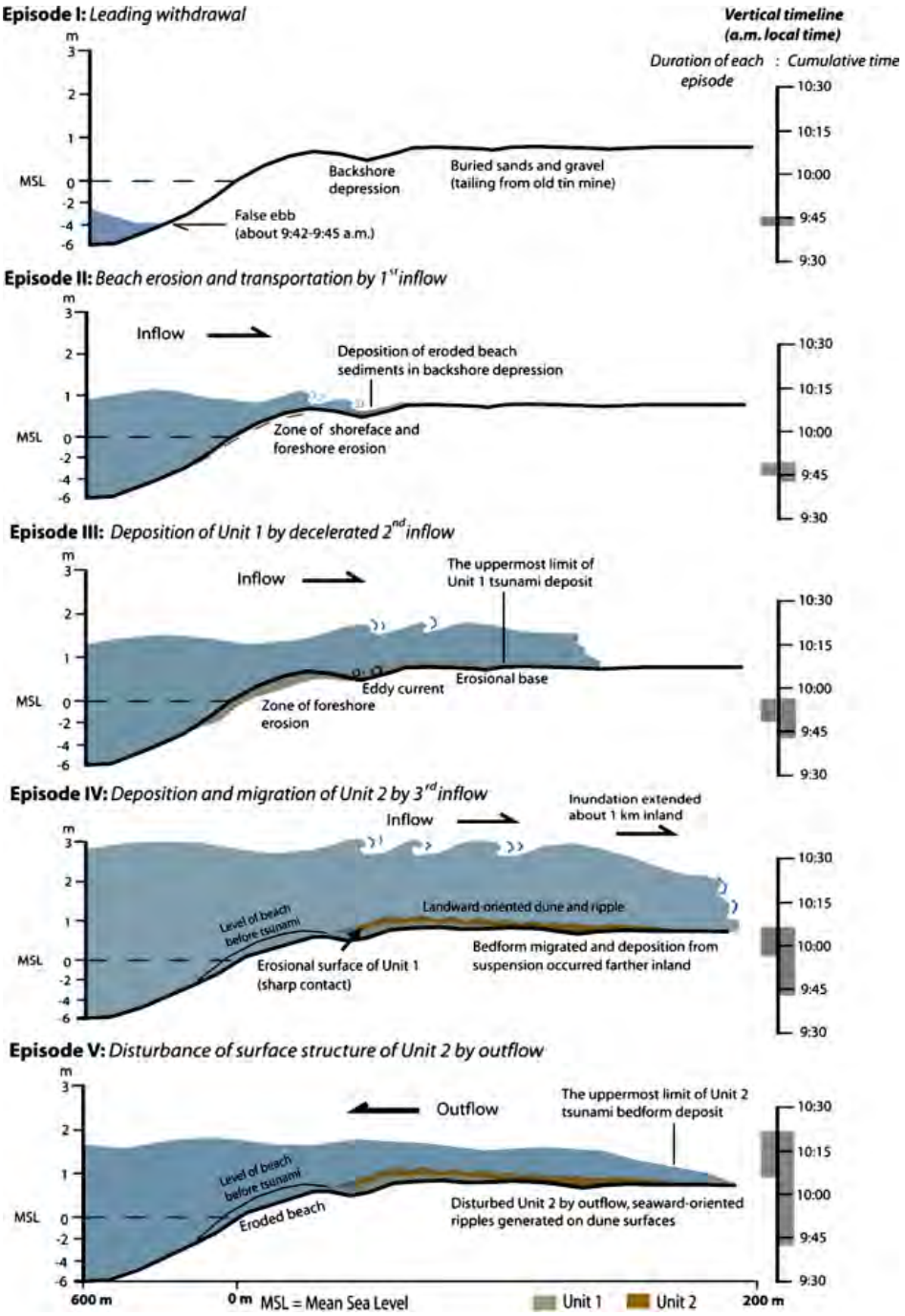

Figure 1.4: Reconstructed hydraulic conditions of the 2004 Indian Ocean tsunami at Bangtao, Phuket. (Choowong et al., 2008, Figure 8)

Liu, 2005; Shi et al., 2012). Older models usually used 2DH Nonlinear Shallow Water Equations (NLSW) with different numerical schemes. However, NLSW models are not able to capture the dispersive behavior of tsunami waves, which can be significant in shallow water and for landslide-induced tsunamis for determining the time history of velocities (Lynett and Liu, 2011). Therefore, Boussinesq models have become a popular tool to simulate tsunamis from deep water to the swash zone. FUNWAVE-TVD (Tehranirad et al., 2011; Shi et al., 2012; Kirby et al., 2013) is an example of the recently improved models implementing a high-order adaptive time-stepping TVD solver for the Boussinesq equations of Chen (2006).

There are a number of previous attempts to model tsunami-induced morphology changes with existing models. Apotsos et al. (2011a) have implemented the Delft3D (Deltares, 2011) model to simulate tsunami sediment transport in Kuala Meurisi, Sri Lanka during the 2004 Indian Ocean tsunami. Although they obtained good agreement with measurements for maximum runup and inundated areas, the calculated sediment deposit thickness at Kuala Meurisi was overpredicted by a factor of 2. More recently, Li and Huang (2013) have studied the change of beach profile under tsunami waves using XBEACH and Delft3D. They simulated sediment movement during tsunami condition for both laboratory and field test cases with different sediment pickup formulations. They showed that using Van Rijn (1985) pickup function generates better results for tsunami flow compared to other available formulas. XBEACH (Deltares, 2010) and Delft3D use NLSW equations for hydrodynamics, which, as mentioned before, neglects dispersive effects of tsunami waves. Several modelers have developed sediment transport models coupled with Boussinesq equations (Long et al., 2006; Teran Cobo et al., 2006; Rahman et al., 2012). More recently, Kim (2015) has generated a morphodynamic model by coupling weakly dispersive Boussinesq equations with a depth-integrated sediment transport model. However, none of these models are calibrated to model tsunami wave conditions and mostly focus on short wave sediment transport modeling. Here, our goal is to couple FUNWAVE-TVD with sediment transport and morphology schemes by considering the physics of tsunami hydrodynamics, to provide

a comparison of the effect of static and dynamic bathymetry assumptions on the levels of tsunami hazard.

Tsunami flow is considered to be quasi-steady for most of its inundation process (Jaffe and Gelfenbaum, 2007; Sugawara et al., 2014). This is because the temporal gradients in mean flow speed are insignificant when averaged over the period of turbulent fluctuations during most of the tsunami inundation. However, inside the surf zone, the flow may be turbulent, and plug flow might form because of high flow acceleration under the tsunami bore. Plug flow is a type of bed instability created under high flow acceleration (Sleath, 1999), which could result in significant bed destabilization and erosion.

One standard procedure to determine if a flow is quasi-steady is to look at flow acceleration averaged over the time scale for the period of changes in flow direction. To investigate if tsunami flow is quasi-steady as well as possibility of plug formation during tsunami inundation, we looked at flow acceleration obtained from simulation of a submarine landslide tsunami in Atlantic City, NJ, which is one of the tsunami hot spots on the USEC (Tehranirad et al., 2014, 2015b-j). Landslide tsunamis have the most fluctuating tsunami signal compared to other tsunami scenarios studied for USEC inundation mapping. This is because landslide-generated tsunamis have shorter wavelengths compared to other sources. Figure 1.5 shows flow properties for this tsunami computed at a point onshore close to the shoreline, where the most significant acceleration and turbulent flows of tsunami occur. Except for a few spikes, the flow acceleration is on the order of 0.001 m/s^2, and the acceleration averaged over 1 minute (which is much smaller than the average period of flow fluctuations) has a maximum value of about 0.1 m/s^2. Based on these numbers, one can infer that the assumption of quasi-steady flow for a tsunami is appropriate. Also, the estimation of the boundary layer thickness ($\delta \sim \sqrt{\nu_t T}$) compared to depth scale of the tsunami in the nearshore shows that quasi-steady assumption for tsunami flow is justifiable. Considering a time scale (T) of about 15 minutes and eddy viscosity of $\nu_t = 10^{-3}$, the boundary layer thickness estimation would be of the order of 1 m, which is similar to the depth scale of

the tsunami flow in the nearshore and during onshore inundation. Thus, the boundary layer thickness during most of the tsunami flow onshore extends up to the surface, meaning that the flow would be in fully developed condition, or in other words quasi-steady.

Because of high acceleration at the tsunami bore front, plug flow formation is possible. To address the plug flow issue, we calculated the Sleath parameter at the same location used for flow condition analysis (Figure 1.5). Foster et al. (2006) provided a description of Sleath parameter based on flow acceleration written as,

$$S(t) = \frac{\partial p/\partial x}{\rho_w (s-1) g} = \frac{Du/Dt}{(s-1)g} \tag{1.1}$$

where s is the sediment specific gravity. Plug flow happens when $S(t)$ is larger than the critical value of 0.29 (Foster et al., 2006). However, as shown at the bottom of Figure 1.5, the Sleath parameter S is almost close to zero for most of the tsunami inundation process. Even the spikes close to the bore's front are small. However, Sleath parameter could probably exceed the critical value at the bore front with higher resolution modeling and smaller time steps. To address this problem in our analysis, we looked at the geometrical features of tsunami bore during onshore inundation. The bore front of the tsunami has the surface gradient of about $\partial\eta/\partial x = 1.0$, and it is in order of hundreds of meters long. However, surface gradient term $\partial\eta/\partial x$ behind bore front is close to zero for a length of several kilometers. Also, considering the hydrostatic approximation for the pressure gradient term ($\partial p/\partial x$) in the Sleath number estimation (1.1), one can use the surface gradient term for a rough estimate of Sleath number ($\partial p/\partial x = \rho g \partial\eta/\partial x$). Thus, we can claim that for most of the tsunami bore propagation onshore, the Sleath number is close to zero and for a small portion of the bore front (which is negligible considering the length scale of tsunami waves) plug formation is possible. Accordingly, we decided to neglect bed destabilization caused by plug flow formation, considering the time and length scales of the tsunami event compared to the time interval and the short bandwidth of high acceleration flow (Figure 1.5). Also, such bed instabilities were not reported in any of the field observations during tsunami

inundation (e.g. Goto et al., 2011a; Udu et al., 2012; Wilson et al. 2012). Sheet flow is the transport of a high-concentration layer of sediment in the near-bed region, and typically occurs when the Shields parameter ($\theta = \tau_b/(\rho g(s-1)d_{50})$) is greater than 1.0 (Sumer et al., 1996). During the inundation process, the Shields parameter exceeds 1.0, and reaches maximum values in the range of 40 to 75 (Figure 1.5), suggesting that sheet flow is occuring. However, the focus of the present work is concentrated on establishing a functional model which couples suspended sediment transport and hydrodynamics during tsunami inundation. Moving forward, the next step should focus on the implementation of the sheet flow transport mode.

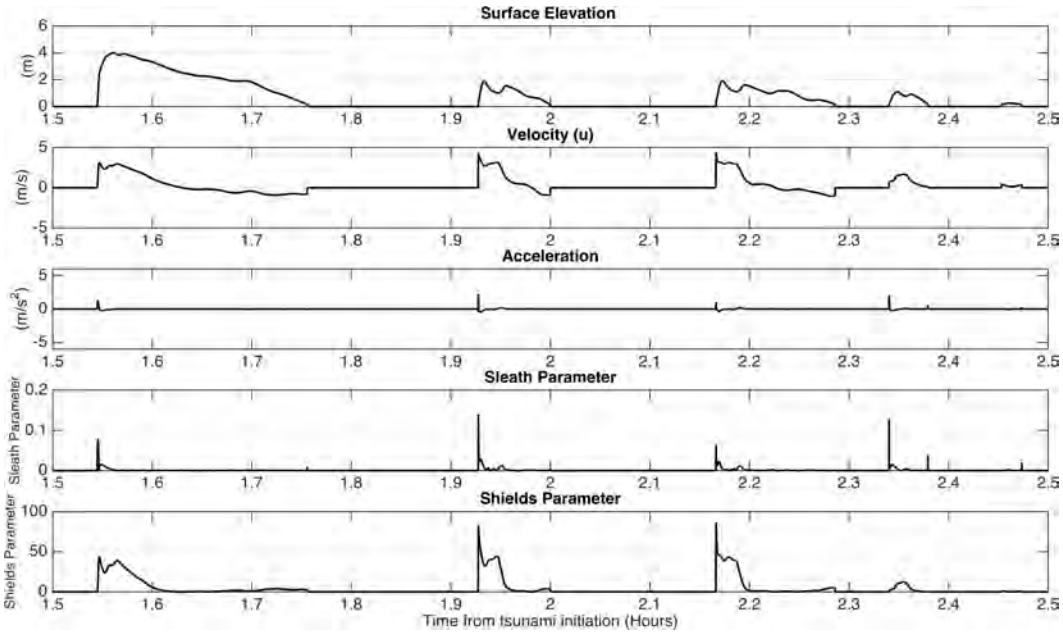

Figure 1.5: Computed gauge data for a submarine landslide tsunami in an onshore location close to Atlantic City, NJ near the shorline.

1.4 Outline of Thesis

In this thesis, we coupled the Advection-Diffusion (AD) continuity equation for sediment transport with the flow solution (FUNWAVE-TVD) to model tsunami sediment transport. In the next chapter, we describe the governing equations for sediment transport. Also, bed evolution equations as well as hard bottom methodology

and slope limiting methods are explained in chapter 2. Next, we provide the numerical implementation of governing equations in chapter 3. Then, in chapter 4, we use the model to simulate two laboratory tests along with a simulation of tsunami-induced morphological changes in Crescent City, CA harbor during the 2011 Japan tsunami as model validations. In chapter 5, we apply the model to investigate the effect of morphological adjustment during tsunami inundation on the levels of hazard. For this purpose, we simulated different tsunami sources for two regions on the USEC with barrier islands, Assateague Island and Ocean City, MD. Finally, in the last chapter, we summarize our work and provide concluding remarks and future directions for the study of tsunami-induced morphological changes.

Chapter 2

GOVERNING EQUATIONS FOR SEDIMENT TRANSPORT AND MORPHOLOGY EVOLUTION

In this chapter, we describe the governing equations used for FUNWAVE-TVD, and explain how the sediment transport module was coupled with hydrodynamic equations to capture morphology changes under various flow conditions. First, a review of governing equations used in FUNWAVE-TVD is provided. Then, the governing equations of sediment motion, as well as morphology evolution equation, are described. Finally, our methodology to limit maximum bottom slope using an avalanching scheme is explained.

2.1 Hydrodynamics Governing Equations

FUNWAVE-TVD solves a set of Boussinesq equations accurate to $O(\mu^2)$ in dispersive effects, where μ is the ratio of water depth to wave length and assumed to be small. Here, we describe the work of Shi et al. (2012) who followed the work of Chen (2006) to obtain model equations for FUNWAVE-TVD. They both started with Nwogu's (1993) description of the horizontal velocity, written as

$$\mathbf{u} = \mathbf{u}_\alpha + \mathbf{u}_2(z), \tag{2.1}$$

to obtain Boussinesq equations accurate to $O(\mu^2)$ where, $\mathbf{u}_\alpha$ is the velocity at the reference elevation $z = z_\alpha$, and $\mathbf{u}_2$ is the depth-dependent velocity correction at $O(\mu^2)$, given by

$$\mathbf{u}_2(z) = (z_\alpha - z)\nabla_h A + \frac{1}{2}\left(z_\alpha^2 - z^2\right)\nabla_h B \tag{2.2}$$

where A and B are given by

$$\begin{aligned} A &= \nabla_h \cdot (h\mathbf{u}_\alpha) \\ B &= \nabla_h \cdot \mathbf{u}_\alpha \end{aligned} \tag{2.3}$$

The difference between the model of Shi et al. (2012) and Chen (2006) is the consideration of the additional effects of variation in time of reference elevation z_α following

$$z_\alpha = \zeta h + \beta\eta \tag{2.4}$$

where h is the still water depth, η is water surface displacement and ζ and β are constants described in Kennedy et al. (2001).

2.1.1 Governing Equations

Shi et al. (2012) extended the equations of Chen (2006) to use a possible moving reference elevation. The corresponding depth-integrated volume conservation equation is given by

$$\eta_t + \nabla_h \cdot \mathbf{M} = 0 \tag{2.5}$$

where

$$\mathbf{M} = H\left\{\mathbf{u}_\alpha + \overline{\mathbf{u}}_2\right\} \tag{2.6}$$

is the horizontal volume flux, $H = h + \eta$ is the total local water depth, and $\overline{\mathbf{u}}_2$ is the depth averaged $O(\mu^2)$ contribution to the horizontal velocity field, defined by

$$\overline{\mathbf{u}}_2 = \frac{1}{H}\int_{-h}^{\eta} \mathbf{u}_2(z)dz = \left(\frac{z_\alpha^2}{2} - \frac{1}{6}(h^2 - h\eta + \eta^2)\right)\nabla_h B + \left(z_\alpha + \frac{1}{2}(h-\eta)\right)\nabla_h A \tag{2.7}$$

The depth-averaged horizontal momentum equation is written as

$$\mathbf{u}_{\alpha,t} + (\mathbf{u}_\alpha \cdot \nabla_h)\mathbf{u}_\alpha + g\nabla_h\eta + \mathbf{V}_1 + \mathbf{V}_2 + \mathbf{V}_3 + \mathbf{R} = 0 \tag{2.8}$$

where g is the gravitational acceleration and $\mathbf{R}$ represents diffusive and dissipative terms including bottom friction and subgrid lateral turbulent mixing. $\mathbf{V}_1$ and $\mathbf{V}_2$ are dispersive Boussinesq terms written as

$$\mathbf{V}_1 = \left\{ \frac{z_\alpha^2}{2} \nabla_h B + z_\alpha \nabla_h A \right\}_t - \nabla_h \left[\frac{\eta^2}{2} B_t + \eta A_t) \right] \tag{2.9}$$

$$\mathbf{V}_2 = \nabla_h \left\{ (z_\alpha - \eta)(\mathbf{u}_\alpha \cdot \nabla_h) A + \frac{1}{2}(z_\alpha^2 - \eta^2)(\mathbf{u}_\alpha \cdot \nabla_h) B + \frac{1}{2}[A + \eta B]^2 \right\} \tag{2.10}$$

The form of (2.9) lets the reference level z_α to be treated as a time-dependent elevation, following the suggestion of Kennedy et al (2001). The expression (2.10) for $\mathbf{V}_2$ was also given by Wei et al (1995), and is not altered by the choice of a fixed or moving reference elevation.

The term $\mathbf{V}_3$ in (2.8) represents the $O(\mu^2)$ contribution to the expression from horizontal vorticity $\boldsymbol{\omega} \times \mathbf{u} = \omega \mathbf{i}^z \times \mathbf{u}$ where $\mathbf{i}^z$ is the unit vector in the z direction. $\mathbf{V}_3$ can be written as,

$$\mathbf{V}_3 = \omega_0 \mathbf{i}^z \times \overline{\mathbf{u}}_2 + \omega_2 \mathbf{i}^z \times \mathbf{u}_\alpha \tag{2.11}$$

where

$$\omega_0 = (\nabla \times \mathbf{u}_\alpha) \cdot \mathbf{i}^z = v_{\alpha,x} - u_{\alpha,y} \tag{2.12}$$

$$\omega_2 = (\nabla \times \mathbf{u}_2) \cdot \mathbf{i}^z = z_{\alpha,x}(A_y + z_\alpha B_y) - z_{\alpha,y}(A_x + z_\alpha B_x) \tag{2.13}$$

z_α can be chosen in a way to optimize the apparent dispersion relation of the linearized model relative to the full linear dispersion (Nwogu, 1993). In particular, the choice of $\alpha = (z_\alpha/h)^2/2 + z_\alpha/h = -2/5$ results in a Padé approximation for the dispersion relation. On the other hand, the choice of $\alpha = -0.39$, corresponds to $z_\alpha = -0.53h$ and minimizes the maximum error in wave phase speed occurring over the range $0 \leq kh \leq \pi$. Kennedy et al. (2001) pointed out that if z_α is allowed to move up and down during the passage of the flow field, a better degree of flexibility in optimizing the nonlinear behavior of the resulting model equations can be achieved. Accordingly, z_α can be written as,

$$z_\alpha = -h + \beta H = (\beta - 1)h + \beta\eta = \zeta h + (1 + \zeta)\eta \tag{2.14}$$

with $\zeta = -0.53$ similar to Nwogu (1993) and $\beta = 1 + \zeta = 0.47$. Thus, the reference elevation is placed at a level 53% of the total local depth below the local water surface, resulting in a σ coordinate approach. In addition, this consideration helps to keep the model reference elevation within the actual water column for all wet points in the entire domain.

2.1.2 Conservative Form of Fully Nonlinear Boussinesq Equations

Shi et al. (2012) implemented the following derivations of the conservative form of the fully nonlinear Boussinesq equations in FUNWAVE-TVD, using $\mathbf{M}$ from (2.6) together with the vector identity

$$\nabla_h \cdot (\mathbf{u} \otimes \mathbf{u}) = (\mathbf{u} \cdot \nabla_h)\mathbf{u} + \mathbf{u}(\nabla_h \cdot \mathbf{u}) \tag{2.15}$$

Multiplying (2.8) by total water depth $H = h + \eta$, and using the descriptions in (2.20) and (2.15), the momentum equation can be written as,

$$\begin{aligned} &\mathbf{M}_t + \nabla_h \cdot \left(\frac{\mathbf{MM}}{H}\right) + gH\nabla_h\eta \\ &= H\left\{\overline{\mathbf{u}}_{2,t} + \mathbf{u}_\alpha \cdot \nabla_h \overline{\mathbf{u}}_2 + \overline{\mathbf{u}}_2 \cdot \nabla_h \mathbf{u}_\alpha - \mathbf{V}_1 - \mathbf{V}_2 - \mathbf{V}_3 - \mathbf{R}\right\} \end{aligned} \tag{2.16}$$

where $\mathbf{M}$ is the flux term described in 2.6. The time derivative dispersion terms are separated in $\mathbf{V}_1$ according to

$$\mathbf{V}_1 = \mathbf{V}'_{1,t} + \mathbf{V}''_1 \tag{2.17}$$

where

$$\mathbf{V}'_1 = \frac{z_\alpha^2}{2}\nabla_h B + z_\alpha \nabla_h A - \nabla_h\left[\frac{\eta^2}{2}B + \eta A\right] \tag{2.18}$$

and

$$\mathbf{V}''_1 = \nabla_h\left[\eta_t(A + \eta B)\right] \tag{2.19}$$

The hybrid numerical scheme used in FUNWAVE-TVD requires a conservative form of continuity equation and momentum equations (Shi et al., 2012). A well-balanced scheme is obtained by a reformulation of the surface gradient term regarding deviations from an unforced but separately specified equilibrium state written as,

$$gH\nabla_h\eta = \nabla_h\left[\frac{1}{2}g(\eta^2 + 2h\eta)\right] - g\eta\nabla_h h \tag{2.20}$$

Shi et. al (2012) showed that using this definition for the surface gradient term results in a well-balanced solution, without adding noise for a rapidly varying bathymetry.

Using (2.20), (2.18) and (2.19), the conservative form of momentum equation can be written as,

$$\begin{aligned} &\mathbf{M}_t + \nabla \cdot \left[\frac{\mathbf{MM}}{H}\right] + \nabla \left[\frac{1}{2} g(\eta^2 + 2h\eta)\right] = \\ &= H\left\{\overline{\mathbf{u}}_{2,t} + \mathbf{u}_\alpha \cdot \nabla \overline{\mathbf{u}}_2 + \overline{\mathbf{u}}_2 \cdot \nabla \mathbf{u}_\alpha - \mathbf{V}'_{1,t} - \mathbf{V}''_1 - \mathbf{V}_2 - \mathbf{V}_3 - \mathbf{R}\right\} + g\eta\nabla h \end{aligned} \tag{2.21}$$

In order to apply the Runge-Kutta adaptive time-stepping scheme used in FUNWAVE-TVD, the equation can be rewritten by combining the time derivatives ($\bar{u}_{2,t}$ and $\mathbf{V}'_{1,t}$) on both sides of the (2.21), and rewrite it as follows,

$$\begin{aligned} \mathbf{V}_t \quad &+\nabla \cdot \left[\frac{\mathbf{MM}}{H}\right] + \nabla \left[\frac{1}{2} g(\eta^2 + 2h\eta)\right] = \eta_t(\mathbf{V}'_1 - \overline{\mathbf{u}}_2) \\ &+H\left(\mathbf{u} - \mathbf{V}''_1 - \mathbf{V}_2 - \mathbf{V}_3 - \mathbf{R}\right) + g\eta\nabla h \end{aligned} \tag{2.22}$$

where

$$\mathbf{V} = H(\mathbf{u}_\alpha + \mathbf{V}'_1) \tag{2.23}$$

Equations (2.5) and (2.23) are the governing equations solved in FUNWAVE-TVD. After the construction of $\mathbf{V}$ by using (2.5) to estimate η_t, the velocity $\mathbf{u}_\alpha$ can be calculated by solving a tridiagonal system of equation based on (2.23), in which all cross-derivatives are moved to the right-hand side of the equation.

2.2 Governing Equations for Sediment Motion

For this work, we couple FUNWAVE-TVD to a sediment transport and morphology sub-model. FUNWAVE-TVD uses depth-averaged quantities of the flow; therefore, it is required to obtain the equation for depth-averaged sediment concentration for proper coupling with the model. Accordingly, we start with the 3D advection-diffusion equation for suspended sediment load, written as follows,

$$\frac{\partial c}{\partial t} + \frac{\partial (uc)}{\partial x} + \frac{\partial (vc)}{\partial y} + \frac{\partial ((w - w_f)c)}{\partial z} = \nabla_h (k \nabla c) + \frac{\partial}{\partial z}(\epsilon \frac{\partial c}{\partial z}) \tag{2.24}$$

where c is the non-dimensional sediment concentration normalized by sediment density ($c = c'/\rho_s$), u,v, and w are flow velocities in x,y and z directions, w_f is the sediment fall velocity, k (m^2/s) is the horizontal sediment diffusion coefficient, and ϵ (m^2/s) is the sediment vertical mixing coefficient. Considering the equilibrium suspended concentration, where $\partial/\partial x = \partial/\partial y = \partial/\partial t = 0$, the basic equation for suspended sediment concentration can be written as,

$$cw_f + \epsilon \frac{\partial c}{\partial z} = 0 \tag{2.25}$$

Using the above equation, the analytical solution for suspended sediment concentration profile can be written using a mixing coefficient (ϵ) as,

$$c(z) = c_0 G(z) \simeq c_0 \exp(-\frac{w_f}{\epsilon}(z+h)) \tag{2.26}$$

where c_0 is sediment concentration at a reference elevation above the bed ($a = 0.01H$), and $G(z)$ is a vertical concentration distribution. Using this definition, the depth-averaged sediment concentration ($\bar{c}$) is defined by,

$$\bar{c} = \frac{1}{h+\eta} \int_{-h}^{\eta} c_0 G(z) dz \tag{2.27}$$

The reference concentration (c_0) can be written as follows,

$$c_0 = \frac{\bar{c}}{\frac{1}{h+\eta}\int_{-h}^{\eta} G(z)dz} = \frac{\bar{c}}{\beta_d} \tag{2.28}$$

where β_d is a conversion function and can be obtained from the vertical mixing coefficient (ϵ) definition. Van Rijn (1985) suggested a distribution for ϵ for currents and short waves. Here, we only consider the current-related mixing coefficient, and the wave-related term is neglected. This is due to the quasi-steady assumption for the tsunami flow, which is discussed in the previous chapter. Van Rijn's (1985) current-related mixing coefficient is written as,

$$\begin{aligned} \epsilon &= \epsilon_{max}\big(1 - \frac{z}{h}\big)^b \qquad z < 0.5h \\ \epsilon &= \epsilon_{max} = 0.25\kappa u_{*c} h \qquad z > 0.5h \end{aligned} \tag{2.29}$$

where $\kappa = 0.4$ is the von Karman constant. In the above equation if $b = 1$, then the approximation for mixing coefficient in the bottom half of the flow depth would be linear where ϵ is zero at the bed. Here we set $b = 2$ which would result in a parabolic approximation. Also, u_{*_c} is the bed shear velocity described by

$$u_{*_c} = \frac{\kappa}{-1 + \log\left(\frac{30H}{k_s}\right)} U_c \tag{2.30}$$

in which ($U_c = \sqrt{U^2 + V^2}$) is depth-averaged total velocity ($\mathbf{u}$ from (2.1)), $k_s = 2.5 d_{50}$ is Nikuradse roughness coefficient, and d_{50} is the median grain diameter. Using the definitions in (2.28)-(2.30), the analytical solution for β_d for an exponential profile of suspended sediment concentration can be written as

$$\beta_d = \frac{1}{h+\eta} \frac{\bar{\epsilon}}{w_f} \left(1 - \exp\left(-\frac{w_f}{\bar{\epsilon}}(h+\eta)\right)\right) \tag{2.31}$$

where

$$\bar{\epsilon} = \frac{1}{h+\eta} \int_{-h}^{\eta} \epsilon dz \tag{2.32}$$

In order to obtain the depth-averaged sediment transport, we integrated (2.24) over total depth. Integration in the z direction will reduce the vertical derivative terms ($\frac{\partial}{\partial z}$) into physical boundary conditions at the free surface and the bottom. At the surface, the vertical sediment flux is zero, resulting in

$$\epsilon \frac{\partial c}{\partial z} + w_f c = 0 \qquad (z = \eta) \tag{2.33}$$

At the bottom, mass exchange of sediment occurs resulting in sediment erosion and deposition. The mass transfer at the bottom can be described as a downward flux (D), and an upward erosional flux (P), also known as deposition and pickup rates, resulting in the following definition,

$$\epsilon \frac{\partial c}{\partial z} + w_f c = D - P \qquad (z = -h) \tag{2.34}$$

For this study, we use van Rijn's (1985) definition of pickup rate (P). Van Rijn (1985) conducted numerous laboratory and field tests to calibrate his formula, which

can be used with depth-averaged information of the flow, making it appropriate for our model. Also, several researchers have reported that his pickup function works properly for flow conditions similar to that of a tsunami. For instance, Li and Huang (2013) have conducted numerical simulations of sediment transport using several pickup functions, including Bagnold (1966). After modeling several solitary wave experiments as well as tsunami field tests, they showed that calculated bottom changes with van Rijn's (1985) formulation had the least error compared to other pickup functions they used using feild and laboratory measurements. Thus, here we use Van Rijn (1985) pickup rate that can be written as,

$$P = 0.015 \frac{d_{50}}{a} \left(\frac{|\tau_b| - \tau_{cr}}{\tau_{cr}} \right) d_*^{-0.3} w_f \tag{2.35}$$

where a is a reference elevation and is a function of total depth ($a = 0.01H$), τ_b is the bed shear stress, and τ_{cr} is the critical shear stress. P has the dimension of velocity (m/s) considering the advection-diffusion equation for non-dimensional sediment concentration ($c = c'/\rho_s$). d_* is dimensionless grain size defined as

$$d_* = d_{50} \left(\frac{(s-1)g}{\nu^2} \right)^{1/3} \tag{2.36}$$

where s is the specific gravity of the sediment. The critical bed shear stress τ_{cr} used in (2.35) is defined as,

$$\tau_{cr} = \rho_w (s-1) g d_{50} \theta_{cr} \tag{2.37}$$

where θ_{cr} is the critical Shields parameter, approximately equal to 0.05. Based on the roughness estimate, the shear stress is expressed as

$$|\tau_b| = \frac{\rho_w \kappa^2}{(-1 + \log(30H/k_s))^2} U_c^2. \tag{2.38}$$

A simple approach to estimate the deposition rate (D) in (2.34) is to use the reference sediment concentration close to the bed (c_0, (2.28)) and multiply it by sediment fall velocity resulting in the following definition,

$$D = c_0 w_f \tag{2.39}$$

which has same dimension the pickup rate for non-dimensional sediment concentration ($c = c'/\rho_s$). This definition of the deposition rate uses β_d to assess c_0. However, this method calculates large deposition rates in small depths close to the shoreline. β_d would be overestimated with total depth at the bottom of (2.31), resulting in wrong assessments for reference concentration (c_0) and deposition rate (D). To avoid this problem, here we use the formula of Cao (1999) for the deposition rate (D) in (2.34), given by

$$D = \gamma \bar{c} w_f (1 - \gamma \bar{c})^{m_0}, \tag{2.40}$$

where γ =min$[2, (1-n)/\bar{c}]$, n is sediment porosity, and m_0 is a constant number given by 2.0. Cao (1999) obtained this formula from the balance between bed sediment erosion and suspended sediment deposition across the near-bed boundary, using the product of near-bed concentration and hindered settling velocity of sediment. He used laboratory data (mostly dam-break tests) to calibrate and verify his approach.

To obtain depth-averaged sediment transport equation, (2.24) is integrated over the total depth, which results in the following,

$$\int_{-h}^{\eta} \frac{\partial c}{\partial t} dz + \int_{-h}^{\eta} \nabla_h \cdot (c\mathbf{u}) dz + \int_{-h}^{\eta} \frac{\partial ((w - w_f)c)}{\partial z} dz - \int_{-h}^{\eta} \nabla_h \cdot (k \nabla_h c) dz - \int_{-h}^{\eta} \frac{\partial}{\partial z} (\epsilon \frac{\partial c}{\partial z}) dz = 0 \tag{2.41}$$

Horizontal gradients can be moved out of the integral using Leibniz's rule in the above equation, while the residual boundary terms are canceled out with each other, resulting in the following equation,

$$\frac{\partial}{\partial t} \int_{-h}^{\eta} c dz + \nabla_h \cdot \int_{-h}^{\eta} (c\mathbf{u}) dz + \left[\epsilon \frac{\partial c}{\partial z} + w_f c \right]_{-h}^{\eta} - \nabla_h \cdot (k \nabla_h \int_{-h}^{\eta} c dz) = 0 \tag{2.42}$$

Moreover, considering Nwogu's (1993) description of horizontal velocity (2.1), horizontal advection term in the left-hand side of the (2.42) can be written as,

$$\nabla_h \cdot \int_{-h}^{\eta} (c\mathbf{u}) dz = \nabla_h \cdot (\mathbf{u} \int_{-h}^{\eta} c dz) + O(\mu^2) \tag{2.43}$$

considering the leading order terms. Using (2.27), (2.33), (2.34), and (2.43) in (2.42) results in the following description for the depth-averaged sediment transport,

$$(\bar{c}H)_t + \nabla_h \cdot (\bar{c}H(\mathbf{u}_\alpha + \bar{\mathbf{u}}_2)) = \nabla_h \cdot (kH(\nabla_h \bar{c})) + P - D + O(\mu^2) \tag{2.44}$$

where $H(\mathbf{u}_\alpha + \bar{\mathbf{u}}_2) = \mathbf{M}$ represents flow rates per unit width in the x and y directions. The horizontal sediment diffusion coefficient k is calculated by the equation proposed by Elder (1959),

$$k = 5.93 u_{*_c} H \tag{2.45}$$

where u_{*c} is the shear velocity and can be obtained from (2.30). Figure 2.2 demonstrates the domain that (2.44) is solved for. In this definition of the conservation law for sediment, the bed load is neglected. Tsunami sediment transport is expected to be suspension-dominant, and bed load can be neglected (Goto et al., 2011a). To investigate if the bed load is neglectable for tsunami flow conditions, we use the Van Rijn's (1985) definition of suspended and bed loads through for a flow depth of 1 m, which is the depth scale of tsunami during onshore inundation. The Van Rijn's (1985) suspended load and bed load formula are written as,

$$q_s = 0.012 \frac{0.012 U_c (U - U_{cr})^{2.4} d_{50} d_*^{-0.6}}{((s-1) g d_{50})^{1.2}} \tag{2.46}$$

$$q_b = 0.05 U_c h \frac{0.012 U_c (U - U_{cr})^{2.4}}{((s-1) g d_{50})^{1.2}} (\frac{d_{50}}{h})^{\frac{1}{3}} \tag{2.47}$$

where U_{cr} is the critical velocity corresponding to τ_{cr}. Figure 2.1 shows the ratio of bed load over suspended load for various grain sizes (d_{50}). For coarse sand ($d_{50} \simeq 1mm$), the bed load is less than 5 percent of the suspended load, where this ratio is even smaller for fine sand ($d_{50} < 0.2mm$). Accordingly, we decided to neglect bed load effects in our analysis.

The sediment transport rate in the x direction q_{sx} shown in Figure 2.2 is defined as follows,

$$q_{sx} = \bar{c}(\mathbf{u})H - kH \frac{\partial \bar{c}}{\partial z} \tag{2.48}$$

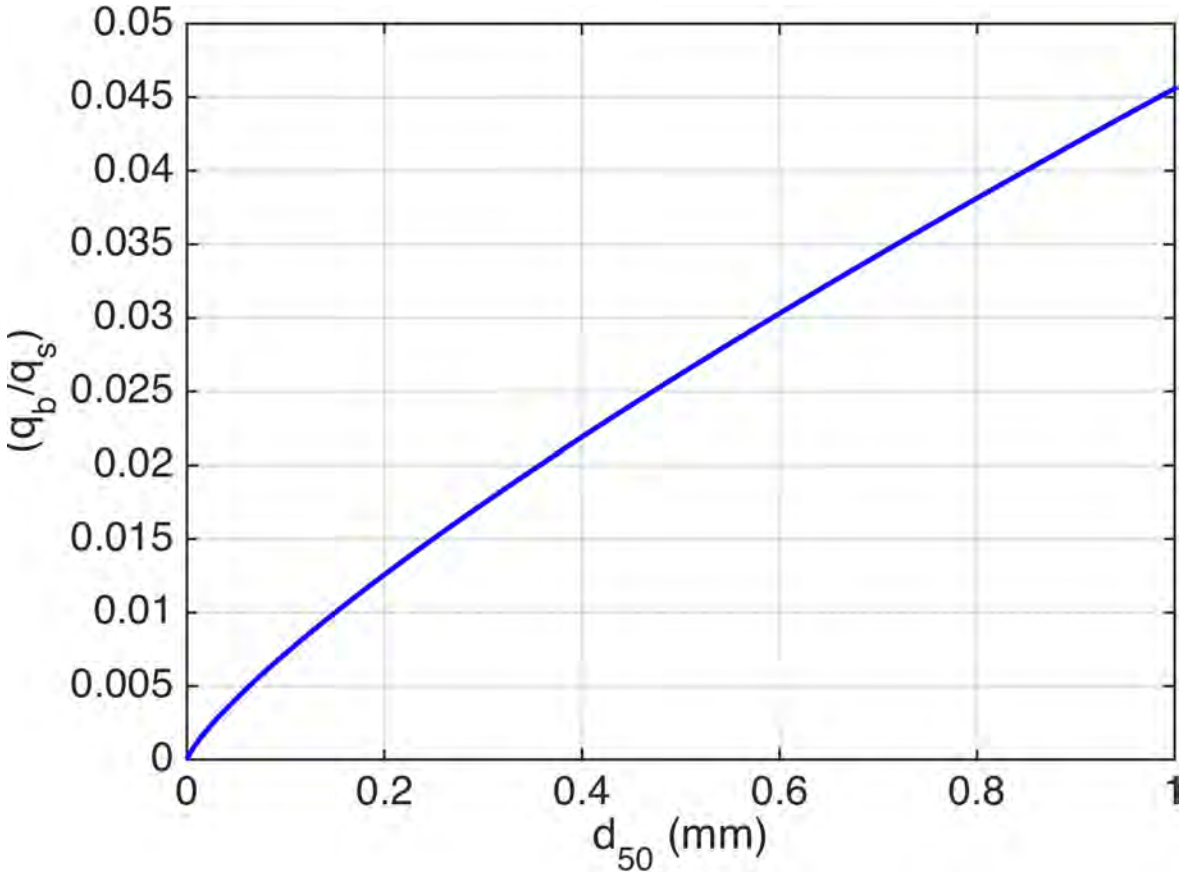

Figure 2.1: The ratio of bed load over suspended load for depth of 1 m for sand ($d_{50} < 1.0mm$).

The horizontal boundary conditions for (2.44) can be defined using the above definition of the transport rate. For closed boundaries, the sediment flux q_{sx} is set to be zero, and for open boundaries the gradient of the transport rate is zero. Thus, the boundary conditions for 2.44 can be written as,

$$\begin{aligned} q_{sx} &= 0 \qquad \text{closed boundary} \\ \frac{\partial q_{sx}}{\partial x} &= 0 \qquad \text{open boundary} \end{aligned} \tag{2.49}$$

Similar boundary conditions are applied for the y direction. Finally, (2.44) needs to be coupled with a sediment continuity equation for bed evolution calculations, which is described in the next section.

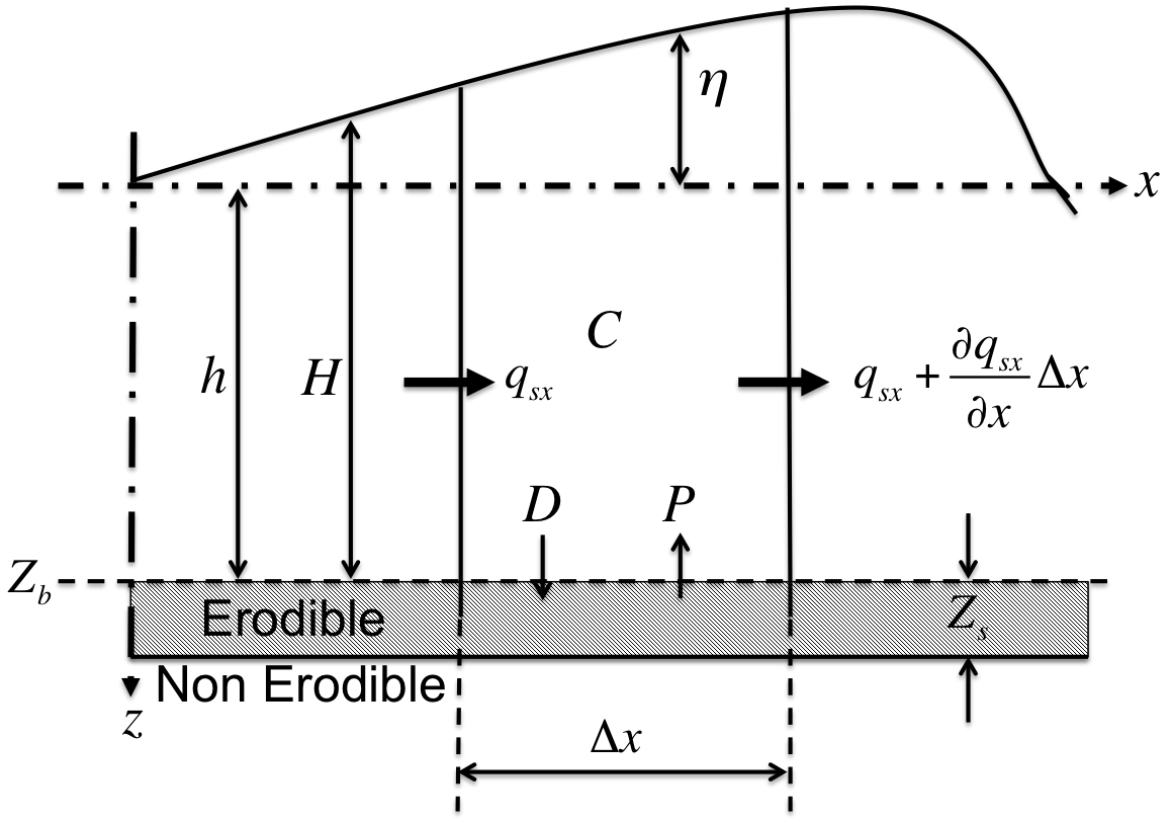

Figure 2.2: Definition of continuity of sediment transport.

2.3 Sediment Continuity Equation

Depth change for the depth-averaged Advection-Diffusion (AD) equation is calculated by the sediment continuity equation, in which the time-averaged pickup and deposition rates are used. In this approach, two-time steps are defined. The sediment continuity equation is written as,

$$\frac{d\bar{Z}_b}{dt} = \frac{1}{1-n}\left(\bar{P} - \bar{D}\right) \tag{2.50}$$

where $\bar{Z}_b(\mathbf{x}, t)$ is the time-averaged depth changes with positive values for erosion and negative values for deposition, n is the sediment porosity, and $\bar{P}$ and $\bar{D}$ are the time-averaged pickup and deposition rates averaged over dt_{morph}. $\bar{Z}_b$, $\bar{P}$, and $\bar{D}$ are averaged over $dt_{morph} = 5 \sim 20dt$, which is recommended to be small enough to capture changes in flow direction (Buttolph et al., 2006). Using time-averaged values in (2.50) helps the model to avoid computing small fluctuation on the bed, which could cause instabilities during simulation. However, using time averaged erosion and deposition rates in sediment continuity equation (2.50) causes conservation problems because instantaneous rates are used in sediment transport equation (2.45) for sediment pickup. We address this issue in section 4.1.3.

2.4 Hard Bottom Methodology

Representation of non-erodible surfaces provides the ability to model mixed bottom types with a single simulation. Here, to consider hard bottom methodology in our calculations, we considered a limited column of erodible sand with the thickness of Z_s (Figure 2.2) over a hard bottom. Because the bed load is neglected in our computation, the hard bottom methodology can be easily implemented by forcing the pickup rate P to be zero wherever there is no erodible sand. Therefore, the hard bottom condition can be described as,

$$P = \bar{P} = 0; \qquad \bar{Z}_b(\mathbf{x}, t) = Z_s(\mathbf{x}) \tag{2.51}$$

This condition is implemented both in the AD and sediment continuity equations.

2.5 Slope Limiting Methodology

For this study, we use an avalanching algorithm to control the maximum bottom slope. By definition, the bottom slope cannot exceed the repose angle of the sediment; avalanching occurs to reform a bed with the maximum slope equal to the sediment repose angle. The repose angle is dependent on the sand grain properties (Usually, between 30^o to 40^o), and can be given to the model as an input value. We used the method of Larson and Kraus (1989) to limit the bed slope. The implementation of the avalanche scheme is described in section 3.5.

2.6 Sand Conservation

It is essential for any sediment transport simulation to conserve sediment throughout the modeling process. The model must assure that the amount of sand eroded from the bed is equal to the amount of suspended sediment in the water columns. Here, we use the following expression derived from (2.44) and (2.51) to ensure sediment conservation,

$$\iint_A \Big[(\bar{c}H)_t + \nabla_h \cdot \mathbf{Q}_s = (1-n)\frac{\partial Z_b}{\partial t}\Big] dA \tag{2.52}$$

where A is the domain area, and $\mathbf{Q_s}$ is sediment flux written as,

$$\mathbf{Q}_s = \bar{c}\mathbf{u}H - kH\nabla_h\bar{c} \tag{2.53}$$

Then, we assume that A is time independent, and apply Green's theorem to (2.52), which results in the following expression of sand conservation,

$$\frac{\partial}{\partial t}\Big[\iint_A (\bar{c}H)dA\Big] + \oint_{\delta A} \mathbf{Q}_s.\mathbf{n}ds = (1-n)\frac{\partial}{\partial t}\Big[\iint_A Z_b dA\Big] \tag{2.54}$$

where s is the boundary of the area A, $\mathbf{n}$ is the outward-pointing unit normal vector on the boundary, and n is the sediment porosity. The first term on the left-hand side of the above equation is suspended sediment, and the second term represents the horizontal fluxes at the boundaries. The term on the right-hand side is the volume

of eroded sand from the bottom. (2.54) can be written as follows to obtain sediment conservation equation,

$$\frac{\partial}{\partial t}\iint_{A}\Big[(\bar{c}H)-(1-n)Z_b\Big]dA=-\oint_{\delta A}\mathbf{Q}_s.\mathbf{n}ds \tag{2.55}$$

For closed boundary conditions, the right-hand side of the above equation which represent fluxes at the boundaries is zero. After the avalanching procedure is implemented, and the sand conservation checked, the updated bed information is transferred to hydrodynamics using updated total depth values ($H=\eta+h+Z_b$). In the next chapter, we explain the numerical implementation of AD equation for depth-average sediment concentration as well as sediment continuity equation ((2.44) and (2.50)).

Chapter 3

NUMERICAL IMPLEMENTATION OF THE GOVERNING EQUATIONS

In this chapter, a description of the numerical implementation of the governing equations is provided. First, we provide a brief review of FUNWAVE-TVD numerics as well as where in the model the modifications are made to integrate the hydrodynamics with sediment transport and morphology modules. Then, we describe the numerical discretization used to solve the sediment concentration Advection-Diffusion (AD) equation (2.44). Two different approaches were used in this study to spatially discretize the AD equation, an Upwind scheme and a TVD-MUSCL scheme similar to FUNWAVE-TVD. A comparison between these two approaches is also provided. Finally, our numerical implementation of boundary conditions, hard-bottom methodology, and morphology module is described. Model validation tests are discussed in chapter 4.

3.1 FUNWAVE-TVD (Shi et al, 2012)

The governing equations in FUNWAVE-TVD are discretized on a regular grid using a hybrid finite-volume/finite-difference approach. The code uses the MUSCL-TVD scheme and the HLL approximate Riemann solver. A MUSCL-TVD scheme up to 4th-order in space and a third-order Strong Stability-Preserving (SSP) Runge-Kutta scheme in time were adopted (Shi et al., 2012).

The wave breaking scheme follows the approach of Tonelli and Petti (2009) who successfully used the ability of Nonlinear Shallow Water Equation (NSWE) with a TVD scheme to model moving hydraulic jumps. The Boussinesq equations are switched to NSWE at cells where the Froude number exceeds a certain threshold. Following Tonelli

and Petti (2009), the ratio of wave amplitude to total water depth is chosen as the criterion to switch from Boussinesq to NSWE. The threshold value is set to be 0.8.

FUNWAVE-TVD uses a non-staggered grid, where the velocity terms (U, V), and total depth (H) are located at the center of each grid cell. The flux terms are calculated at the cell faces to be used in the Riemann solver. Figure 3.1 shows the gridding used in FUNWAVE-TVD, as well as where the sediment variables are introduced to the model.

The wetting-drying scheme used for modeling the moving boundary is straightforward. The normal flux (Figure 3.1) at the cell interface of a dry cell is set to zero. A mirror boundary condition is applied to the high-order MUSCL-TVD scheme and discretization of dispersive terms at dry cells. The technique to locate the moving shoreline during runup is based on the volume of water entering the dry cells, using computed total depth $(H = h + \eta)$. This process is performed using a minimum depth value (H_{min}) as the determining criteria. If the fluid depth for a dry cell is greater than the threshold (H_{min}), the cell is inundated, and at the next time step the cell will be treated as a wet point. The drying scheme which locates the dry cells during the rundown works in similar fashion to the wetting procedure. If a wet cell has lower total depth value than the minimum depth, the cell is removed from the computational domain and becomes a dry cell. The cell face between a wet cell and a dry cell is treated as a closed boundary, where Riemann solver flux terms are forced to be zero. This technique has been successfully used to locate the shoreline in previous works (e.g. Brocchini et al., 2002), and Tehranirad et al. (2013) showed that this scheme can predict runup for various laboratory and field tsunami benchmark tests with error margins less than 20 percent.

3.2 Sediment Transport Module

Figure 3.2 demonstrates a flow chart of the numerical steps implemented in FUNWAVE-TVD to solve the hydrodynamic equations of a flow field. The red boxes in this figure show the location of the modification made to the code to integrate sediment

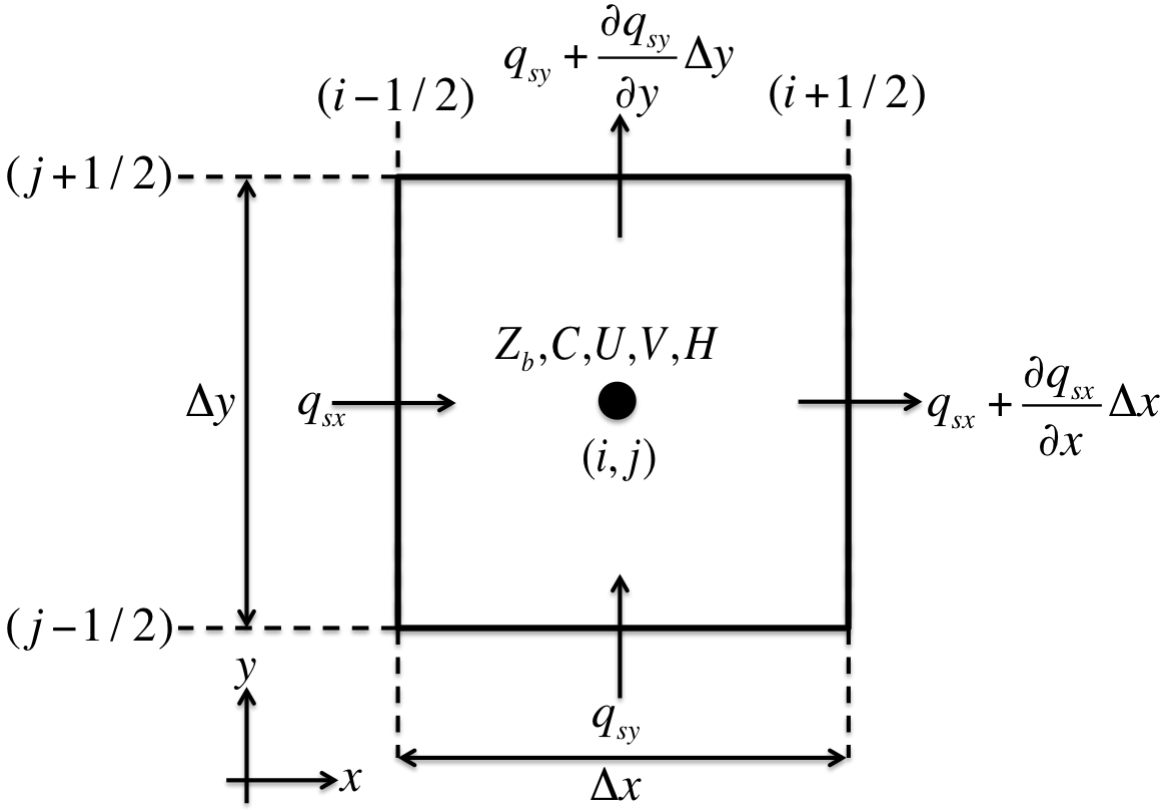

Figure 3.1: The staggered grid used in FUNWAVE-TVD with velocities, sediment concentration, and depth values at the cell center and the fluxes on the cell faces.

transport and morphology modules with hydrodynamics. In this section, we explain how the AD equation is numerically discretized to track sediment movement during the tsunami event. There are numerous methods to discretize (2.44) numerically. For this purpose, Upwind schemes have been tested successfully over years (e.g. Buttolph et al., 2006). Although Upwind schemes have been shown to have acceptable stability, their disadvantage is that they are known to be numerically diffusive. To avoid this problem, most finite volume models now employ shock-capturing schemes like MUSCL-TVD to spatially discretize the AD equation. Thus, we used a similar MUSCL-TVD scheme and the HLL approximate Riemann solver to discretize the Advection-Diffusion Equation. The scheme can be chosen to have 2nd to 4th-order accuracy in space. Also, as in FUNWAVE-TVD, a third-order Stability-Preserving (SSP) Runge-Kutta scheme is used to march the Advection-Diffusion equation (2.44) as well as bed evolution ODE equation (2.50) forward in time. In this chapter, we explain the details of the numerics of these modules. Here, we have implemented both Upwind and MUSCL-TVD schemes to solve the sediment transport problem. We use a pure advection test to illustrate the advantage of the MUSCL-TVD scheme to avoid numerical diffusion compared to the Upwind scheme.

3.2.1 CMS-M2D scheme

For this work, we initially used the finite volume scheme used in CMS-M2D, a depth-averaged circulation model generated by US Army Corps of Engineers (Buttolph et al., 2006). The scheme used here is a Forward-Time Backward Space (FTBS) scheme, accurate to the first order in time and space. The AD equation (2.44) is solved explicitly for depth-averaged concentration with a finite-volume approximation. A staggered grid is used in which depth-averaged concentration C, pickup rate P, and deposition rate D are estimated at each cell center, and fluxes are approximated at the cell faces (Figure 3.1). The numerical discretization of AD equation can be written as,

$$\frac{\Delta C^k_{i,j}}{\Delta t} H^k_{i,j} + \frac{\left(F^k_{i+1/2,j} - F^k_{i-1/2,j}\right)}{\Delta x} + \frac{\left(F^k_{i,j+1/2} - F^k_{i,j-1/2}\right)}{\Delta y} - \left(P^k_{i,j} - D^k_{i,j}\right) = 0 \qquad (3.1)$$

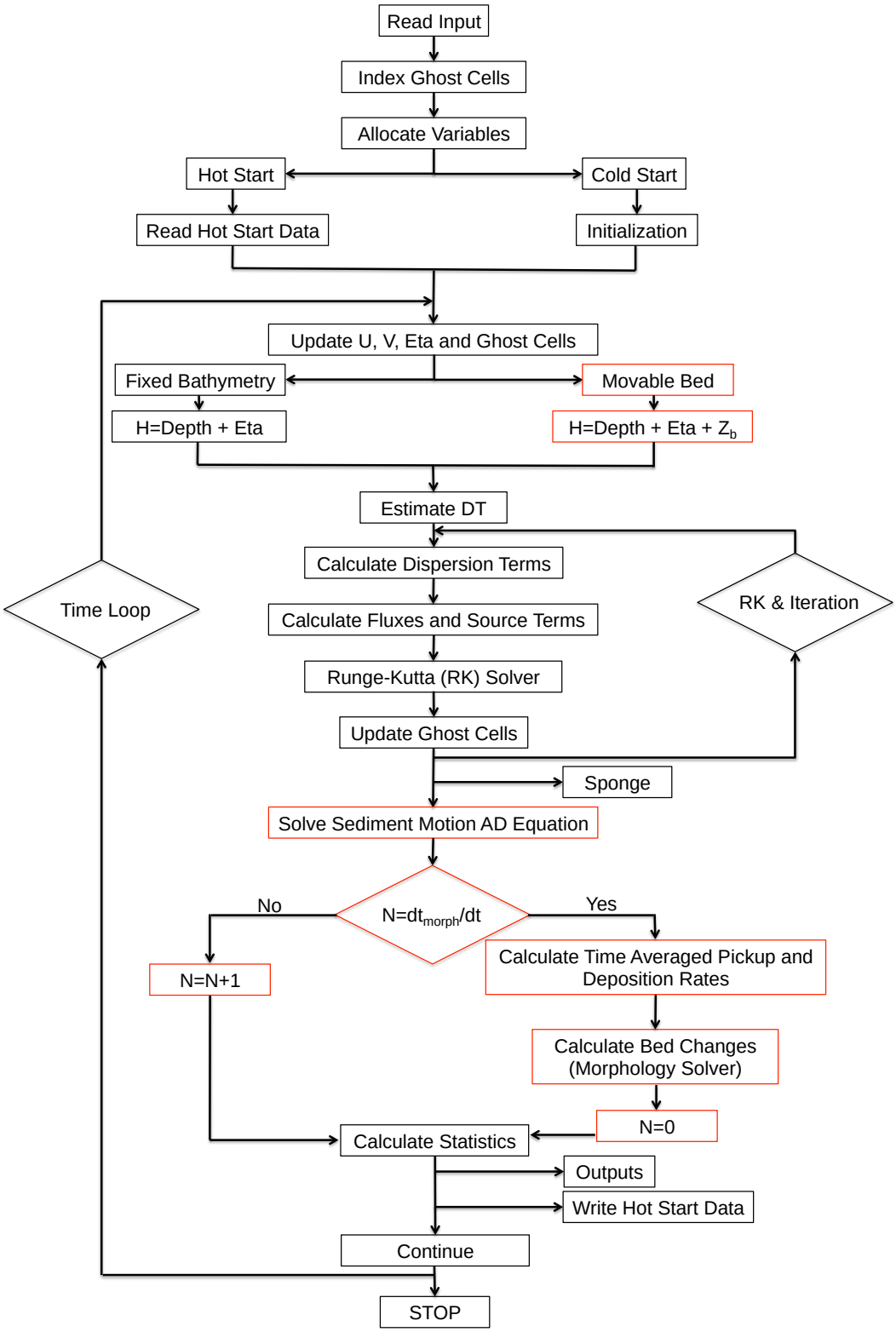

Figure 3.2: Flow chart of FUNWAVE-TVD. Red boxes indicate where modifications are implemented to consider bed changes.

where $\Delta C^k_{i,j} = C^{k+1}_{i,j} - C^k_{i,j}$ with C defined as the depth-averaged non-dimensional sediment concentration normalized by sediment grain density ($C = C'/\rho_s$), $H^k_{i,j}$ is the total depth ($h^k_{i,j} + \eta^k_{i,j}$), i and j are location of the cell center, k is the time step, P and D are pickup and deposition rates, and F represents sediment fluxes at cell faces. The flux terms (F) in (3.1) are written as

$$
\begin{aligned}
F^k_{i+1/2,j} &= C^{*k}_{i+1/2,j} Q^k_{x_{i+1/2,j}} - K^k_{x_{i+1/2,j}} (H^k_{i+1,j} + H^k_{i,j}) \left(\frac{C^k_{i+1,j} - C^k_{i,j}}{2\Delta x} \right) \\
Q^k_{x_{i+1/2,j}} &= U^k_{i+1,j} \left(\frac{H^k_{i,j} + H^k_{i+1,j}}{2} \right) \\
C^{*k}_{i+1/2,j} &= \begin{cases} C^k_{i,j} & \text{if} \quad U^k_{i+1,j} > 0 \\ C^k_{i+1,j} & \text{if} \quad U^k_{i+1,j} < 0, \end{cases}
\end{aligned}
\tag{3.2}
$$

$$
\begin{aligned}
F^k_{i-1/2,j} &= C^{*k}_{i-1/2,j} Q^k_{x_{i-1/2,j}} - K^k_{x_{i-1/2,j}} (H^k_{i,j} + H^k_{i-1,j}) \left(\frac{C^k_{i,j} - C^k_{i-1,j}}{2\Delta x} \right) \\
Q^k_{x_{i-1/2,j}} &= U^k_{i,j} \left(\frac{H^k_{i,j} + H^k_{i-1,j}}{2} \right) \\
C^*_{i-1/2,j} &= \begin{cases} C^k_{i-1,j} & \text{if} \quad U^k_{i,j} > 0 \\ C^k_{i,j} & \text{if} \quad U^k_{i,j} < 0, \end{cases}
\end{aligned}
\tag{3.3}
$$

$$
\begin{aligned}
F^k_{i,j+1/2} &= C^{*k}_{i,j+1/2} Q^k_{y_{i,j+1/2}} - K^k_{y_{i,j+1/2}} (H^k_{i,j+1} + H^k_{i,j}) \left(\frac{C^k_{i,j+1} - C^k_{i,j}}{2\Delta y} \right) \\
Q^k_{y_{i,j+1/2}} &= V^k_{i,j+1} \left(\frac{H^k_{i,j} + H^k_{i,j+1}}{2} \right) \\
C^{*k}_{i,j+1/2} &= \begin{cases} C^k_{i,j} & \text{if} \quad V^k_{i,j+1} > 0 \\ C^k_{i,j+1} & \text{if} \quad V^k_{i,j+1} < 0 \end{cases}
\end{aligned}
\tag{3.4}
$$

$$
\begin{aligned}
F^k_{i,j-1/2} &= C'_{i,j-1/2} Q^k_{y_{i,j-1/2}} - K^k_{y_{i,j-1/2}} (H^k_{i,j} + H^k_{i,j-1}) \left(\frac{C^k_{i,j} - C^k_{i,j-1}}{2\Delta y} \right) \\
Q^k_{y_{i,j-1/2}} &= V^k_{i,j} \left(\frac{H^k_{i,j} + H^k_{i,j-1}}{2} \right) \\
C^{*k}_{i,j-1/2} &= \begin{cases} C^k_{i,j-1} & \text{if} \quad V^k_{i,j} > 0 \\ C^k_{i,j} & \text{if} \quad V^k_{i,j} < 0 \end{cases}
\end{aligned}
\tag{3.5}
$$

which are accurate to the first order in time and space. The sediment diffusion coefficients ($K_{x,y}$) used in (3.2)-(3.5) are defined at cell faces similar to the flux terms. They are calculated as follows,

$$K^k_{x_{i+1/2,j}} = 5.93\left(\frac{u^k_{*c_{i+1,j}} + u^k_{*c_{i,j}}}{2}\right)\left(\frac{H^k_{i+1,j} + H^k_{i,j}}{2}\right) \tag{3.6}$$

$$K^k_{x_{i-1/2,j}} = 5.93\left(\frac{u^k_{*c_{i-1,j}} + u^k_{*c_{i,j}}}{2}\right)\left(\frac{H^k_{i-1,j} + H^k_{i,j}}{2}\right) \tag{3.7}$$

$$K^k_{y_{i,j+1/2}} = 5.93\left(\frac{u^k_{*c_{i,j+1}} + u^k_{*c_{i,j}}}{2}\right)\left(\frac{H^k_{i,j+1} + H^k_{i,j}}{2}\right) \tag{3.8}$$

$$K^k_{y_{i,j-1/2}} = 5.93\left(\frac{u^k_{*c_{i,j-1}} + u^k_{*c_{i,j}}}{2}\right)\left(\frac{H^k_{i,j-1} + H^k_{i,j}}{2}\right) \tag{3.9}$$

The shear velocity ($u_{*c_{i,j}}$) is calculated as follows,

$$u_{*c_{i,j}} = \frac{\kappa U^k_{c_{i,j}}}{-1 + \ln(30H^k_{i,j}/k_s)} \tag{3.10}$$

$U_{c_{i,j}}$ in the above equation is the total velocity estimated using the following equation,

$$U^k_{c_{i,j}} = \sqrt{(U^k_{i,j})^2 + (V^k_{i,j})^2} \tag{3.11}$$

where the velocity terms are obtained from the following definition,

$$U^k_{i,j} = U^k_{\alpha_{i,j}} + U^k_{2_{i,j}} \tag{3.12}$$

$$V^k_{i,j} = V^k_{\alpha_{i,j}} + V^k_{2_{i,j}}, \tag{3.13}$$

corresponding to the reference velocity ($\mathbf{u}_\alpha$) and depth averaged velocity correction ($\bar{\mathbf{u}}_2$) described in (2.1) and (2.7) from FUNWAVE-TVD computations for hydrodynamics.

3.2.1.1 Pickup and Deposition Rates

The pickup rate ($P^k_{i,j}$) is calculated using van Rijn(1985) formula (2.35). The numerical pickup rate calculation is performed using the following definition,

$$P^k_{i,j} = c^k_{0_{i,j}} w_f \tag{3.14}$$

where c_0 is the reference concentration calculated by following definition,

$$c^k_{0_{i,j}} = R0.015\left(\frac{d_{50}}{0.01H_{i,j}}\right)\left(\frac{\tau^k_{b_{i,j}} - \tau_{cr}}{\tau_{cr}}\right)^{1.5} d_*^{-0.3} \tag{3.15}$$

where d_{50} is median grain size, τ_{cr} is critical shear stress (2.37), d_* is dimensionless grain size (2.36), and R is a reduction factor introduced by Buttolph et al. (2006) to avoid overestimation of pickup rate under strong shear stresses defined as follows,

$$R = \min\left(1.0, \frac{0.65}{c_b}\right) \tag{3.16}$$

where

$$c_b = 0.015\left(\frac{\tau^k_{b_{i,j}} - \tau_{cr}}{\tau_{cr}}\right)^{1.5} D_*^{-0.3} \tag{3.17}$$

The bottom shear stress used in (3.15) is given by,

$$\tau^k_{b_{i,j}} = \frac{\rho_w \kappa^2}{\left(-1 + \ln(k_s/30H^k_{i,j})\right)^2}\left(U^k_{c_{i,j}}\right)^2 \tag{3.18}$$

where $k_s = 2.5d_{50}$ is Nikuradse bottom roughness and $\kappa = 0.4$ is von Karman constant. The deposition rate $d^k_{i,j}$ is calculated following the Cao et al. (1999) approach as follows,

$$D^k_{i,j} = \gamma^k_{i,j} C^k_{i,j} w_f \left(1 - \gamma^k_{i,j} C^k_{i,j}\right)^{2.0} \tag{3.19}$$

where,

$$\gamma^k_{i,j} = \min\left(2.0, (1-n)/C^k_{i,j}\right) \tag{3.20}$$

3.2.2 MUSCL-TVD Scheme

In recent years, higher order TVD (Total Variation Diminishing) schemes have become a popular tool for numerical discretization of partial differential equations. The CMS-2D scheme is a first order TVD scheme and proven to be stable. However, they have low accuracy and known to cause numerical diffusion. More recently, higher order TVD schemes have shown to be better suited than first order finite volume schemes for modeling sediment transport and morphology evolution (Long, 2008). A finite-volume

model coupled with Riemann solvers is a good method to generate a TVD scheme able to capture shocks and discontinuities in the model, avoiding the numerical diffusion observed in first order schemes. The generalized conservative form of the AD Equation (2.44) to be used in TVD scheme can be written as follows,

$$\frac{\partial \Psi}{\partial t} + \nabla \cdot \mathbf{F}(\Psi) = S \tag{3.21}$$

where Ψ and $F(\Psi)$ represent the conserved variables and the sediment flux function, given by

$$\Psi = CH \tag{3.22}$$

and

$$\mathbf{F} = CH\mathbf{u} - KH(\nabla C) \tag{3.23}$$

where $\mathbf{u} = (\mathbf{u}_\alpha + \bar{\mathbf{u}}_2)$ is the velocity vector, $H = h + \eta$ is the total water depth, and $C = \frac{C'}{\rho_s}$ is the dimensionless depth-averaged sediment concentration in the water column.The sediment diffusion coefficient (K) used in (3.23) is calculated at cell faces similar to the CMS-2D scheme, using (3.6)-(3.9). The source term S on the right-hand side of the (3.21) is the difference between the pickup rate (P) and the deposition rate (D) at the center of each cell written as follows,

$$S = P - D \tag{3.24}$$

The pickup rate (P) is calculated at the cell centers, using van Rijn's (1985) formula same as in the Upwind scheme using (3.14)-(3.18). Similarly, the deposition rate (D) is also calculated at the cell centers using (3.19) and (3.20).

A combined finite-volume and finite-difference method is applied to construct the flux terms (F) in (3.21) at cell interfaces. Similar to FUNWAVE-TVD hydrodynamics, the first-order derivative terms are discretized using the high-order MUSCL-TVD scheme introduced by Yamamoto et al. (1998). The advection term ($\nabla_h(CH\mathbf{u})$) on the right-hand side of (3.23) is treated using the 4th-order compact MUSCL scheme, which can be simply set up to have lower accuracy down to 2nd order. Ordinary finite-difference discretization is used for $\nabla_h \cdot C$ inside the diffusion term in (3.23). The

combined form of the interface construction for the flux terms (F) (defined by (3.23)) in x and y directions can be written as follows:

$$F^L_{i+1/2} = F_i + \frac{1}{4}\left[(1-\kappa_1)\chi(r)\Delta^* F_{i-1/2} + (1+\kappa_1)\chi(1/r)\Delta^* F_{i+1/2}\right] \tag{3.25}$$

$$F^R_{i-1/2} = F_i - \frac{1}{4}\left[(1+\kappa_1)\chi(r)\Delta^* F_{i-1/2} + (1-\kappa_1)\chi(1/r)\Delta^* F_{i+1/2}\right] \tag{3.26}$$

$$F^L_{j+1/2} = F_j + \frac{1}{4}\left[(1-\kappa_1)\chi(r)\Delta^* F_{j-1/2} + (1+\kappa_1)\chi(1/r)\Delta^* F_{j+1/2}\right] \tag{3.27}$$

$$F^R_{j-1/2} = F_j - \frac{1}{4}\left[(1+\kappa_1)\chi(r)\Delta^* F_{j-1/2} + (1-\kappa_1)\chi(1/r)\Delta^* F_{j+1/2}\right] \tag{3.28}$$

where $F^L_{i+1/2}$ is the constructed value at the left-hand side of the interface $i+\frac{1}{2}$ and $F^R_{i-1/2}$ is the value at the right-hand side of the interface $i-\frac{1}{2}$. Similarly, $F^L_{j+1/2}$ and $F^R_{j-1/2}$ are the left- and right-hand side of the interface $j-\frac{1}{2}$. For conciseness, the x direction terms are only explained from here on. Accordingly, the values of $\Delta^* F$ for x direction are evaluated as follows:

$$\begin{aligned}
&\Delta^* F_{i+1/2} = \Delta F_{i+1/2} - \kappa_2 \Delta^3 \bar{F}_{i+1/2}/6, \\
&\Delta F_{i+1/2} = F_{i+1} - F_i, \\
&\Delta^3 \bar{F}_{i+1/2} = \Delta \bar{F}_{i+3/2} - 2\Delta \bar{F}_{i+1/2} + \Delta \bar{F}_{i-1/2},
\end{aligned} \tag{3.29}$$

κ_1 and κ_2 in (3.25) -(3.29) are parameters to control the order of the scheme in the compact form. Following Yamamoto et al. (1995), the complete form with $(\kappa_1, \kappa_2) = (1/3, 1)$ gives the fourth-order scheme accuracy. Moreover, $(\kappa_1, \kappa_2) = (1/3, 0)$ yields a third-order scheme, while the second-order scheme can be reached using $(\kappa_1, \kappa_2) = (-1, 0)$.

$\chi(r)$ in (3.25)-(3.28) is the limiter function. The original scheme introduced by Yamamoto et al. (1998) uses the Minmod limiter as used in (3.29). Erduran et al.

(2005) tested four limiters (Superbee, Minmod, van-Albada, and van-Leer) and found that the van-Leer limiter was the most suitable to be used with the MUSCL-TVD scheme. The van-Leer limiter can be expressed as

$$\chi(r) = \frac{r + |r|}{1 + r} \tag{3.30}$$

where

$$r = \frac{\Delta^* F_{i+1/2}}{\Delta^* F_{i-1/2}}. \tag{3.31}$$

The numerical fluxes for each cell face are computed using a HLL approximate Riemann solver

$$F(\Psi^L, \Psi^R) = \begin{cases} F(\Psi^L) & \text{if} \quad s_L \geq 0 \\ F^*(\Psi^L, \Psi^R) & \text{if} \quad s_L < 0 < s_R \\ F(\Psi^R) & \text{if} \quad s_R \leq 0, \end{cases} \tag{3.32}$$

where

$$F^*(\Psi^L, \Psi^R) = \frac{s_R F(\Psi^L) - s_L F(\Psi^R) + s_L s_R (\Psi^R - \Psi^L)}{s_R - s_L} \tag{3.33}$$

The wave speeds of the Riemann solver are given by

$$s_L = \min(\mathbf{V}^L \cdot \mathbf{n} - \mathbf{u}^L, u_s - \sqrt{\varphi_s}), \tag{3.34}$$

$$s_R = \max(\mathbf{V}^R \cdot \mathbf{n} + \mathbf{u}^R, u_s + \sqrt{\varphi_s}), \tag{3.35}$$

in which u_s and φ_s are estimated as

$$u_s = \frac{1}{2}(\mathbf{V}^L + \mathbf{V}^R) \cdot \mathbf{n} + \mathbf{u}^L - \mathbf{u}^R \tag{3.36}$$

$$\sqrt{\varphi_s} = \frac{(\mathbf{u}^L + \mathbf{u}^R)}{2} + \frac{(\mathbf{V}^L - \mathbf{V}^R) \cdot \mathbf{n}}{4} \tag{3.37}$$

where $\mathbf{n}$ is the outward normal vector for a cell face. $\mathbf{V} = (U, V)$ is the velocity terms constructed at left and right cell faces for x and y directions. Higher derivative terms in ψ_x and ψ_y (3.23) were discretized using a central difference scheme at the cell centers.

3.2.2.1 Time Stepping

Similar to FUNWAVE-TVD, here, for time stepping we used a third order Strong Stability-Preserving (SSP) Runge-Kutta scheme for nonlinear spatial discretization (Gottlieb et al., 2001). The scheme is written as,

$$\begin{aligned}
\Psi^{(1)} &= \Psi^k + \Delta t(-\nabla \cdot F(\Psi^k) + S^{(1)}) \\
\Psi^{(2)} &= \frac{3}{4}\Psi^k + \frac{1}{4}\left[\Psi^{(1)} + \Delta t\left(-\nabla \cdot F(\Psi^{(1)}) + S^{(2)}\right)\right] \\
\Psi^{k+1} &= \frac{1}{3}\Psi^k + \frac{2}{3}\left[\Psi^{(2)} + \Delta t\left(-\nabla \cdot F(\Psi^{(2)}) + S^{k+1}\right)\right]
\end{aligned} \tag{3.38}$$

in which Ψ^k represents Ψ at time level k. $\Psi^{(1)}$ and $\Psi^{(2)}$ are values at intermediate stages in the Runge-Kutta integration. As Ψ is obtained at each intermediate step, the depth-averaged sediment concentration ($\bar{C}$) can be solved directly from the last step of the (3.26). S is updated using updated flow information at the corresponding intermediate time steps (1,2) and $(k+1)$.

3.2.3 Stability Criterion

For this work, we chose an adaptive time step, following the Courant-Friedrichs-Lewy (CFL) criterion for tsunami flow to ensure model stability. Similar to FUNWAVE-TVD, time steps are computed for the Upwind and MUSCL-TVD schemes using the following condition,

$$\Delta t = C\min\left(\frac{\Delta x}{|u| + \sqrt{g(h+\eta)}}, \frac{\Delta y}{|v| + \sqrt{g(h+\eta)}}\right) \leq 0.5 \tag{3.39}$$

where $C = \frac{\mathbf{u}\Delta t}{(\Delta x, \Delta y)}$ is the CFL number.

3.2.4 Boundary Conditions

Two types of boundary conditions are defined for the fluxes $\mathbf{F}$ in (3.23). Closed boundary condition is used next to walls as well as the shoreline, which is defined for each cell face as follows,

$$F^R_{i-1/2} = 0 \qquad \text{closed left face for the cell i} \tag{3.40}$$

$$F^L_{i+1/2} = 0 \qquad \text{closed right face for the cell i} \tag{3.41}$$

$$F^R_{j-1/2} = 0 \qquad \text{closed bottom face for the cell j} \tag{3.42}$$

$$F^L_{j+1/2} = 0 \qquad \text{closed top face for the cell j} \tag{3.43}$$

Open boundary conditions are used in nesting mode as well as periodic boundary conditions, and are defined for each cell face as follows,

$$F^R_{i-1/2} = F^L_{i-1/2} \qquad \text{open left face for the cell i} \tag{3.44}$$

$$F^L_{i+1/2} = F^R_{i+1/2} \qquad \text{open right face for the cell i} \tag{3.45}$$

$$F^R_{j-1/2} = F^L_{j-1/2} \qquad \text{open bottom face for the cell j} \tag{3.46}$$

$$F^L_{j+1/2} = F^R_{j+1/2} \qquad \text{open top face for the cell j} \tag{3.47}$$

Left, right, bottom and top faces are shown in Figure 3.1. The boundary conditions (3.40)-(3.47) are implemented in both Upwind and MUSCL-TVD schemes described above.

3.2.5 Pure Advection Test

If the diffusion coefficient K is zero, the AD equation (2.44) becomes a hyperbolic partial differential equation; therefore, the equation should be able to simulate a discontinuous concentration problem. As mentioned in the previous sections of this chapter, Upwind scheme is expected to be numerically diffusive in such conditions, while the MUSCL-TVD scheme should be able to capture shocks associated with discontinuities in sediment concentration distribution in the numerical domain. Here, we

have performed a pure advection test to demonstrate the advantage of MUSCL-TVD scheme compared to the Upwind scheme.

To perform the pure advection test, a 1D flume condition is simulated. The length of the flume is set to be 40 km, with a width of 200 m, and the grid sizes of $\Delta x = \Delta y$ =100.0 m. The diffusion coefficient K in (3.1) and (3.23) is set to be zero to construct pure advection condition for the Upwind and the MUSCL-TVD schemes. A uniform flow condition $U = 1.0$ m/s in the x direction is created by forcing the left and right boundaries, generating a flow from left to right. For the initial condition of the sediment concentration, a block of sediment is placed 1 km away from the left boundary, with a depth-averaged concentration of 100 g/l, and width of 250 m (Figure 3.3, top left).

Figure 3.3 illustrates the difference between pure advection of the Upwind and MUSCL-TVD schemes after 100, 200 and 300 minutes of the uniform flow simulations. As expected, the Upwind scheme shows strong numerical diffusion in contrast to the MUSCL-TVD scheme, which, due to the absence of artificial diffusion, can conserve the discontinuity in the sediment concentration distribution. The results show that MUSCL-TVD scheme is better-suited to the sediment transport problem; however, the Upwind Scheme implementation is left in the model as an option for comparison purposes.

3.3 Morphology Module

The sediment continuity equation (2.50) is solved to calculate depth changes Z_b. Time-averaged sediment transport rates $(\bar{P}, \bar{D})$ are computed from instantaneous transport rate values (P, D) calculated for the sediment transport module, and are used in the sediment continuity equation to calculate bed changes. Following this approach, the discretized form of the sediment continuity equation can be written as,

$$\left(\frac{\Delta Z_b}{\Delta t_{morph}}\right)^k_{i,j} = \frac{1}{1-n}\left(\bar{P}^k_{i,j} - \bar{D}^k_{i,j}\right) \tag{3.48}$$

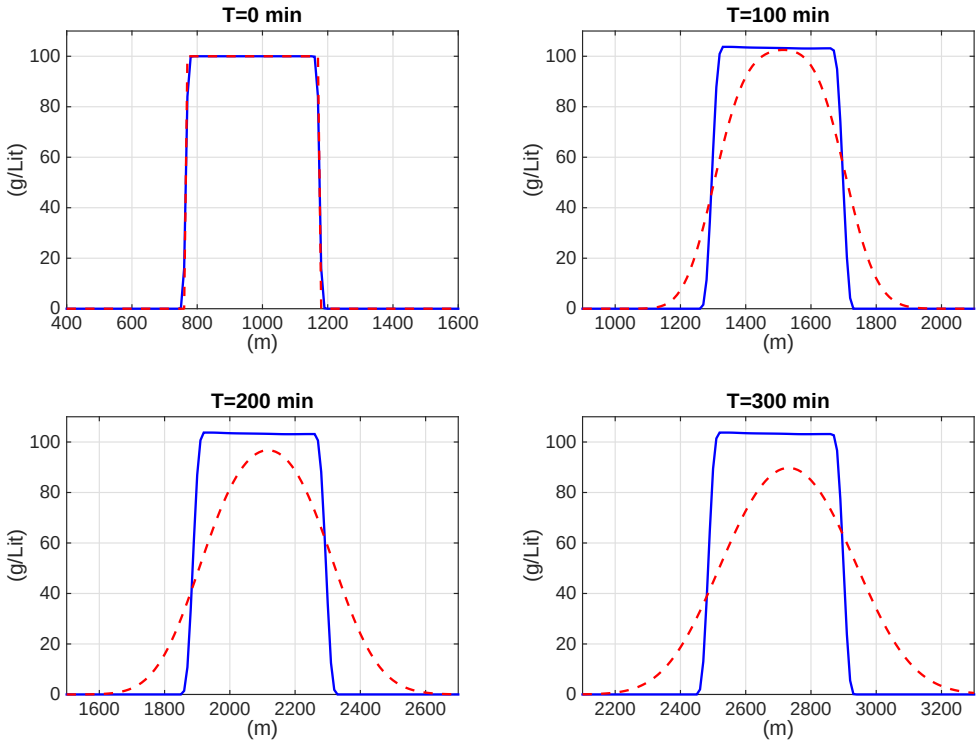

Figure 3.3: Comparison between results of the Upwind scheme (dashed red line), and the MUSCL-TVD scheme (solid blue line) for the pure advection test after 0, 100, 200 and 300 minutes of 1D uniform flow simulation in a 1D flume.

The averaged transport rates were calculated using the following approach,

$$\bar{P}_{i,j}^{k} = \frac{1}{N}\sum_{l=1}^{N} P_{i,j}^{l} \tag{3.49}$$

$$\bar{D}_{i,j}^{k} = \frac{1}{N}\sum_{l=1}^{N} D_{i,j}^{l} \tag{3.50}$$

where,

$$N = \frac{\Delta t_{morph}}{\Delta t} \tag{3.51}$$

where N is defined as an input in the model with suggested values in the range of 5 to 20. Finally, the updated bed elevation is calculated using a third order Strong Stability-Preserving (SSP) Runge-Kutta scheme as follows,

$$\begin{aligned}
{Z_b}^{(1)} &= {Z_b}^{k} + \Delta t_{morph}(\bar{P}^{(1)} - \bar{D}^{(1)}) \\
{Z_b}^{(2)} &= \frac{3}{4}{Z_b}^{k} + \frac{1}{4}\left[{Z_b}^{(1)} + \Delta t_{morph}\left(\bar{P}^{(2)} - \bar{D}^{(2)}\right)\right] \\
{Z_b}^{(k+1)} &= \frac{1}{3}{Z_b}^{(2)} + \frac{1}{4}\left[{Z_b}^{(2)} + \Delta t_{morph}\left(\bar{P}^{(k+1)} - \bar{D}^{(k+1)}\right)\right]
\end{aligned} \tag{3.52}$$

where $\bar{P}$ and $\bar{D}$ are averaged pickup and deposition rates updated using updated flow information at the corresponding intermediate time steps (1,2), and $(k+1)$. The depth values (Z_b) are updated for the hydrodynamic part of the model before the next time step calculations as shown in Figure 3.2. In this implementation of the sediment continuity equation, Z_b represents a depth change with positive values for eroded and negative values for deposition areas. Considering that the bed evolution scheme uses time averaged deposition and pickup rates ($\bar{D}, \bar{P}$) over a larger time step (e.g. for this test $\Delta T_{morph} = 5\Delta T$), the bed changes occur with a short lag compared to sediment suspension process. This lag difference causes some mass conservation problems close to the shoreline because the morphology module does not march forward with the hydrodynamics and sediment transport module. Because $N = dt_{morph}/dt$ is a number between 5 to 20, a grid point close to the shoreline could fall into the dry region for some of the time steps of the hydrodynamic model, and the other time steps into the

wet region, before the morphology is updated. Although using time-averaged pickup and deposition rates in sediment continuity equation (2.50) could result in a small sand loss during the computation, smoother bed computed with time-averaged rates removes small perturbation on the bottom which potentially could cause instabilities in the model. Instabilities occur when the total depth in hydrodynamics is updated using the updated bed elevations, transferring bed perturbations to the surface. In the next chapter, we perform a sand conservation test and show that the model eventually balances itself and the errors in sand conservation are negligible.

3.4 Hard-Bottom Methodology

The sand layer thickness Z_s (shown in Figure 2.2) at each grid point can be defined as an input for the model to implement the hard bottom condition. The areas where $Z_s = 0.0$ is considered to be non-erodible. This condition can occur after the sediment layer is completely eroded or as an initial condition for regions with no sand such as street pavements. When the hard bottom is exposed, the upward sediment flux (Pickup rate) is set to be zero in both Upwind and MUSCL-TVD schemes for the sediment transport module, as well as time-averaged pickup rate ($\bar{P}$) used in sediment continuity equation. This condition is implemented in the model using the following expression,

$$P^k_{i,j} = \bar{P}^k_{i,j} = 0.0; \qquad Z^k_{b_{i,j}} = Z_{s_{i,j}}, \tag{3.53}$$

which ensures the depth change Z_b to be smaller or equal to the sand layer thickness Z_s. In other words, the above equation forces the maximum erosion value $Z_{b_{max}}$ to be less or equal to sand layer thickness Z_s.

3.5 Slope Limiting Methodology

Here, we use the avalanching method of Larson and Kraus (1989) which has been successfully used and tested for the Storm-Induced Beach (SBEACH) model. After calculation of morphological changes at each time step, the avalanching procedure is performed starting at the deepest points of the domain. The bottom slopes are

calculated and compared to the critical value of repose angle. If the bed slope exceeds the critical value, the avalanching scheme will smooth and reshape the bed with the maximum slope of the sediment repose angle. For example, in Figure 3.4 the slope between i and $i+1$ cells are larger than the repose angle ($\tan(\phi) = \Delta h/\Delta x$). The change in depth for $i+1$ and i cells can be written as,

$$\Delta h_1 = \frac{-(Z_{i+1} - Z_i)}{2} + \frac{1}{2}\Delta h \tag{3.54}$$

$$\Delta h_2 = \frac{(Z_{i+1} - Z_i)}{2} - \frac{1}{2}\Delta h = -\Delta h_1 \tag{3.55}$$

where $Z = -Z_b$ is the elevation above the initial depth used here instead of Z_b for the clarity of description.

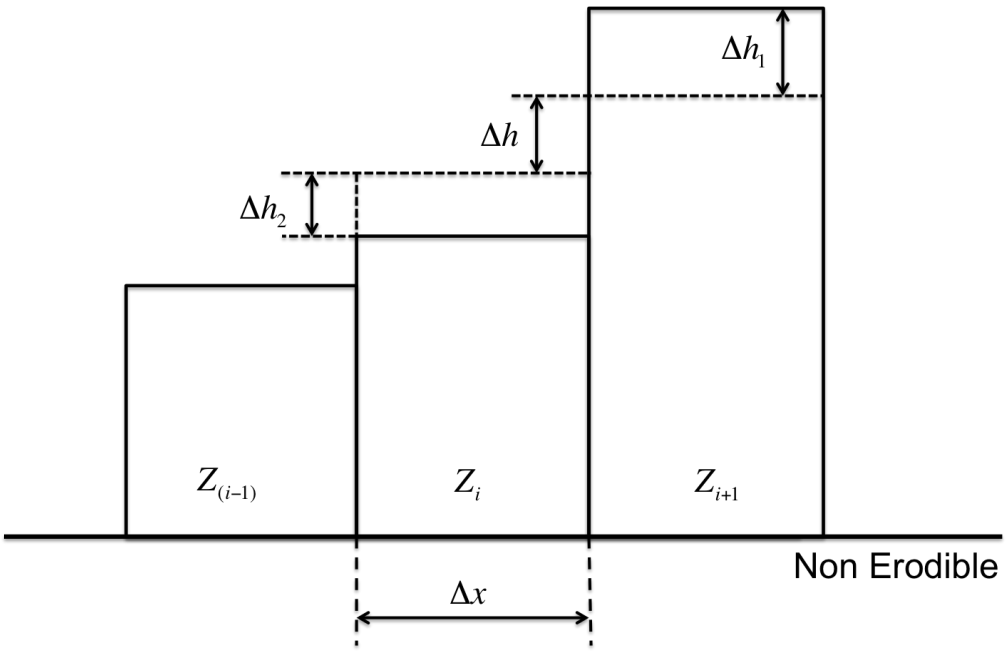

Figure 3.4: Definition sketch for describing avalanching along the profile.

The avalanching procedure is only implemented in erodible areas where $Z_b \leq Z_s$ (Figure 2.2). In other words, the avalanching does not occur in areas where hard bottom is exposed ($Z_b = Z_s$), and only sandy areas of the domain have limitations

for the maximum bed slope. There can be two possible avalanching scenarios when an erodible cell neighbors a non-erodible one. First, if the erodible cell has higher elevation compared to the neighboring non-erodible cell, such that the slope between two points is larger than the repose angle of the sediment, sand avalanches from erodible point to the non-erodible point to limit the maximum slope (Figure 3.5a). However, if the erodible cell has the lower elevation, the avalanching does not occur even if the bed slope is larger than the sediment repose angle (Figure 3.5b).

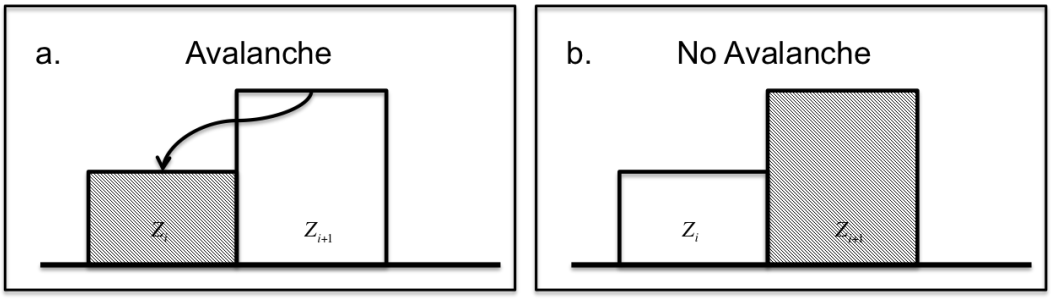

Figure 3.5: (a.) Avalanching occurs when an erodible cell $(i + 1)$ is higher than a neighboring non-erodible cell (i) when the slope is larger than the sediment repose angle. (b.) Avalanching does not occur when an erodible cell (i) is lower than a neighboring non-erodible cell $(i + 1)$ even if the slope is larger than the sediment repose angle.

Similar to Larson and Kraus (1989), for this model the avalanching starts from the deepest point of the domain. The model calculates the four slopes around the deepest cell (top, bottom, left, and right in Figure 3.1), and if the bed slope exceeds the critical value, avalanching occurs. If more than one slope around the cell is larger than the repose angle, the avalanching occurs at the largest slope first. In rare cases when two or more slopes around a cell are more than the critical value and identical to each other, the avalanching starts from north to west in a clockwise fashion around that cell.

3.6 Parallelization

Similar to FUNWAVE-TVD parallelization (Shi et al., 2012, 2013), we use the domain decomposition technique to divide the problem into multiple regions and assign each subdomain to a separate processor core. Each subdomain region contains an overlapping area of ghost cells three rows deep, as required by the fourth order MUSCL-TVD scheme. The Message Passing Interface (MPI) with non-blocking communication is used to exchange the data in the overlapping region between neighboring processors. To illustrate the performance of the parallel program, numerical simulations of a breaking solitary wave runup case (Kobayashi and Lawrence, 2004) are tested with 10, 20, and 30 processors in the next chapter of this thesis. These tests were conducted using the Linux cluster mills.hpc.udel.edu located at University of Delaware. In the next chapter, the results of the model for several validation tests including convergence and sand conservation test are provided.

Chapter 4

MODEL VALIDATION

In this chapter, we present the results of a model validation conducted using simulations of two laboratory experiments and a field test. First, results of the model for simulation of beach evolution under a series of solitary waves are examined. We use the data provided by Kobayashi and Lawrence (2004) to perform this test. Mass conservation and convergence of the model is checked during this test. Next, we model the dam-break experiment of Pintado-Patiño et al. (2016). The dam-break waves are better models for tsunami waves compared to solitary waves, with more realistic wave steepness compared to tsunamis. Also, the availability of sediment profiles and velocity measurements during this test was another reason we chose this test. Finally, we modeled morphological changes in the Crescent City, CA harbor by the 2011 Tohoku-Oki tsunami. The availability of the data along with a tested source model for the event (Grilli et al., 2011), as well as an environment where the hard bottom condition of the model could be tested in complex bathymetries, were the reasons this test was chosen here.

4.1 Kobayashi and Lawrence (2004) Experiment on Bed Evolution Under Breaking Solitary Waves

Kobayashi and Lawrence (2004) conducted laboratory experiments to examine cross-shore sediment transport under breaking solitary waves over a fine sand beach, in a 30 m long, 2.4 m wide, and 1.5 m deep wave tank. Waves were generated by a piston wavemaker, and the flume was filled with water 0.8 m deep. A fine sand beach with an initial slope of 1/12 was built at the end of the tank. Kobayashi and Lawrence (2004) recorded surface elevation and velocity at 8 locations shown in Figure 4.1, for a

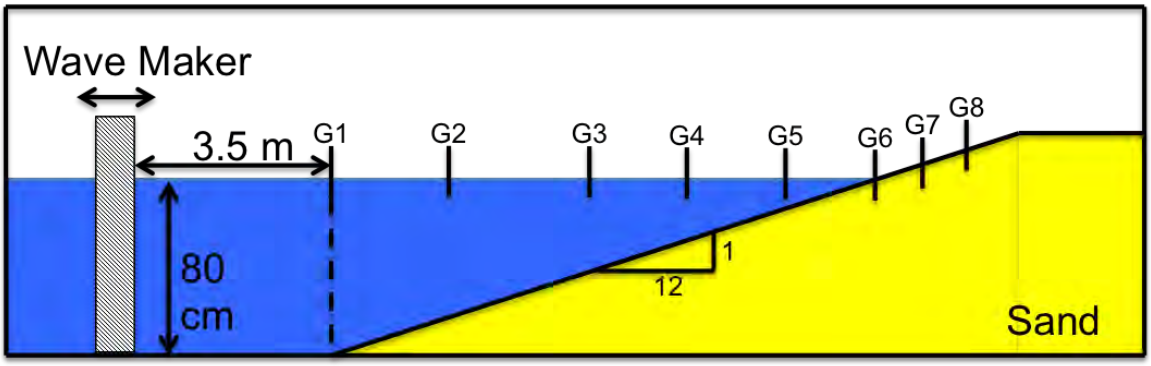

Figure 4.1: Kobayashi and Lawrence (2004) experimental setup.

sequence of eight solitary waves. The first gauge (G1 in Figure 4.1) was located at the toe of the slope while four other gauges (G2-5) were deployed on the slope to measure the solitary wave shoaling and breaking over the slope. Another three gauges (G6-8) were located onshore to measure wave runup and rundown in the swash zone. The sand was well sorted with median diameter of $d_{50} = 0.18$ mm, with porosity coefficient $n = 0.4$, specific gravity $s = 2.6$, and fall velocity of $w_f = 2.0$ cm/s. The recorded initial wave height was $H_o = 0.216$ m. Figure 4.1 demonstrates the experiment setup including the location of the gauges. Using the model described in previous chapters, we modeled sediment transport and resulting bed changes for the first four waves and compared results to the measured data to validate the model.

4.1.1 Model Setup

To model the Kobayashi and Lawrence (2004) experiment of sediment transport under breaking solitary waves, we used a grid size of $\Delta x = 25$ mm with a grid size of 1240×6 in x and y directions considering the length and width of the flume. The initial solitary waves were generated using the internal solitary wavemaker of FUNWAVE-TVD with the amplitude of 0.216 m over the initial depth of 0.80 m. The internal solitary wavemaker follows Nwogu's extended Boussinesq equations with

centroid located at $x = 5.0$ m at time $t = 0$ s. Also, we used a drag coefficient of $C_d = 0.01$ for the bottom friction. After each sequence of the solitary wave, we used the computed bed changes to update depth information for the next run.

4.1.2 Results

Figure 4.2 shows the comparison between model results and measured surface elevation during the fourth solitary wave for the eight gauges illustrated in Figure 4.1. The results show good agreement with the recorded data, showing that the model simulated the hydrodynamics appropriately. Moreover, Figure 4.3 illustrates the comparison between recorded and modeled surface elevation, horizontal velocity, and sediment concentration at gauge three (G3 in Figure 4.1) during the fourth solitary wave. As shown in this figure, the model successfully simulated the surface elevation and velocity. Gauge three was located 6.0 cm above the bed and sediment concentration values were measured at that elevation. However, the model calculated the depth-averaged sediment concentration which roughly falls somewhere between 7.0 to 10.0 cm (considering the depth change during the passage of the wave) above the bed assuming the exponential profile for sediment concentration. As shown in the bottom plot in Figure 4.3, the lag between sediment movement and wave passage is not captured in the model results. This lag difference could be because of the time lag between the wave at the surface and bottom stress which occurs during the unsteady condition. As mentioned in the previous chapters, the model considers quasi-steady flow condition. Although Kobayashi and Lawrence (2004) measurements of sediment transport were during an unsteady flow, the model calculated the deposition and erosion areas correctly, with reasonable error margin.

Figure 4.4 shows the comparison between measured and simulated beach profiles after four solitary waves changed the beach profile. The most significant change in the bottom profile occurred during wave rundown, where the sand was eroded from the region close to the shoreline and deposited further offshore. This process was also observed during the experiment. As shown in Figure 4.4, the model provides a good

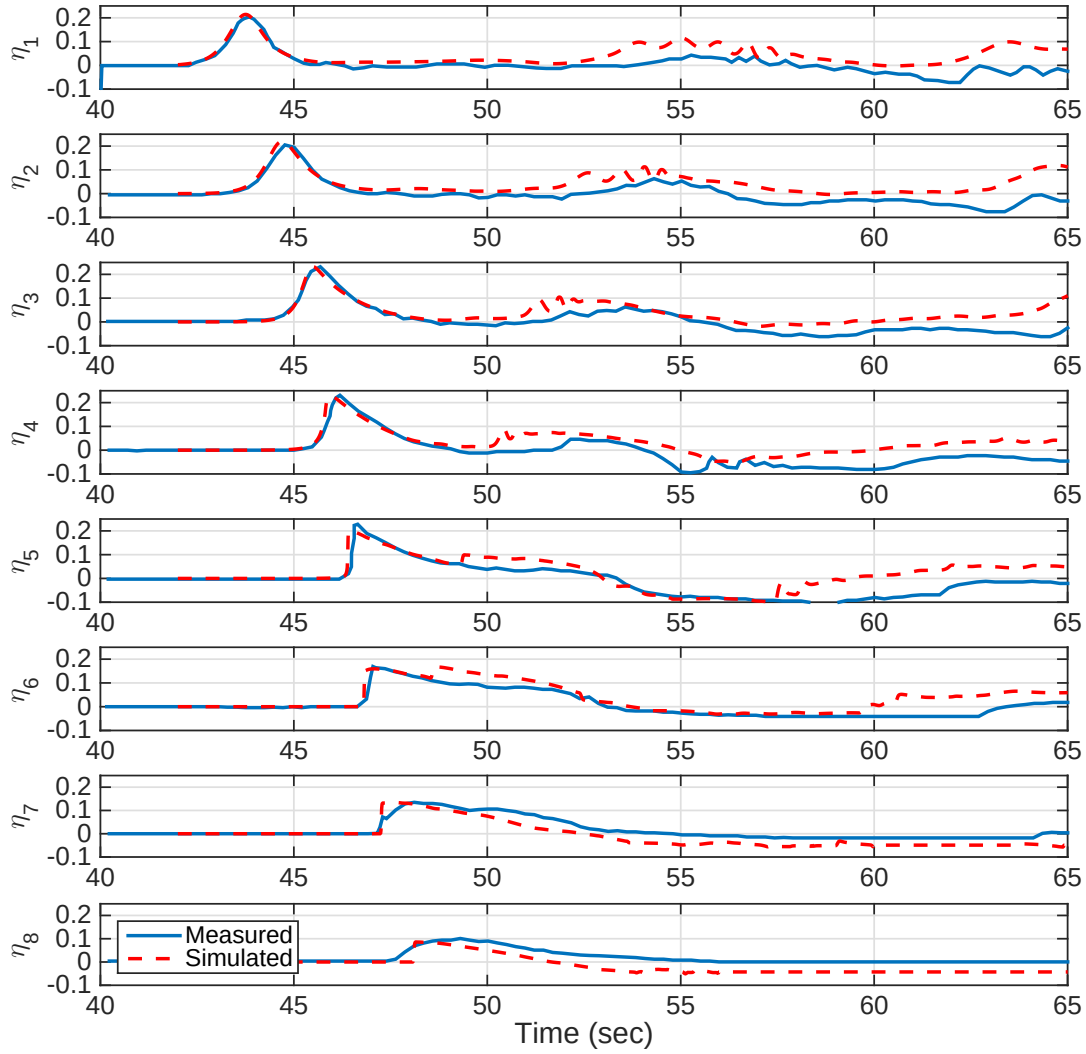

Figure 4.2: Comparison between measured (blue) and simulated (red) surface elevations for the fourth solitary. Measurements were performed with 8 wave gauges shown in Figure 4.1.

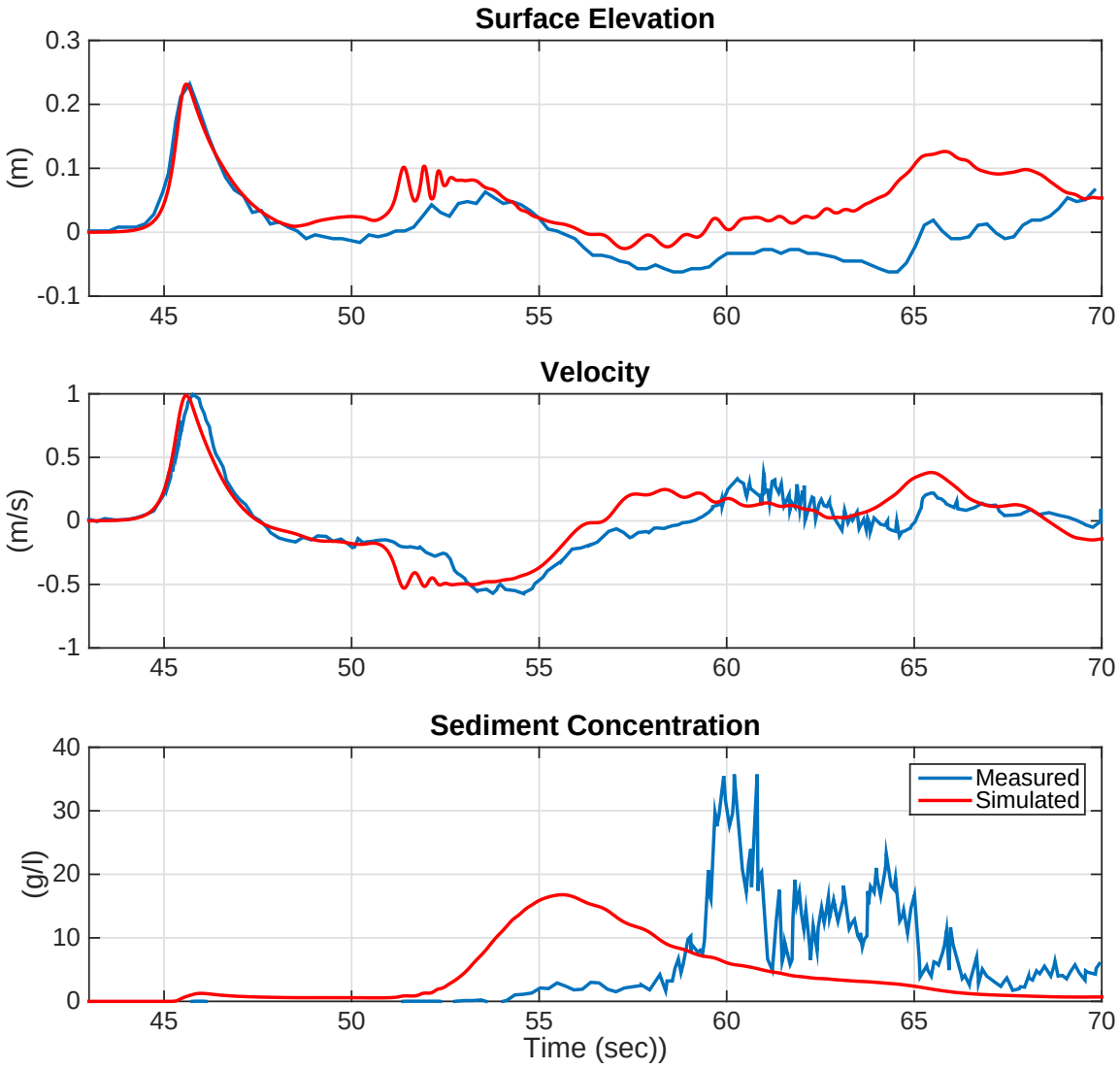

Figure 4.3: Comparison between measured (blue) and simulated (red) surface elevation (Top), horizontal velocity (middle), and sediment concentrations for gauge three measured 6 cm above the bed and computed depth-averaged values during the fourth solitary wave. Velocity and sediment concentration measurements were performed with a micro Acoustic-Doppler Velocimeter (ADV), and a Fiber Optic Sediment Monitor, located at G3 (Figure 4.1).

estimate of the location and magnitude of shoreline erosion and deposition. Moreover, Figure 4.5 indicates the comparison between measured and simulated maximum deposition and erosion values for the first four waves in the experiment. While the maximum erosion and deposition values are underestimated, the beach profile from the simulation is generally in good agreement with measured data (Figure 4.4). Overall, the model was able to predict the bottom morphological changes with an error of 26 percent averaged cross-shore, compared to the measured profile after four solitary waves changed the slope profile.

4.1.3 Sediment Conservation

An accurate morphology evolution model must conserve sediment mass. To address this issue, the total mass of suspended sand calculated during computing the Advection-Diffusion Equation (2.44) for sediment transport is compared to total mass changes of the bed calculated from the sediment continuity equation (2.50). Following the mass conservation expression (2.52) provided in Chapter 2, we examined our model's sand conservation ability in all calculations provided in this document. Figure 4.6 demonstrates a comparison between the suspended sediment and the moved sediment mass from the bed, both calculated with the model for the first solitary wave. Considering that the bed evolution scheme uses time averaged deposition and pickup rates ($\bar{D}, \bar{P}$) over a larger time step (e.g. for this test $\Delta T_{morph} = 5\Delta T$), it is expected that the bed changes occur with a short lag compared to sediment suspension process. Also, bed changes occur with a smoother pattern compared to sand suspension due to time averaging. This difference is shown in Figure 4.6 in the time slot between 5 to 10 seconds, while the initial runup occurs. This is because of shoreline issues explained in the previous chapters. Although these differences indicate that the model does not conserve throughout the whole computation time, the similar trend between two schemes and the fact that two curves in Figure 4.6 representing the volume of moved sand in both schemes converge at the end of the computations show that the model conserves sand. For example, a maximum suspended value of 0.016 m^3 is computed

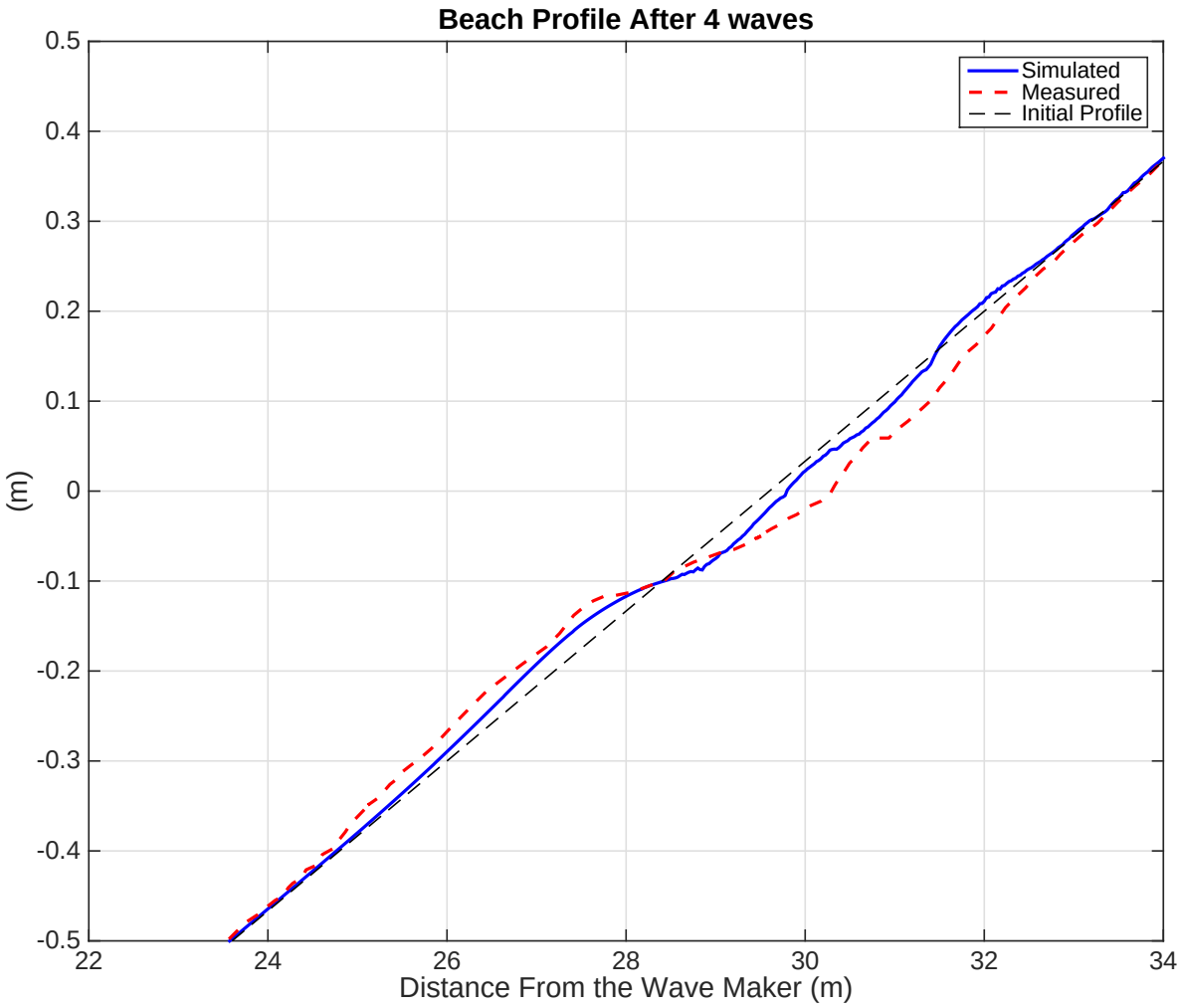

Figure 4.4: Comparison between measured and simulated beach profiles after four solitary waves.

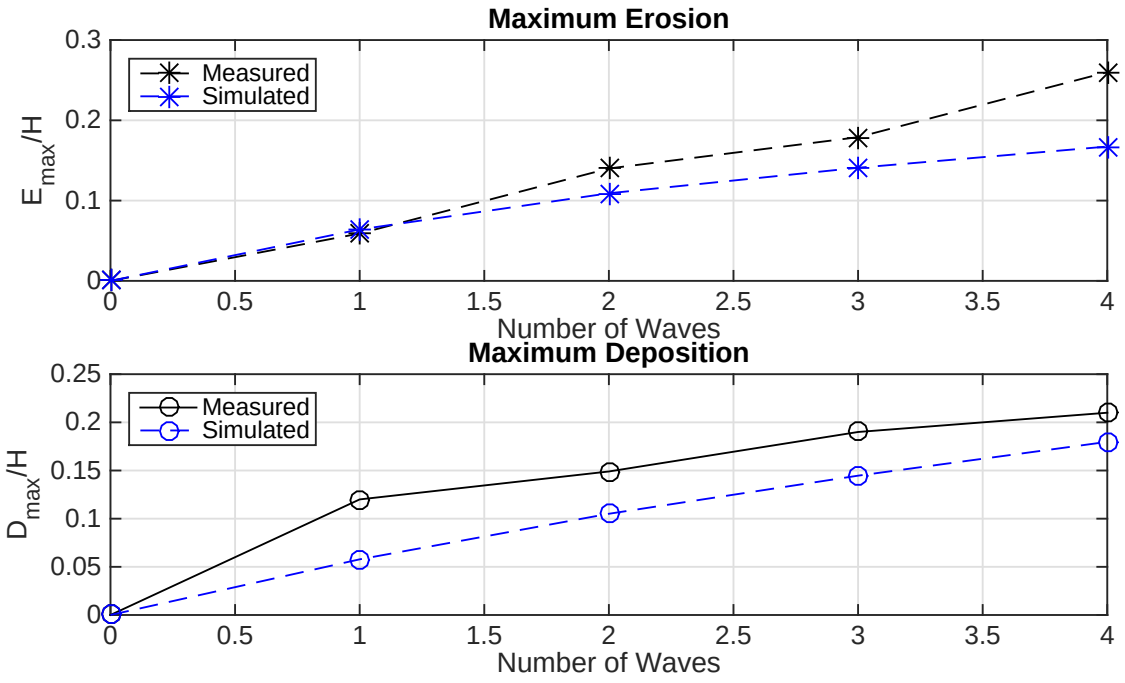

Figure 4.5: Comparison between measured maximum erosion (E_{max}, top) and deposition (D_{max}, bottom) for 4 solitary waves, normalized by wave height ($H = 0.216$ m).

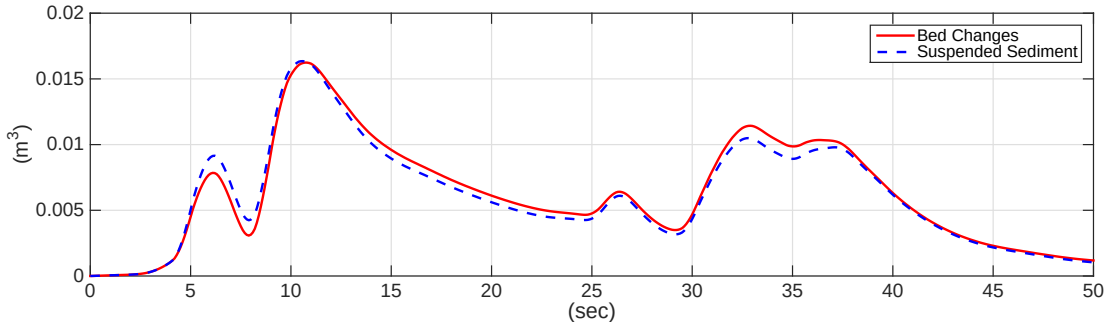

Figure 4.6: Comparison between the total mass of suspended sediment (dashed blue line), and the total mass of moved sediment from the bed (solid red line) during the simulation of Kobayashi and Lawrence (2004) experiment, to show the ability of the model to conserve sand

in both schemes. Finally, both schemes deposit the total mass in a similar manner until the total amount of sand in the water column (Suspended sediment), and total overall bed changes (Total erosion - Total deposition) converges to zero at the end of simulations.

4.1.4 Model Convergence

In addition to mass conservation, the second basic validation step is to check if the model results converge to an asymptotic limit with smaller time steps. Here we checked the convergence of both the sediment transport and bed evolution schemes, as well as the hydrodynamics model. Figure 4.7 shows the calculated surface elevation, velocity, and sediment concentration at gauge location 3 for different grid sizes. The grid steps Δx and Δy has been halved, and the time step Δt automatically reduced appropriately to conform to the Courant-Friedrichs-Lewy (CFL) criterion. We performed several tests starting from a coarse grid of $\Delta x = 10$ cm down to a fine grid of $\Delta x = 1.25$ cm to check model convergence. Figure 4.8 illustrates the calculated bed changes after the passage of the first solitary wave. These results show that the model is converging to an asymptotic limit, where the results for grid sizes of $\Delta x = 2.5$ cm

and $\Delta x = 1.25$ cm are almost identical to each other. However, the comparison between results in Figures 4.7 and 4.8 shows that sediment transport model is converging faster than the bed evolution scheme. This is due to larger time steps of the sediment continuity equation compared to that of the sediment transport scheme.

4.1.5 Parallel Computing Performance

As mentioned in the previous chapter of this thesis, the model has been modified to perform parallel computing with a Message Passing Interface (MPI). We simulated the first solitary wave of Kobayashi and Lawrence (2004) experiment with 1, 10 and 20 processors on the Linux cluster Mills (mills.hpc.udel.edu) located at University of Delaware to check the performance of the parallel model. Figure 4.9 shows the model speedup versus the number of processors. The model performance scales nearly proportional to the number of processors, with some delay caused by inefficiencies in parallelization, such as inter-processor communication time. Mills nodes consist of 24 cores, so the present simulations on fewer cores do not test inter-node communication performance on the system. The computational speed increases with a similar pattern to what Shi et al.(2012) reported for FUNWAVE-TVD. The grid dimension must be divisible by the number of processors defined for it, else complications arise at the end of the domain where some grid points do not fall into the computation domain. For example, for a grid size of 50, the numbers 1, 2, 5, 10, and 25 are appropriate choices, but any other number between 1 to 50 will cause errors in the simulation.

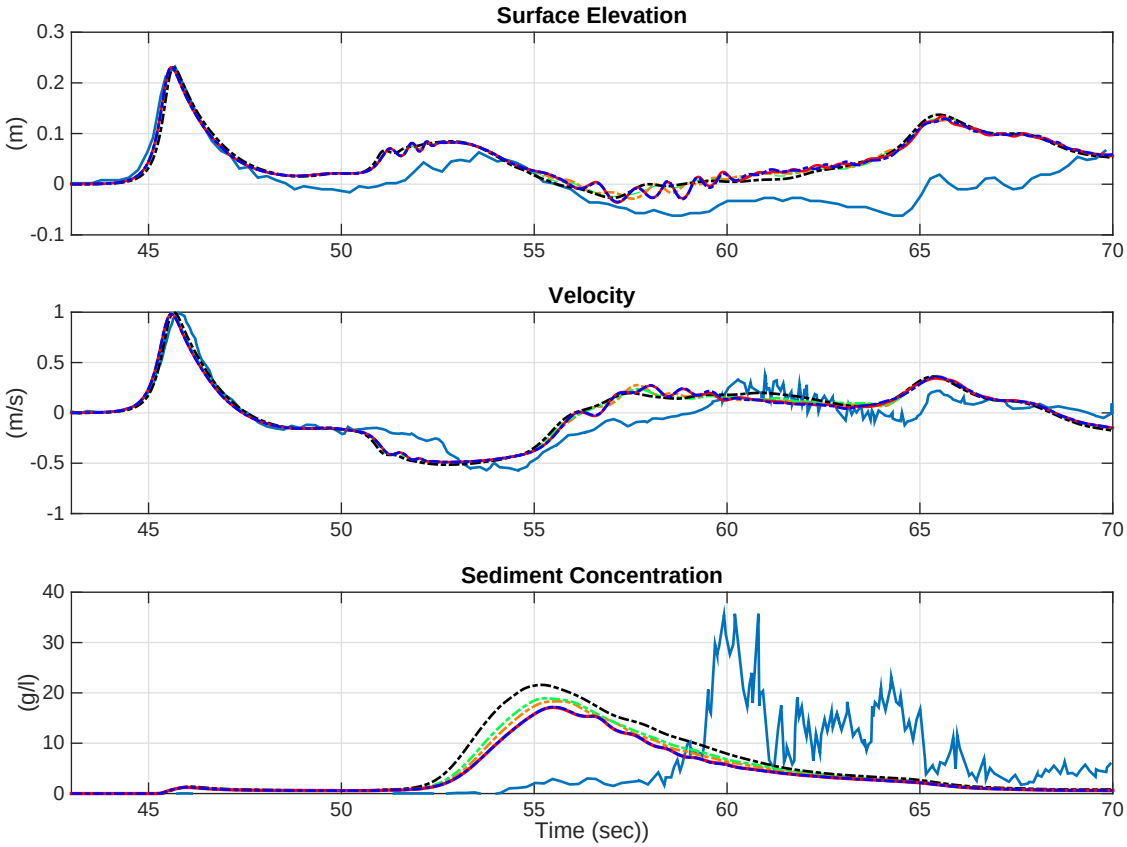

Figure 4.7: Comparison between computed surface elevation (Top), velocity (Middle) and sediment concentration value (Bottom) for the simulation of the first solitary wave at gauge 3 (Shown in Figure 4.1). Simulations were performed with different grid sizes to show the convergence of the model; $\Delta x = 10$ cm (black), $\Delta x = 5$ cm (green), $\Delta x = 3.75$ cm (orange), $\Delta x = 2.5$ cm (red), $\Delta x = 1.125$ cm (dark blue), and measured (light blue).

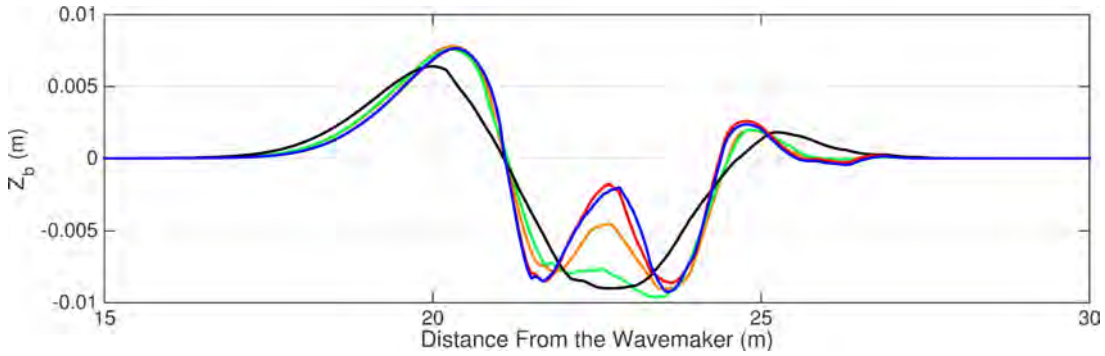

Figure 4.8: Comparison between calculated bed changes after the first solitary wave for grid sizes of $\Delta x = 10$ cm (black), $\Delta x = 5$ cm (green), $\Delta x = 3.75$ cm (orange), $\Delta x = 2.5$ cm (red), and $\Delta x = 1.125$ cm (blue).

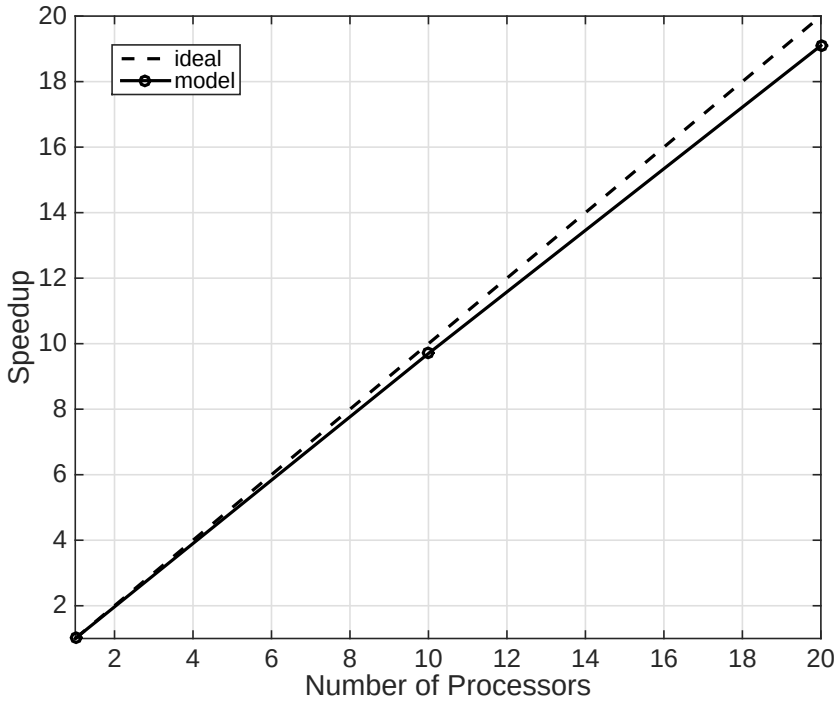

Figure 4.9: Variation in model performance with different numbers of processors (1, 10, and 20) for the Kobayashi and Lawrence (2004) simulation. The straight line indicates arithmetic speedup. Actual performance is shown with the curved line.

4.2 Pintado-Patiño et al. (2016) Dam-Break Test

During recent decades, lots of laboratory experiments have been conducted to study tsunami generation, propagation and inundation processes (e.g. Synolakis et al., 2006). However, most of these tests have used solitary waves to reconstruct tsunami conditions. Although solitary waves have helped researchers during past decades enhance their knowledge about tsunamis, they are increasingly disregarded as an appropriate model for tsunamis for several reasons. Aside from the significant time scale differences between actual tsunamis and solitary waves (which have smaller time scales), tsunamis are usually comprised of several waves and the first wave is not necessarily the largest one. Even those tsunamis which could be considered similar to solitary waves have much longer length scales compared to laboratory solitary waves. Recently, use of surge waves resulting from dam-breaks is becoming popular to model tsunami conditions. Waves generated by dam-breaks have closer time scales to tsunamis in comparison with solitary waves. Also, dam-break surge waves produce a bore front structure similar to tsunami waves, which is another advantage of these types of waves compared to solitary waves. In this section, we examine our model in comparison to recorded measurements of a dam-break experiment. For this purpose, the dam-break test of Pintado-Patiño et al. (2016) was chosen. In the upcoming sections, we described their experiment setup and explained our approach to simulate it.

4.2.1 Experiment Setup

Pintado-Patiño et al.'s (2016) dam-break experiments were carried out in a flume which was 16 m long, 0.6 m wide and 0.80 m deep. Figure 4.10 illustrates the experiment setup. The reservoir behind the gate shown in Figure 4.10 contained a water volume of 0.468 m^3 ($h_d = 0.78$ m) at the upstream section, as opposed to the flat downstream section with $h_0 = 0.06$ m initial water depth. Following the opening of the gate, the dam-break wave was generated. This process created a turbulent bore with an approximate flow speed of $U = 2.0$ m/s, and 0.25 m water depth. The turbulent bore then collapsed onto a planar sand beach, causing a swash event similar

to those found on natural beaches (Pintado-Patiño et al., 2016). Right after the first runup-rundown process finished, a second gate held 0.6m above the planar beach toe was then manually released to diminish potential effects of the reflected bore from the upstream end of the experiment setup. The beach was built with a steep 1:7 planar slope, composed of very well sorted, medium silica sand with a median grain size of $d_{50} = 0.40$ mm.

Pintado-Patiño et al. (2016) used a beach profiling system to measured beach changes after the passage of the bore. For this purpose, they used a rail-mounted profiling system to measure the longshore and cross-shore profile changes with 5 mm resolution to generate ensemble averaged information of beach change at high resolution. As shown in Figure 4.10, the turbulent bore in the flat region was captured by custom made resistive wave gages (WG) measuring water depth (h) at six different locations (WG 1 to WG6). Five other stations (S1 to S5) were deployed with co-located instruments across the beach profile to measure flow and sand related quantities over the sandy slope. At station S1 located 0.4 m downstream of the beach toe, a wave gauge, an Ultrasonic Distance Meter (UDM, Massa M300/150 with 0.255 m resolution) and an Acoustic Doppler Profiling Velocimeter (ADVP, Nortek Vectrino II profiler) were deployed to measure the surface elevation and velocity profile. The UDMs were located at all stations on the beach profile (S1 to S5) to measure surface elevation. Also, for stations S1 and S2, the ADVPs were deployed to measure velocity profile near the bed. Electromagnetic current meters (EM) were placed at stations S2 to S5 to measure the velocity 3 cm above the bed. Also, the suspended sediment concentration fraction was measured at stations S1 and S2 using Fiber Optical Backscatter Sensors (FOBS). Each of the two FOBS used in this experiment come with ten probes stacked at 1 cm spacing as a single unit. Accordingly, FOBS provided simultaneous sediment concentration profiles over a 0.10 m vertical range from the bottom at stations S1 and S2.

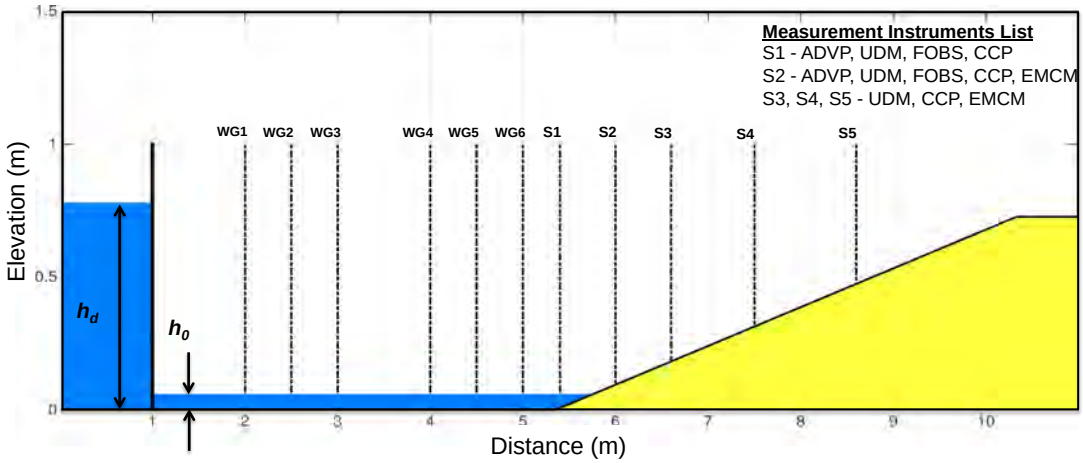

Figure 4.10: Pintado-Patiño et al. (2016) Dam-Break Experiment Setup.

4.2.2 Model Setup

To simulate the Pintado-Patiño et al. (2016) dam-break test, we generated a grid with dimensions of 1100×3 in x and y directions with $\Delta x = \Delta y$ =1 cm corresponding to 11 m long flume, in which the experiments were conducted (Figure 4.10). The median grain size of $d_{50} = 0.4$ mm was used in the model, and the fall velocity was calculated to be $w_f = 0.0514$ m/s using Rubey's (1933) formula

$$w_f = \sqrt{(s-1)gd_{50}}\left(\sqrt{\frac{2}{3} + \frac{36\nu^2}{(s-1)gd_{50}^3}}\sqrt{\frac{36\nu^2}{(s-1)gd_{50}^3}}\right) \tag{4.1}$$

where S is the specific gravity, d_{50} is the median grain size, and ν is the kinematic viscosity. The hard bottom condition was implemented for the region in front of the sandy beach toe, and the drag coefficient of $C_d = 0.0025$ was used for the bottom of the flume. The sand thickness (Z_s) for the beach profile was simply the profile elevation from the flume floor. Eleven gauges were deployed in the model to record surface elevation, depth-averaged velocity, and depth-averaged sediment concentration for comparison with WG1-6 and S1-5 measured data (Figure 4.10). The dam-break condition was implemented in the simulations using an initial surface condition. The water depth for the first 100 points on the left of the domain (1 m) was set to be 0.78

m, and 0.06 m initial depth was used for the rest of the domain. Unfortunately, it was impossible to simulate the second gate which blocks the reflective effects from the left of the domain in the model. Therefore, our results are only comparable to measured data before the reflected wave reaches the shoreline, which is about the first 10 seconds of the experiment.

4.2.3 Results

Figure 4.11 demonstrates a comparison between measured and calculated surface elevations for the gauges inside the flume (WG1-6). The measured data shown in the figure are ensemble averaged for 30 repetitions of the experiment. Calculated surface elevations for WG 1-6 shows good agreement with recorded data, although the reflection of the bore front seems to occur faster during simulation. This difference could be because of the existence of the porous beach, which in reality decelerates wave runup and rundown (Pintado-Patiño et al., 2015). However, this process is left out of the model. Therefore, the runup and rundown process in the model happens faster than in the actual experiment.

Figure 4.12 shows the recorded surface elevations from UDMs on the slope compared to simulation results. The surface elevation results in the flume and on the beach show good agreement with recorded data. The differences between the measured and computed bore front are due to the smoothing that was performed on the recorded data to remove measurement noise. Our results show that the dam-break bore is generated in the flume after releasing the gate with about 25 cm water depth. The bore front height decreases after breaking over the beach slope, and for the gauges S2 to S5 a wave height about 10 cm is recorded both in measurement and in the model. The bore front height decreases from 20 cm to 5 cm over the distance between gauges S1 and S5 (Figure 4.12).

Figure 4.13 illustrates the comparison between the measured velocities and simulation results for gauges S2-5. The measured data shown in this figure are obtained from EM recording in gauges S2 to S5 which measures the velocity 3 cm above the bed.

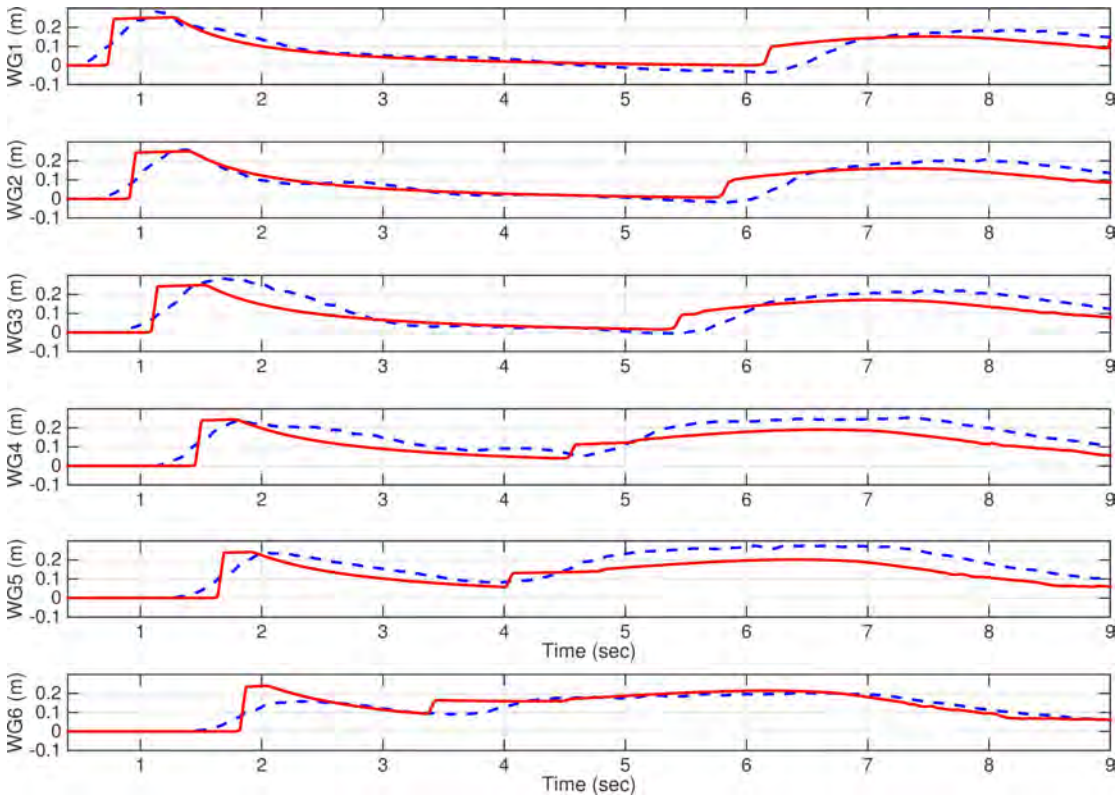

Figure 4.11: Comparison between measured (blue dotted lines) and computed (solid red lines) surface elevations at wave gauges WG1-6. The gauge locations are shown in Figure 4.10.

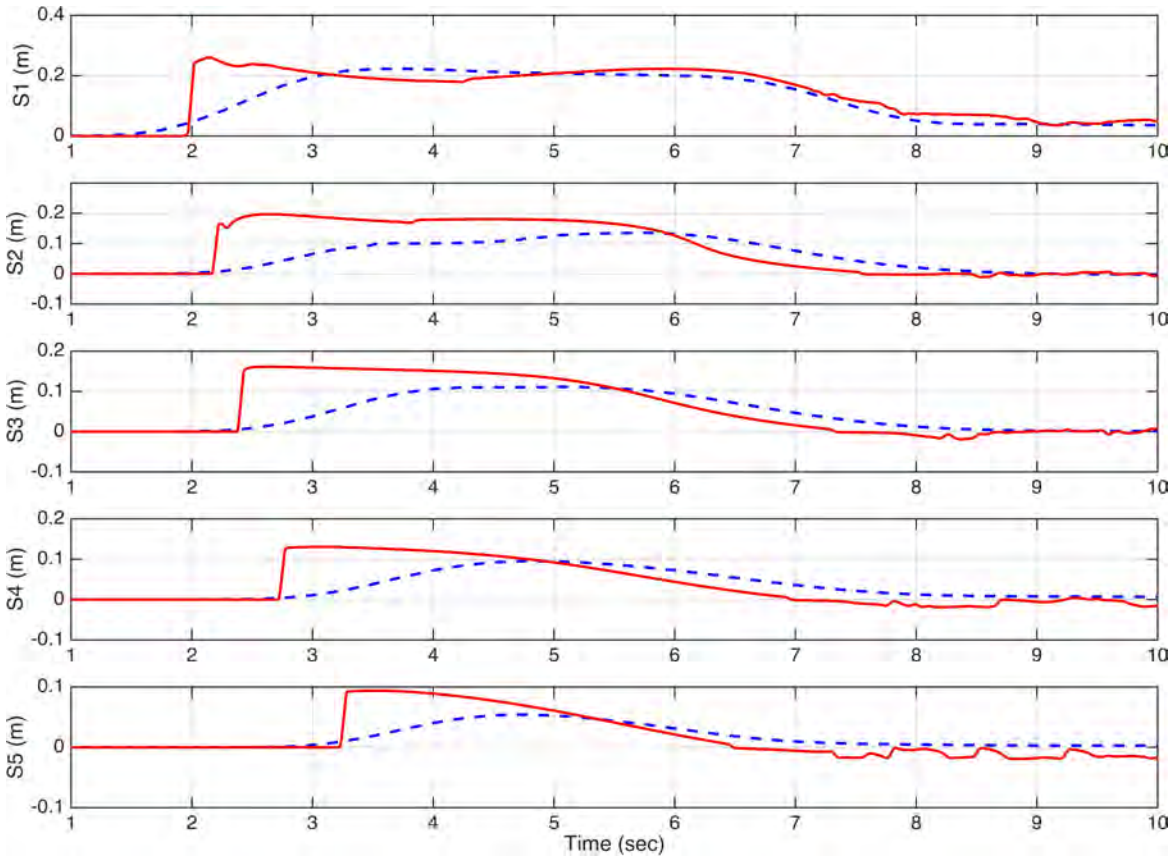

Figure 4.12: Comparison between measured flow depths (blue dotted lines) from UDMs and simulated values (solid red lines) at stations S1-5. The gauge locations are shown in Figure 4.10.

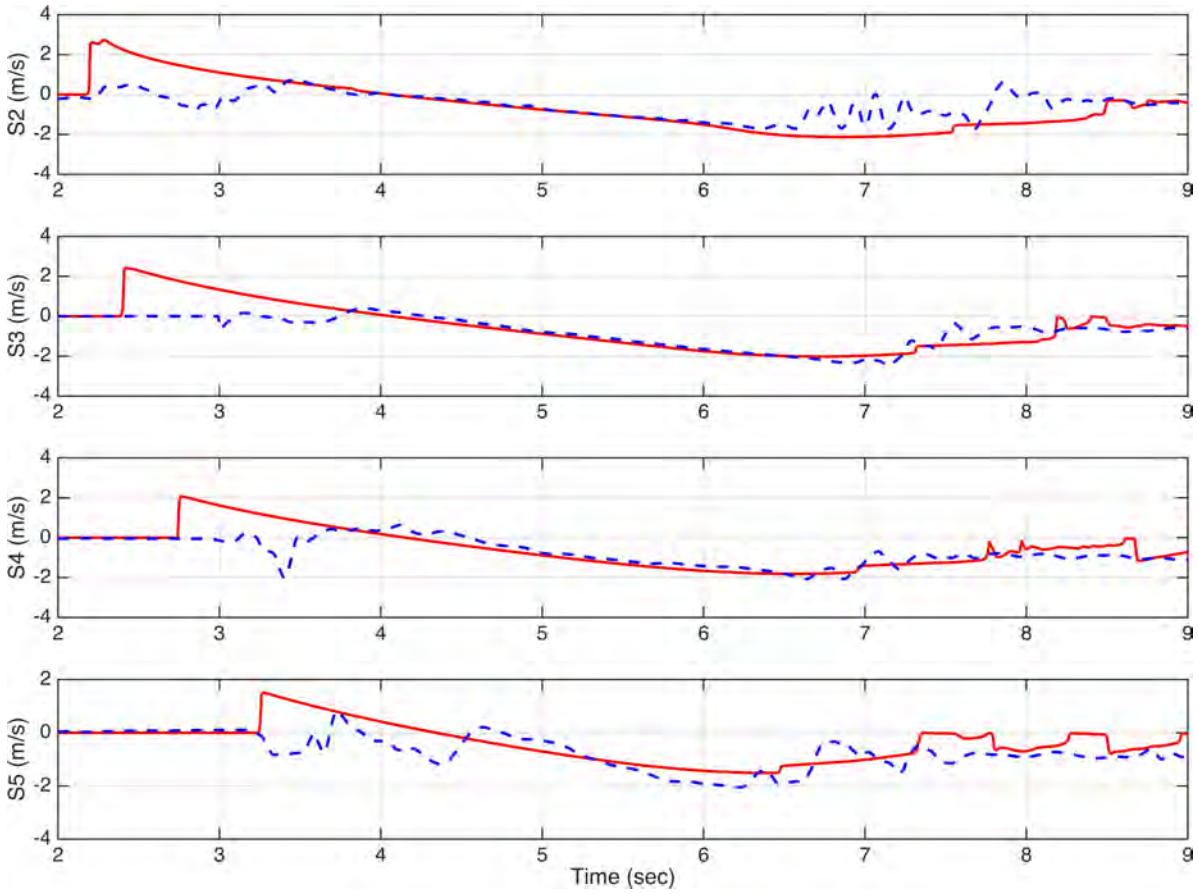

Figure 4.13: Comparison between measured velocities 3 cm above the bed (blue dotted lines) with EMs, and calculated depth-averaged values (solid red lines) at stations S2-S5. The gauge locations are shown in Figure 4.10.

Although the bore front velocity is not captured in EM recordings, depth-averaged velocities calculated by the model shows good agreements with measured data during the rundown process.

Figures 4.11-4.13 showed that the model can successfully capture the hydrodynamics of the dam-break experiment. To study the difference between sediment transport process computed with the model to the measurements, we used the recorded data from FOBSs located at stations S1 and S2 (Figure 4.10) to depict a comparison between measured and recorded depth-averaged sediment concentration. As mentioned above,

FOBS records the sediment concentration from 1 to 10 cm above the bed. To calculate the depth-averaged sediment concentration from the experiment data, we used the UDMs surface elevation recordings at locations S1 and S2. For flow depths smaller that 10 cm the depth-averaged sediment concentration were simply calculated directly from FOBS measurements. Figure 4.14 shows a comparison between the measured sediment concentration profile at S1 versus the assumed exponential profile (2.26) for the time between 7 to 10 seconds after the gate was released. We used the lowest recorded sediment concentration as the reference value (c_0) to depict the exponential profile. The assumed exponential profile in generally in good agreement with recorded data. Accordingly, to obtain the depth-averaged sediment concentration values from measurements for situations where the flow depth was larger than 10 cm, we extrapolated the sediment concentration values for the upper regions of the water column using the exponential profile assumption. Then, simply we performed depth averaging to obtain comparable data to the model results.

Figures 4.14 showed that the model simulates sediment transport processes in the dam-break test properly in addition to the hydrodynamics. Bed changes are shown after the rundown of the first wave and before the reflected wave reaches the beach profile (Figure 4.15). The solid red line in Figure 4.15 depicts bed changes after 10 seconds of simulation compared to measured data (solid blue line). Similar to solitary wave condition discussed in previous sections of this chapter, bed changes are significantly larger during rundown compared to runup, where the dam bore erodes the shoreface and deposits the eroded sand close to the slope toe. In Figure 4.15, simulated bed elevations are less than measured values almost everywhere. However, after 10 seconds from the beginning of the experiment, there is still a significant mass of suspended sediment in the water column, and not all of the sediment gets deposited after 10 seconds. This is the reason why calculated bed changes are less than recorded values which were measured after flow field were completely settled, and all of the suspended sand deposited on the bed. Overall, similar to calculated results of Kobayashi and Lawrence (2004) solitary wave experiment, the model was able to predict the location

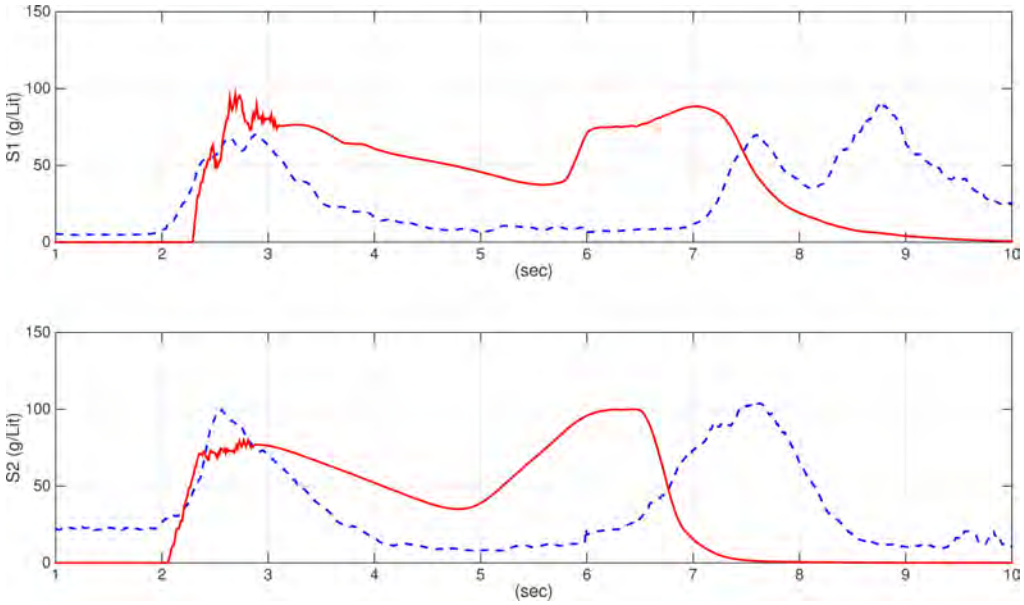

Figure 4.14: Comparison between measured depth-averaged sediment concentrations (blue dotted lines) recorded with FOBS and computed values (solid red lines) at stations S1 and S2. The gauge locations are shown in Figure 4.10.

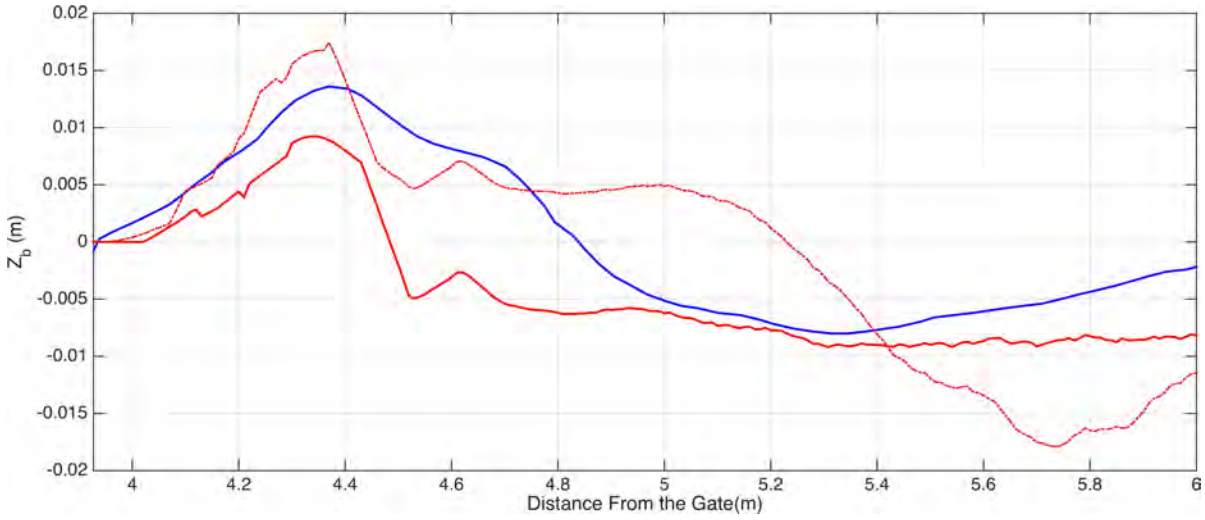

Figure 4.15: Comparison between measured bed changes (solid blue line) and calculated Z_b after 10 seconds of simulation (solid red line), and after all the suspended sediment deposits on the bed (red dotted line), which is influenced by reflection effects.

of erosion and deposition correctly. The black dotted line in Figure 4.15 shows bed changes calculated by the model after all the suspended sediment is deposited on the bed. It must be noted that this result is obtained with reflection effects included, which were blocked during the experiment with a wooden gate.

4.3 Crescent City, CA Harbor Sediment Scour and Deposition, Caused by the 2011 Tohoku-oki Tsunami

Two recent tsunami events impacted the west coast of the United States, one originating off the coast of Chile on February 27, 2010, and the other off Japan on March 11, 2011. Both tsunami events created strong currents within harbors in California, causing significant damage. During the 2011 tsunami, the maximum tsunami amplitude was measured at 2.47 m (Figure 4.24) in Crescent City harbor. Over 50-million dollars in damage resulted in California harbors (Wilson et al., 2013). In California, the most severe tsunami effects were observed in Crescent City harbor, a harbor known for vulnerability to tsunamis because of offshore bathymetry as well as

harbor configuration. During the first two hours of the tsunami activity, the tide gauge recorded a peak amplitude of almost 2.5 m (Figure 4.23), which fortunately occurred at low tide, producing very limited inundation of dry land.

Figure 4.16: Tsunami flow-regime map for Crescent City Harbor. Current directions and velocities, and areas of sediment erosion and deposition are based on observations of the various (30) ground-level and aerial video, pre- and post-tsunami bathymetry, and sediment analyses (Figure taken from Wilson et al., 2012, Figure 5)

Figure 4.16 (taken from Wilson et al., 2012) shows the erosional flow patterns, with current velocity estimates from video analysis and areas of sediment deposition and erosion within the harbor. Video analysis indicated peak currents of 4.5 m/s at the mouth of the basin. Also, some overland flooding was observed in the recreational vehicle park near the mouth of Elk River. All docks inside the small boat basin

were extensively damaged or destroyed during the tsunami (Figure4.16). Because of tide-gauge recordings as well as the availability of pre- and post-tsunami bathymetry measurements, we decided to simulate 2011 Tohoku-Oki morphological effects inside Crescent City harbor. This test case examines whether the model can work effectively in complex bathymetric conditions, where the hard bottom condition of the model could be tested in areas such as the breakwater, jetties, and seawalls.

4.3.1 Pre- and Post-Field Measurements

Wilson et al. (2012) have investigated two sets of pre- and post-tsunami bathymetric data for the Crescent City harbor to assess the morphological changes induced by 2011 tsunami. They concluded that the best comparison could be obtained from NOAA's multi-beam bathymetry collected on November 18−23 2008 and March 17−21, 2011 (NOAA, 2008 and NOAA, 2011). The difference between these datasets is shown in Figure 4.17. This figure shows bathymetric changes observed between the 2011 and 2008 NOAA DEMs, for the Crescent City small-boat basin and outer/mid-harbors. Figure 4.17 show the overlap area between two datasets where about 289,360 m^3 of sediment was scoured and an approximate 154,600 m^3 of sediment deposition was observed. However, the surveys do not extend throughout all parts of the harbor, and they do not include deposition in the west of the small boat basin. Wilson et al. (2012) reported that significant deposition within portions of the mid-harbor and the small boat basin rendered much of the inner harbor unusable for navigation.

Through the analysis of videos, as well as pre- and post-tsunami bathymetric datasets, Wilson et al. (2012) were able to provide a detailed picture of how sediment transport occurred during the 2011 tsunami in Crescent City harbor. They reported that during the most active parts of the 2011 tsunami, water surged into and out of the outer harbor entrance rapidly, causing bathymetric changes inside the harbor. Significant scouring was observed close to the jetties (as much as 4 m of scouring off the jetty tip), with erosive pattern continuing along the backside of the jetty and into

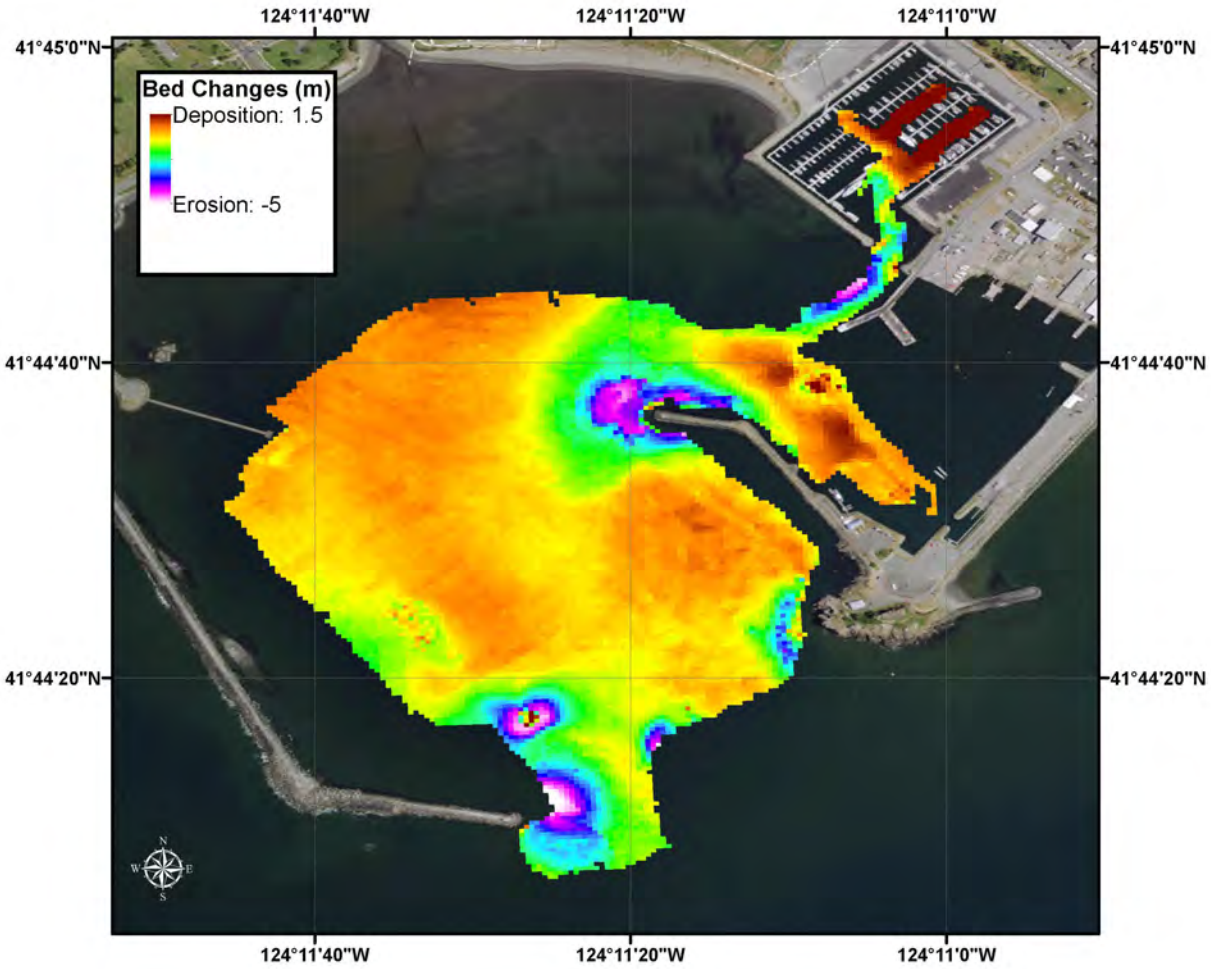

Figure 4.17: Bed changes inside the Crescent City harbor during the 2011 tsunami. Wilson et al. (2012) performed this analysis through comparison of two NOAA datasets, one measured in 2008 (NOAA, 2008), and the other in March 2011 (NOAA, 2011), few days after the event.

the south-east portion of the mid-harbor (Figure 4.17). Tsunami also scoured the mid-harbor area and the region next to the small boat basin's entrance. Also, a layer of sediment up to 1 m thick was deposited along the central portion of the entry of the outer boat basin, parallel to the scoured zone. In summary, major erosion occurred around outer and mid-harbor jetties and at the mouth of the small boat basin due to water current velocities which observed to be up to 4.6 m/s. In contrast, sediment accretion was observed in central parts of the outer harbor, as well as inside the small boat basin shown in Figure 4.17.

4.3.2 Model Setup

To simulate the effects of 2011 tsunami in Crescent City harbor, we used the tsunami source described in Grilli et al. (2011), who employed a 3D finite elements model (FEM) to model the Tohoku-Oki tsunami source. They derived source specifications from a combination of seismic and GPS inversion to specify the earthquake-induced bottom uplift or subsidence as a function of time. They modelled the first 5 minutes of the tsunami using the non-hydrostatic model NHWAVE (Ma et al., 2012) using a 1 km resolution grid near Japan coastline, which is illustrated with a black box in Figure 4.18. Later, Kirby et al. (2013) used the surface elevation and depth-averaged horizontal velocity calculated by NHWAVE for 5 minutes after the earthquake as inputs for a spherical coordinate version of FUNWAVE-TVD to simulate the tsunami across the Pacific Ocean. They showed the ability of the spherical FUNWAVE-TVD model to reproduce results compared to measurements. Thus, for this study, we used a similar approach to capture tsunami effects in Crescent City harbor. Similar to Kirby et al. (2013), we use a computational domain that covers a region of the Pacific Ocean from 60^oS to 60^oN in the south-north direction, and from 132^oE to 68^oW in the west-east direction. Figure 4.18 shows the grid used for ocean-basin computations, which is 4800 $\times$ 3600 grid points in longitudinal and latitudinal directions. The simulations are performed with 2 arc-min resolution over the bathymetry data from ETOPO1 (Amante and Eakins, 2009) 1 arc-min database.

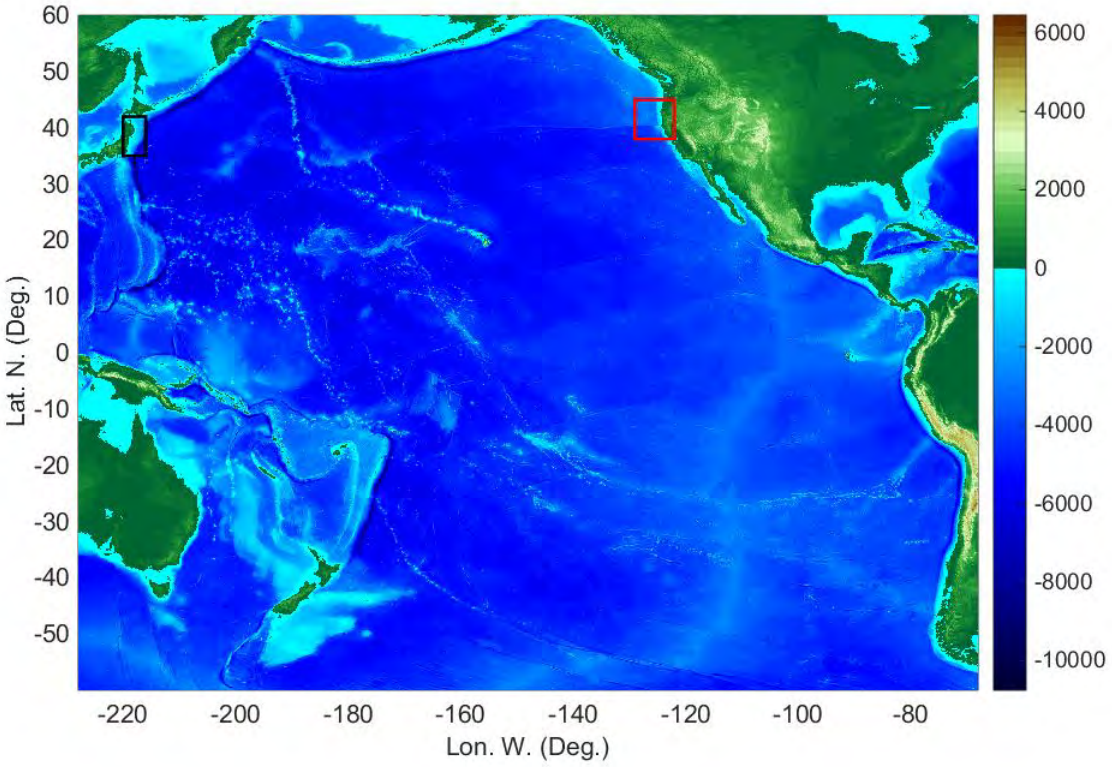

Figure 4.18: The bathymetry data used for Ocean-basin modeling of Tohoku-Oki 2011 tsunami in the Pacific Ocean. The black box shows the computational domain Grilli et al. (2013) used to simulate the tsunami source with NHWAVE model. The red box depicts the location of gauges deployed in the computational domain to record surface elevation and velocities for nearshore modeling through nesting.

The red box in Figure 4.18 indicates the location of gauges deployed in the computational domain near the California coast to perform nesting for nearshore tsunami modeling. Figure 4.19 shows the maximum surface elevation in the Pacific Ocean calculated by spherical Boussinesq version of FUNWAVE-TVD. The green circle in Figure 4.19 indicates the location of DART buoy 46407, which we used to provide a comparison between measured and simulated water surface elevation during the tsunami event. For this figure, we shifted model results 8 minutes forward in time to match the arrival of the measured and computed tsunami wave for a better comparison. The reason for this time shift is the effect of ocean compressibility, which is not considered in FUNWAVE-TVD (Wang, 2015). The comparison depicted in Figure 4.20 shows that the model was able to capture the incoming wave properly, with limited variances in the latter parts of the tsunami signal. The comparison with several other DART buoys inside the Pacific Ocean is provided in Kirby et al. (2013). They used the same model setup for their simulations and provided the comparison of the computed surface elevation with DART buoy measurements with good agreements.

We used the results of the ocean-basin simulation to perform five levels of nesting to simulate the tsunami flow conditions inside Crescent City harbor with higher resolution. Figure 4.21 demonstrates the nesting process to scale down the resolution from 16 arc-seconds to 1/6 arc-second. All of the nearshore runs were modeled with Cartesian grids with offsets fixed around Crescent City for minimal error around the study area. This approach was similar to that used by Tehranirad et al. (2015b-j), resulting in a passage of flow properties with negligible losses of information on nesting boundaries from lower to higher resolution domains.

For the first step, we used the recorded surface elevation and velocity terms (u, v) around the 16 arc-second domain illustrated with a red box in Figures 4.18 and 4.21. The 16 arc-second bathymetry was obtained from Coastal Relief Model (CRM) 3 arc-second data (NGDC, 2003) in nearshore areas, and through interpolation of 1 arc-min ETOPO1 data (Amante and Eakins, 2009) in areas not covered by CRM data. 16 arc-second corresponds to 367.2 m in East-West, and 493.2 m in North-South

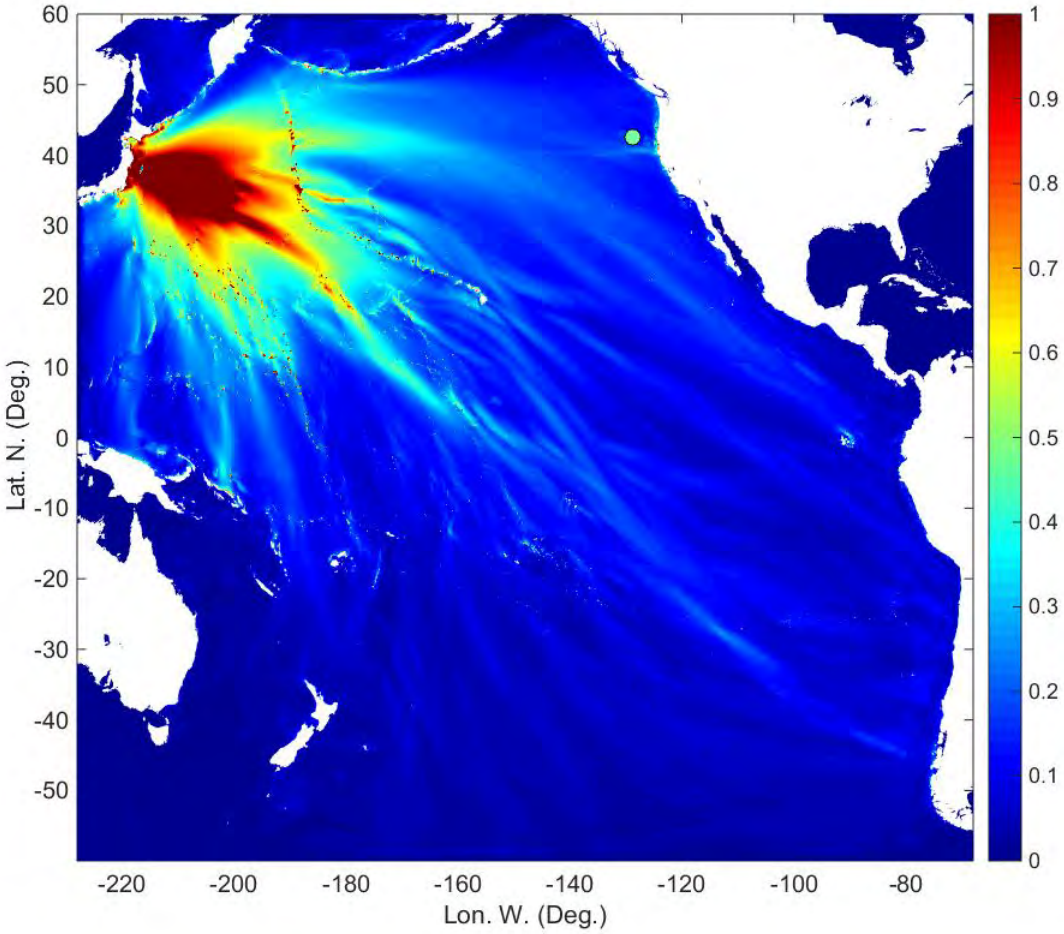

Figure 4.19: Maximum surface elevations calculated by the spherical version of FUNWAVE-TVD during simulation of 2011 Tohoku-Oki tsunami. The green circle close to California shorelines locates the DART buoy 46407.

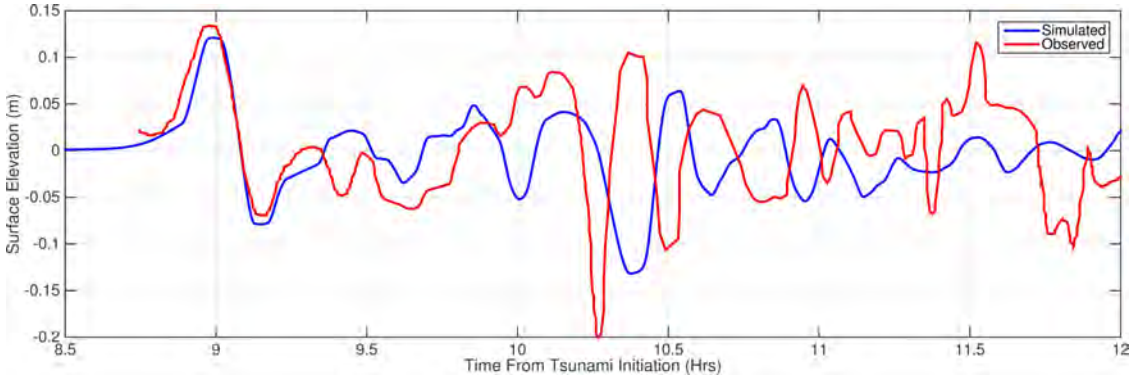

Figure 4.20: Comparison between surface elevation measurements during 2011 tsunami by DART buoy 46407(red line), and calculated results (blue line). The location of the buoy is demonstrated in Figure 4.19 by a green circle. The model results are shifted 8 minutes forward to match the arrival of the measured and computed tsunami wave.

directions at the latitude of the Crescent City. The 16 arc-sec square grid shown in Figure 4.21 has 1200 grid points in both x and y directions. The flow information of 16 arc-second simulations was recorded around the Crescent City harbor DEM (Grothe et al., 2011) depicted with a blue box in Figure 4.21. The Crescent City harbor DEM is the data that Wilson et al. (2012) used as their pre-tsunami bathymetry. The DEM has 1/3 arc-second resolution and was used to generate bathymetry data for 4, 1, 1/3 and 1/6 arc-second simulations. The bathymetry data for 1/6 was obtained through linear interpolation of the original 1/3 arc-second data. Also, knowing that the tsunami reached the Crescent City at low tide condition, we converted the vertical datum of the DEM from Mean High Water (MHW) to Mean Low Water (MLW) using VDATUM software. The nesting approaches for 4, 1 and 1/3 runs were similar to that of 16 arc-second shown in Figure 4.21. Finally, the results of 1/3 arc-second run were used to construct 1/6 arc-second run where simulations were performed with morphology and sediment transport modules activated.

Figure 4.22 shows the computational domain of 1/6 arc-second simulation grid used to model morphological changes during 2011 tsunami inside the Crescent City

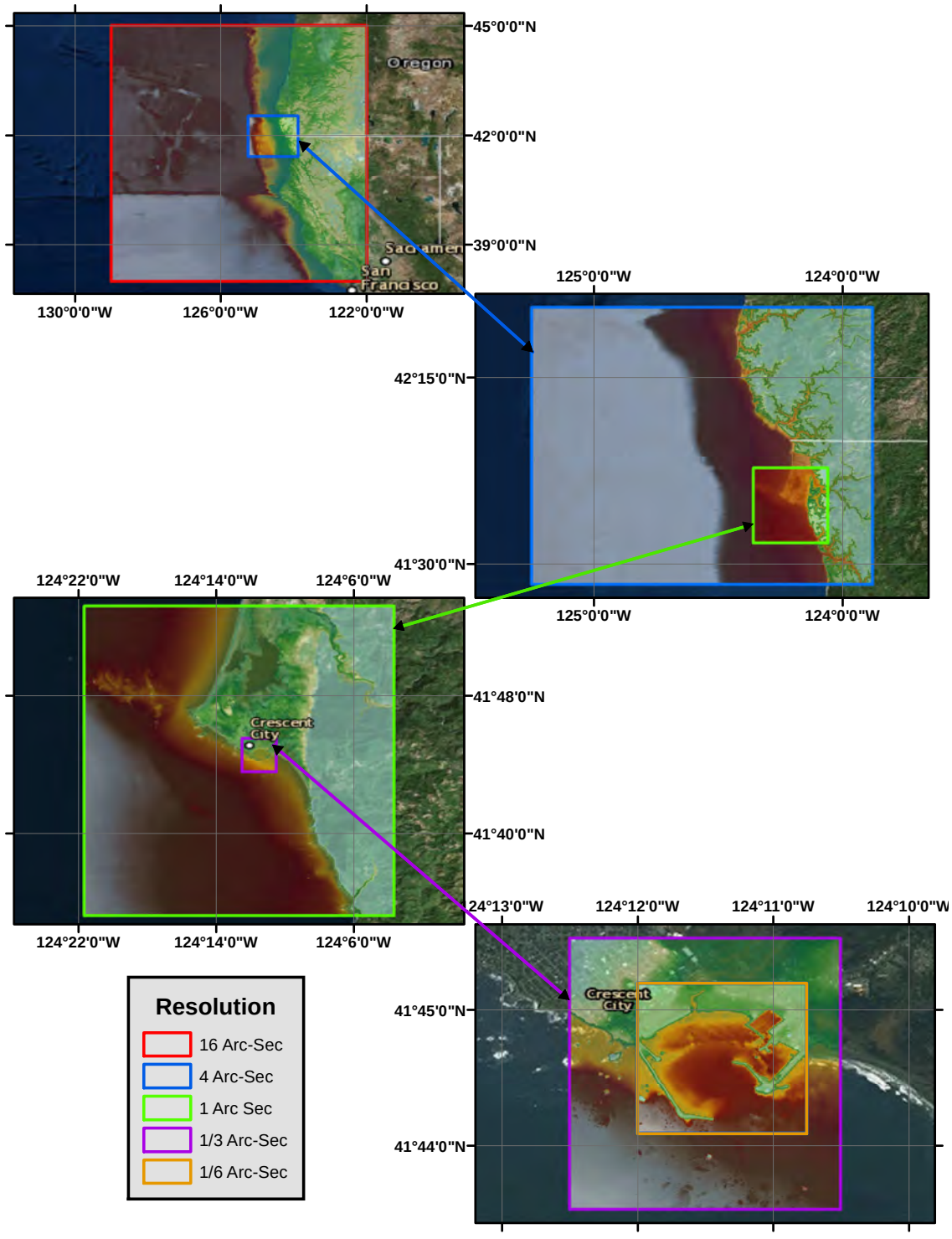

Figure 4.21: The nesting process used in this study to scale down the resolution from 16 arc-seconds down to 1/6 arc-second.

harbor. The grid size is 450 $\times$ 400 in x and y directions, with $\Delta x = 3.83$ m and $\Delta y = 5.15$ m corresponding to 1/6 arc-second in Crescent City latitude. Using a combination of GIS work and calculation of bed slope, we were able to distinguish the sandy regions of the harbor from hard bottom areas. We assumed that the areas with slopes larger than 0.5 were either rocky points or coastal structure regions.

Figure 4.23 illustrates the sandy regions inside the harbor. Wilson et al. reported that deposited sediments were mostly fine sand and silt, mainly from the inside of the harbor. Therefore, the median grain size was considered to be 0.2 mm, with 2.0 cm/s fall velocity. We performed several tests with different grain sizes, which showed that sediment size changes in a range of 0.1 to 0.4 mm have negligible effects on the final results. The angle of repose of the sediment used in the avalanching scheme was set to be $\tan(\phi) = 0.5$ for consistency of assumptions. Also, due to the shortage of information, the porosity coefficient is considered to be the standard value of 0.4. During simulations, while considering a uniform drag coefficient for the whole domain, we noticed that some of the jetties were inundated and overtopped in contrast to the reports. Thus, to address this issue, we used different drag coefficients for harbor structures compared to sandy regions. For jetties, breakwaters, and rocky regions we used the drag coefficient of $C_d = 0.1$, and for the sandy bottom, the $C_d = 0.005$ was used corresponding to the sediment grain size. We observed that defining large drag coefficients for coastal structures improve the results significantly, especially around the jetties where large scours occur.

4.3.3 Results

Figure 4.24 shows the comparison between calculated and measured surface elevations in the entrance of small boat basin. The location of the gauge is depicted in Figure 4.22. As shown in Figure 4.24, tide gauge data between 10.2 to 10.7 hours after the tsunami initiation is not available during the time when the first significant wave of the tsunami signal enters the harbor area. Overall, model results show good agreement with recorded data, although the model underestimates the largest crests

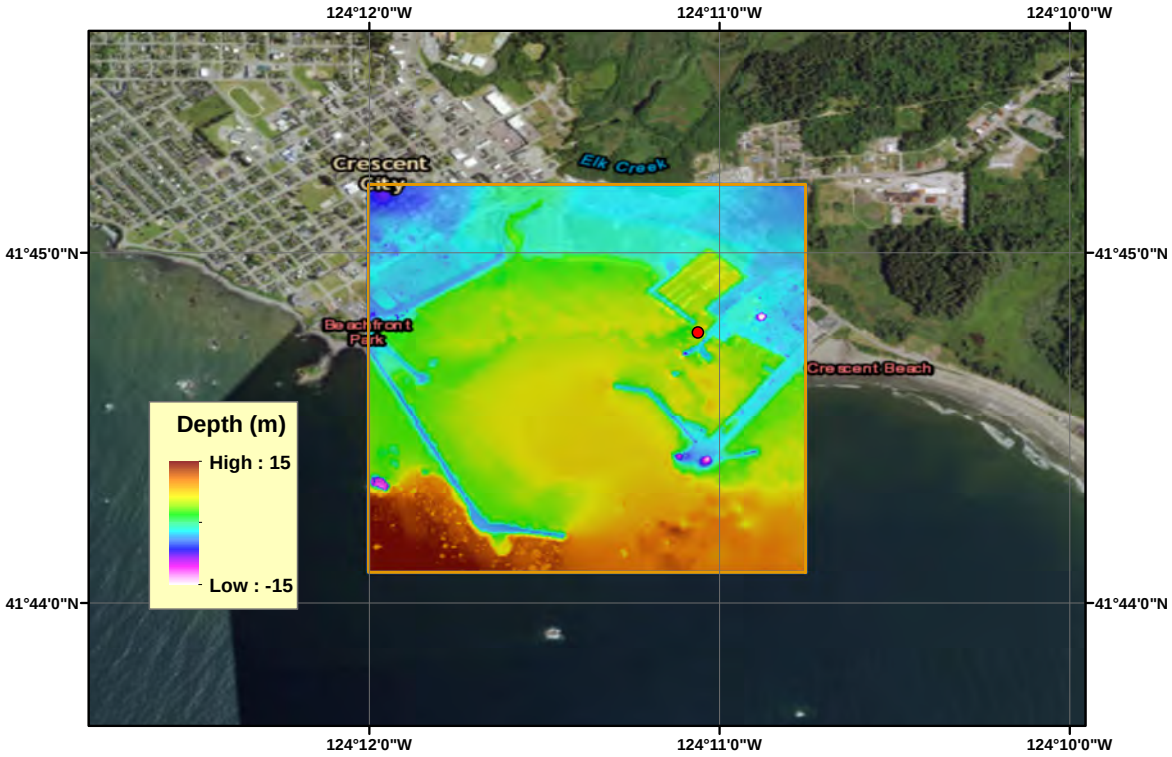

Figure 4.22: Computational domain of 1/6 arc-second grid used for modeling tsunami-induced morphological changes inside the Crescent City harbor. The red circle shows the location of the tide gauge inside the harbor.

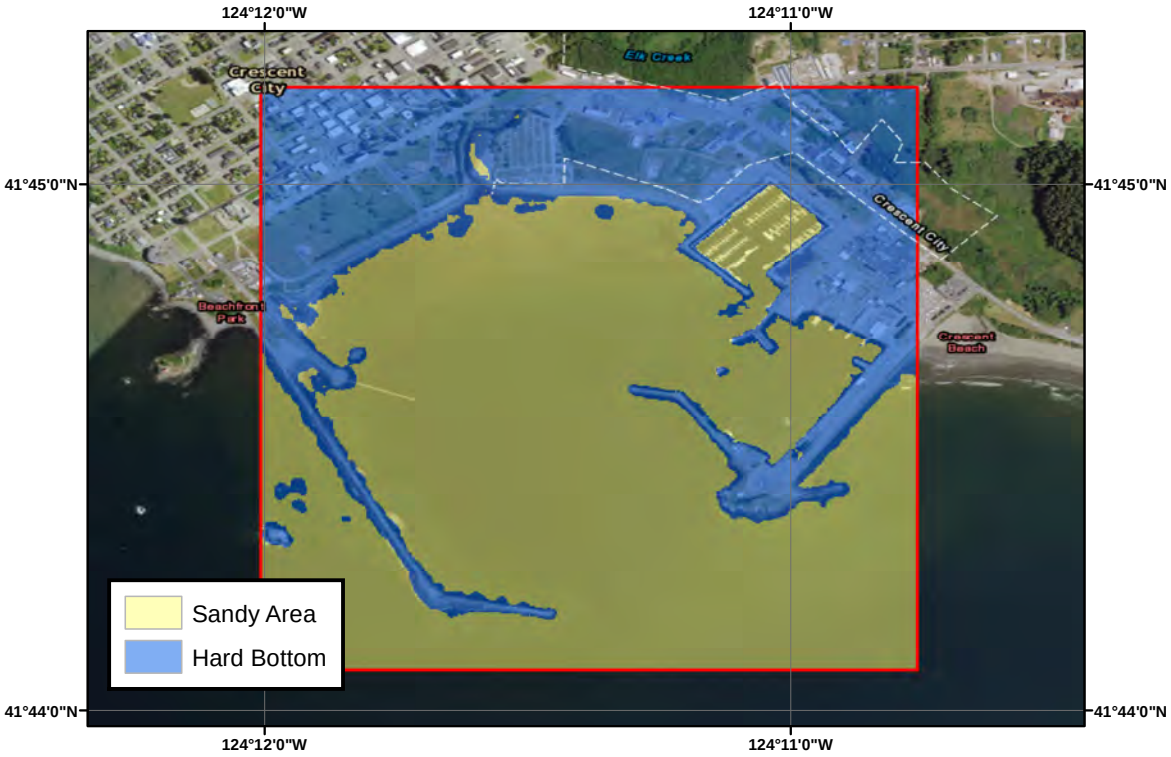

Figure 4.23: Hard bottom areas defined in the model for simulation of sediment transport during the 2011 tsunami inside the Crescent City harbor (Blue regions).

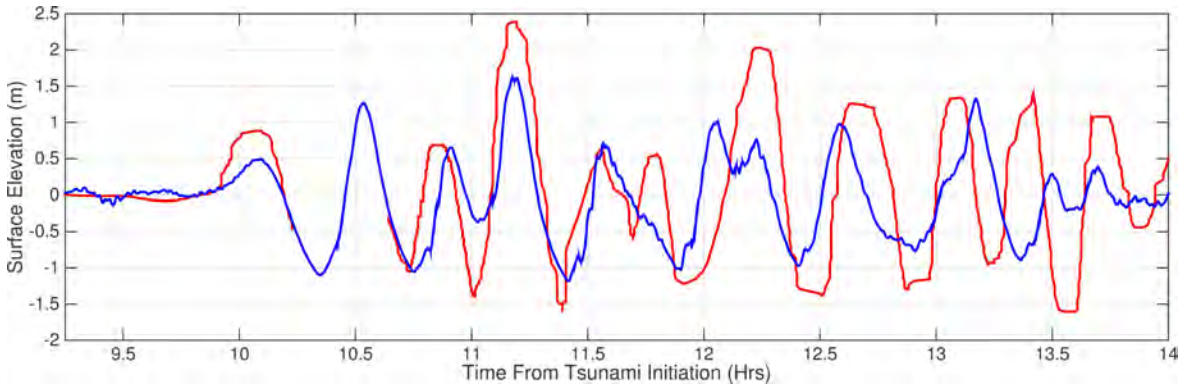

Figure 4.24: Comparison between measured (red line), and calculated (blue line) surface elevations at the entrance of the small boat basin of the Crescent City harbor. The location of the tide gauge is shown in Figure 4.22. For this figure, we shifted model results 8 minutes forward in time to match the arrival of the measured and computed tsunami wave for a better comparison.

elevations of the tsunami signal in the small boat basin entrance. After the first wave of the 2011 tsunami had reached California, the reflected waves caused edge waves along the coastlines propagating from north to south (Figure 4.25). These edge waves were created because the continental shelf is narrow and the sudden change in depth acted as wall trapping the reflected waves close to the shorelines, causing edge waves. Horrillo et al. (2008) performed an analysis to study tsunami enhancement around Crescent City and concluded that the shelf trapping mechanism tends to enhance the lowest natural modes of the tsunami signal, causing edge waves. The model successfully simulated this process. However, the model only captured the first 6 hours of the tsunami impact, while the tsunami signal lasted for three days in reality. This can be because of the numerical dissipation during the low-resolution 2 arc-min ocean basin simulations. Shi et al. (2012) addressed this issue, however; because of the computational limitations higher resolution simulations of the ocean-basin tsunami propagation was not possible.

Figure 4.26 illustrates the maximum surface elevation calculated by the model inside Crescent City harbor. Similar to the observations during the tsunami, the small boat basin experienced the largest surface elevations. The geometry of the harbor is

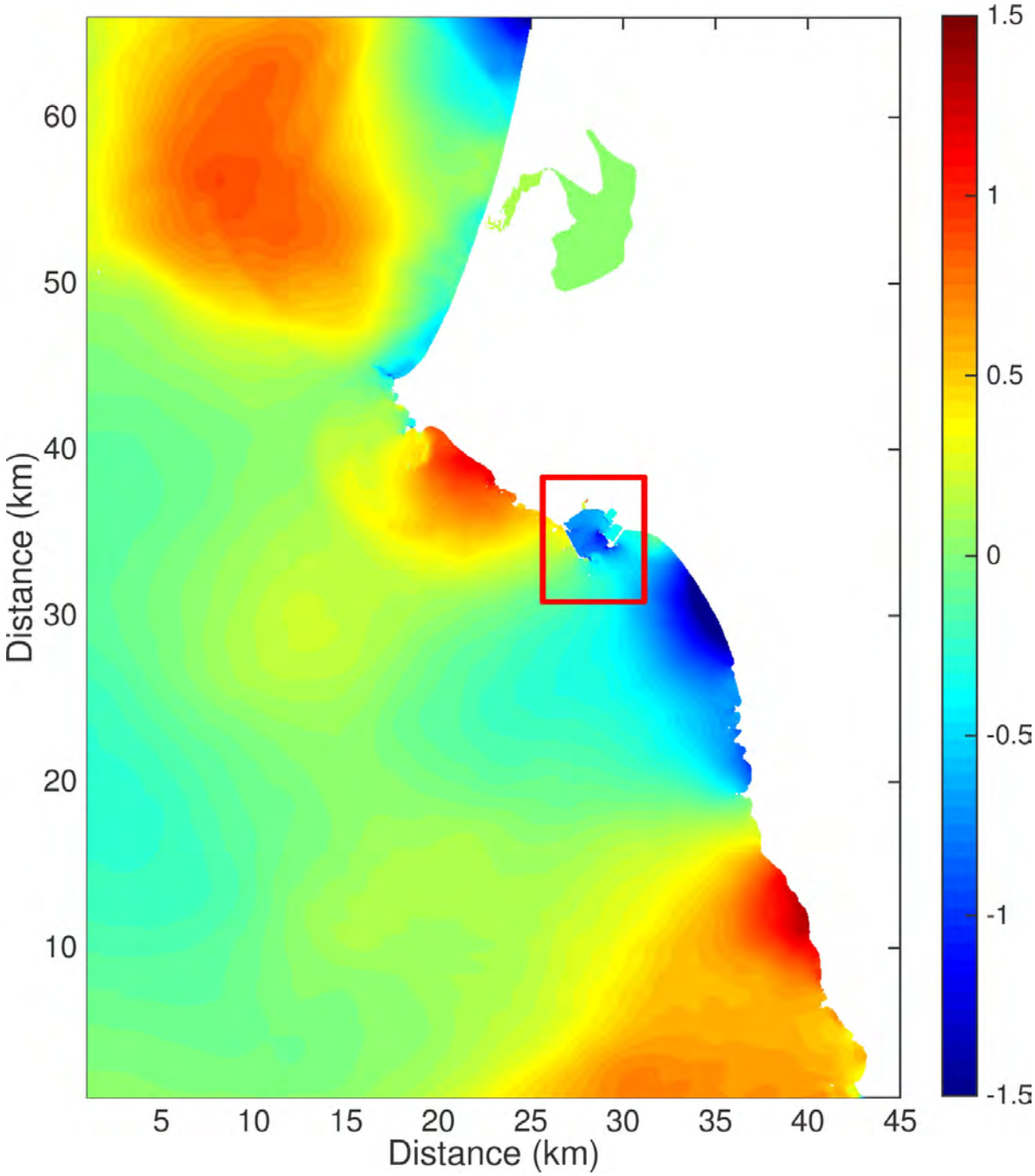

Figure 4.25: Formation of edge waves along California coast 11 hours after the tsunami initiation. The red box shows the location of the Crescent City DEM (Grothe et al., 2011)

Figure 4.26: Maximum computed surface elevation inside the Crescent City harbor for 2011 Japan tsunami.

one of the determining factors for the vulnerability of the small boat basin of Crescent City harbor to tsunamis, in addition to offshore bathymetry (Horrillo et al., 2008; Wilson et al., 2012). During the simulations, it was observed that the water mass was pushed toward the small boat basin area during the tsunami flow condition due to the harbor geometry, where the largest change in surface elevation was observed. This process has resulted in the partial or complete destruction of the docks during previous tsunamis that impacted the US West Coast.

Wilson et al. reported that the dominant process causing bed changes in the

small boat basin entrance was the outflow-inflow regime caused by 2011 tsunami inside the harbor. The agreement between the frequency of measured and calculated surface elevation shows that the model could capture the inflow-outflow regime correctly. Moreover, Lee et al. (2012) reported that at low tide conditions the resonant wave period in the harbor is 20 minutes, through spectral analysis of 2011 Japan and 2010 Chile tsunami signals in Crescent City harbor. They used idealized cases to calculate the resonance of the harbor during different tide conditions, where large waves were propagated toward the harbor, and the following perturbation frequency was considered to be the natural frequency of the harbor. They used the mild-slope equation to model the response curves at the tide gauge in Crescent City, and showed that the resonance period for the harbor is 20 minutes at low tide. The 20 minute period is comparable to measured and computed results shown in Figure 4.24, where at a similar period, a large volume of water enters the harbor causing significant wave-induced currents which led to the destruction of harbor facilities.

The maximum velocity calculated by the model inside the Crescent City harbor is demonstrated in Figure 4.27. The largest velocities were recorded along the navigation channel where the deepest parts of the inner harbor are located. Wilson et al. (2012) using video analysis of water surface during the tsunami concluded that the inflow-outflow velocity in the entrance channel of the small boat basin was 4.5 m/s, and about 3.0 m/s inside the small boat basin (Figure 4.16), similar to the values calculated by the model. Large velocities with the similar order of magnitude were observed during the simulation close to the jetties in the inner and outer harbor, correlating to the location of largest erosion observed in the harbor after the tsunami.

Maximum vorticity is another quantity recorded during the simulation of 2011 tsunami in Crescent City harbor illustrated in Figure 4.28. The largest values of vorticity and velocity mostly are located at similar locations inside the harbor. However, the vorticity is large close to the structures even in areas where large velocities are not calculated. The largest vortices are located close to the jetty in the inner harbor and the entrance of the small boat basin as well as along navigation channels.

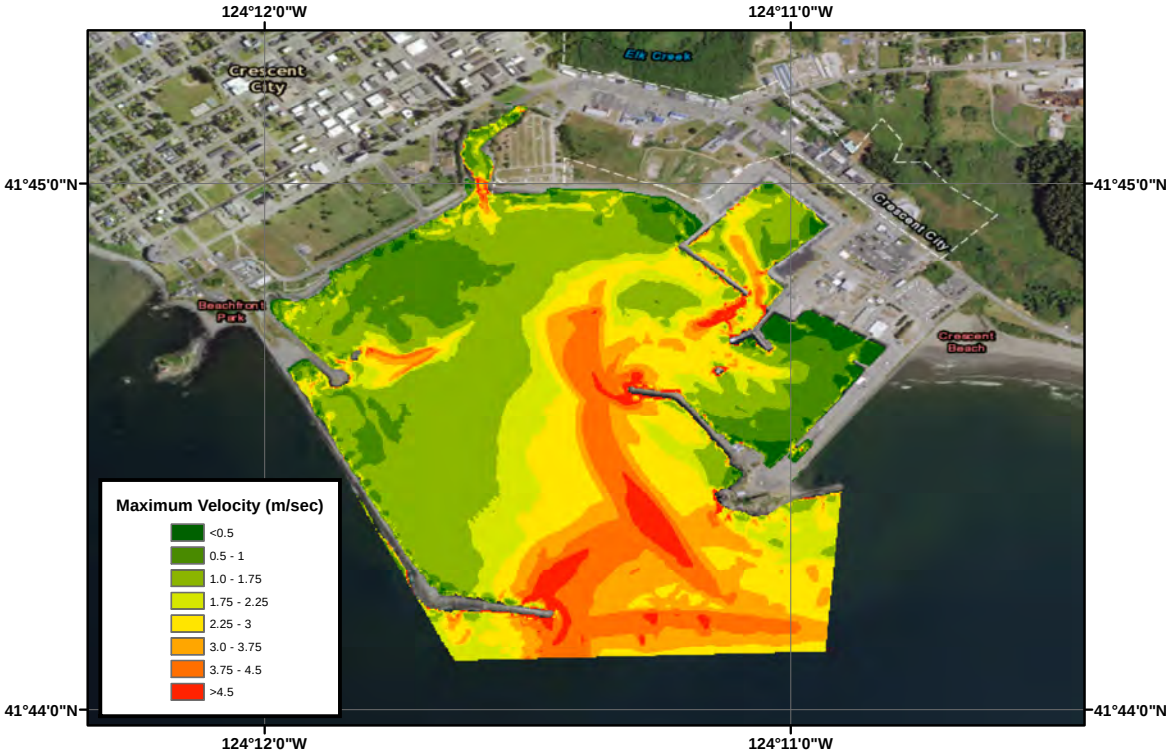

Figure 4.27: Maximum computed velocity inside Crescent City harbor during the simulation of the 2011 Tohoku-Oki tsunami.

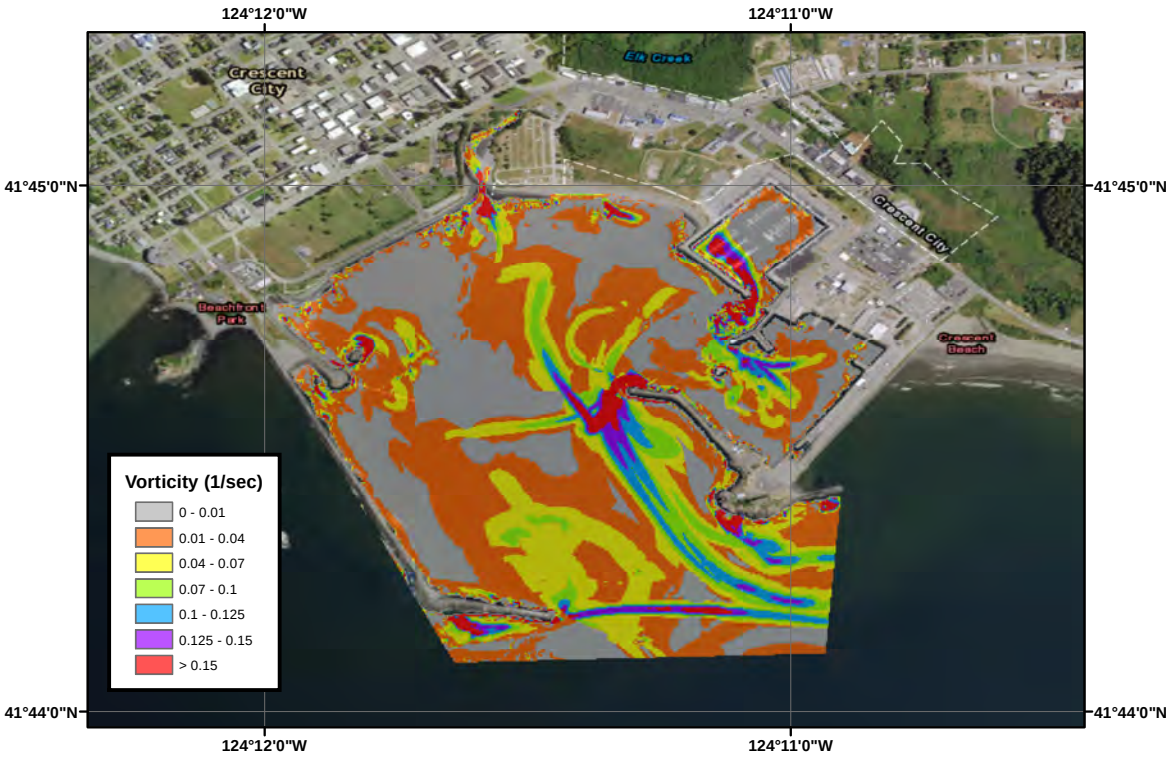

Figure 4.28: Maximum vorticity in Crescent City harbor calculated by the model during the simulation of the 2011 tsunami.

The computed bed changes after the 2011 tsunami inside the Crescent City harbor are illustrated in Figure 4.29. The model results show significant erosion near the jetties in the entrance of the harbor, similar to the field observations. The largest scours are calculated on the back side of the jetty in the mid harbor entrance and along the mouth of the small boat basin, with erosions between 2 to 3 m. Also, the model calculated a significant amount of sediment deposition inside the boat basins where in the low current velocity regime, parallel to observations. Wilson et al. (2012) reported that the deposition inside the boat basin was significant, making them unfunctional for navigation after the tsunami. The model computed accretion of a sediment layer with a thickness between 0.75 to 2 m in both of the boat basins.

Figure 4.30 compares measured and calculated erosion-deposition patterns inside Crescent City harbor after the 2011 tsunami. The results are generally in good agreement with field observations, where erosions were computed near the jetties and at the mouth of the small boat basin. Also, the model computed accretion of sediment in the middle of the outer harbor and inside the boat basins. The similarity between modeled and measured erosion-deposition patterns illustrate that the model is capable of locating erosion or deposition correctly. However, there are some differences between the bed change values, especially for the maximum erosion calculated by the model in comparison to the observations.

The model was able to capture the general trend of morphological change inside Crescent City harbor, although larger erosions were observed in field surveys. The model computed a maximum erosion value of 2.5 m around the jetties, where the measured scour holes were almost 5.5 m deep. Also, the erosion in the entrance channel of the small boat basin is underestimated by 2 m in the model, where scour of about 5.5 m was observed in the field. Two different reasons could be the cause of this difference between model results and field observations. First, because of the resolution of the grid used for simulations, the scour holes are not allowed to grow larger than a value determined by the avalanching limit (repose angle of sediment), which forces the slope to be the maximum value of 0.5. Although the avalanching scheme is constrained by

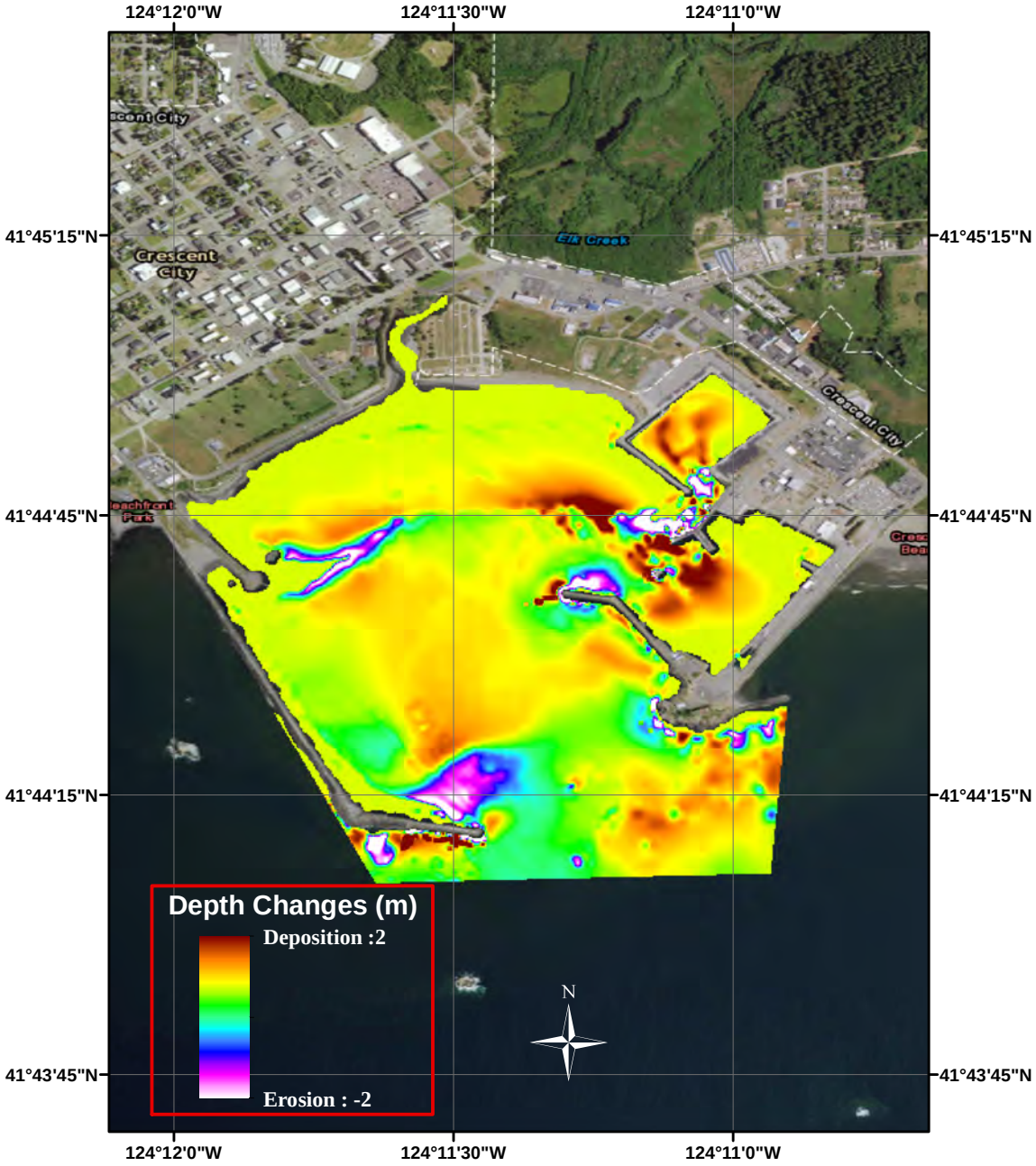

Figure 4.29: Computed bed changes in the Crescent City harbor during 2011 Tohoku-Oki Tsunami. Green, blue, purple and white colors represent the eroded areas.

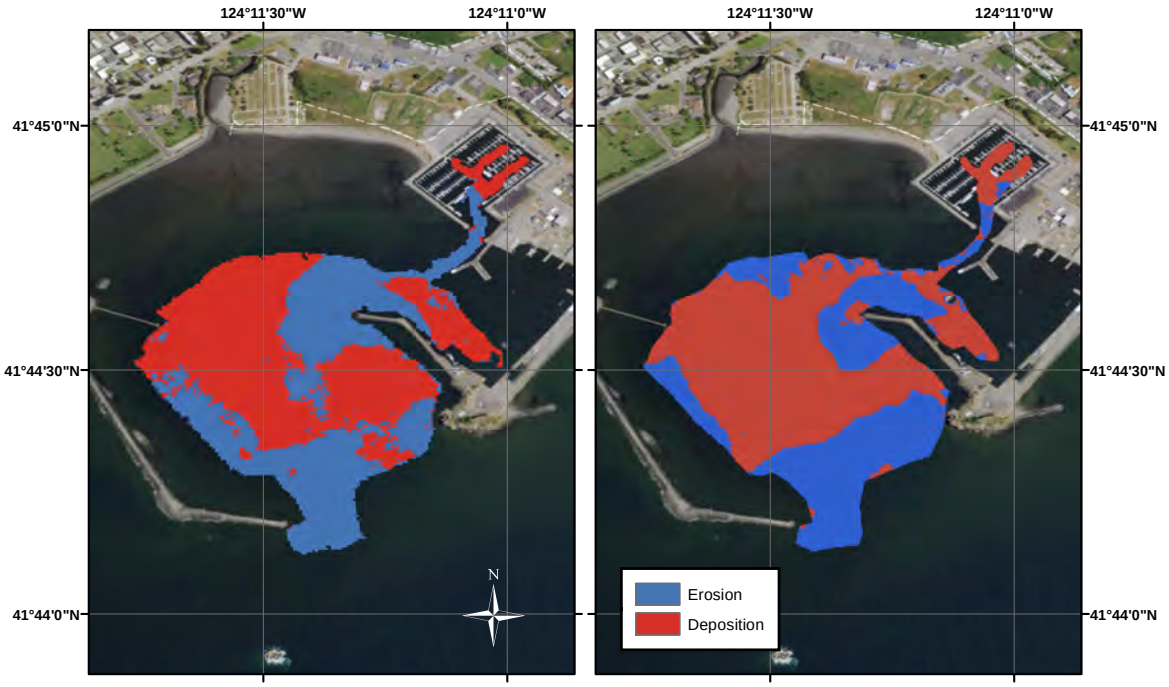

Figure 4.30: Erosion-deposition pattern inside the Crescent City harbor after 2011 tsunami; measured (left), computed (right). In both figures the blue color represents erosion and red color show deposition

the grid size, it is a vital part of the bed evolution simulation process and the results in its absence would be inaccurate. The other reason for the underestimation of significant erosions could be the shorter tsunami duration captured by the model compared to the observations. Wilson et al. (2012) reported that the tsunami signal lasted for three days in Crescent City harbor, with the inflow-outflow regime constantly changing the harbor bed. However, the model only captures 6 hours of the event. This could be because of convergence issues for the ocean-basin simulation where the reflective waves that generate the edge waves are not captured properly. During our simulations, we observed that each inflow-outflow occurrence resulted in a similar pattern of erosion-deposition shown in Figure 4.30, with the values of accretion and scour increasing, but the erosion-deposition pattern stayed constant after the first inflow-outflow event. Thus, if the model could have captured the duration of the tsunami correctly, probably better estimates of the erosion depths would have been achieved. This is also reflected in the total volume of computed erosion and deposition volumes inside the harbor. Overall, the model computed about 95,000 m^3 of erosion and 65,000 m^3 deposition inside the harbor, with the residual sediment either deposited outside the harbor or forced out of the computational domain boundaries. The total computed deposition and erosion volumes are about one-third of the measured values reported by Wilson et al. (2012). Considering the similar erosion-deposition pattern of measured and simulated bed changes (Figure 4.30), the differences between erosion and deposition volumes are mainly because of the difference between the captured and actual time scale of the event. However, neglection of 3D effects through using a depth-averaged model could be another reason for the difference between computed and measured bed changes.

Overall, the model successfully computed the erosion-deposition pattern inside Crescent City harbor during the 2011 tsunami. Although some differences existed between model results and field observations, mainly over the magnitude of the largest scours around the jetties, the outcome shows that the model is capable of simulating

tsunami-induced morphological changes over complex bathymetries and in the existence of structures and hard bottom regions.

Chapter 5

BARRIER ISLAND MORPHOLOGICAL RESPONSE TO TSUNAMI CONDITIONS

In the previous chapters of this thesis a description of a new model capable of simulating the tsunami-induced sediment transport was provided. In this chapter, we use the model to find an answer to the question asked at the beginning of this thesis; Does morphological adjustment during tsunami inundation increase the levels of hazard?

During the last several years, Tehranirad et al. (2014, 2015b-j) have studied several tsunami scenarios to generate tsunami inundation maps for the populated communities on the United States East Coast (USEC). Communities such as New York City, Nantucket, Myrtle Beach, and Savannah were studied and mapped for the inundation of various tsunami sources. Many coastal communities on the USEC are guarded against tsunami thread by barrier islands. In simulations with fixed bathymetry condition, these barriers diminish the tsunami waves in a way that protects the mainland behind them from notable inundation. Tehranirad et al. (2014, 2015b-j) showed that in areas such as Ocean City, MD, Atlantic City, NJ, and Long Island, NY, barrier islands of those regions were heavily inundated (Figures 5.1-5.3) with significant velocities recorded on top of them. In most of these locations, the mainland behind was computed to be tsunami safe. As mentioned before, tsunamis consist of several waves, and if the first wave flattens the barrier island or creates breaches, the latter waves might penetrate further onshore on the mainland behind them. However, this process cannot be captured using fixed bathymetries in the modeling. We study this idea using the model described and validated in previous chapters.

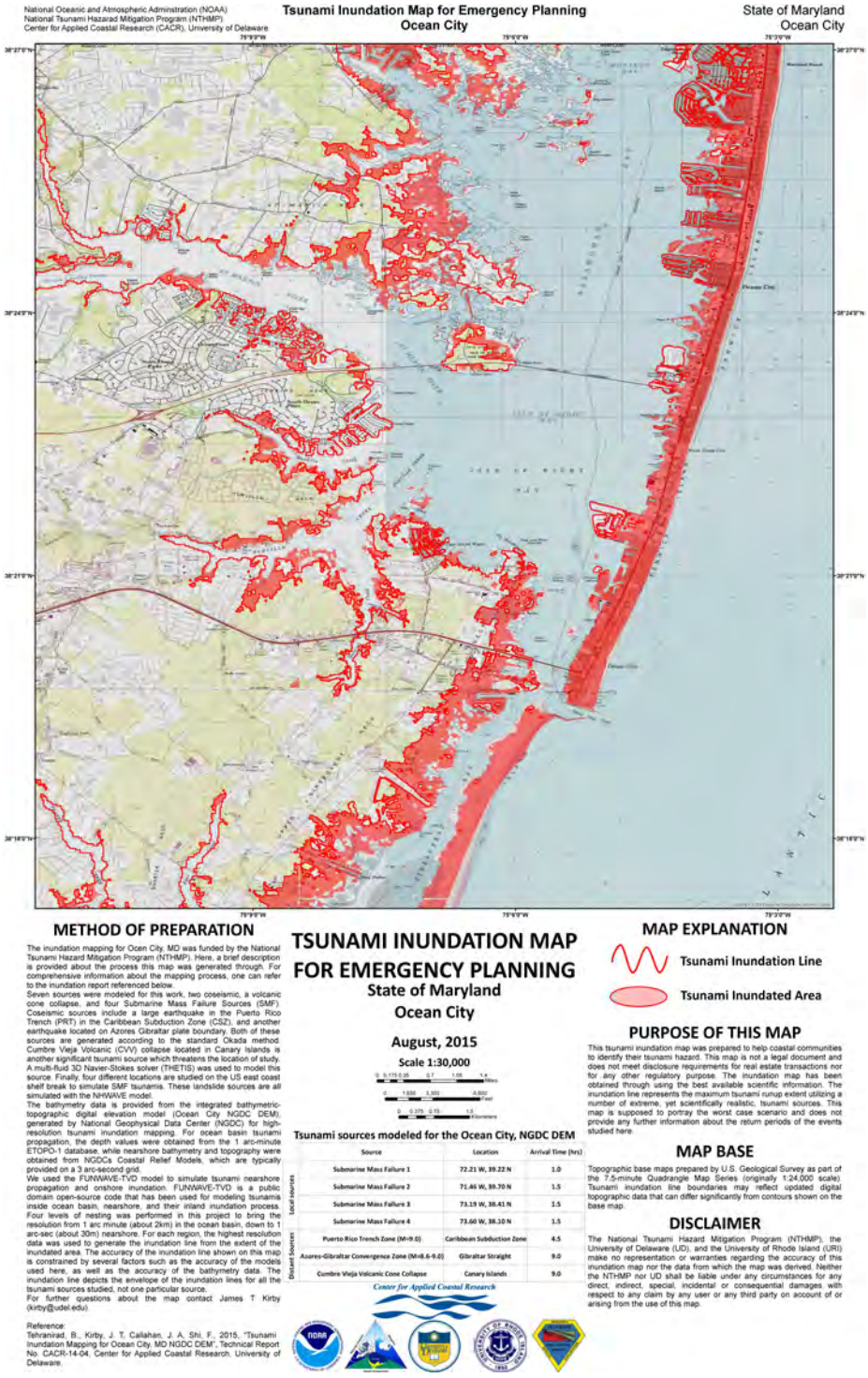

Figure 5.1: Tsunami inundation map for Ocean City, MD (Tehranirad et al., 2014).

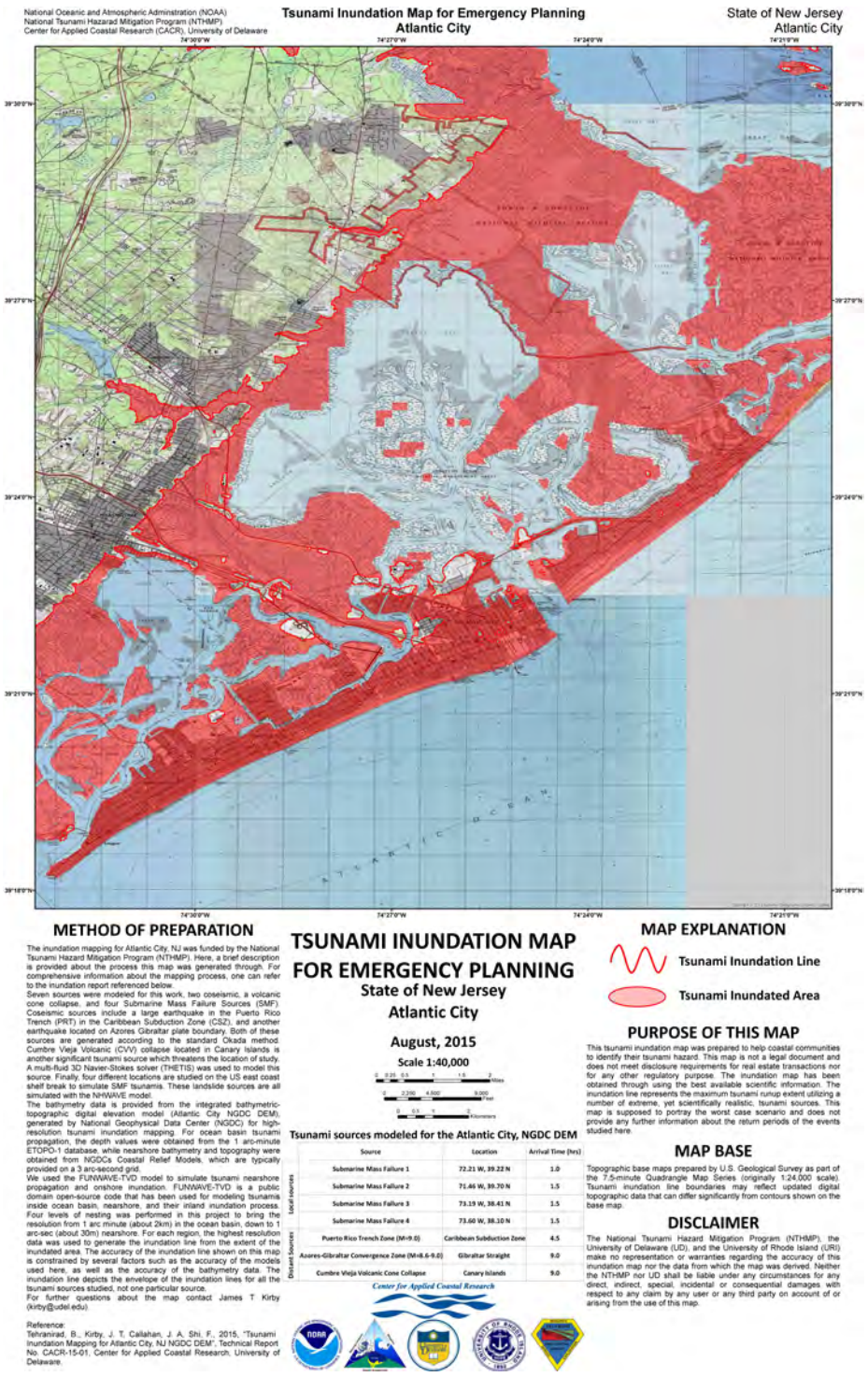

Figure 5.2: Tsunami inundation map for Atlantic City, NJ (Tehranirad et al., 2015b).

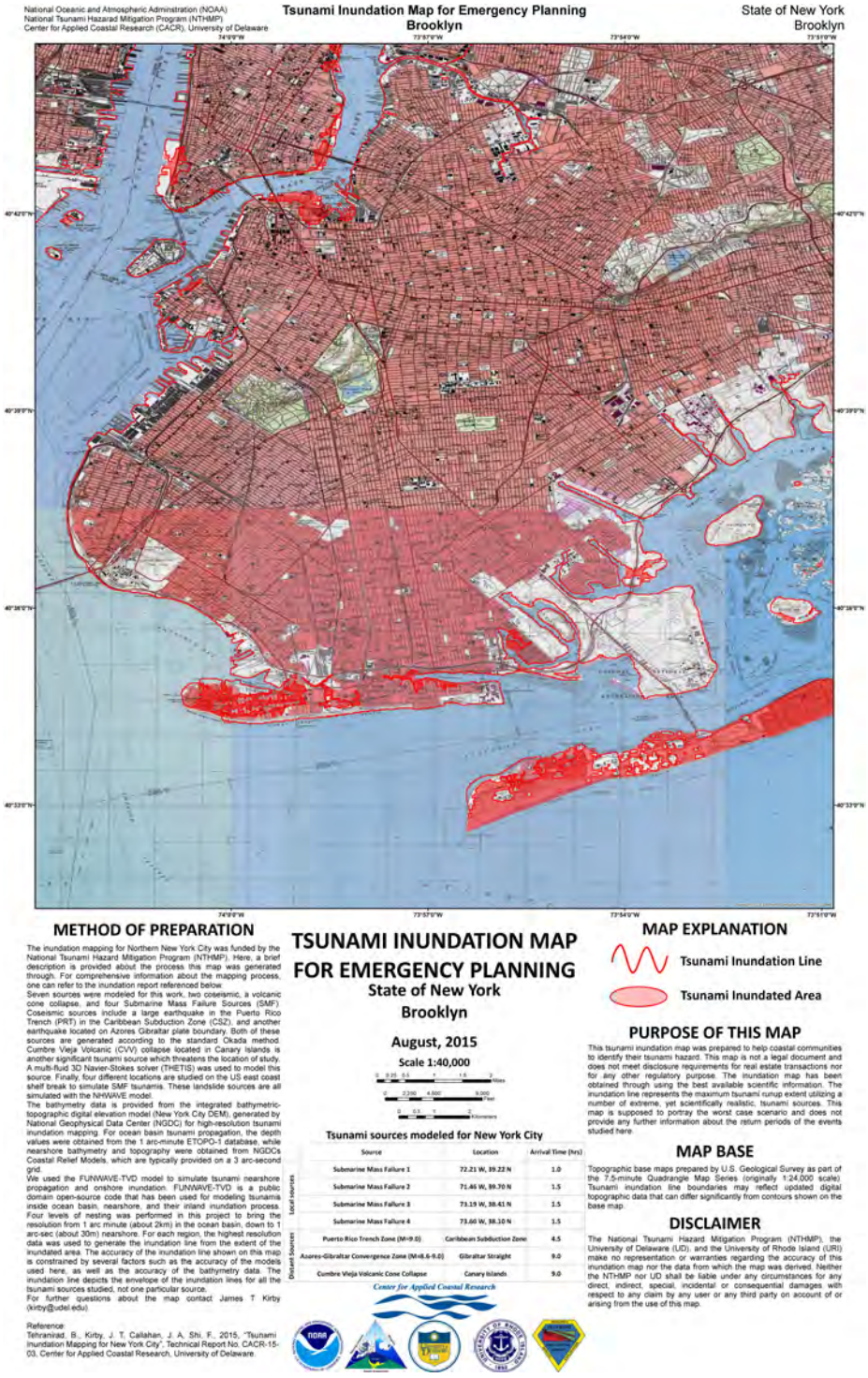

Figure 5.3: Tsunami inundation map for Brooklyn, NY (Tehranirad et al., 2015d).

In this chapter, a brief review of tsunami sources that threaten USEC is provided. I describe the origin of the tsunamis as well as the nesting process performed to achieve the resolution needed for nearshore inundation mapping. To investigate barrier island response to tsunami attack, I initially study the tsunami-induced morphological changes on the Assateague Island for different tsunami sources. This area was chosen to study barrier island deformation during tsunami inundation since there is infrastructure such as buildings, pavements, and artificially built sand dunes. Next, using the insights from previous simulations, Ocean City, MD inundation mapping was performed with dynamic bathymetry condition to provide a comparison with fixed bathymetry outcomes. I chose the area close to Ocean City Inlet where significant inundation depths are expected during tsunamis. The mainland behind the barrier is home to some populated communities which did not fall into inundation zone during previous simulations with fixed bathymetry assumption. The results suggest that it is probably necessary for regions similar to Ocean City to consider morphological adjustments during inundation mapping.

5.1 Potential Tsunami Sources Threatening the United States East Coast (USEC)

Several potential tsunami sources located in the Atlantic Ocean pose threats to US East Coast (USEC) communities. Some of these sources previously caused tsunamis in recent centuries. The tsunami caused by Lisbon earthquake of 1755 in the northwest Atlantic impacted coasts of Portugal, Ireland, Brazil, Morocco, and some parts of North America. Also, in the northeastern Caribbean, the Puerto Rico earthquake of 1918 caused a tsunami that reached the US shores, killing over 100 people in Puerto Rico. In addition to those recorded in recent history, other possible tsunami sources exist in the Atlantic Ocean (USGS, 2008). Close to African shorelines in the west side of the Atlantic Ocean, a volcanic cone collapse of Cumbre Vieja Volcano (CVV) in the Canary Islands could generate a tsunami, which potentially would pose a significant threat to the US and all Atlantic countries. Also, similar to Grand Banks tsunami

of 1929, a possible landslide on the edge of continental shelf can generate tsunamis affecting USEC shorelines. There are several locations along continental shelf edge where these landslides could potentially occur (Grilli et al., 2015).

In recent years, various sources were studied and modeled as part of National Hazard Mitigation Program (NTHMP) efforts to generate Probable Maximum Tsunami (PMT) inundation maps for the USEC populated communities. A magnitude 9.0 earthquake in Azores-Gibraltar convergence zone (Grilli and Grilli, 2013), a magnitude 9.0 earthquake in the Caribbean Subduction Zone (Grilli et al., 2010), as well as two volcanic cone collapses in Canary Islands (Tehranirad et al., 2015a) were simulated. Also, several landslides along the USEC shelf edge were simulated as near-field tsunami threats (Grilli et al., 2015). For all of these sources, the largest possible event was considered to create PMT condition. Finally, FUNWAVE-TVD was used to simulate tsunami propagation offshore, and its inundation inland to generate inundation maps for the USEC communities (Tehranirad et al. 2014, 2015b-j).

For this work, we modeled four of the sources that were previously simulated for the NTHMP project for tsunami inundation mapping of Ocean City, MD (Tehranirad et al., 2014) to investigate the effects of morphological changes during tsunami inundation process on the levels of hazard. These sources can be categorized into three groups: 1) co-seismic sources, 2) volcanic cone collapse, and 3) submarine mass failure (SMF) sources. In the upcoming sections, a brief introduction to the sources is provided.

5.1.1 Coseismic Sources

5.1.1.1 Puerto Rico Trench (PRT)

The Puerto Rico Trench (PRT) is located in one of the most seismically active regions of the Atlantic Ocean, the Caribbean Subduction Zone (CSZ). Grilli et al. (2010) have studied possibilities of tsunamis caused by subductive activities in the PRT. Their studies implied that extreme seismic activities with the return period of 200 to 600 years could be powerful enough to rupture the entire PRT and cause a tsunami that could impact the USEC. For the NTHMP inundation mapping on the

USEC, Tehranirad et al. (2014, 2015b-j) used the most significant PRT tsunami source that Grilli et al. (2010) introduced, generated by a massive earthquake ($M_w = 9.0$) with estimated 600-year return period. However, it is controversial among scientists whether there is any fault thrust activity in PRT region (e.g. Ten Brink, 2005). Tehranirad et al. (2014, 2015b-j) concluded that among the coseismic sources they studied, the PRT event is the largest threat for the USEC. Therefore, for this work, we decided to simulate the tsunami-induced morphological changes of the $M_w = 9.0$ PRT over the barrier islands.

Similar to Tehranirad et al. (2014, 2015b-j), we used the result of Grilli and Grilli (2013a) who carried out detailed computations for the PRT event, to be used as initial conditions for tsunami inundation mapping on the USEC. They used FUNWAVE-TVD over a 1 arc-min resolution computational domain to model the tsunami in the Caribbean and the Atlantic Ocean. Figure 5.4 illustrates the maximum recorded surface elevation recorded during the ocean-basin modeling of the PRT tsunami. The rectangles show the location of the nesting boundary in the 1 arc-min simulations to perform nesting in the nearshore.

5.1.1.2 Azores-Gibraltar Convergence Zone

The other coseismic source used here is located on the Azores-Gibraltar plate boundary, known as the source of the biggest historical tsunami event in the North Atlantic Basin. The 1755 Lisbon earthquake ($M_w = 8.6 - 9.0$) generated tsunami waves with heights between 5 to 15 meters, impacting the coasts of Morocco, Portugal, Newfoundland, Antilles, and Brazil. The procedure for obtaining the initial condition for tsunami propagation is quite similar to the PRT rupture and is discussed in Grilli and Grilli (2013b).

We used the results of Grilli and Grilli (2013b) for the Lisbon source. They used FUNWAVE-TVD over a 1 arc-min computational domain to model the tsunami across the Atlantic Ocean. Figure 5.5 show the maximum elevation recorded for the

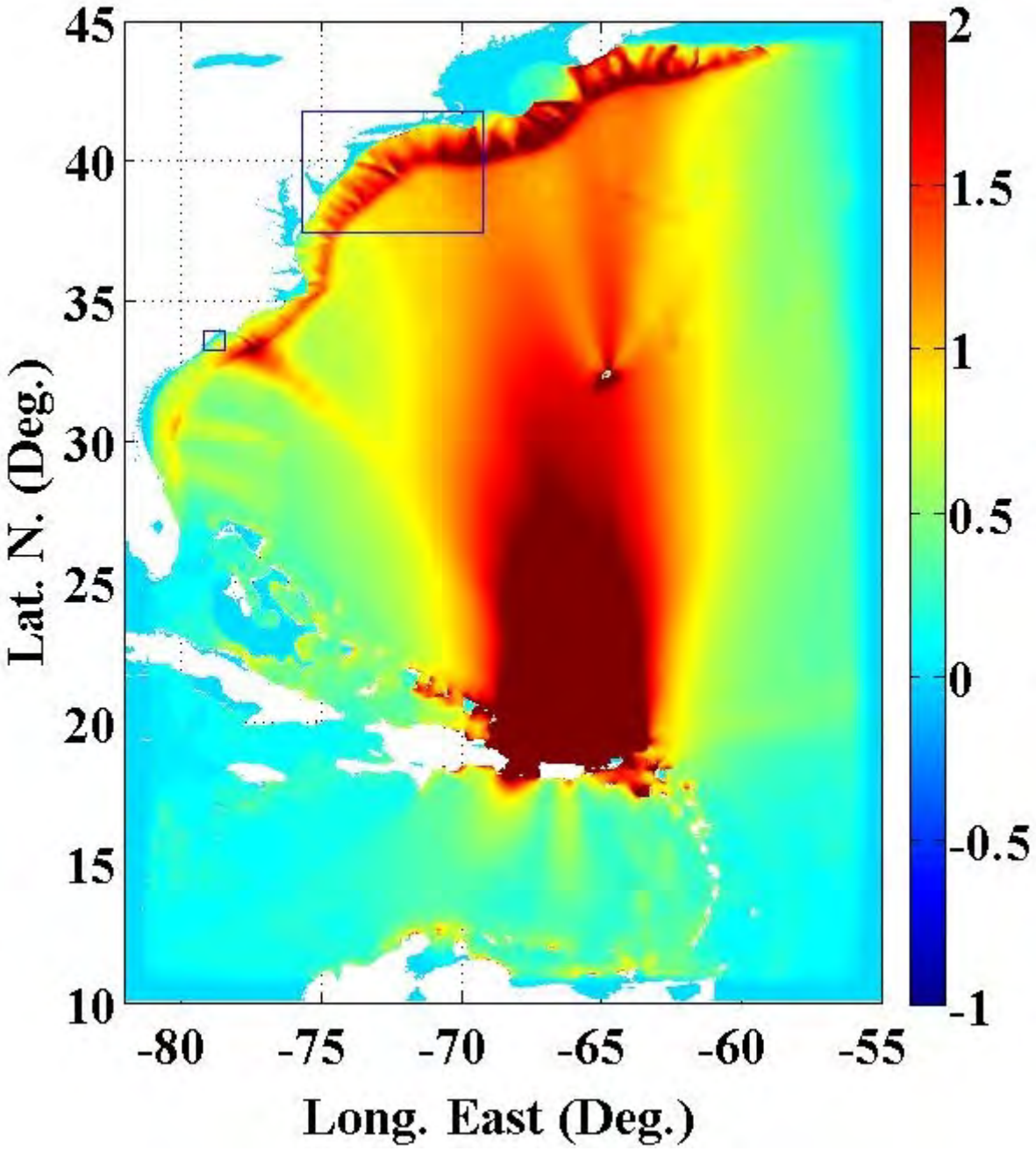

Figure 5.4: The maximum recorded surface elevation during the ocean-basin modeling of the PRT tsunami (Grilli and Grilli, 2013a). The rectangles locate the gauges deployed in the model for nearshore nesting process.

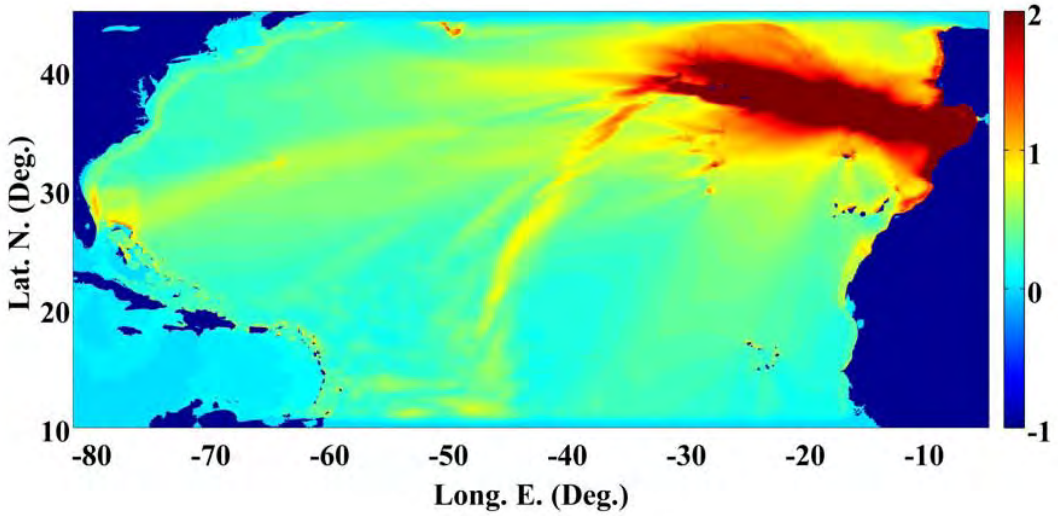

Figure 5.5: The maximum recorded surface elevation recorded during the ocean-basin modeling of the Lisbon tsunami (Grilli and Grilli, 2013b).

Lisbon source in the Atlantic Ocean. A similar nesting approach to the PRT source was used to increase the resolution in the nearshore.

5.1.2 Volcanic Cone Collapse

In recent years, a potential collapse of the volcanic cone Cumbre Vieja (CVV) in the Canary Islands has received attention as a possibly catastrophic source threatening the USEC. Abadie et al. (2012) used a multi-fluid 3D Navier-Stokes solver (THETIS) to compute this volcanic collapse tsunami source. They studied two different slide magnitudes for this work; an 80 km^3 slide, representing a plausible event in a return period window on the order of 10,000 years, and a 450 km^3 source, consistent with estimates of the maximum event for the geological feature. The magnitude of the latter event is significantly larger than all of the other cases studied in the NTHMP project. Thus, considering the purpose of the current study, we modeled the 80 km^3 slide source, which causes larger tsunami wave near USEC compared to the coseismic sources previously introduced.

For this work, we used the tsunami source calculated by Abadie et al. (2012). The event's propagation over the ocean basin was simulated using a similar configuration as for the Lisbon source, with a 1 arc-min domain. A detailed description of the CVV modeling is provided in Grilli and Grilli (2013c). Figure 5.6 demonstrates the maximum recorded surface elevation in the Atlantic Ocean that Grilli and Grilli (2013c) computed during their simulations.

5.1.3 Submarine Mass Failure (SMF)

Grilli et al. (2015) have noted that there is a potential of a Submarine Mass Failure (SMF) on or near the continental shelf break, causing tsunamis that affect neighboring coastal areas. An example of this is the Grand Banks tsunami of 1929, which is the only tsunami event that has caused fatalities in the North America in recent history (Ruffman and Hann, 2001). The Currituck slide is the largest paleoslide identified along the western Atlantic shelf edge, located off the coastlines of North

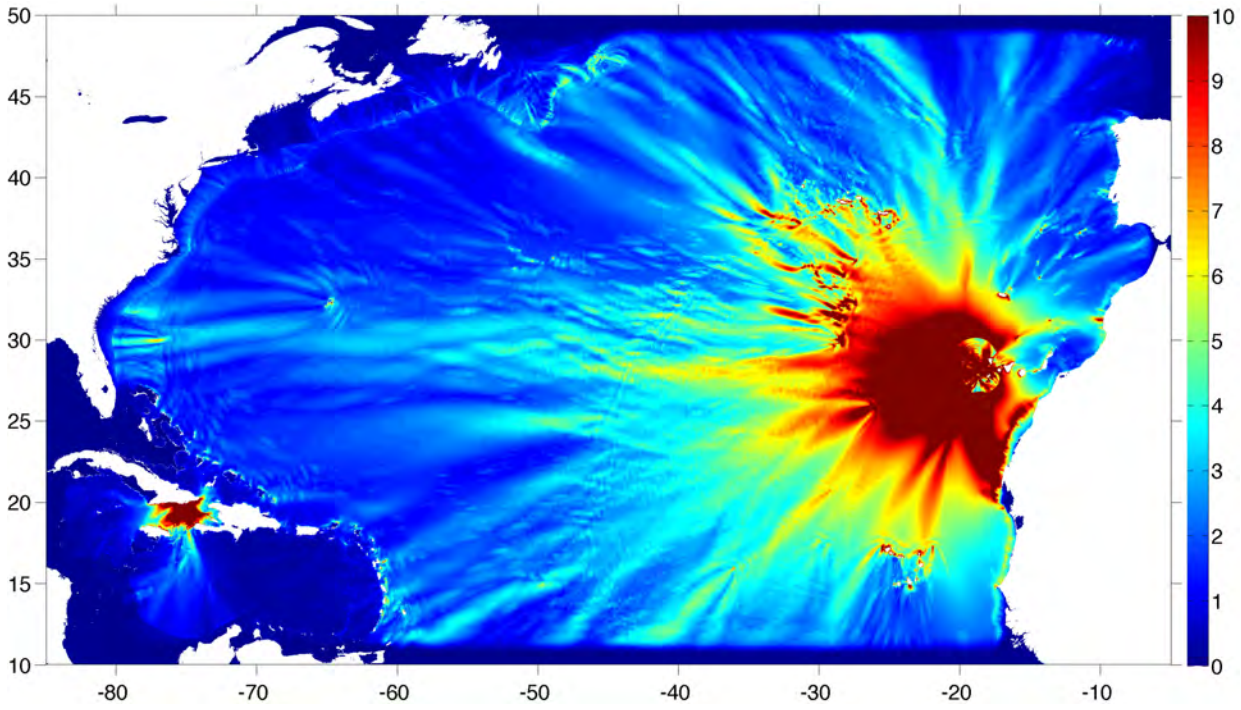

Figure 5.6: The maximum recorded surface elevation recorded during the ocean-basin modeling of the CVV 80 km^3 slide tsunami (Grilli and Grilli, 2013c). The axes represent the Longitude and Latitude in degrees(^{o}).

Carolina, and its geology and slide triggering dynamics have been extensively studied (e.g. Chaytor et al., 2009; ten Brink et al., 2009). For the inundation mapping of the upper USEC, Tehranirad et al. (2014, 2015b-f) used hypothetical slides at four different locations which would cause the most significant impact on the USEC, following the work of Grilli et al. (2015). They parameterized an extreme SMF source at four locations along the shelf edge close to the upper USEC as the historical Currituck slide proxies. Grilli et al. (2015) used same volume, dimensions, and geometry as the Currituck event to generate SMF tsunami in the upper USEC. The process of obtaining the initial condition for near-shore propagation for all of these sources is comprehensively documented in Grilli et al. (2013d). The landslide movement is simulated using a solid slide motion in the NHWAVE model (Ma et al., 2012) and the results were interpolated onto 500-meter grids for propagation and inundation modeling 800 seconds after slump movement is initiated (Grilli et al., 2013d).

Figure 5.7 shows the surface elevation of four SMF sources used in the NTHMP project after 800 seconds of simulations of the landslides with NHWAVE. Tehranirad et al. (2014) used these results as initial conditions in FUNWAVE-TVD for inundation mapping for the Ocean City, MD. They showed that the SMF4 source, which is the closest out of the four to the study area, causes the largest impact on the Ocean City, MD, and Assateague Island regions compared to the other three SMF sources. Accordingly, we chose to study the SMF4 source and investigate if the morphological adjustment during tsunami inundation modeling increases the levels of hazard for this source.

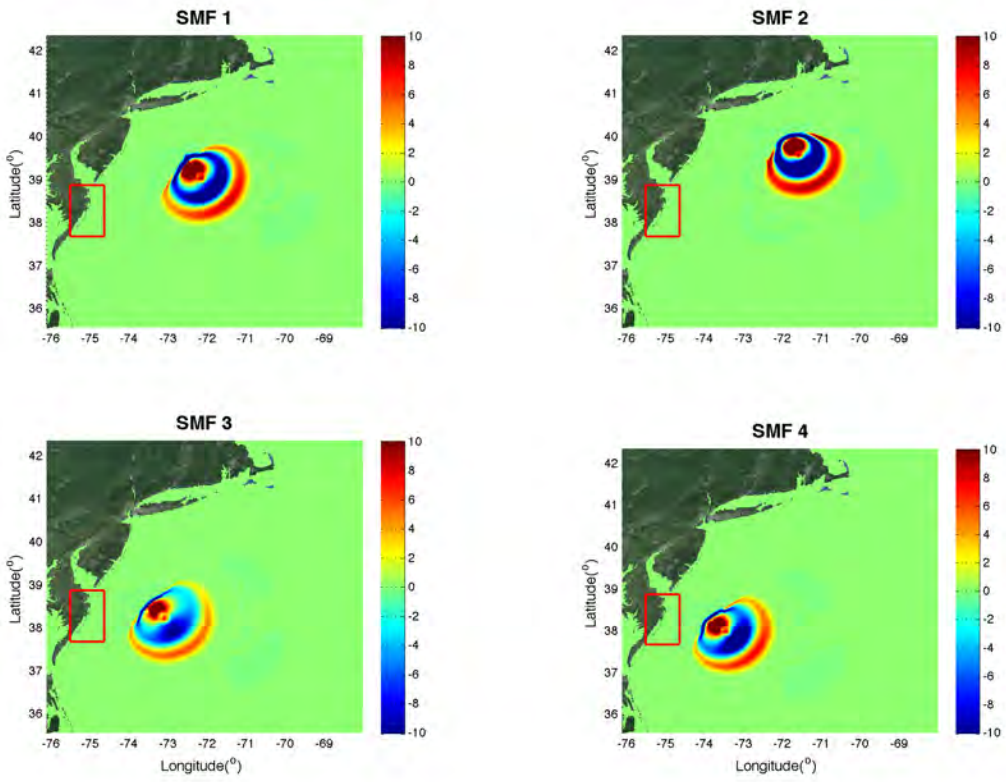

Figure 5.7: The surface elevation of four SMF sources 800 seconds after slide initiation modeled with NHWAVE, and used in FUNWAVE-TVD for nearshore inundation mapping of the upper USEC. The red boxes show the location of the Ocean City DEM, explained in the nesting process section.

5.2 Bathymetry Data

Three different bathymetry sources were used to model the tsunami-induced morphological changes in Ocean City and Assateague Island. For low-resolution modeling in the ocean-basin and over the continental shelf, computational grids were obtained from the 1 arc-min ETOPO-1 (Amante and Eakins, 2009) database, while nearshore bathymetry and topography were obtained from the 3 arc-sec Coastal Relief Model (CRM) (NGDC, 1999). Then, for higher resolution simulations close to the study areas, we used the integrated bathymetric-topographic Digital Elevation Model (DEM) generated by NGDC (Grothe et al., 2010) for tsunami inundation mapping studies of Ocean City, MD and surrounding region.

Figure 5.8 shows the two grids that were generated for low-resolution modeling over the ocean basin and continental shelf. Grid A is used to model Coseismic and CVV sources, which were simulated in larger scale model runs, with flow information recorded on the boundaries of Grid A. The grid resolution of the Grid A are $\Delta y = 503.2$ m in the north-south direction and $\Delta x = 535.0$ m in the east-west direction. The SMF source fall within the modeled region and are initially modeled with a Cartesian grid using NHWAVE (Ma et al., 2012) with 500 m resolution. It was required to generate another grid larger than Grid A to allow space for sponge layers (or damping regions) on the boundaries. The input data was in the form of initial conditions, in contrast to the first category where the data was in the form of boundary conditions. Accordingly, we generated Grid B with 500 m resolution to simulate the SMF source in the ocean and over the continental shelf. The results of Grids A and B were recorded on the boundaries of the Ocean City DEM for high-resolution modeling of Ocean City and Assateague Island. In figure 5.8, the location of Ocean City DEM is illustrated. The boundary coordinates and other detailed information for Grids A and B are provided in Tehranirad et al. (2014).

Figure 5.9 illustrates the area covered by the Ocean City DEM used as bathymetry data for high-resolution simulations in Ocean City and Assateague Island. The horizontal datum of this DEM is World Geodetic System of 1984 (WGS 84), and the

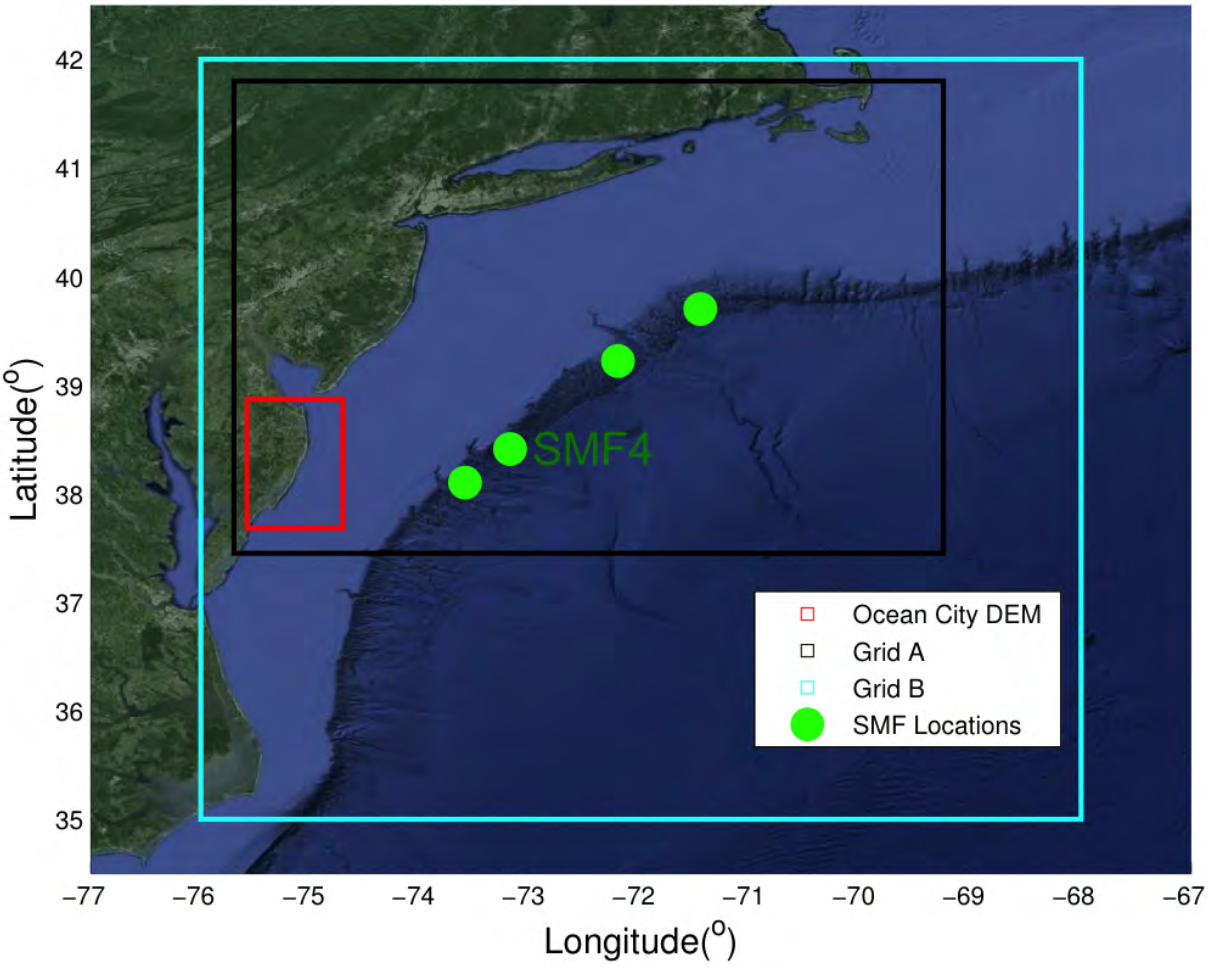

Figure 5.8: The location of the grids used for low resolution modeling in the ocean-basin and over the continental shelf. The red box shows the location of the Ocean City DEM which falls within the low resolution grids. Green circles demonstrate the location of the SMF sources studied for inundation mapping of the upper USEC. SMF4 is chosen to be modeled in this work amongst SMF sources due to its proximity to Ocean City and Assateague Island.

vertical datum is Mean High Water (MHW). The resolution of the Ocean City DEM is 1/3 arc-second. Considering the latitude of the study area, 1/3 arc-sec corresponds to $\Delta y = 10.27$ m in North-South, and $\Delta x = 8.10$ m in East-West directions. All of the runs in this domain were performed using Cartesian coordinates.

5.3 Nesting Process

Simulations with grid sizes of roughly 125.0 meters (4 arc-sec) are performed to record flow information around two 1 arc-sec computation domains, using the recorded data on the boundaries of Ocean City NGDC DEM during the low-resolution simulations (Grid A and B). Then, tsunami inundation for Assateague Island and Ocean City were modeled with 1/3 arc-sec resolution. Figure 5.10 illustrates the nesting approach used in this study to model different tsunamis on Assateague Island and Ocean City. Tehranirad et al. (2014) used a similar nesting approach and showed the efficiency of this method with the consistency of results between different levels of nesting.

Figures 5.11 and 5.12 show the surface elevation data recorded during 1 arc-sec resolution modeling of PRT, Lisbon, CVV and SMF sources on the southeastern edge of 1/3 arc-sec grids, both shown at the bottom of Figure 5.10. The recorded surface elevation in addition to computed velocity terms (u, v) were used to conduct 1/3 resolution simulations for Assateague Island and the Ocean City. The calculated nearshore tsunami signal (Figures 5.11 and 5.12) for both areas are similar. However, the first wave of each tsunami reaches to the south-east of the Assateague Island computational domain about 10 minutes earlier than Ocean City.

5.4 Assateague Island Morphological Response to Tsunami Inundation

To model the tsunami-induced morphological changes of Assateague Island, we used the computational domain shown in the bottom left of Figure 5.12. The domain grid size was 810 × 810 with 1/3 arc-sec resolution corresponding to $\Delta x = 8.10$ m and $\Delta y = 10.27$ m, extracted from the Ocean City DEM. Surface elevations and velocity terms (u, v) were forced on the boundaries using the information recorded during the

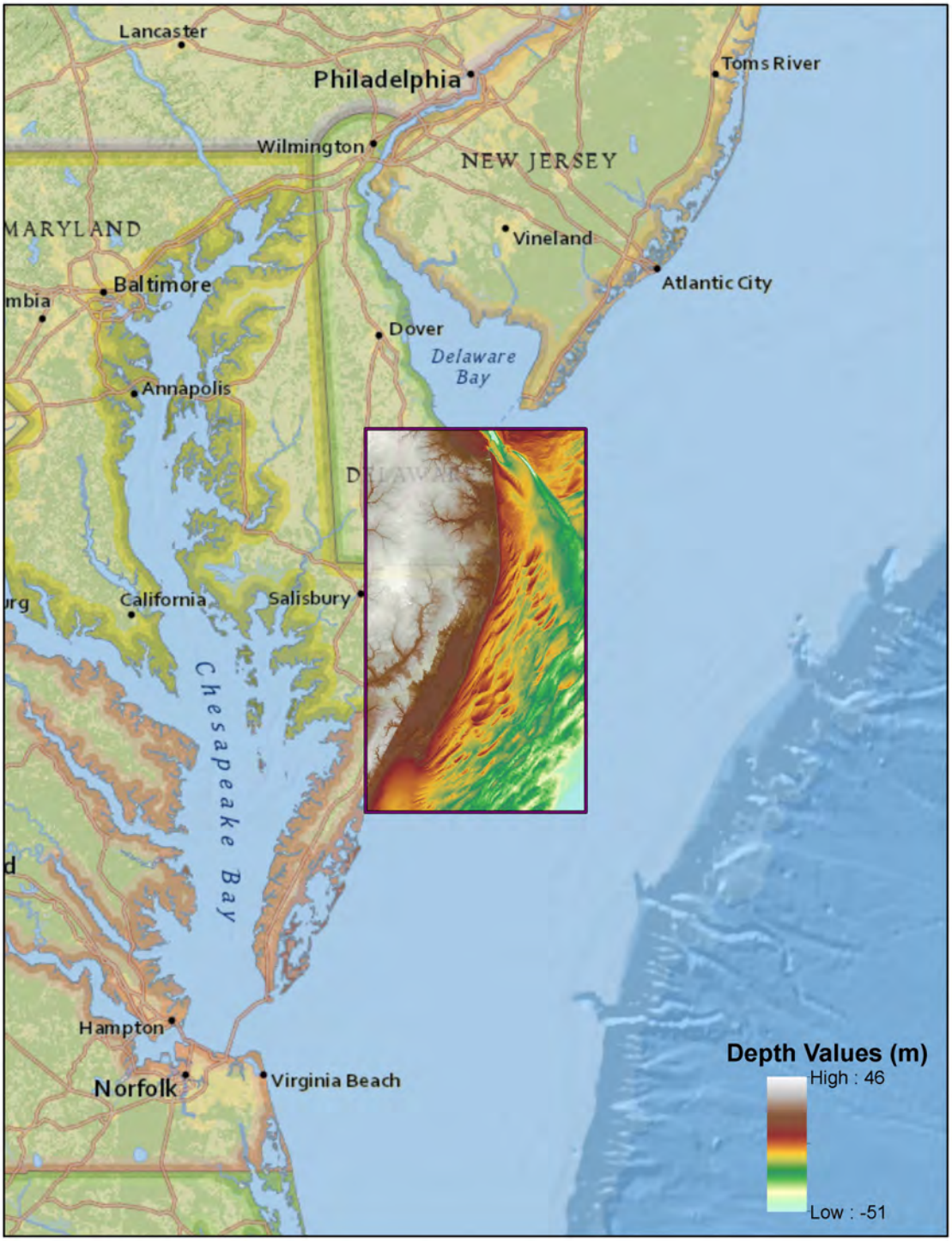

Figure 5.9: Coverage location of the Ocean City DEM. Color bar shows depth values in meters for areas inside of the DEM boundary.

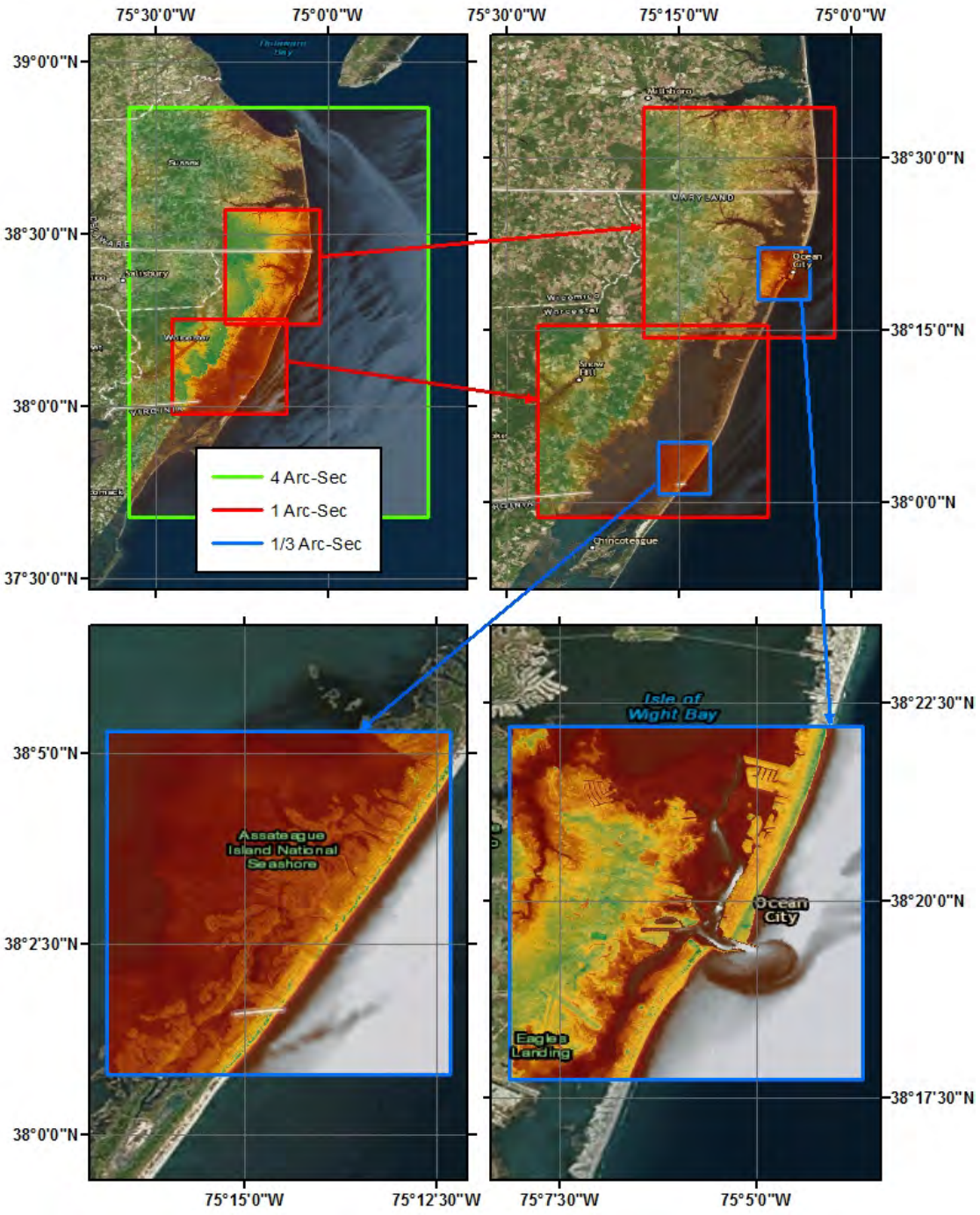

Figure 5.10: Nesting approach used to model tsunami morphological effects in Assateague Island (Bottom-Left), and Ocean City (Bottom-Right). Computations were performed using 4, 1 and 1/3 arc-sec resolution grids, which are depicted with different colors.

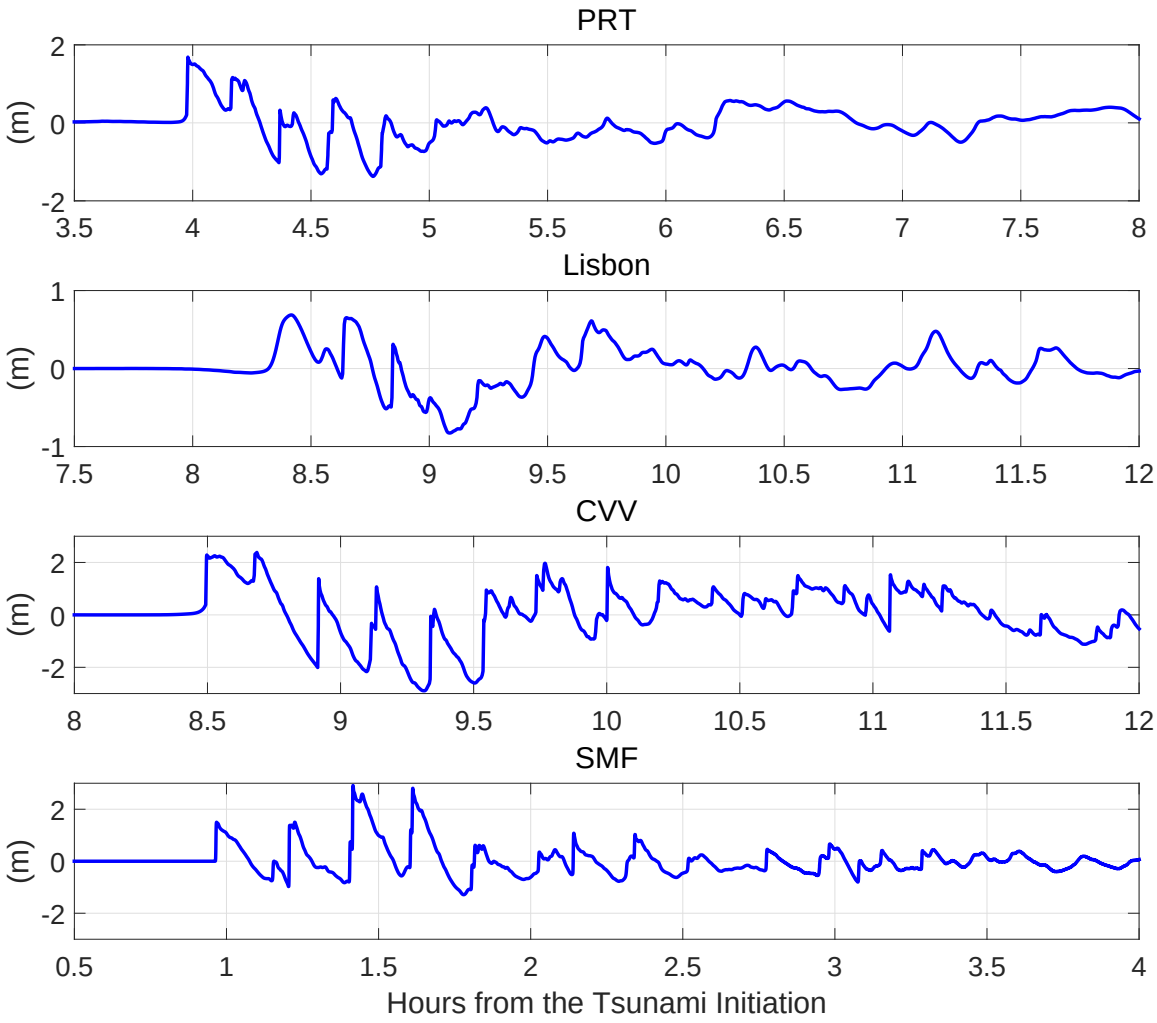

Figure 5.11: Surface elevation at the southeastern edge of the 1/3 arc-sec Assateague Island computational domain (bottom-left of Figure 5.10) for all of the tsunami sources studied in this work.

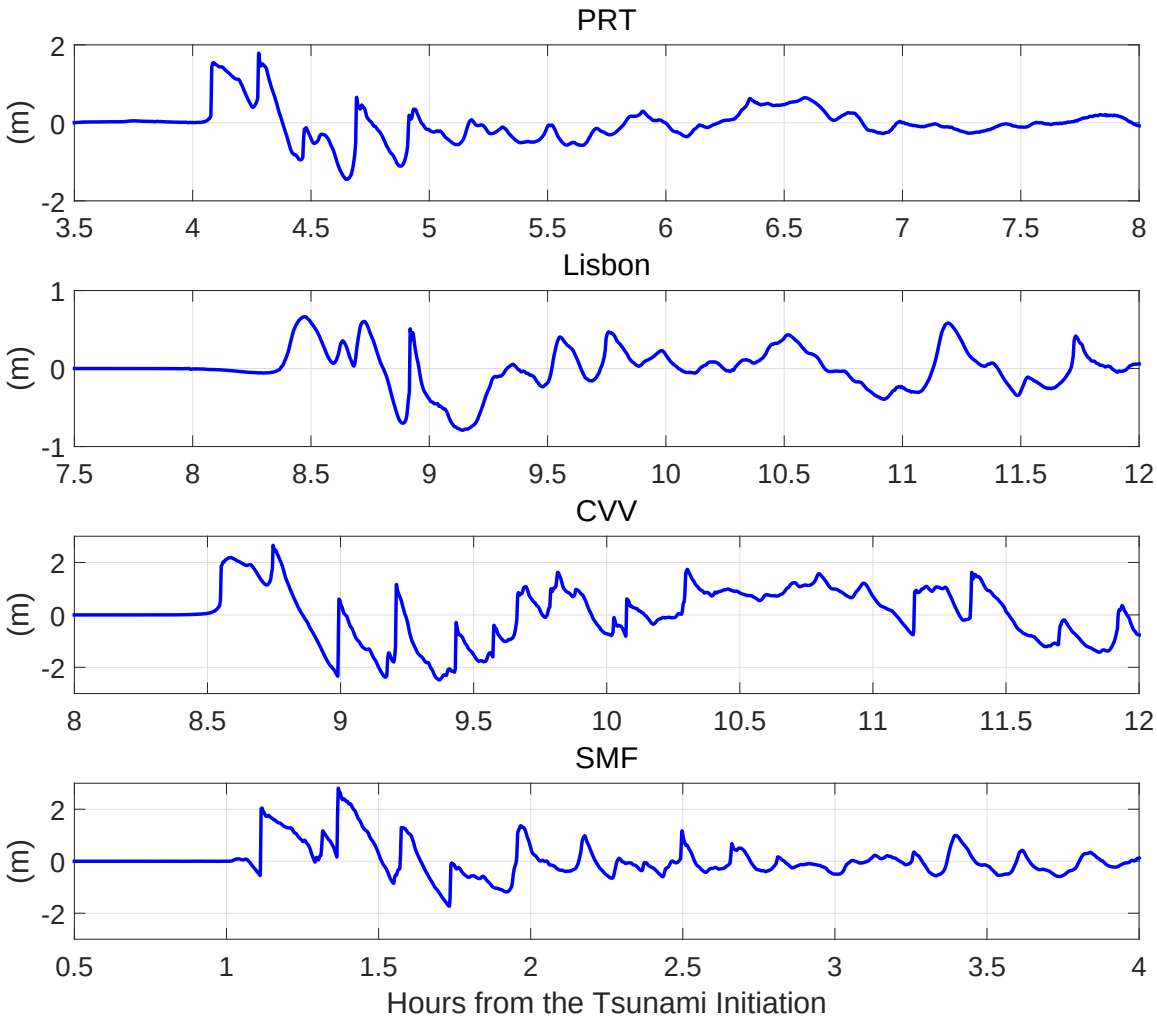

Figure 5.12: Surface elevation at the southeastern edge of the 1/3 arc-sec Ocean City computational domain (bottom-right of Figure 5.10) for all of the tsunami sources studied in this work.

1 arc-sec simulations for CVV, Lisbon, PRT, and SMF sources introduced previously in this chapter.

Fenser et al. (2016) have conducted experiments to measure sediment grain size distribution along the southern Maryland and Virgina barrier islands. They reported that for Assateague Island, the median grain size (d_{50}) is 0.36 $\pm$ 0.09 mm. Thus, for our simulations, we used the reported median grain size with computed fall velocity of $w_f = 0.$ cm/s (4.1) and angle of repose corresponding to $\tan(\phi) = 0.5$, to be used in the avalanching scheme. We assumed that the study area is entirely covered by sand with no pavement and no vegetation. The Manning coefficient of $n = 0.025$ was used during simulations, following the values that Sugawara et al. (2014) provided for a similar environment. The porosity was assumed to be the standard value of 0.4. The time step (Δt) varies between 0.07 to 0.3 seconds during the simulations corresponding to grid resolution and CFL condition. The ratio of morphology time step over hydrodynamics time step ($\Delta t_{morph}/\Delta t$) is set to be 20.

Figures 5.13-5.20 illustrate the computed surface elevation and bed changes resulting from the CVV tsunami, during its inundation process over the Assateague Island for the first hour of the tsunami impact with 10-minute increments. Figure 5.13 pictures the leading wave of the CVV tsunami as it approaches the barrier shoreline, which is roughly about 9 hours after the initiation of the tsunami. For simplification, the timing of the Figures 5.14-5.20 is set relative to Figure 5.13, starting from when the leading tsunami wave reaches the proximity of the shoreline. The surface elevation and sediment concentration values are shown at the top of these figures. High values for sediment concentration locates the regions where significant sediment movements occur. Also, for a better understanding of the barrier islands' morphological response under tsunami flow, we depicted a cross-section of bottom changes and flow conditions in Figures 5.13-5.20. Consequently, using the results recorded on the cross-section during the tsunami flow, we were able to provide a detailed picture of tsunami-induced morphological changes during the inundation process.

Figures 5.13-5.15 show the first 20 minutes of the tsunami flow over the Assateague Island, during which the first wave of the tsunami signal overtops the barrier. During the overtopping, major erosion occurs on the back slope of the barrier, while the water passes over the slope into the back bay and caused large scour. Also, the shallow regions in the back bay behind the barrier get eroded, and the moved sediment deposits in the deeper areas. High sediment concentration on the back of barrier is observed during this process (Figure 5.14). After 20 minutes, when the overtopping of the first wave is finished, the water trapped onshore starts to flow back into the ocean and the back bay, while the ocean water level is dropped. This process causes large erosions on the shoreface, where the dune gets eroded and its sediment gets deposited offshore. Figure 5.15 demonstrates this process, where large sediment concentrations are observed on the shoreface representing significant sediment action in this area before the second wave reached the shoreline. After 30 minutes, the second wave of the CVV tsunami reaches the barrier island. However, because of the bed changes on the shoreface due to the passage of the first wave, the second wave experiences a smoother bathymetry with a smaller dune in front of the island. Therefore, the second wave overtops the barrier with less dissipation, causing larger waves in the back bay.

A morphological process similar to that of the first wave keeps happening for several successive waves during the time between 20 to 120 minutes of simulating nearshore effects of CVV tsunami on Assateague Island. This process can be divided into two steps. First, the tsunami wave overtops the barrier, erodes the top and back of the island and deposits the sand in the back bay. Next, during the rundown the shoreface on both sides of the barrier and the front dune gets significantly eroded, and the sediment gets deposited offshore, both in the ocean and the back bay. Consequently, the next wave reaches the shoreline facing a smoother bathymetry, flattened by previous waves.

Two hours after the first wave of the CVV tsunami reached the shoreline, a significant volume of water was trapped in the bay between the barrier island and the mainland behind it (Figure 5.20). This causes a gradient between water surface

elevations on two sides of the barrier island, where the back bay water surface is about 2 to 5 meters higher than that of the ocean. Therefore, because of this hydraulic head, the trapped water between the barrier and the mainland starts to pour back into the ocean, causing substantial morphological changes. The water flows back into the ocean continuously for 3 to 4 hours, almost in quasi-uniform condition with velocities in order of 0.2 to 0.5 m/s. Although some of the residual waves in the tsunami signal overtop the barrier during this time, the flow regime is mainly directed offshore when the water surface on the back bay is higher than the ocean. This continuous flow regime moves the sediment offshore. In the bay, the sediment gets accumulated behind the original shoreline on the back side of the barrier, where was previously deposited during the overtopping process. Moreover, the shoreface and the front dune get heavily scoured, and their corresponding sediment deposited offshore.

The computed results for other tsunami sources showed a similar morphological response for the Assateague Island during tsunami inundation compared to the CVV source. Figure 5.21 depicts the computed bed level changes for all of the sources studied in this work on the cross-section illustrated in Figures 5.14-5.20. The calculated results for the PRT and SMF sources show significant bed changes on top of the barrier similar to the CVV tsunami. However, the Lisbon tsunami, which has much smaller waves (Figure 5.11) compared to three other sources did not overtop the Assateague Island barrier and correspondingly did not cause any notable change to the topography of the study area.

Figures 5.22-5.29 show the computed bed changes of Assateague Island during simulations of PRT, Lisbon, CVV and SMF tsunami sources. Bed changes less than 20 cm are filtered out of these figures for clarity. Significant tsunamis (PRT, CVV and SMF) changed the coastal morphology in a similar manner. The shoreface and the front dune of the barrier island got eroded, and the moved sand got deposited either in the back bay or offshore in the ocean. However, in contrast to the large tsunami sources, the Lisbon tsunami does not effectively overtop the Assateague Island barrier in a way to create notable changes on the coastal morphology. The computed bed

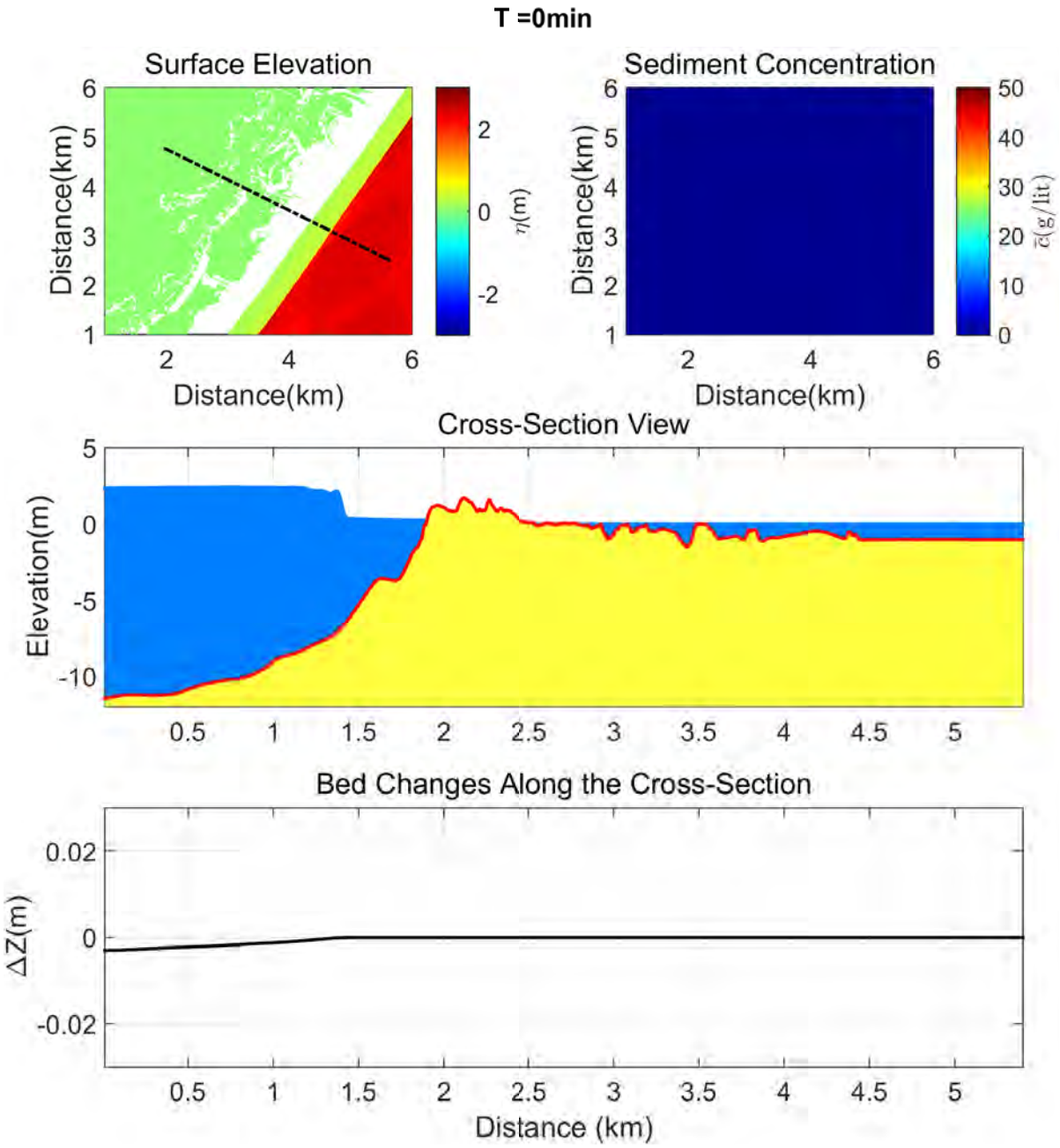

Figure 5.13: Water surface (top-left) and sediment concentration (top-right) 0 minutes after the CVV tsunami reaches the Assateague Island. The figure in the middle shows the water surface (blue surface), initial bathymetry (black line), and computed bed levels (red line, yellow surface) at the cross-section shown in the top-left figure. The bottom figure shows the computed bed elevation changes ($\Delta Z = -\Delta Z_b$) along the cross-section.

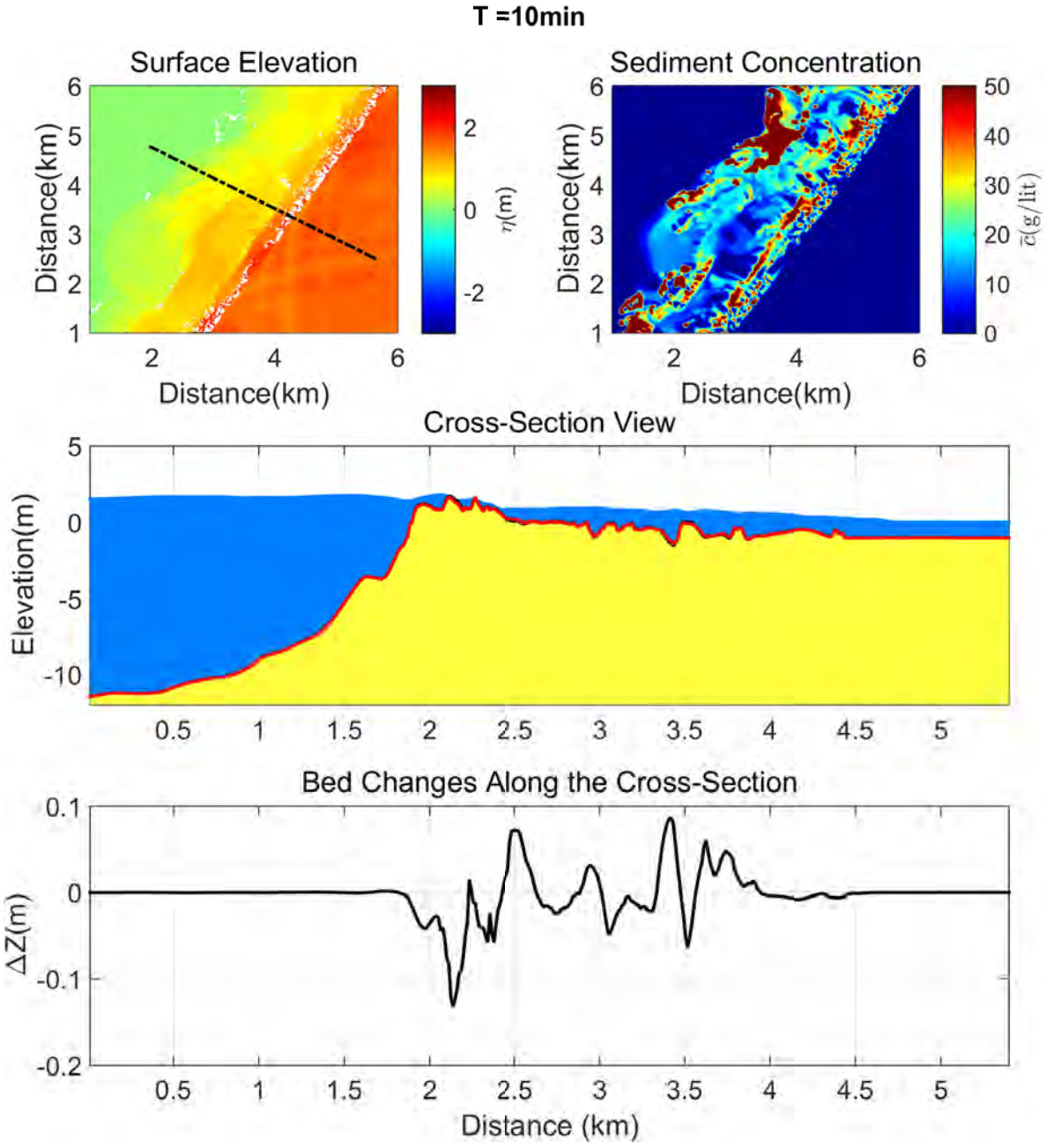

Figure 5.14: Water surface (top-left) and sediment concentration (top-right) 10 minutes after the CVV tsunami reaches the Assateague Island. The figure in the middle shows the water surface (blue surface), initial bathymetry (black line), and computed bed levels (red line, yellow surface) at the cross-section shown in the top-left figure. The bottom figure shows the computed bed elevation changes ($\Delta Z = -\Delta Z_b$) along the cross-section.

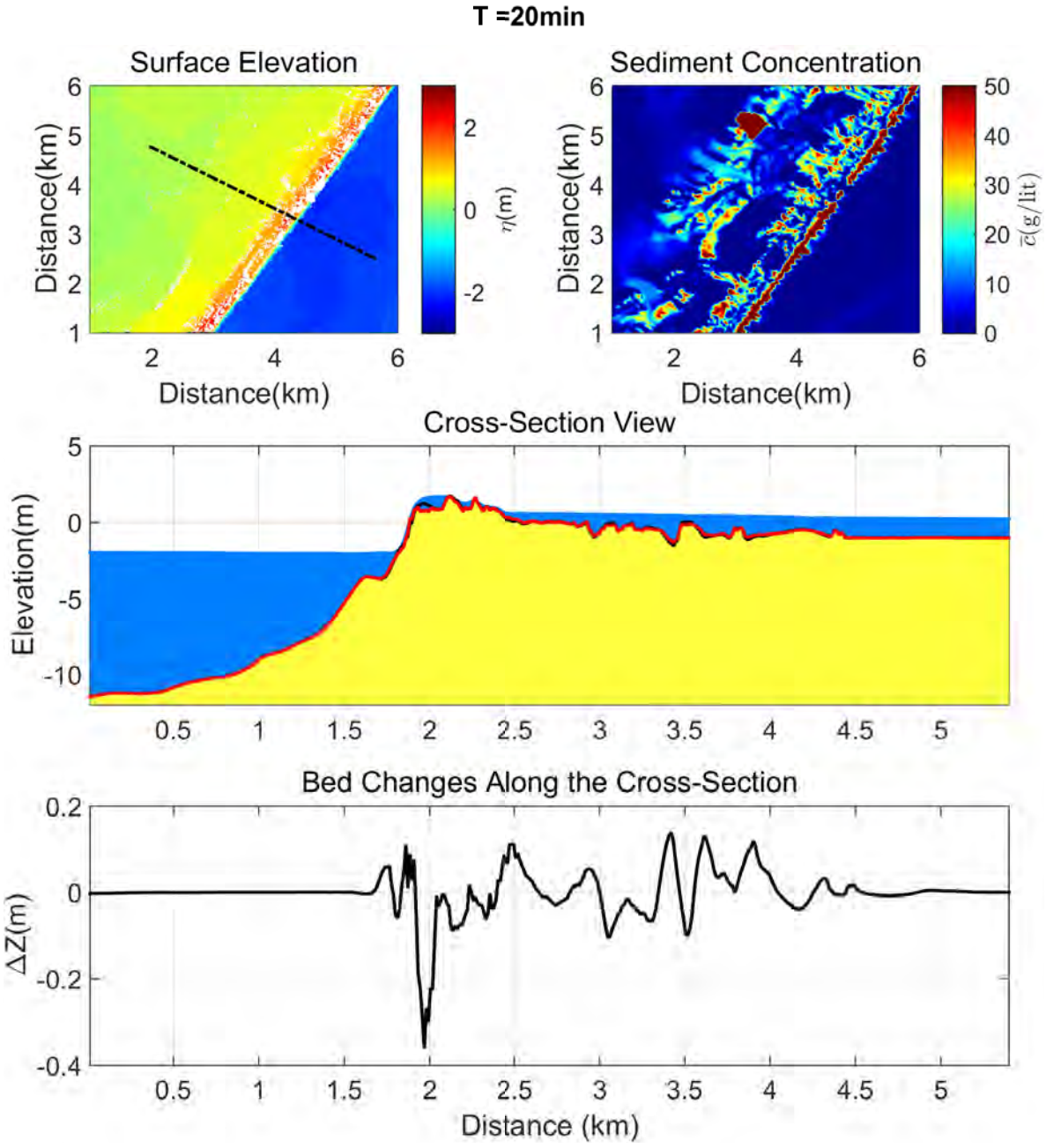

Figure 5.15: Water surface (top-left) and sediment concentration (top-right) 20 minutes after the CVV tsunami reaches the Assateague Island. The figure in the middle shows the water surface (blue surface), initial bathymetry (black line), and computed bed levels (red line, yellow surface) at the cross-section shown in the top-left figure. The bottom figure shows the computed bed elevation changes ($\Delta Z = -\Delta Z_b$) along the cross-section.

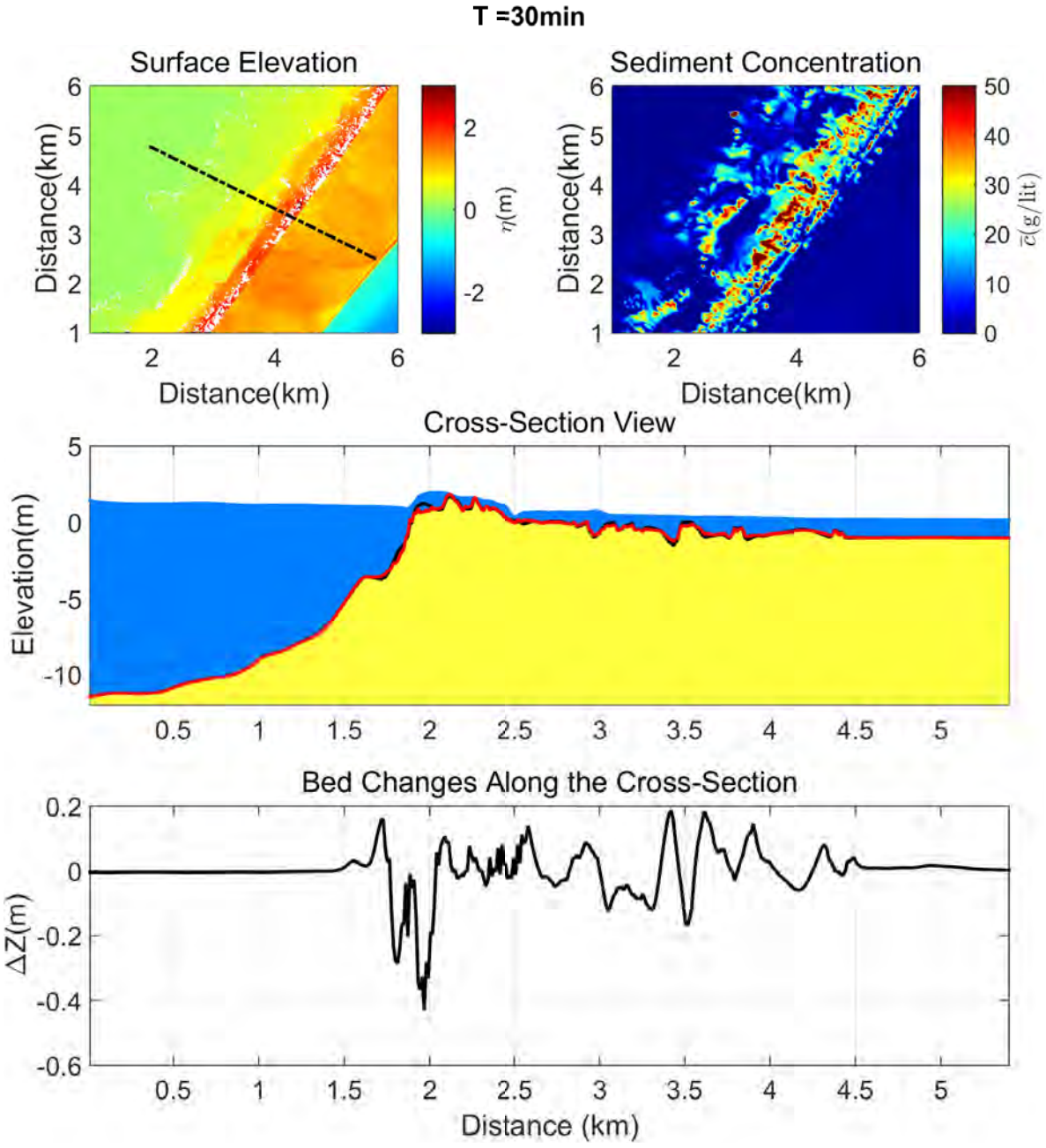

Figure 5.16: Water surface (top-left) and sediment concentration (top-right) 30 minutes after the CVV tsunami reaches the Assateague Island. The figure in the middle shows the water surface (blue surface), initial bathymetry (black line), and computed bed levels (red line, yellow surface) at the cross-section shown in the top-left figure. The bottom figure shows the computed bed elevation changes ($\Delta Z = -\Delta Z_b$) along the cross-section.

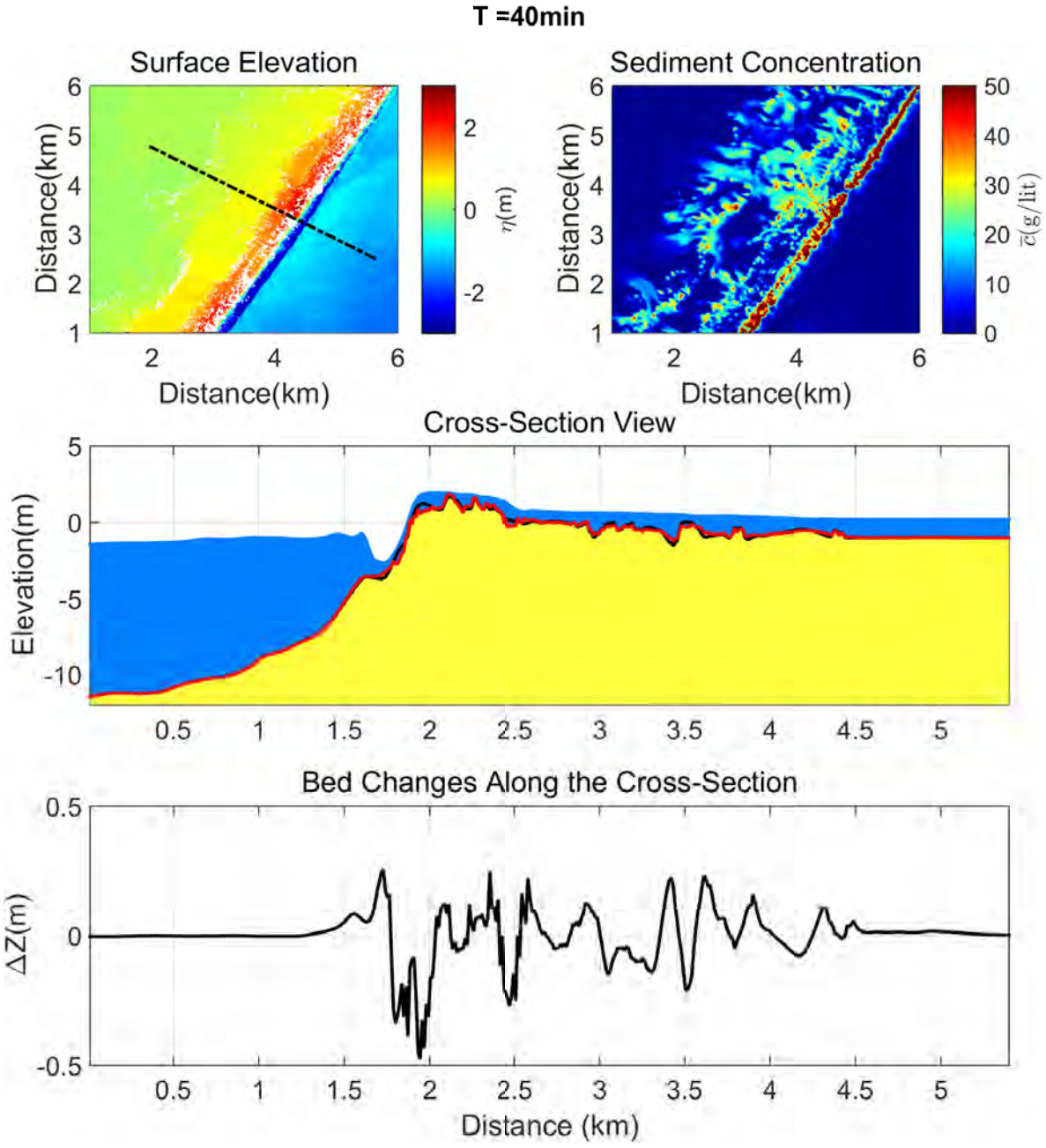

Figure 5.17: Water surface (top-left) and sediment concentration (top-right) 40 minutes after the CVV tsunami reaches the Assateague Island. The figure in the middle shows the water surface (blue surface), initial bathymetry (black line), and computed bed levels (red line, yellow surface) at the cross-section shown in the top-left figure. The bottom figure shows the computed bed elevation changes ($\Delta Z = -\Delta Z_b$) along the cross-section.

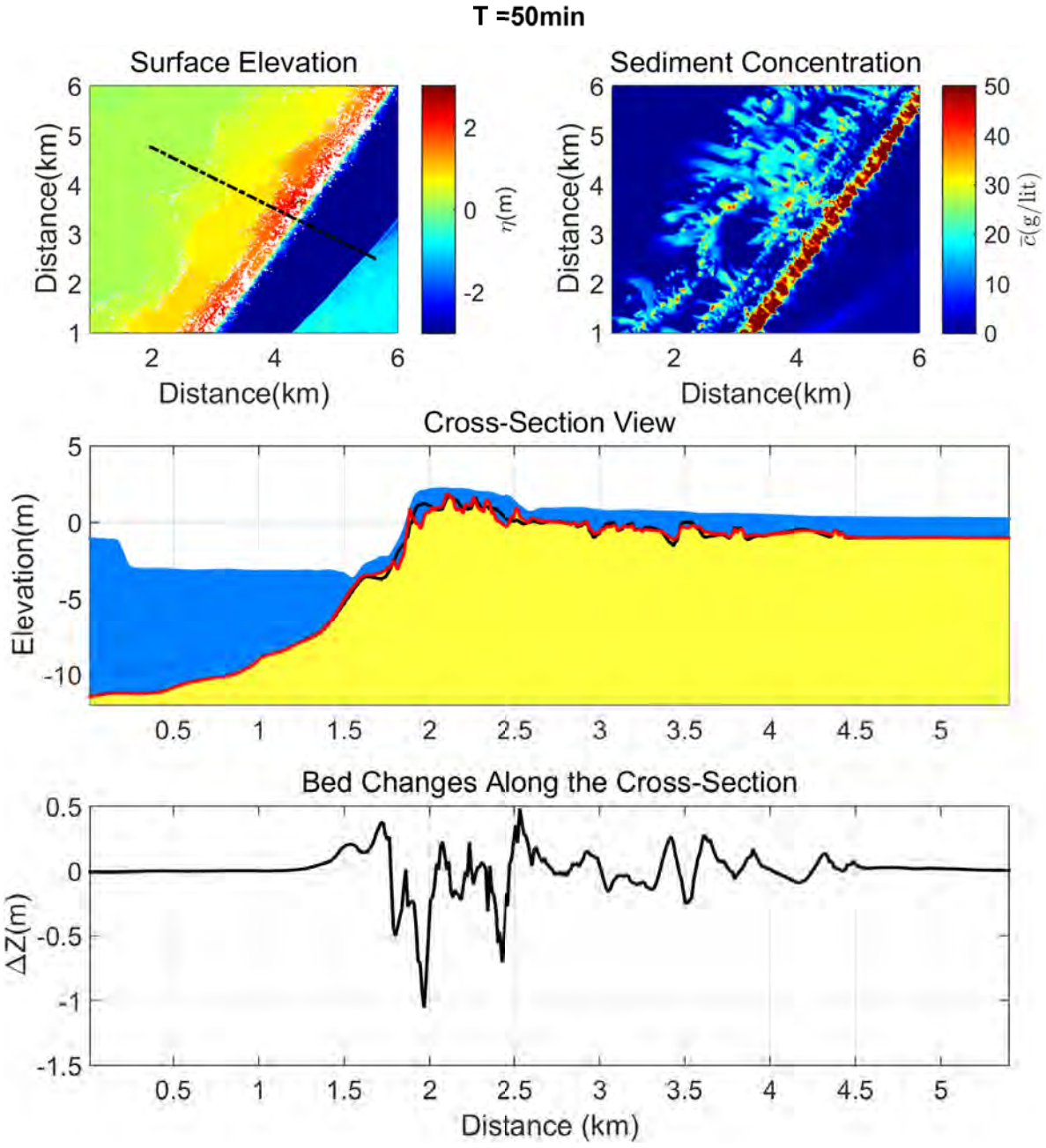

Figure 5.18: Water surface (top-left) and sediment concentration (top-right) 50 minutes after the CVV tsunami reaches the Assateague Island. The figure in the middle shows the water surface (blue surface), initial bathymetry (black line), and computed bed levels (red line, yellow surface) at the cross-section shown in the top-left figure. The bottom figure shows the computed bed elevation changes ($\Delta Z = -\Delta Z_b$) along the cross-section.

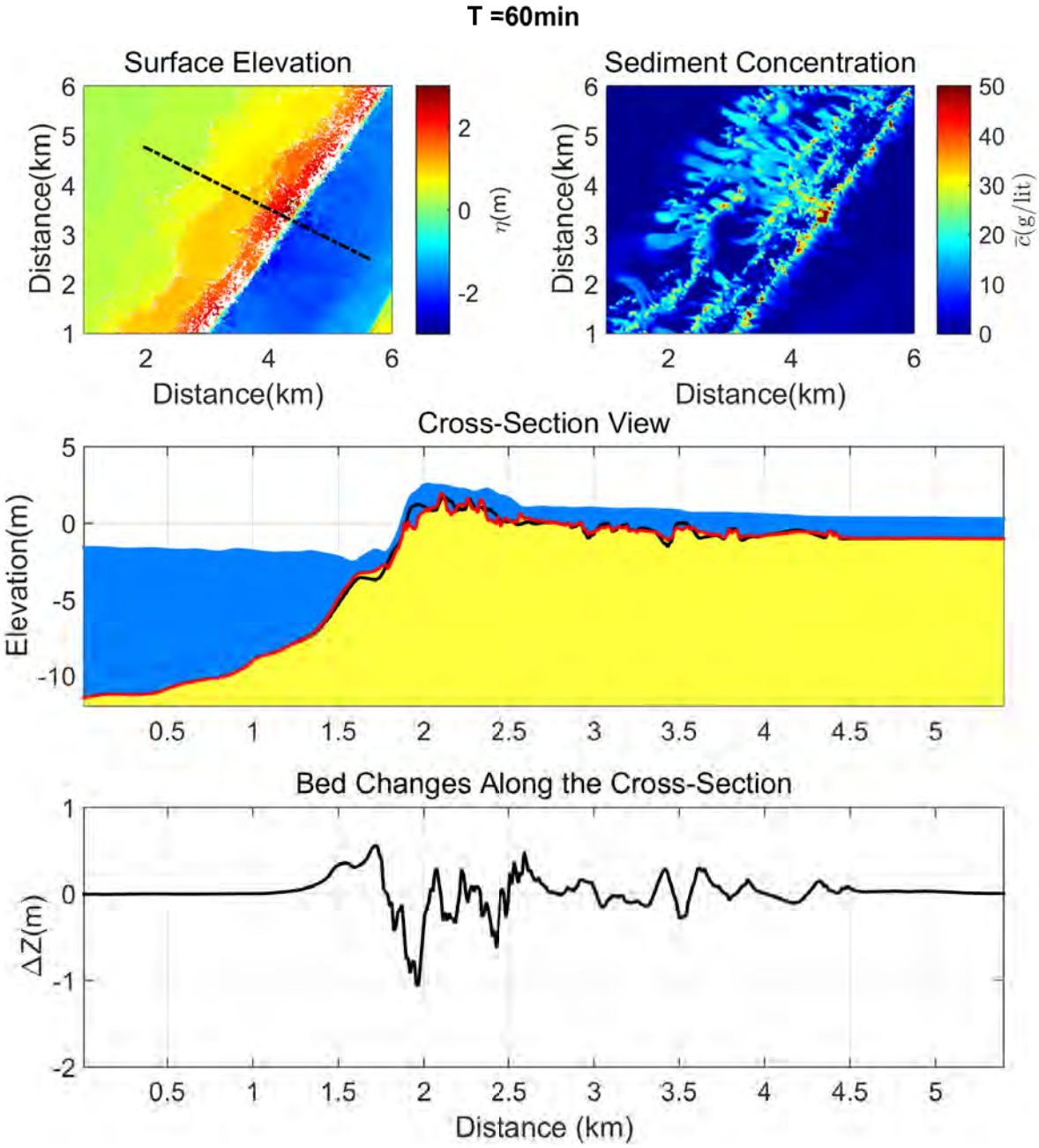

Figure 5.19: Water surface (top-left) and sediment concentration (top-right) 60 minutes after the CVV tsunami reaches the Assateague Island. The figure in the middle shows the water surface (blue surface), initial bathymetry (black line), and computed bed levels (red line, yellow surface) at the cross-section shown in the top-left figure. The bottom figure shows the computed bed elevation changes ($\Delta Z = -\Delta Z_b$) along the cross-section.

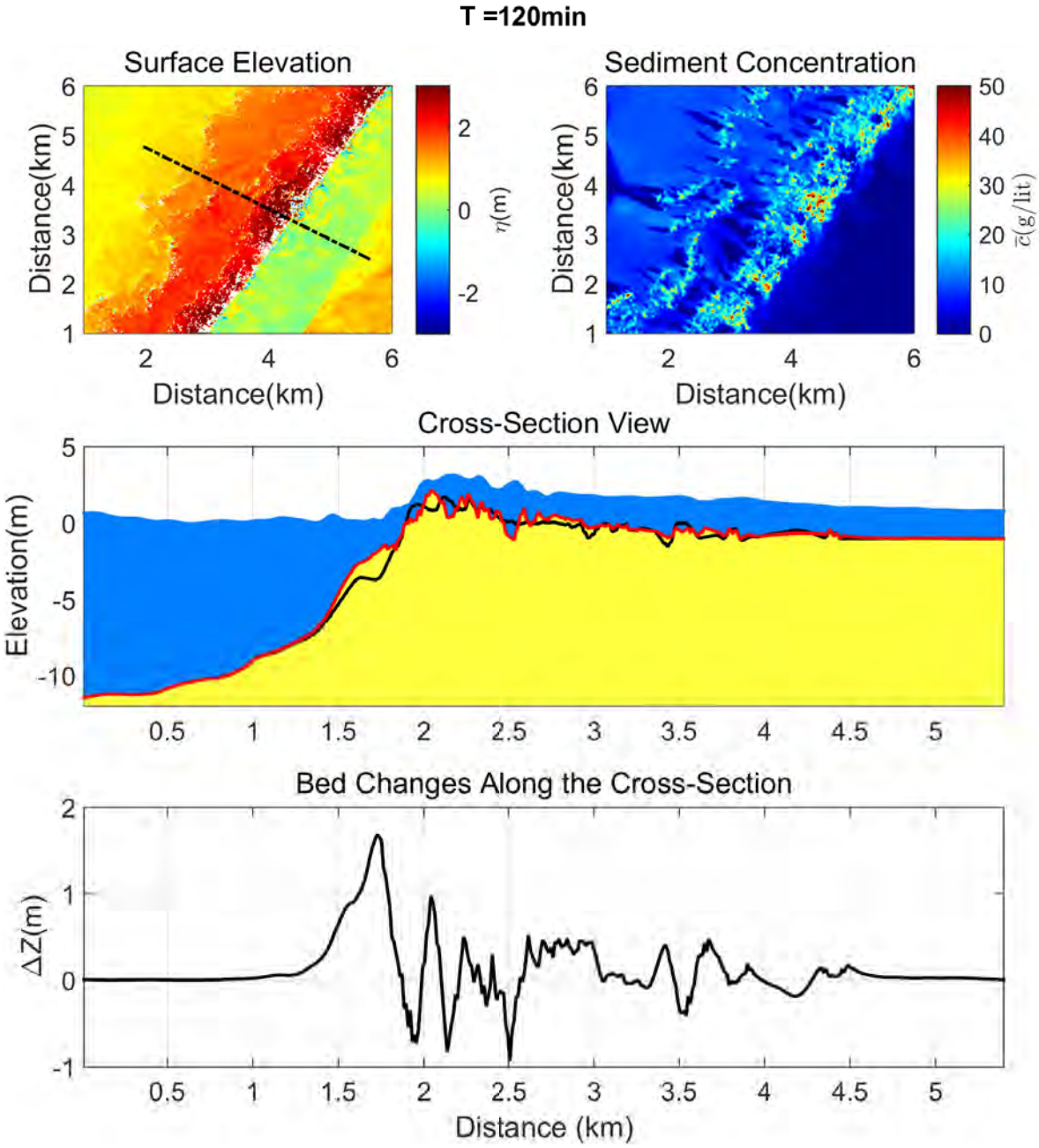

Figure 5.20: Water surface (top-left) and sediment concentration (top-right) 120 minutes after the CVV tsunami reaches the Assateague Island. The figure in the middle shows the water surface (blue surface), initial bathymetry (black line), and computed bed levels (red line, yellow surface) at the cross-section shown in the top-left figure. The bottom figure shows the computed bed elevation changes ($\Delta Z = -\Delta Z_b$) along the cross-section.

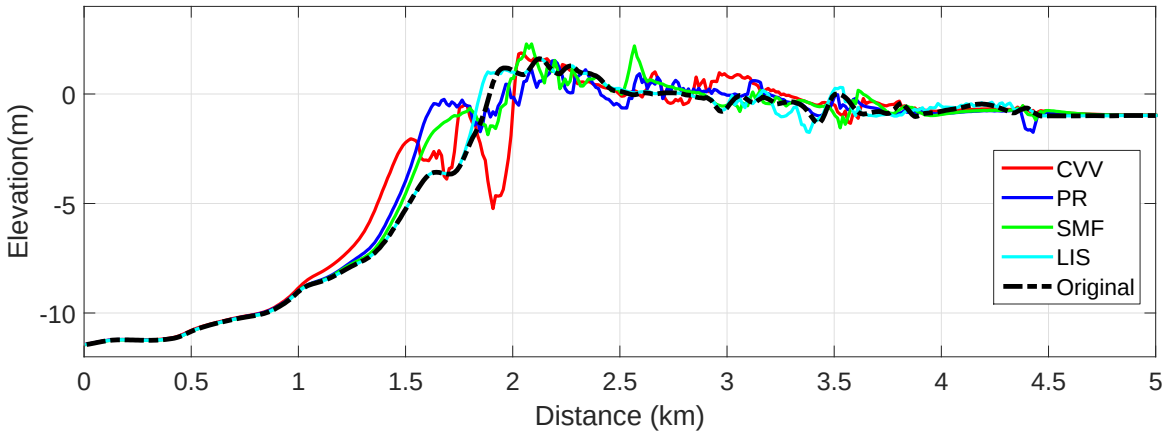

Figure 5.21: Computed bed changes at the cross-section showed in Figures 5.13-5.20 for the CVV, PRT, SMF and Lisbon tsunami sources.

changes for the CVV is larger than other sources, regarding its magnitude compared to PRT and SMF tsunamis. The computed bed changes for PRT and SMF tsunamis are comparable to each other, with PRT source causing larger erosions on the shoreface.

Figures 5.26-5.27 illustrate the onshore portion of Assateague Island which is above MHW tide before and after the tsunamis simulated in this work. Except for the Lisbon tsunami, results of other sources suggest that during a significant tsunami the barrier island location moves onshore. This migration occurs mainly because of two processes. First, during the overtopping, tsunami waves erode the top and back of the barrier and deposit the sand in the back bay, and during rundown the shoreface gets eroded, and the corresponding sand gets accreted further offshore. Second, when the trapped water between the mainland and the barrier start to flow back into the ocean, significant amounts of sand get accumulated in the back bay around the eastern shoreline of the barrier, while massive scouring occurs on the shoreface. Both of these processes scour the shoreface and the dune system of the Assateague Island barrier, and accumulate the sand in behind, causing the island to emerge from water further onshore compared to its original location, with much flatter topography compared to pre-tsunami bathymetry.

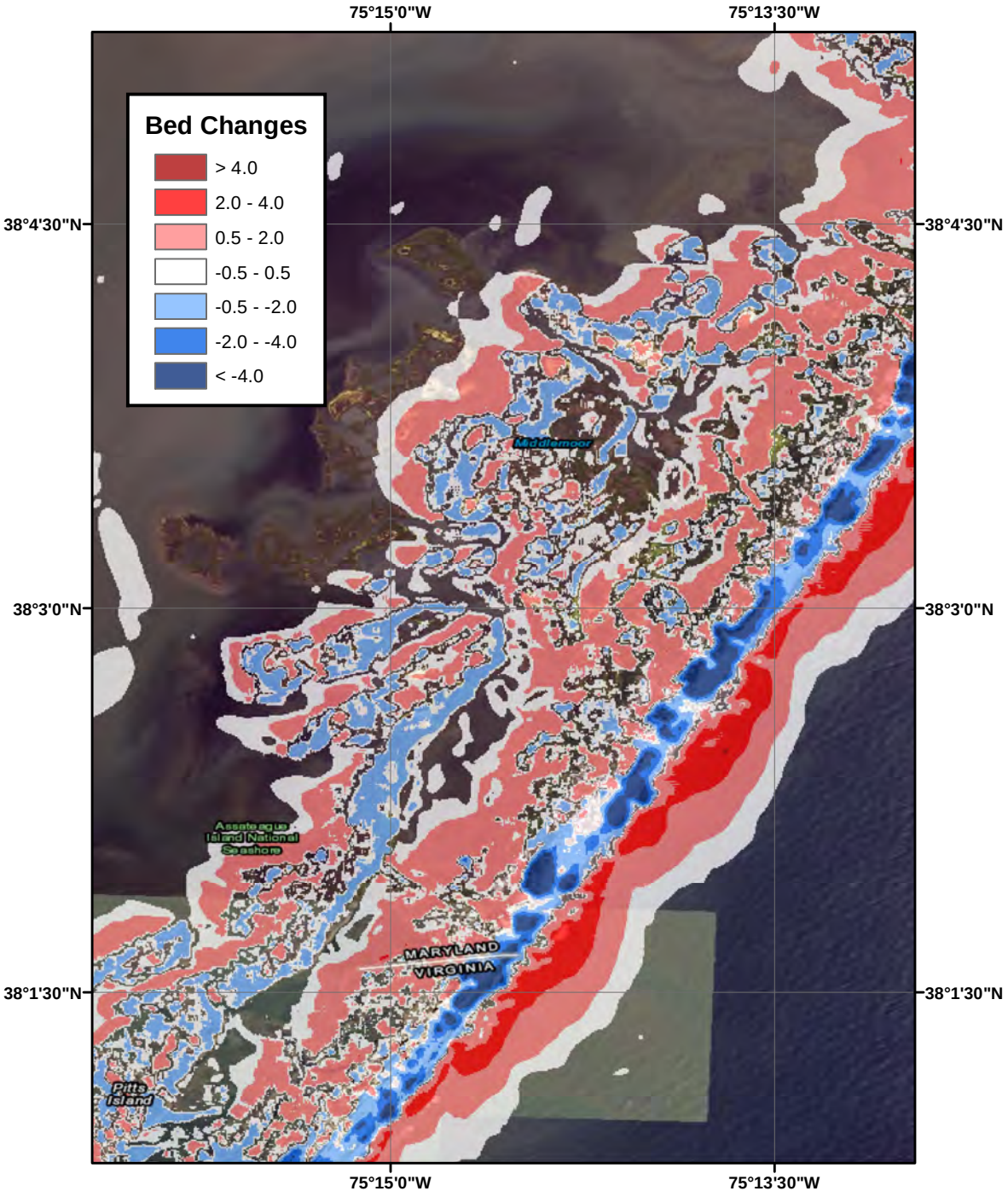

Figure 5.22: The computed bed changes of Assateague Island during simulations of the PRT tsunami source. Bed changes less than 20 cm are filtered out for clarity.

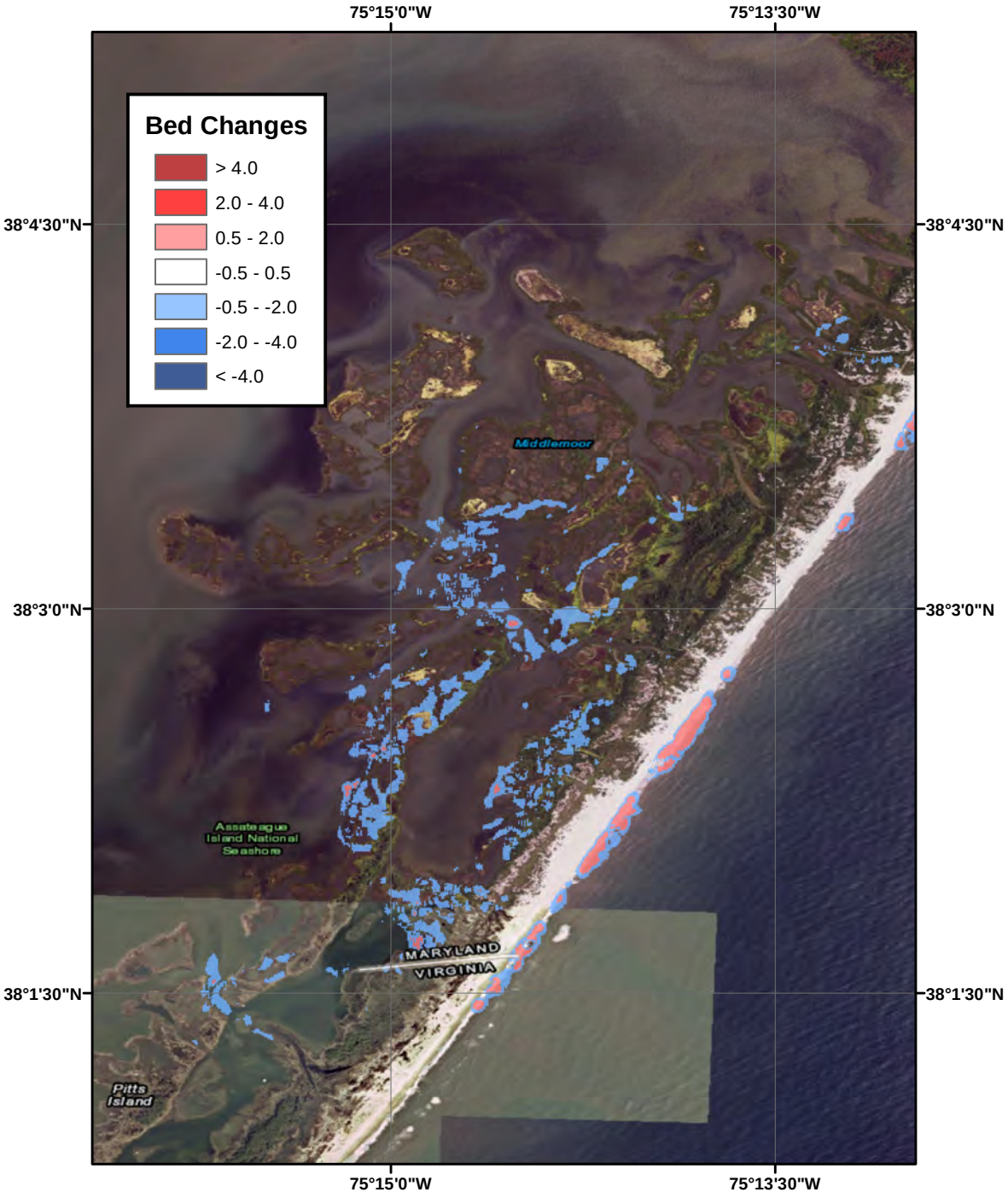

Figure 5.23: The computed bed changes of Assateague Island during simulations of the Lisbon tsunami source. Bed changes less than 20 cm are filtered out for clarity.

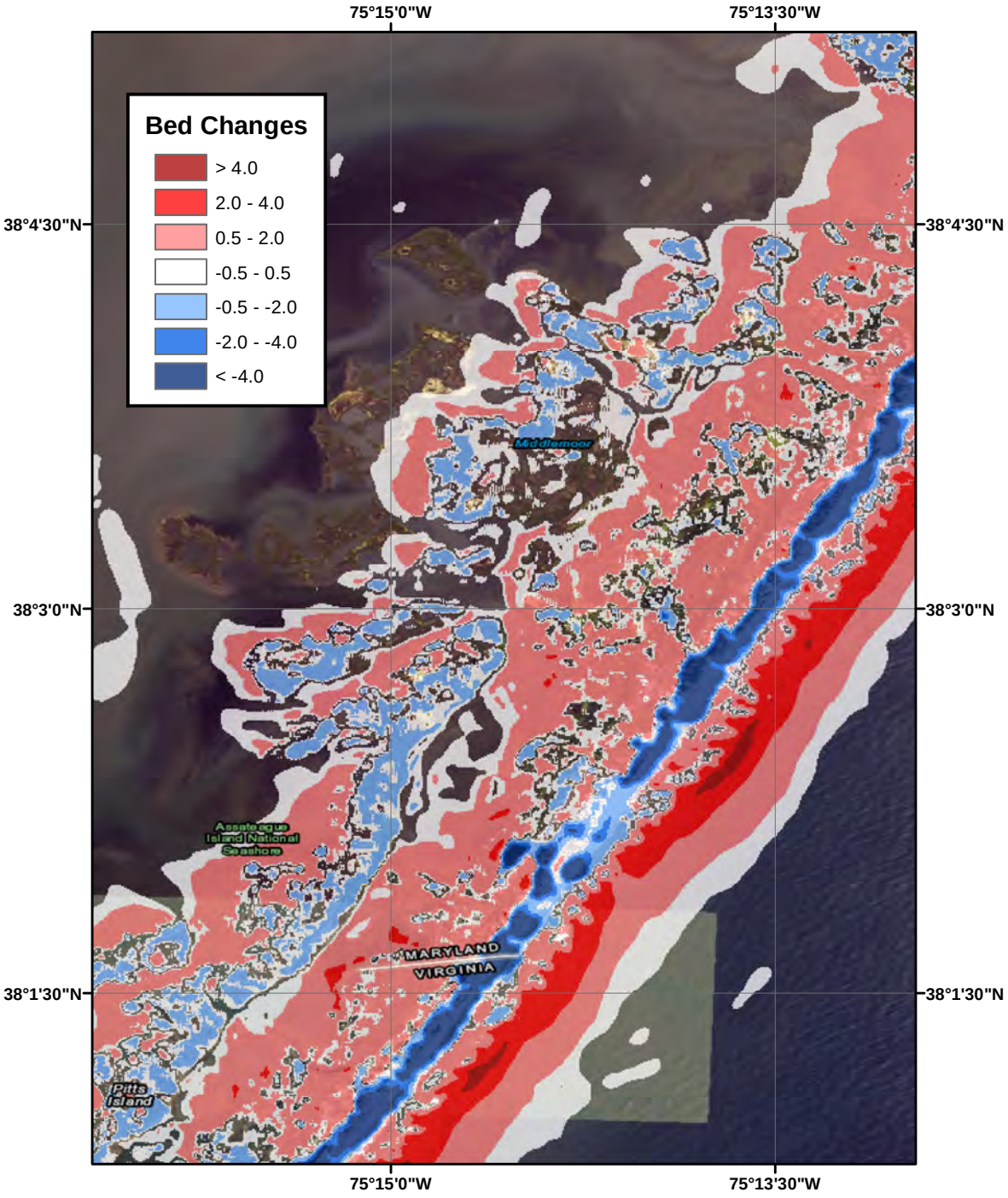

Figure 5.24: The computed bed changes of Assateague Island during simulations of the CVV tsunami source. Bed changes less than 20 cm are filtered out for clarity.

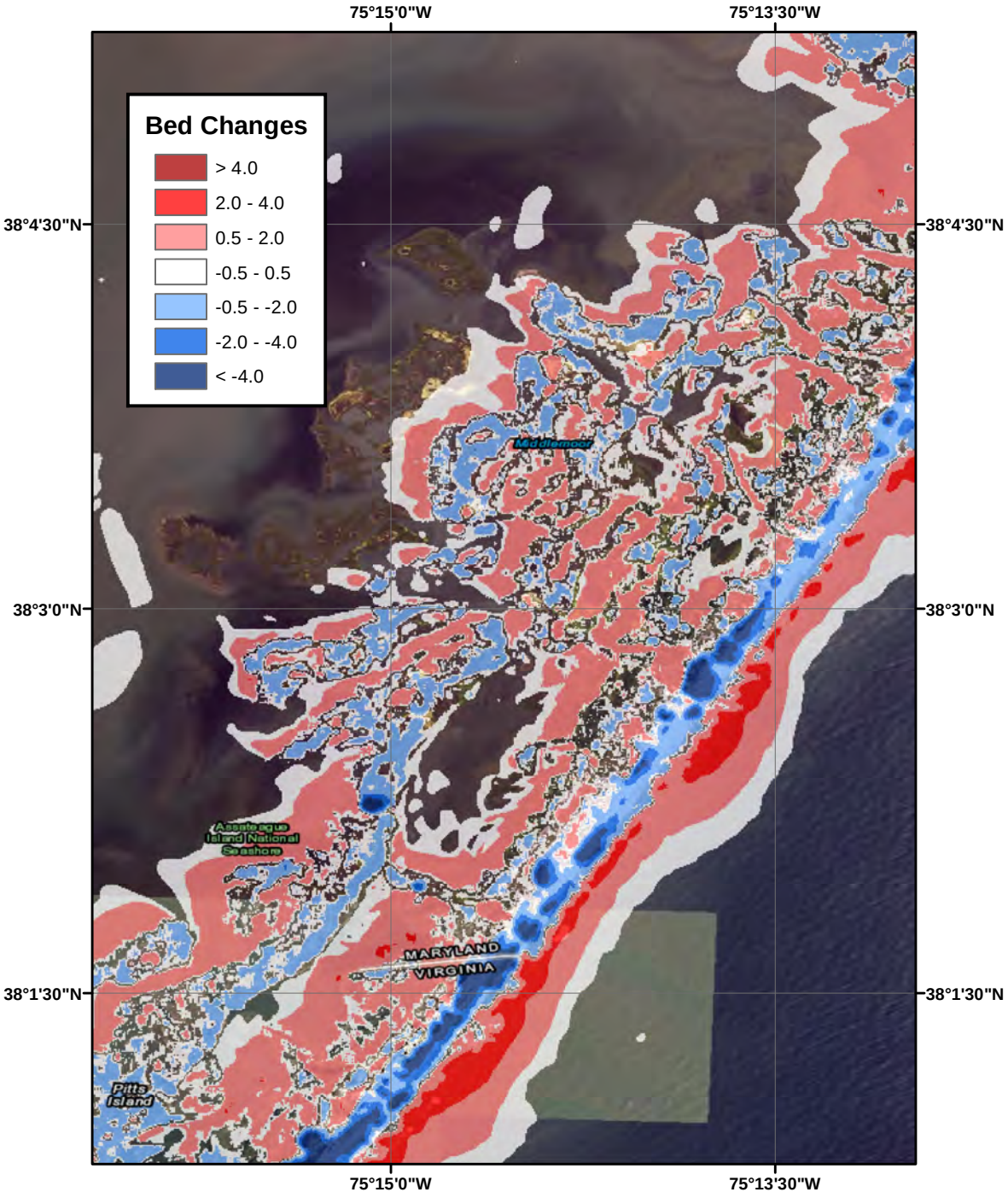

Figure 5.25: The computed bed changes of Assateague Island during simulations of the SMF tsunami source. Bed changes less than 20 cm are filtered out for clarity.

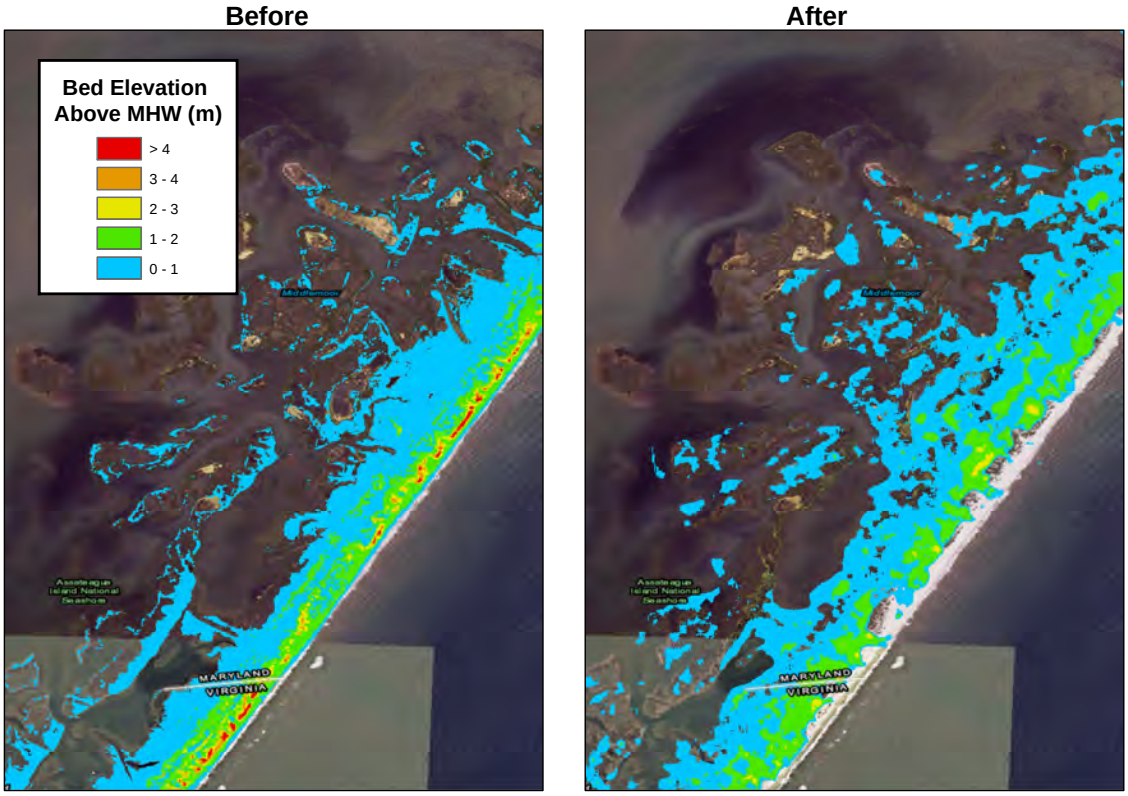

Figure 5.26: The onshore portion of the Assateague Island above MHW level before (Left) and after (Right) the PRT tsunami.

5.5 Ocean City Inlet Morphological Response to Tsunami Inundation

We used the computational domain shown in the bottom right of Figure 5.12 to model the tsunami-induced morphological changes around Ocean City inlet. Similar to the Assateague Island simulations, the grid size used here is 810 × 810 with 1/3 arc-sec resolution corresponding to $\Delta x = 8.10$ m and $\Delta y = 10.27$ m, extracted from the Ocean City DEM. Surface elevations (η) and velocity terms ($\overrightarrow{u_\alpha}$) were forced on the boundaries using the information recorded during the 1 arc-sec simulations for CVV, Lisbon, PRT, and SMF sources introduced previously in this chapter. Figure 5.30 shows the location of the study area. The red box depicts the boundaries of the grid

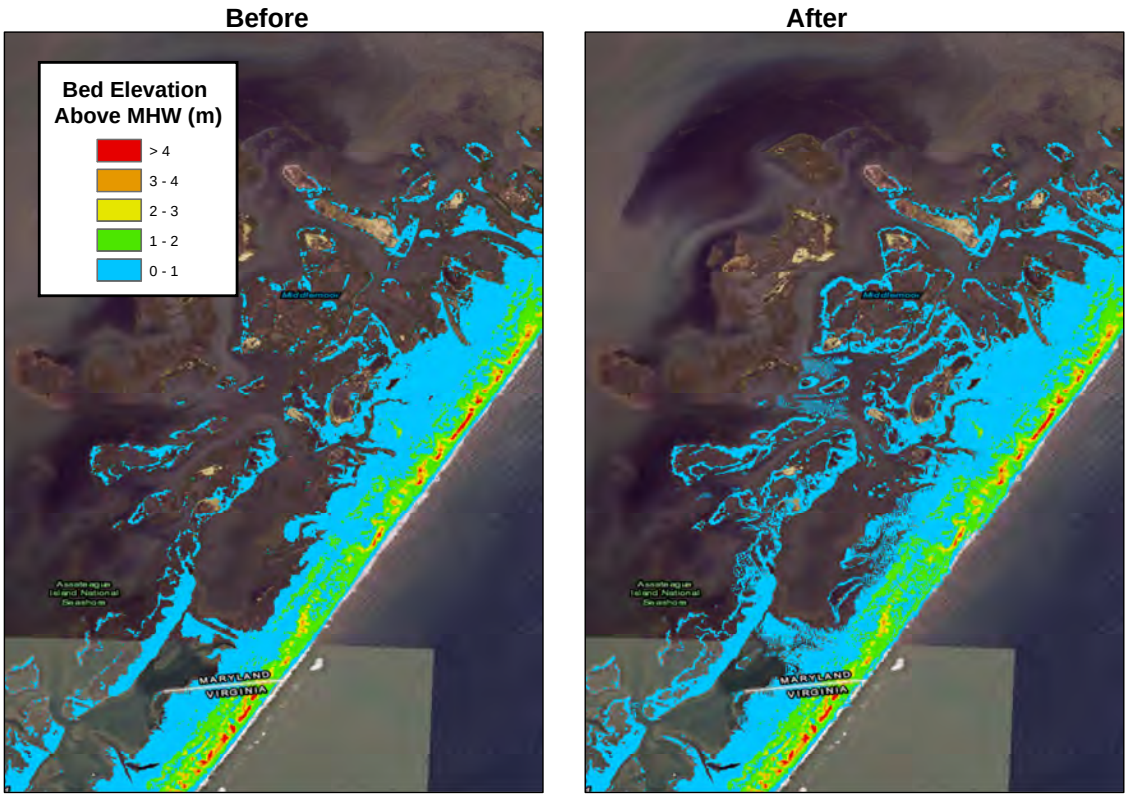

Figure 5.27: The onshore portion of the Assateague Island above MHW level before (Left) and after (Right) the Lisbon tsunami.

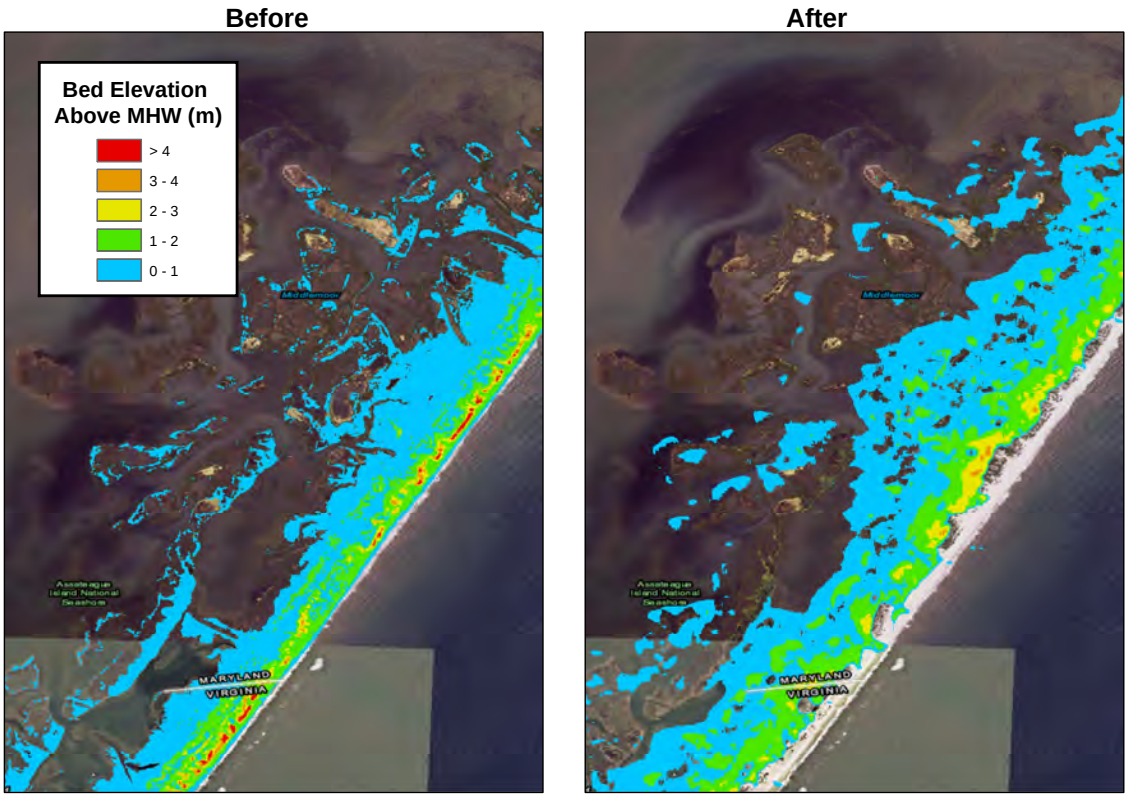

Figure 5.28: The onshore portion of the Assateague Island above MHW level before (Left) and after (Right) the CVV tsunami.

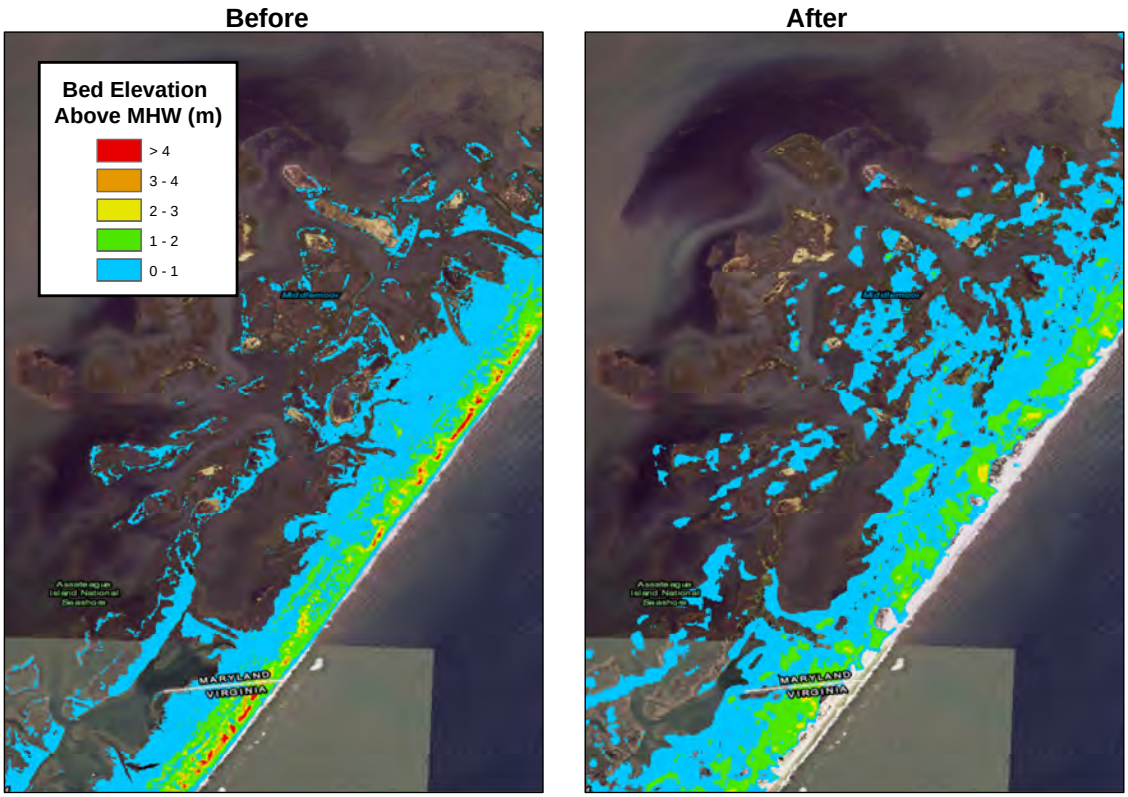

Figure 5.29: The onshore portion of the Assateague Island above MHW level before (Left) and after (Right) the SMF tsunami.

we used for our simulations.

Similar to the Assateague Island simulations, we used Fenser et al. (2016) experiment results to determine the median grain size with $d_{50} = 0.36$ mm, and $w_f = 0.046$ cm/s. Also, we used the repose angle corresponding to $\tan(\phi) = 0.5$ in our simulations to be implemented in the avalanche scheme. In contrast to the Assateague Island location, the Ocean City barriers are covered with paved surfaces and vegetation in addition to sandy regions. Therefore, through GIS work and image processing we distinguished the sandy areas from non-erodible regions. Figure 5.31 demonstrates different categories used to define land use bed information for our simulations. Four different regions were defined, two erodible and two non-erodible. The jetties surrounding the inlet and the paved regions on the northern barrier and mainland are defined as non-erodible regions. The areas covered by sand and vegetation are considered to be erodible, as well as underwater regions. Following the works of Sugawara et al. (2014) the Manning coefficients were defined for different bottom types as follows, $n = 0.025$ for sandy regions, $n = 0.03$ for vegetated regions, and $n = 0.04$ for paved regions and building. For jetties, the Manning coefficient of $n = 0.1$ was assumed. Finally, the bed porosity in sandy regions was assumed to be the standard value of 0.4.

Figures 5.32-5.35 demonstrate computed bed changes around Ocean City inlet for all of the tsunami sources that we studied. The erosion and deposition zones on the southern part of the inlet are comparable to the results obtained for the Assateague Island. The onshore portion of the barrier experienced extensive erosion, while the mobilized sediment was deposited either offshore or in the bay behind the barrier. The pattern of morphology changes was different on the north barrier due to the existence of non-erodible surfaces. Although the tsunamis caused extensive scour on the shoreface and deposited a portion of it offshore, more sand deposits occurred on top of the barrier where non-erodible regions were located, and not in the back bay. In other words, the northern barrier did not migrate shoreward during the tsunami inundation in contrast to the southern part of the inlet which is the northern extent of the Assateague Island. Similar to the result shown in the previous section, it was observed that the width of the

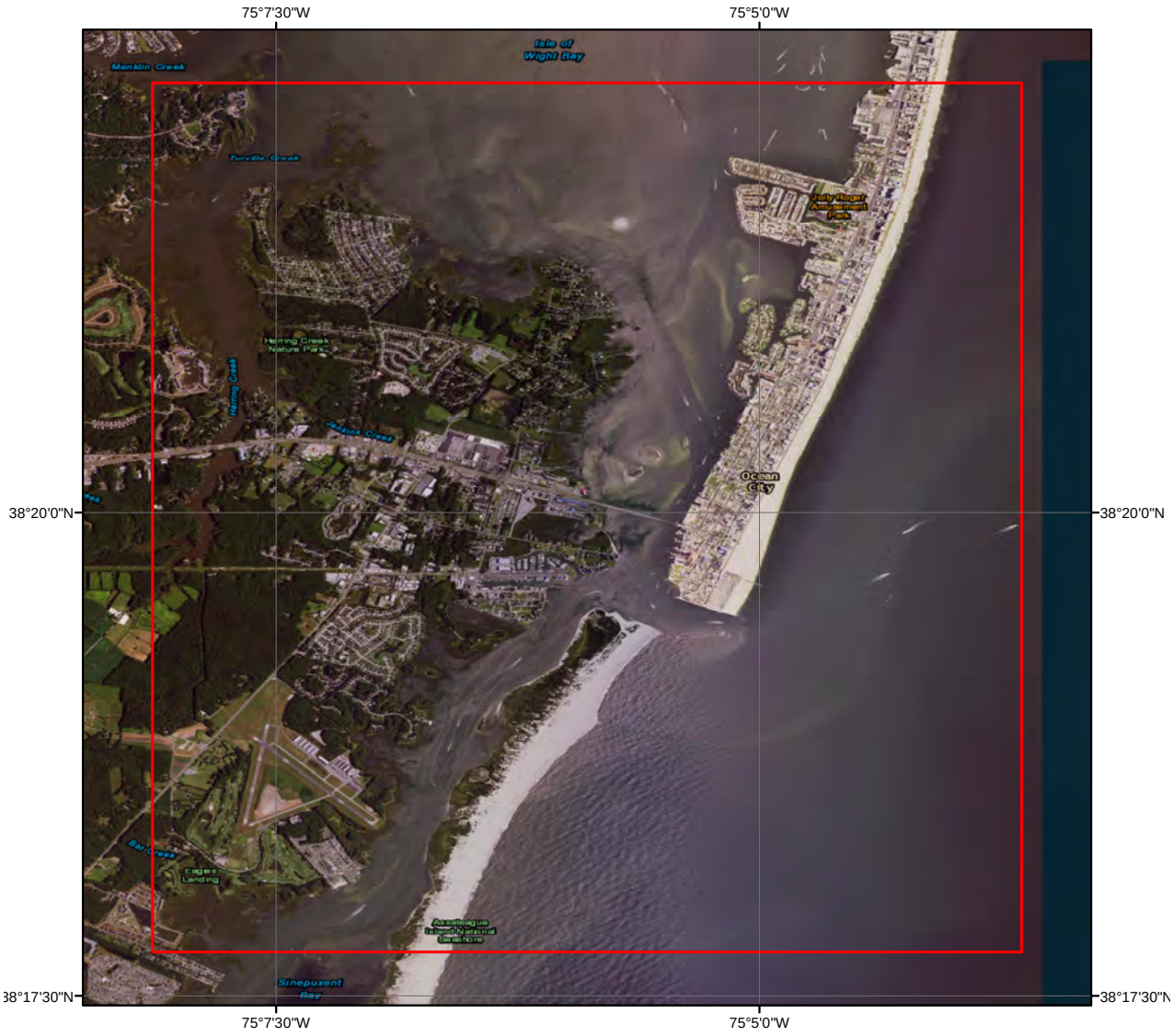

Figure 5.30: The red box depicts the boundaries of the computational grid used to simulate tsunami-induced morphological changes in the area around Ocean City inlet.

Figure 5.31: The land use map used for simulation of morphological changes in the surrounding area of the Ocean City inlet.

barrier island in the south of the Ocean City inlet increases after the tsunami. However, the width of the north barrier decreases during simulations of all tsunami sources. Also, larger erosions were computed in the northern half. The decline in barrier width and larger erosions mainly occurred because of the existence of non-erodible regions, which resulted in significant scouring of sandy areas in the neighborhood of paved surfaces and jetties.

The process of inundation and sequence of morphological changes are similar to that of the Assateague Island for the three large tsunami sources (PRT, CVV, and SMF), explained in the previous section. However, in Ocean City inlet case the Lisbon tsunami overtops this portion of the Assateague Island and causes significant morphological changes during inundation. The northern extent of the Assateague Island close to the inlet has lower elevations above the water surface compared to the part of the Assateague Island studied in the previous section and the north barrier of the inlet, and probably will get flooded during minor tsunami events that are comparable to the Lisbon source. Also, because the north barrier is almost non-erodible, the morphological impact on the south barrier is extensive. A similar pattern has been observed in the field surveys after the tsunamis, where an erodable region in proximity of non-erodible got significantly scoured (Goto et al., 2011). Figure 5.33 illustrates the computed bed changes during the simulation of the Lisbon tsunami source in the Ocean City inlet. At the northern tip of the south barrier, next to the inlet jetty, large scours are calculated which exposed the mainland behind it to tsunami action and latter waves.

Figures 5.36-5.39 illustrate comparisons between pre- and post-tsunami topography of the Ocean City inlet. For clarity, only the regions that are above MHW level are shown in these figures. The shoreface of both barriers on the north and south of the Ocean City inlet is entirely eroded for all of the tsunami sources, even the Lisbon tsunami. Because the eastern half of the barrier in the northern part of the domain is assumed to be non-erodible in our simulations (paved/buildings), the eastern shoreline of this barrier is barely moved, in contrast to the Assateague Island where the whole

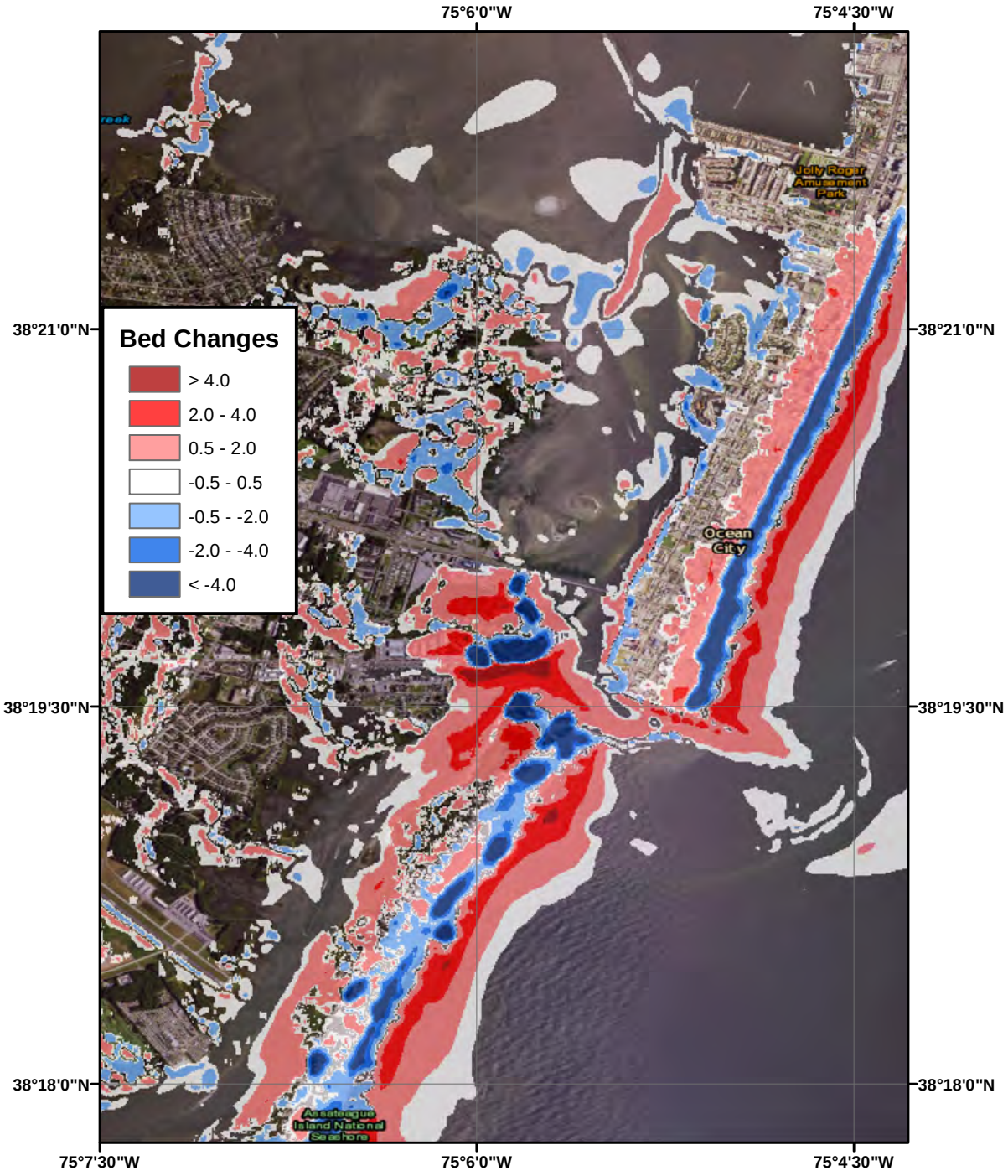

Figure 5.32: The computed bed changes of Ocean City inlet during simulation of the PRT tsunami source. Bed changes less than 20 cm are filtered out for clarity.

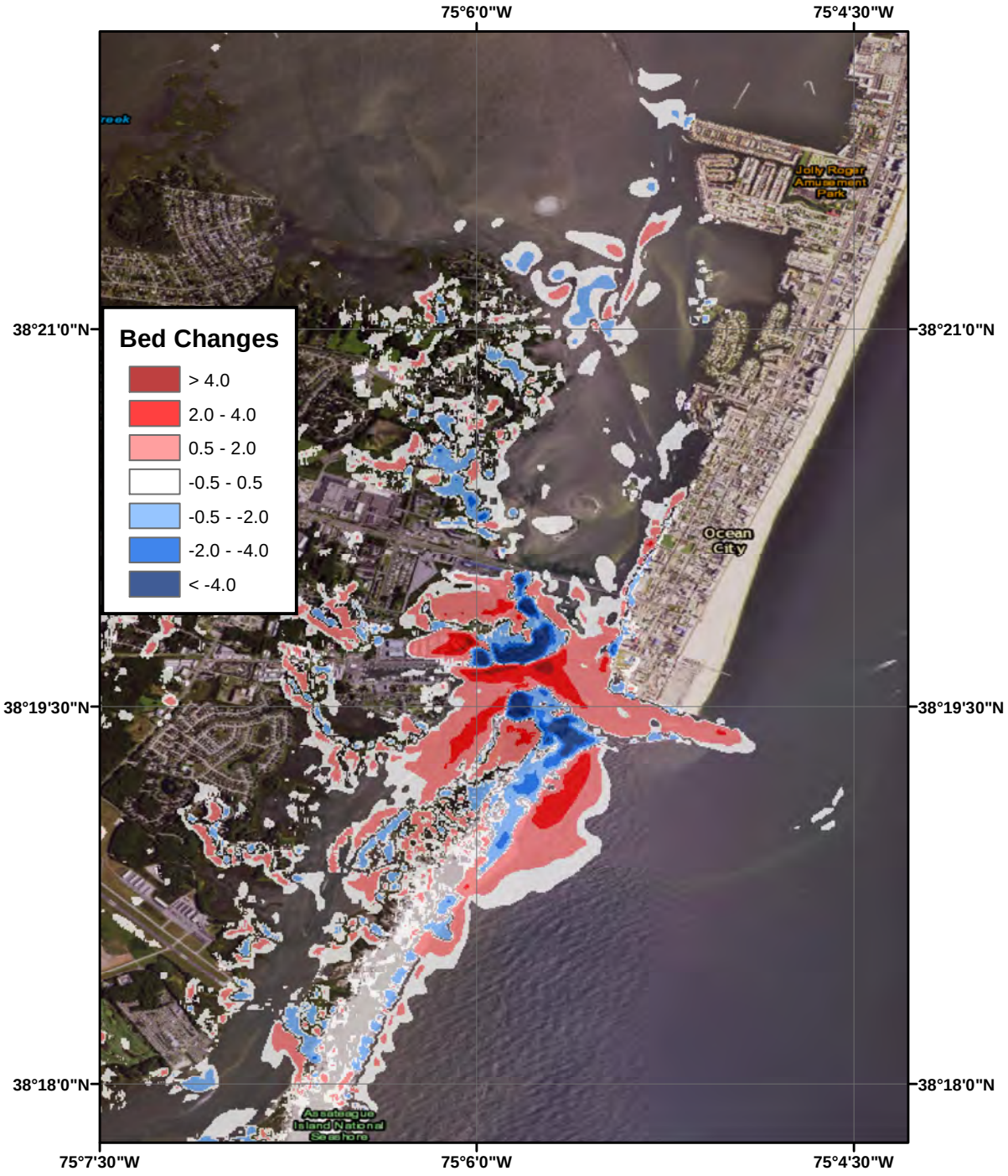

Figure 5.33: The computed bed changes of Ocean City inlet during simulation of the Lisbon tsunami source. Bed changes less than 20 cm are filtered out for clarity.

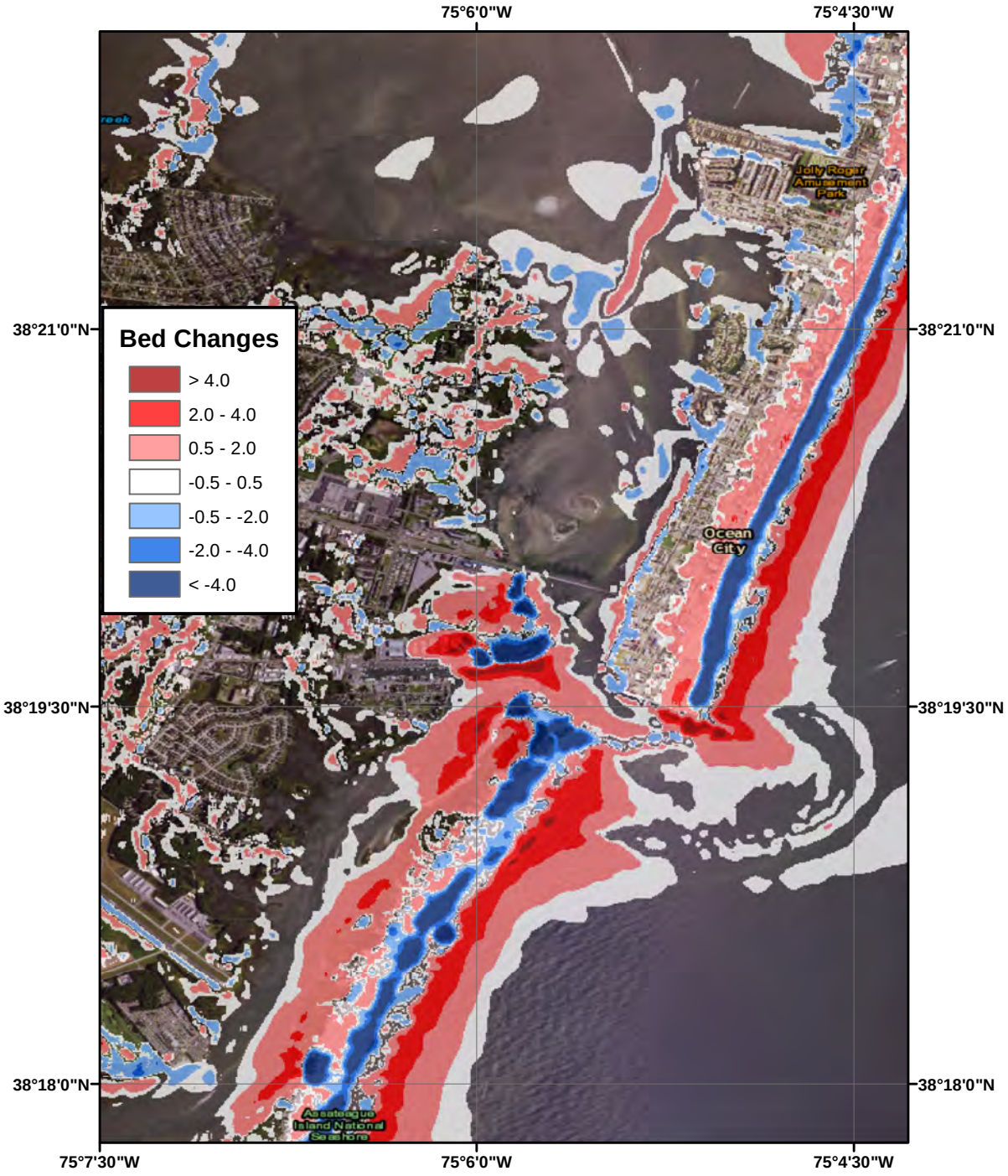

Figure 5.34: The computed bed changes of Ocean City inlet during simulation of the CVV tsunami source. Bed changes less than 20 cm are filtered out for clarity.

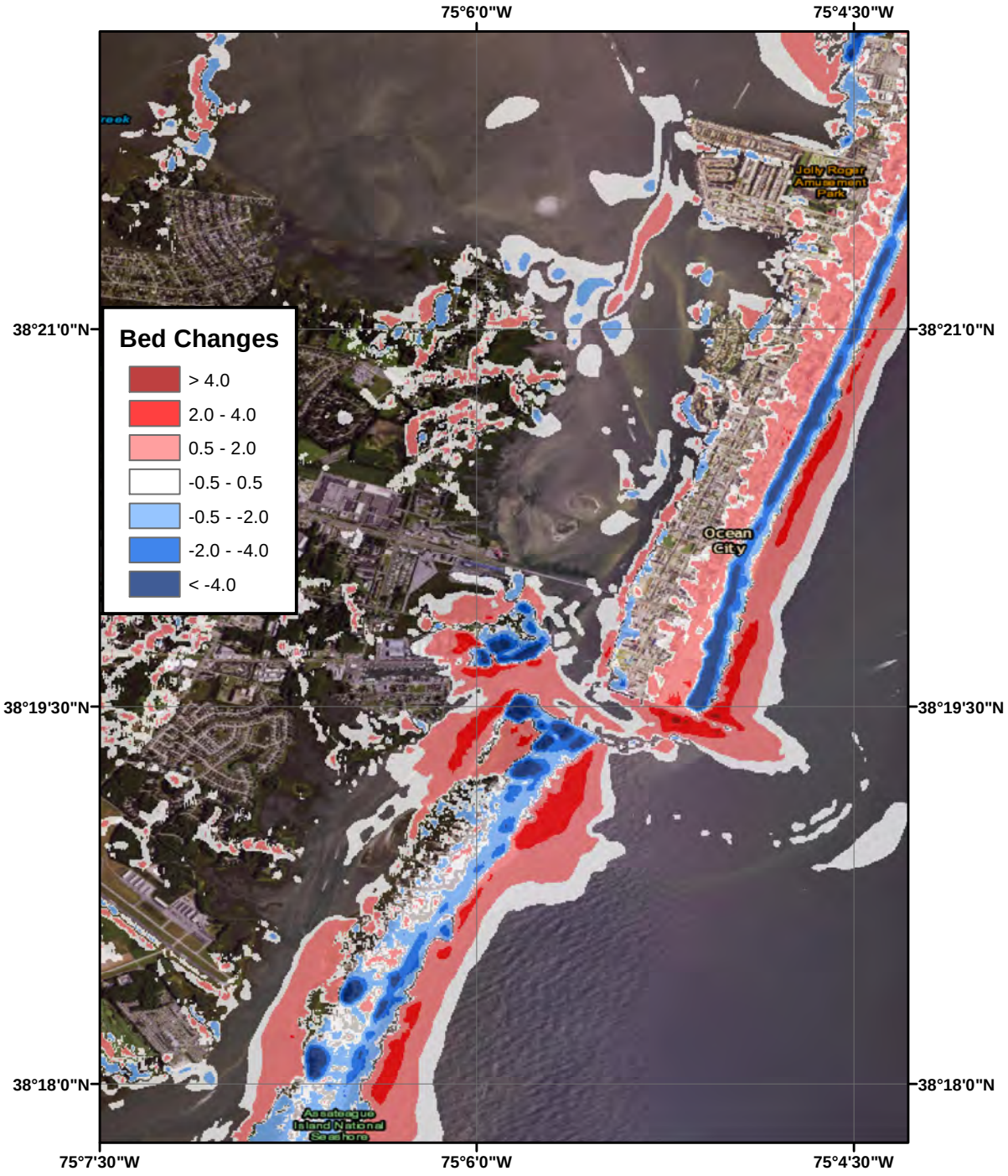

Figure 5.35: The computed bed changes of Ocean City inlet during simulation of the SMF tsunami source. Bed changes less than 20 cm are filtered out for clarity.

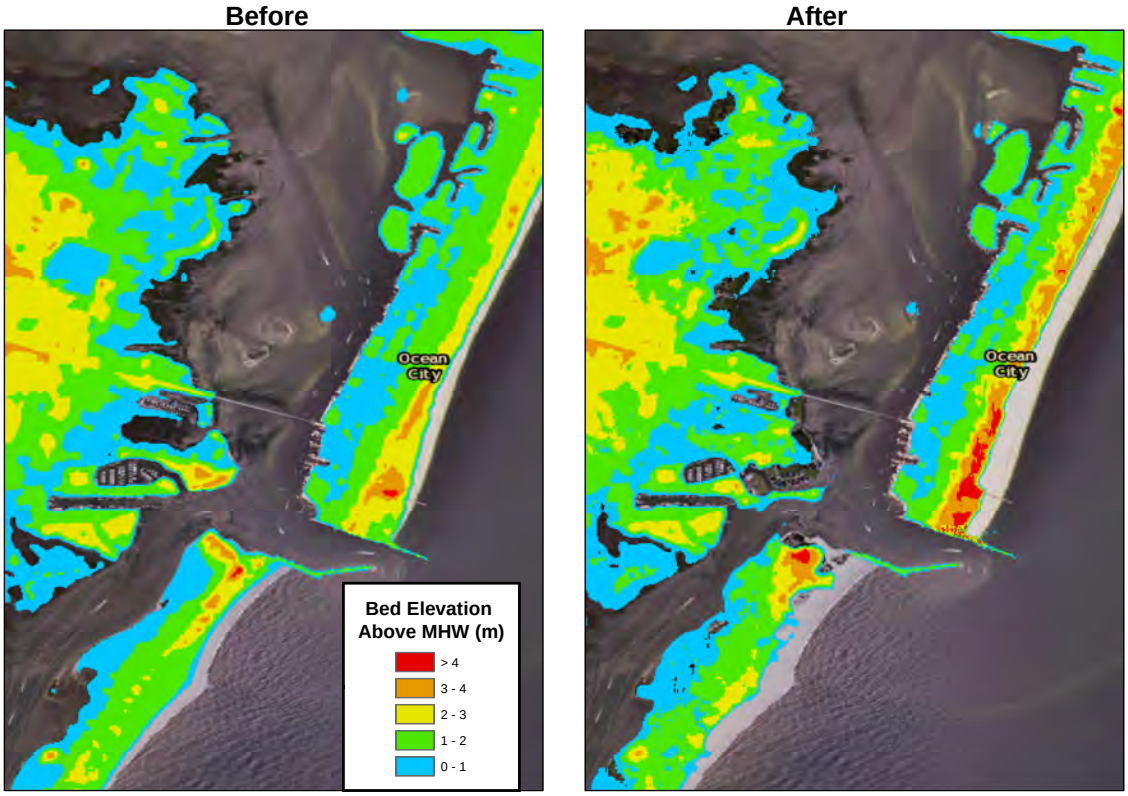

Figure 5.36: The onshore portion of the Ocean City inlet above MHW level before (Left) and after (Right) the PRT tsunami

barrier is erodible, and it migrates toward mainland during tsunami inundation. For all of the sources studied here, the northern tip of the Assateague Island gets eroded extensively, and consequently creates a much wider entrance compared to the original width of the inlet for tsunami waves to enter the back bay.

In addition to the test with hard bottom consideration, we modeled the CVV tsunami in the Ocean City inlet assuming sandy bottom for the entire domain to investigate the effect of such considerations on the morphological changes during tsunami inundation. The comparison between results of two conditions is shown in Figure 5.40. In the south of the domain, the results look similar although the values for erosion

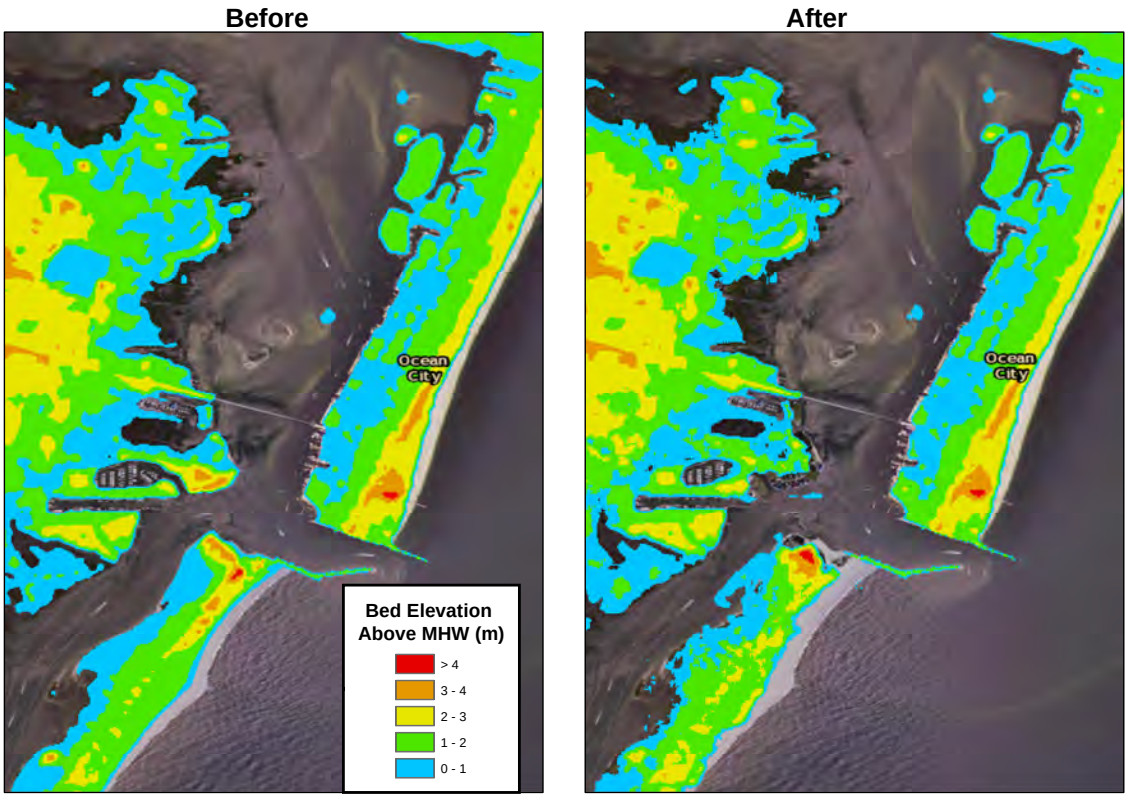

Figure 5.37: The onshore portion of the Ocean City inlet above MHW level before (Left) and after (Right) the Lisbon tsunami

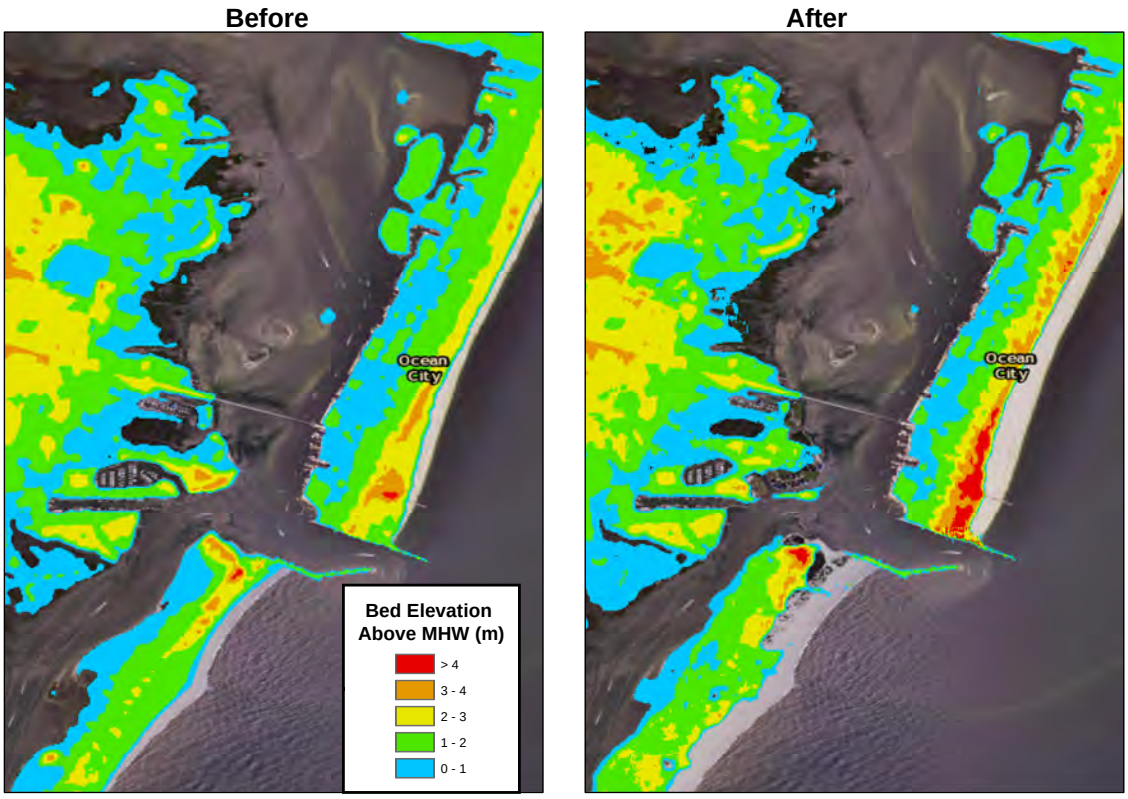

Figure 5.38: The onshore portion of the Ocean City inlet above MHW level before (Left) and after (Right) the CVV tsunami

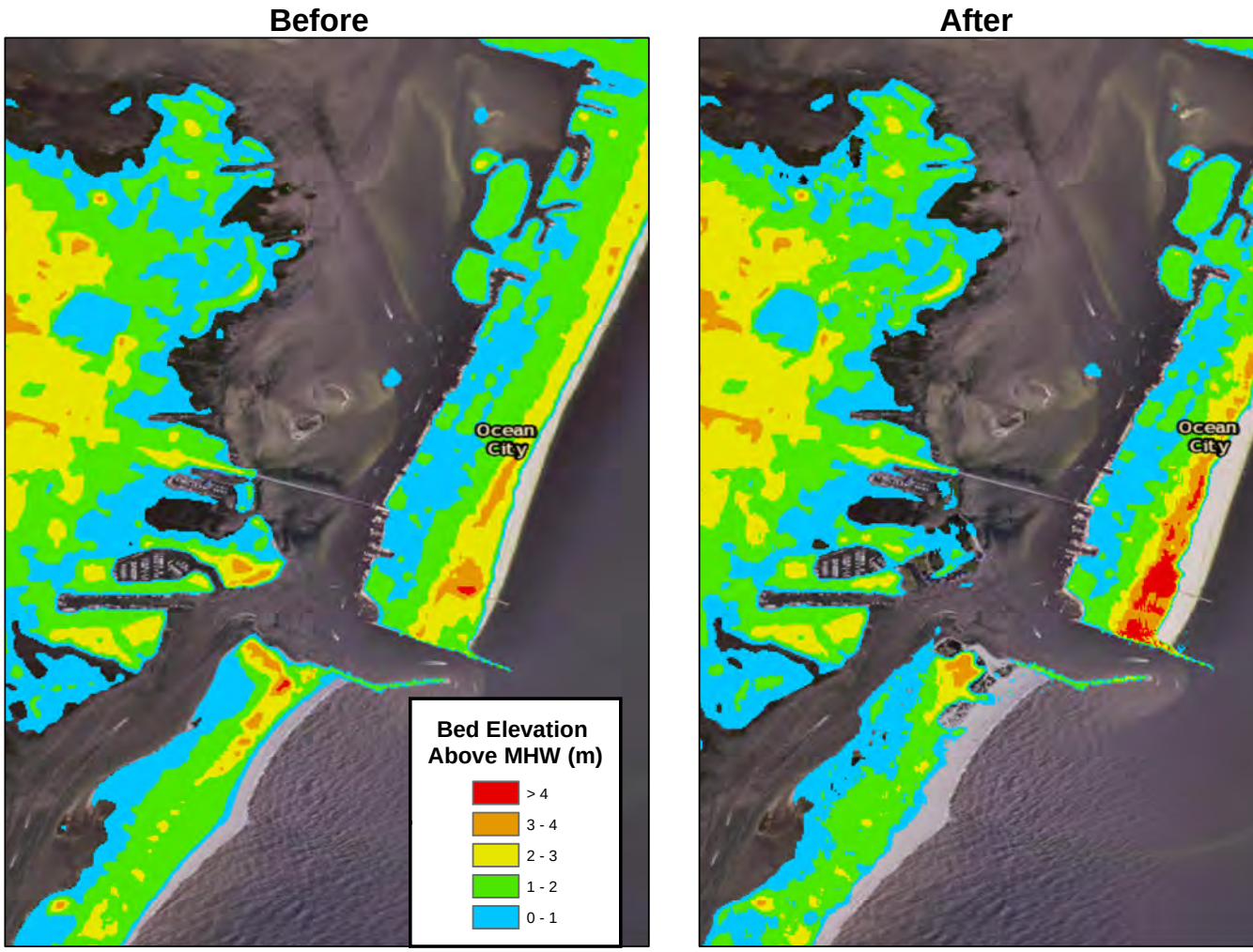

Figure 5.39: The onshore portion of the Ocean City inlet above MHW level before (Left) and after (Right) the SMF tsunami

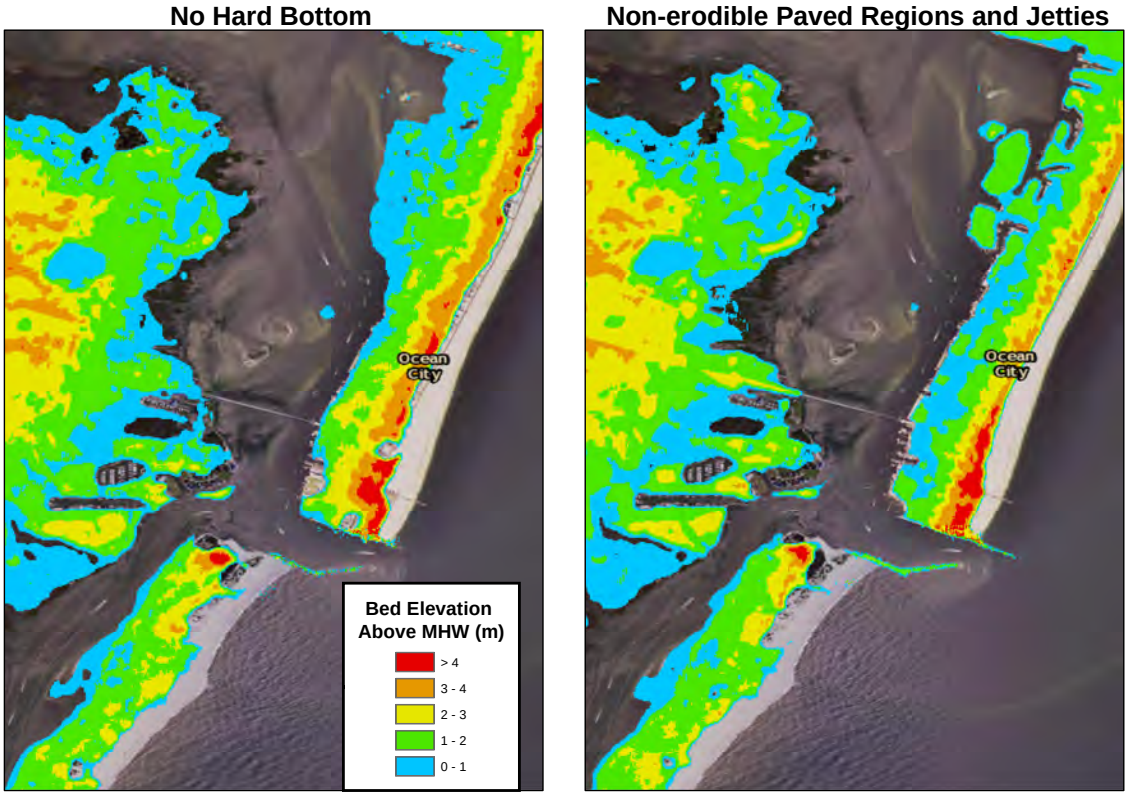

Figure 5.40: Comparison between computed bed changes for CVV tsunami in Ocean City, with sandy bottom assumption for the entire domain (Left), and with implemented hard bottom condition for paved areas (Right).

are slightly larger for the run with the hard bottom condition. The main difference is observed on the north barrier, where the erosion zone is extended further onshore on the shoreface for the simulation without non-erodible areas. Also, the eastern shoreline of the north barrier migrated toward the mainland similar to the Assateague Island barrier under CVV tsunami.

Finally, we investigated if considering the morphological changes during the tsunami inundation increase the level of hazard. For this purpose, we calculated the inundation line of each tsunami source for the Ocean City and compared them to results of Tehranirad et al. (2014) who used fixed bathymetry assumption for the

derivation of the inundation line. The inundation line of each tsunami is the extent of the tsunami propagation onshore. Figures 5.41-5.44 show the computed inundation line for the PRT, Lisbon, CVV and SMF tsunamis with fixed and dynamic bathymetry conditions. It is clear that for all of the sources we studied here, larger areas fall into the tsunami inundation zone when morphological impacts are included in simulations. For this particular area, the scours around the Ocean City inlet caused by initial waves of a tsunami, create a wider and smoother path for latter tsunami waves to attack the mainland behind and cause larger inundation zones compared to the condition that the inlet topography was fixed for the entire simulation.

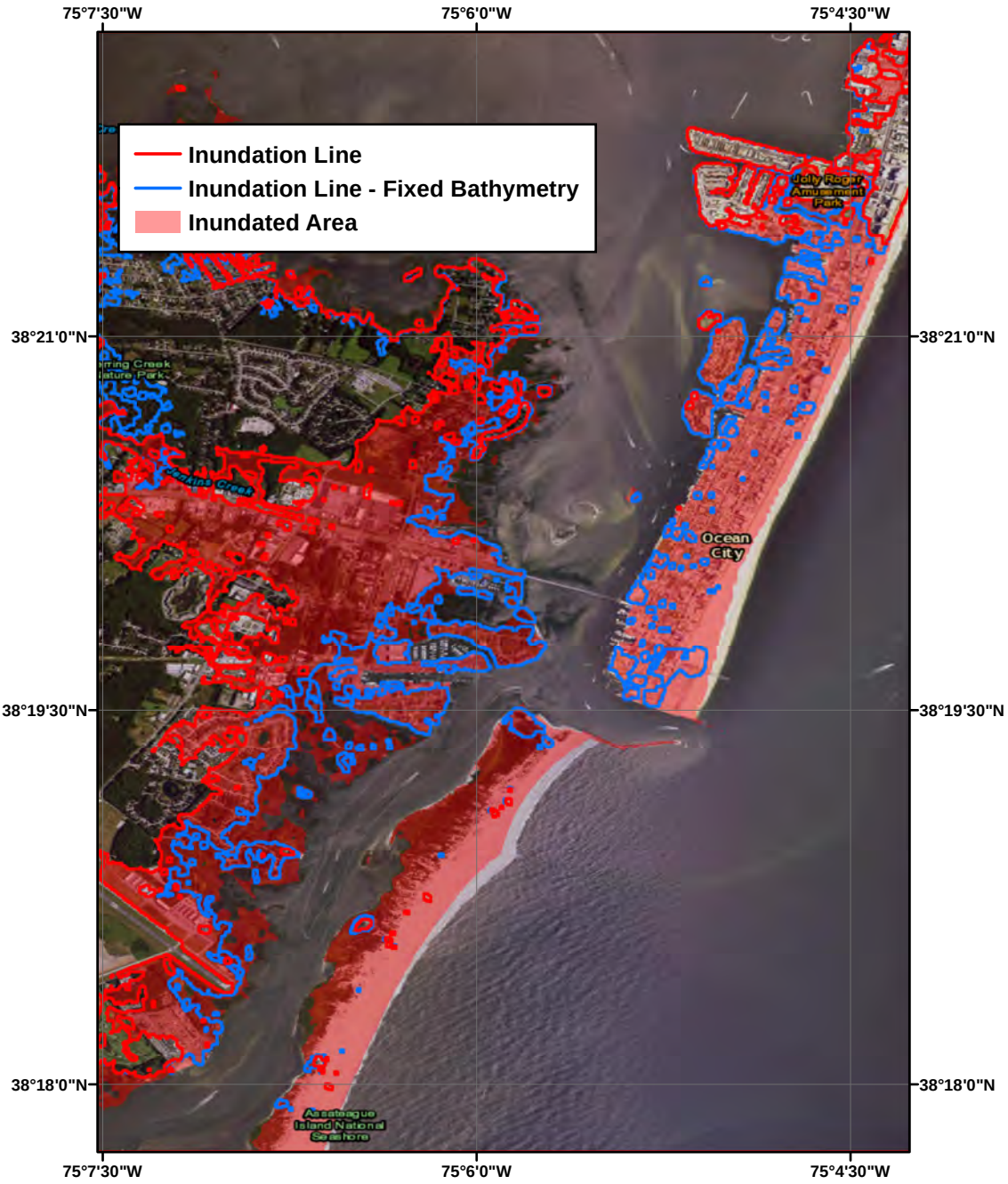

Figure 5.41: PRT tsunami inundation line for fixed (blue) and dynamic (red) bathymetry conditions. The red area shows the inundated region for the dynamic run which considers bed changes during the simulations of tsunami inundation.

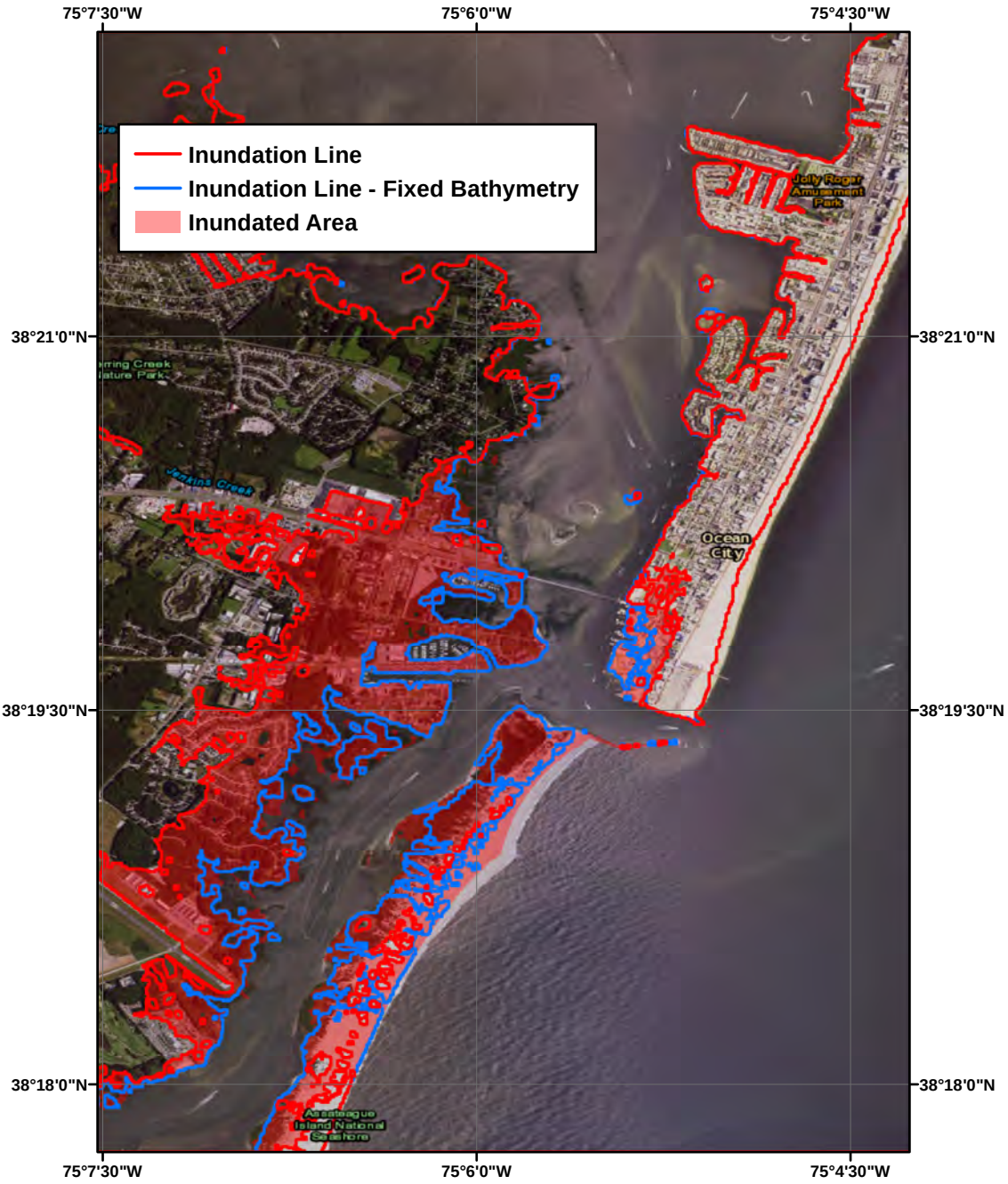

Figure 5.42: Lisbon tsunami inundation line for fixed (blue) and dynamic (red) bathymetry conditions. The red area shows the inundated region for the dynamic run which considers bed changes during the simulations of tsunami inundation.

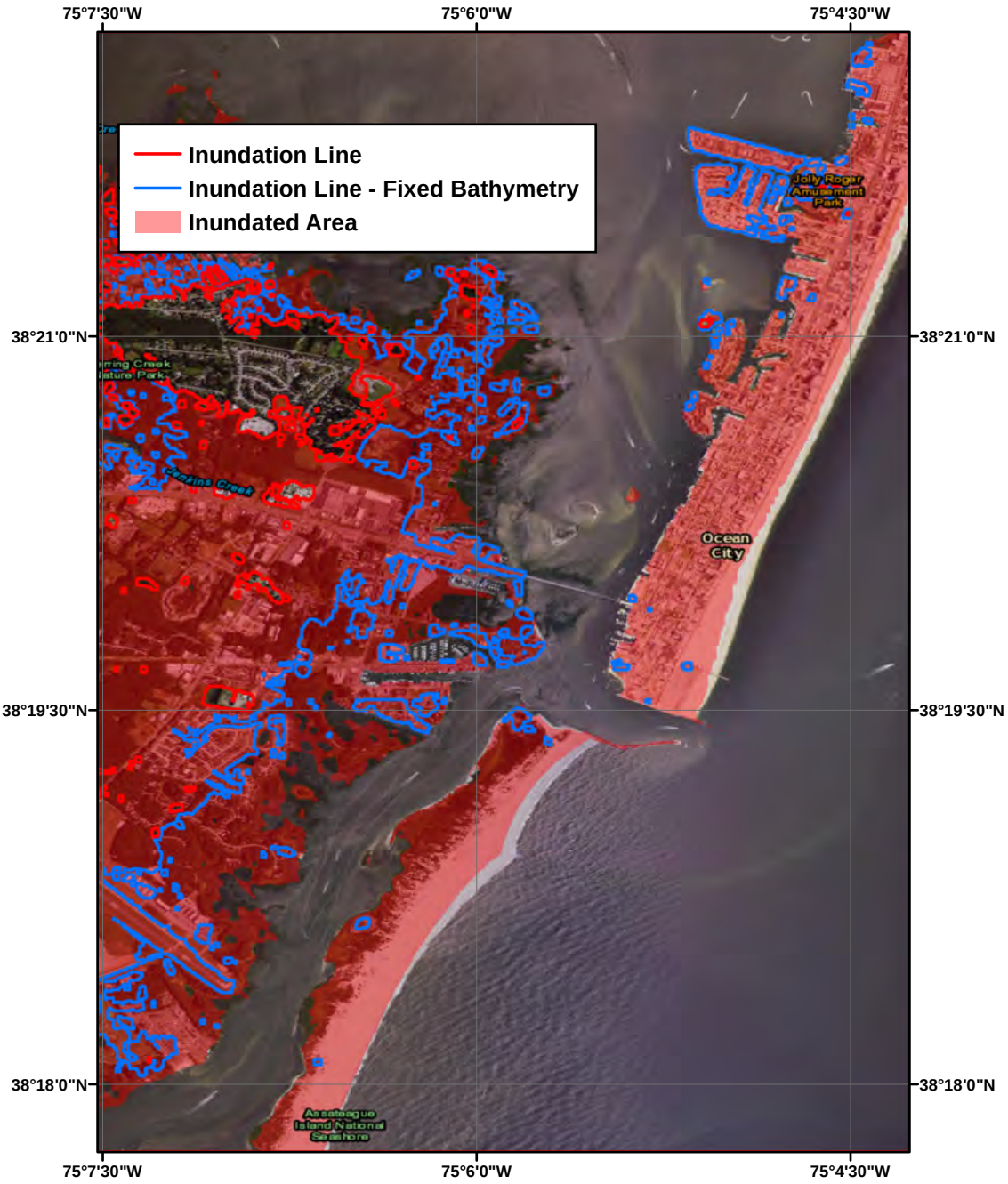

Figure 5.43: CVV tsunami inundation line for fixed (blue) and dynamic (red) bathymetry conditions. The red area shows the inundated region for the dynamic run which considers bed changes during the simulations of tsunami inundation.

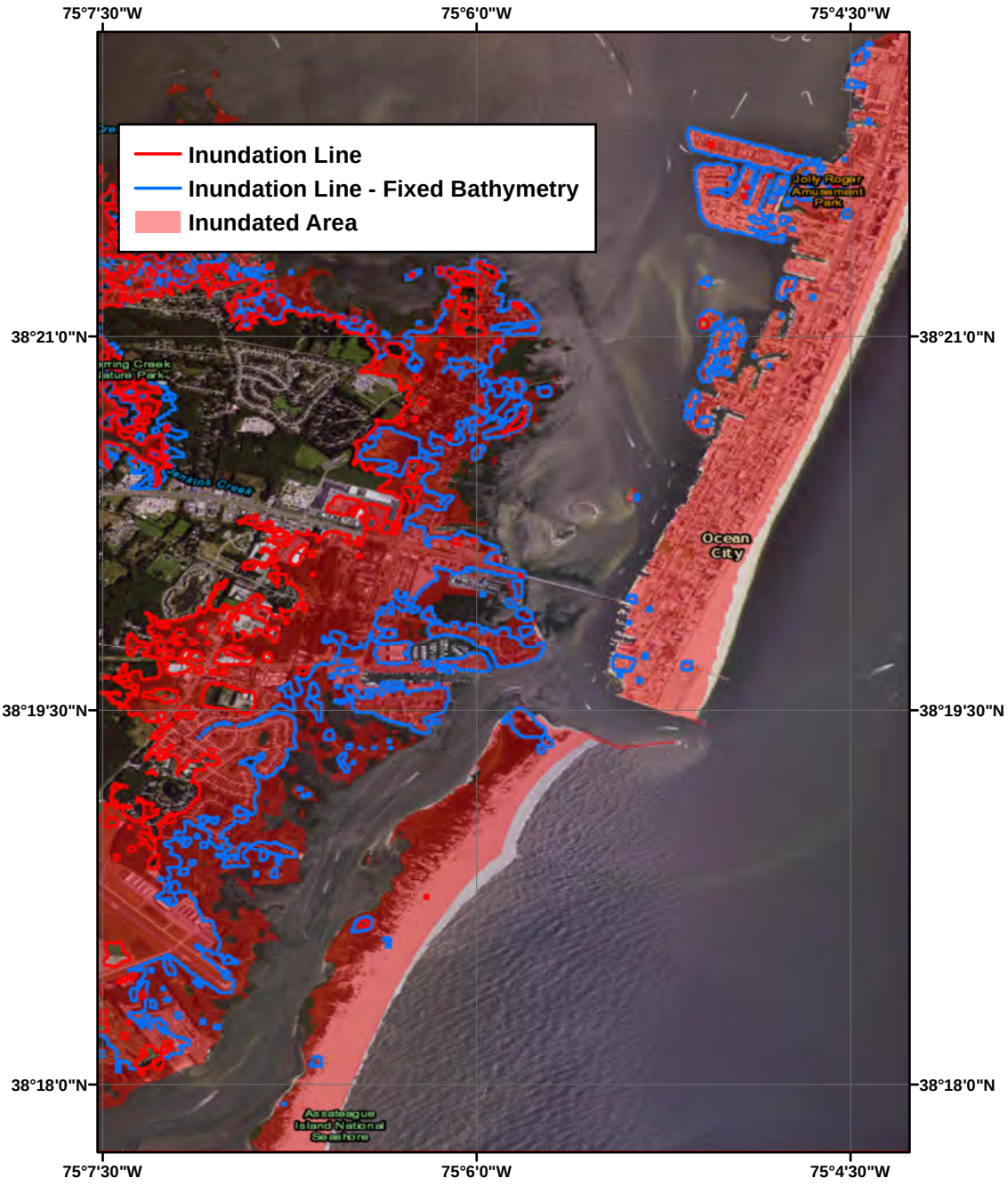

Figure 5.44: SMF tsunami inundation line for fixed (blue) and dynamic (red) bathymetry conditions. The red area shows the inundated region for the dynamic run which considers bed changes during the simulations of tsunami inundation.

Chapter 6

SUMMARY, CONCLUSION AND FUTURE DIRECTIONS

6.1 Summary

In this thesis, we showed that considering morphological adjustments during tsunami inundation mapping can increase the level of tsunami hazard. For this purpose, we coupled FUNWAVE-TVD model with a sediment transport and a bed evolution module. The sediment transport module is based on an Advection-Diffusion (AD) equation for depth-averaged sediment concentration which uses Van Rijn's (1985) pickup function to calculate the sediment erosion rate, and Cao's (1999) formula to estimate sediment deposition rate. The bed evolution module is based on sediment continuity equation and uses time averaged pickup and deposition rates to compute morphological changes. We used a 4th order accurate MUSCL-TVD scheme for spatial discretization of the AD equation, as well as a third order Runge-Kutta scheme for time stepping. Also, we considered an avalanche scheme as slope limiting method for the bed, as well as a hard bottom methodology to account for non-erodible regions.

We tested our model versus two laboratory experiments. First, we modeled the Kobayashi and Lawrence (2004) experiment of beach evolution under breaking solitary waves. The model was able to predict the deposition and erosion location correctly, although the bed changes were underestimated by an average cross-shore error of 25 percent. Also, we used the results of this experiment to conduct basic model validation tests, such as mass conservation, convergence, and parallel performance tests. Next, we modeled the experiment of Pintado-Patiño et al. (2016) who studied the morphological changes of a planar beach under a dam-break bore. For this test, we provided sediment concentration, velocity, and inundation depth comparisons between modeled and

measured data. The model performed well in predicting the depth-averaged sediment transport regime. We provided a comparison between computed bed changes before the reflected waves from downstream reach the shoreline. Similar to Kobayashi and Lawrence (2004) test, the model was able to locate the deposition and erosion regions correctly.

We simulated the 2011 tsunami-induced morphological changes in Crescent City, CA harbor as a field test validation for the model. We used the results of Grilli et al. (2013) and Kirby et al. (2013) for tsunami source generation and ocean-basin propagation and used a nesting approach to increase the resolution in the nearshore. We used the Wilson et al. (2012) analysis as measurement data, who provided a detailed picture of the harbor topography for pre- and post-tsunami conditions. The model was able to assess bed changes inside the harbor with good agreements, locating the deposition and erosion regions correctly similar to the lab experiments. The results of this test showed that the model is capable of estimating tsunami-induced morphological changes in environments with complex bathymetries and in the existence of non-erodible regions, although the magnitude of the largest observed erosions around the jetties were underestimated by a factor of two.

Next, we used the model to study barrier islands morphological response to tsunami inundation. Our previous findings (Tehranirad et al., 2014, 2015b-j) showed that the barrier islands of the United States East Coast (USEC) would be significantly impacted by a possible tsunami. A significant change in the topography of the barrier island can results in an extension of the inundation zone further onshore on the mainland behind. For this purpose, we studied two different environments, a portion of the Assateague Island without any infrastructure as well as a populated region around the Ocean City, MD inlet. Four different tsunami sources were simulated, including tsunamis caused by an earthquake in Puerto Rico Trench (PRT) zone (Grilli et al., 2010), an earthquake in Azores-Gibraltar convergence zone (Grilli et al., 2013b) (Lisbon source), a volcanic cone collapse in the Canary Islands (CVV) (Tehranirad et al., 2015), and a Submarine Mass Failure (SMF) on the edge of the continental shelf break

(Grilli et al., 2015). A nesting approach was used to perform 1/3 arc-sec (about 10m) resolution simulations in the nearshore.

The simulations showed that the Assateague Island morphology can significantly change during tsunami inundation. During the overtopping of the first waves of the tsunami, erosive currents scour the top of the barrier as well as the back slope, and deposit the mobilized sand in the back bay. Then, during the rundown, significant erosion occurs on the shoreface while the corresponding sediment gets deposited further offshore. A similar process continues to happen for the next waves of the tsunami signal while each wave flattens the barrier in a way that the next wave experiences less dissipation compared to fixed bathymetry condition, causing larger waves in the back bay. However, this process changes when the elevation of the trapped water between the barrier and the mainland reaches to a point that causes a gradient between water elevation in the back bay and ocean. This gradient creates an offshore directed current which could last for hours depending on the tsunami magnitude. The offshore directed current is a continuous process which causes large erosions on the shoreface, making it the most vulnerable region of the barrier overall. The results showed that the Assateague Island would become flatter and wider after the tsunami. Also, the barrier migrates toward the mainland in the aftermath of the tsunami.

Next, we simulated tsunami-induced bathymetry changes in a region around Ocean City, MD inlet. Through a GIS analysis, we were able to consider non-erodible regions in our simulations. Also, we categorized the topography of the inlet into four different categories (paved, vegetated, jetty, and sandy) and defined a different Manning coefficient for each category following the works of Sugawara et al. (2014). We considered the paved regions as well as the jetties to be non-erodible and implemented hard bottom condition in those areas. Similar morphological changes to the Assateague Island case was observed in the southern part of the domain which is, in fact, the northern tip of the Assateague Island itself. However, in the north portion of the inlet where non-erodible regions exist, the pattern of morphology changes was slightly different. The shoreface was eroded, and its sand got deposited either on the paved region on

the western side of the barrier or offshore, while the barrier did not migrate eastward in contrast to fully erodible barrier islands. The most notable morphological change was recorded close to the southern jetty of the Ocean City inlet where a large breaching occurred. This significant erosion widened the mouth of the inlet in a way that tsunami waves could easily penetrate in the back bay and cause large inundations on the mainland behind.

Finally, we obtained the inundation line using the results of tsunami inundation with dynamic bathymetry condition in Ocean City inlet region and compared it to the results achieved from fixed bathymetry simulations (Tehranirad et al., 2014). For all of the four sources that were studied here, the area of the inundation zone on the mainland increased significantly. For the CVV tsunami source, the inundated area on the computational domain grew by 76 percent with dynamic bathymetry assumption compared to static condition. Similarly, for the PRT and SMF sources, the inundated area increased by 51 and 42 percent. The largest difference between static and dynamic bathymetry conditions was recorded for the Lisbon source, which is a small tsunami compared to other sources. In fixed bathymetry calculations 1.28 km^2 of the Ocean City inlet computational domain was inundated. However, the computed inundated area was 7.07 km^2 with considering the morphological adjustments, about five times more than the inundated area obtained with fixed bathymetry assumption.

6.2 Conclusion

In this work, we developed a model to study tsunami-induced morphological changes and validated it with laboratory and field measurements. Then, we used the model to provide a comparison between the inundation area of different tsunamis for dynamic and static bathymetry condition. Our results showed that morphological adjustments during tsunami inundation increase the levels of hazard, especially on the mainland behind the barrier islands. Tsunami-induced morphological changes would probably be more significant that what our model computed for Assateague Island

and Ocean City inlet, considering the fact that the model underestimated the morphological changes for the laboratory and field tests. The results of this work indicated that tsunami inundation mapping without considering morphological changes could be underestimated significantly, especially in areas with barrier island. Since barrier islands are a common topographic feature on the USEC, it is required to consider the morphological adjustment during the tsunami inundation mapping process for coastal communities such as Atlantic City, NJ, Southern Long Island, NY, Cape Hatteras, NC, and many other populated regions along coastlines of North Carolina, Virginia, Delmarva Peninsula and New Jersey.

6.3 Future Directions

There could be many future directions for the current research. In this section, we briefly discuss some of the ideas that we can work on them in the future. It would be informative to compare results of the current model with a 3D model (e.g. NHWAVE) to investigate the differences between the results of a depth-averaged and 3D formulation. Also, we can modify the expression for the bottom stress to consider short wave effects, and apply the model for storms. In terms of the application of the current model for the future research, we plan to take a deeper look into the tsunami-induced morphological changes. We can use the model to study the geometry of tsunami return flow, the channelization effects, as well as delta formation processes. Moreover, the model can be used to investigate the tsunami morphological changes in inlets, ports, harbors, and predict maritime hazard in such regions. Finally, the model can be used for tsunami inundation mapping with morphological adjustments included.

REFERENCES

Abadie, S.M., Harris, J.C., Grilli, S.T. and Fabre, R., "Numerical modeling of tsunami waves generated by the flank collapse of the Cumbre Vieja Volcano (La Palma, Canary Islands): tsunami source and near field effects", *Journal of Geophysical Research: Oceans*, **117**, 2012.

Amante, C., and Eakins, B. "ETOPO1 1 arc-minute global relief model:Procedures, data sources and analysis", Tech. rep., *NOAA Technical Memorandum NESDIS NGDC-24.* National Geophysical Data Center, NOAA, 2009.

Apotsos, A., Buckley, M., Gelfenbaum, G., Jaffe, B., and Vatvani, D., "Nearshore tsunami inundation model validation: toward sediment transport applications", *Pure and Applied Geophysics*, **168**, 2097-2119, 2011a.

Apotsos, A., Gelfenbaum, G., and Jaffe, B., "Process-based modeling of tsunami inundation and sediment transport", *Journal of Geophysical Research: Earth Surface (20032012)*, **116**, F01006, 2011b.

Atlantic and Gulf of Mexico Tsunami Hazard Assessment Group, "Evaluation of Tsunami Sources with the Potential to Impact the U.S. Atlantic and Gulf Coasts - A Report to the Nuclear Regulatory Commission", U.S. Geological Survey Administrative Report, 2008.

Bagnold, R., "An approach to the sediment transport problem from general physics", *US Geol. Surv. Prof. Paper*, **422**, 231-291, 1966.

Brocchini, M., Svendsen, I. A., Prasad, R. S., and Bellotti., G., "A comparison of two different types of shoreline boundary conditions", *Computer Methods in Applied Mechanics and Engineering*, **191**, 4475-4496, 2002.

Buttolph, A.M., Reed, C.W., Kraus, N.C., Ono, N., Larson, M., Camenen, B., Hanson, H., Wamsley, T. and Zundel, A.K., "Two-dimensional depth-averaged circulation model CMS-M2D: Version 3.0, Report 2, sediment transport and morphology change", *Engineer Research and Develpment Center Vicksburg MS Coastal and Hydraulics Lad*,No. ERDC/CHL-TR-06-9., 2006.

Cao, Z. "Equilibrium near-bed concentration of suspended sediment", *Journal of Hydraulic Engineering*, **125**, 1270-1278, 1999.

Chaytor, J.D., Uri, S., Solow, A.R. and Andrews, B.D., "Size distribution of submarine landslides along the US Atlantic margin.", *Marine Geology*, **264**, 16-27, 2009.

Chen, Q., "Fully nonlinear Boussinesq-type equations for waves and currents over porous beds", *Journal of Engineering Mechanics.* **132**, 220-230, 2006.

Choowong, M., Murakoshi, N., Hisada, K.I., Charusiri, P., Charoentitirat, T., Chutakositkanon, V., Jankaew, K., Kanjanapayont, P., and Phantuwongraj, S., "2004 Indian Ocean Tsunami inflow and outflow at Phuket, Thailand", *Marine Geology*, **248**, 179-192, 2008.

Cobo, P.T., Kirby, J.T., Haller, M.C., Ozkan-Haller, H.T., Magallen, J. and Guannel, G., "Model Simulations of Bar Evolution in a Large Scale Laboratory Beach", *Coastal Engineering*, p.2567, 2006.

Deltares, "XBeach testbed reportRep", *Delft, The Netherlands*, 2010.

Deltares, "Delft3D-FLOW, User Manual, Simulation of multi-dimensional hydrodynamic flows and transport phenomena, including sedimentsRep.", *The Netherlands*, 2011.

Elder, J. W., "The dispersion of marked fluid in turbulent shear flow", *Journal of fluid mechanics* , **5**, 544-560, 1959.

Erduran, K. S., Ilic, S., and Kutija, V., "Hybrid finite-volume finite-difference scheme for the solution of Boussinesq equations", *Int. J. Numer. Meth. Fluid.*, **49**, 1213-1232, 2005.

Fenster, M. S., Dolan, R., and Smith, J. J., "Grain-size distributions and coastal morphodynamics along the southern Maryland and Virginia barrier islands", *Sedimentology*, **63**, 809823, 2016.

Fritz, H. M., et al., "Insights on the 2009 south Pacific tsunami in Samoa and Tonga from field surveys and numerical simulations", *Earth-Science Reviews*, **107**, 66-75, 2011.

Gelfenbaum, G., and Jaffe, B., "Erosion and sedimentation from the 17 July, 1998 Papua New Guinea tsunami", *Pure and Applied Geophysics*, **160**, 1969-1999, 2003.

Goto, K., Takahashi, J., Oie, T., and Imamura, F., "Remarkable bathymetric change in the nearshore zone by the 2004 Indian Ocean tsunami: Kirinda Harbor, Sri Lanka", *Geomorphology*, **127**, 107-116, 2011.

Goto, K., Chagu-Goff, C., Goff, J., and Jaffe, B., "The future of tsunami research following the 2011 Tohoku-oki event", *Sedimentary Geology*, **282**, 1-13, 2012a.

Goto, K., Sugawara, D., Abe, T., Haraguchi, T., and Fujino, S, "Liquefaction as an important source of the AD 2011 Tohoku-oki tsunami deposits at Sendai Plain, Japan", *Geology*, **40**, 887-890, 2012b.

Gottlieb, S., Shu, C., Tadmor, E., "Strong stability-preserving high-order time discretization methods." *SIAM review*, **43**, 89-112, 2001.

Grilli, S. T., Dubosq, S., Pophet, N., Prignon, Y., Kirby, J. T., and Shi, F., "Numerical simulation and first-order hazard analysis of large co-seismic tsunamis generated in the Puerto Rico trench: near-field impact on the North shore of Puerto Rico and far-field impact on the US East Coast", *Natural Hazards and Earth System Sciences*, **10**, 2109-2125, 2010.

Grilli, S. T., Harris, J. C., Tajalli Bakhsh, T., Masterlark, T., Kyriakopoulos, C., Kirby, J. T., and Shi, F., "Numerical simulation of the 2011 Tohoku tsunami based on a new transient FEM co-seismic source: Comparison to far-and near-field observations", *Pure and Applied Geophysics*, **170**, 1333-1359, 2013.

Grilli, A. R., and Grilli, S. T., "Modeling of tsunami generation, propagation and regional impact along the upper US East Coast from the Puerto Rico trench", Research Report, No. CACR-13-02, Center for Applied Coastal Research, University of Delaware, 2013a.

Grilli, A. R., and Grilli, S. T., "Modeling of tsunami generation, propagation and regional impact along the upper US East Coast from the Azores convergence zone", Technical report, No. CACR-13-04, Center for Applied Coastal Research, University of Delaware, 2013b.

Grilli, A. R., and Grilli, S. T., "Far-field tsunami impact on the U.S. East Coast from and extreme flank collapse of the Cumbre Vieja Volcano (Canary Islands)", Research Report, No. CACR-13-03, Center for Applied Coastal Research, University of Delaware, 2013c.

Grilli, S. T., O'Reilly, C. and Tajalli Bakhsh, T., "Modeling of SMF tsunami generation and regional impact along the upper US East Coast", Research Report

No. CACR-13-05, Center for Applied Coastal Research, University of Delaware, 2013d.

Grilli, S. T., OReilly, C., Harris, J. C., Tajalli Bakhsh, T., Tehranirad, B., Banihashemi, S., Kirby, J. T., Baxter, C. D. P., Eggeling, T., Ma, G. and Shi, F.,"Modeling of SMF tsunami hazard along the upper U. S. East Coast: Detailed impact around Ocean City, MD, *Natural Hazards*, **76**, 705-746, doi:10.1007/s11069-014-1522-8, 2015.

Grothe, P. R, Taylor, L. A, Eakins, B. W, Warnken, R. R, Carignan, K. S, Lim, E, Caldwell, R. J, and Friday, D.Z., "Digital Elevation Model of Ocean City, Maryland: Procedures, Data and Analysis", *NOAA Technical Memorandum NESDIS NGDC-37*, , Dept. of Commerce, Boulder, CO, 37 pp, 2010.

Grothe, P.R., Taylor, L.A., Eakins, B.W., Carignan, K.S., Caldwell, R.J., Lim, E., and Friday, D.Z., "Digital Elevation Models of Crescent City, California: Procedures, Data Sources and Analysis", *NOAA Technical Memorandum NESDIS NGDC-51*, U.S. Dept. of Commerce, Boulder, CO, 31 pp, 2011.

Haraguchi, T., Goto, K., Sato, M., Yoshinaga, Y., Yamaguchi, N., and Takahashi, T., "Large bedform generated by the 2011 Tohoku-oki tsunami at Kesennuma Bay", *Japan. Marine Geology*, **335**, 200-205, 2012.

Hori, K., Kuzumoto, R., Hirouchi, D., Umitsu, M., Janjirawuttikul, N., and Patanakanog, B., "Horizontal and vertical variation of 2004 Indian tsunami deposits: an example of two transects along the western coast of Thailand", *Marine Geology*, **239**, 163-172, 2007.

Horrillo, J., Knight, W. and Kowalik, Z., "Kuril Islands tsunami of November 2006: 2. Impact at Crescent City by local enhancement", *Journal of Geophysical Research: Oceans*, **113**, 2008.

Kennedy, A. B., Kirby, J. T., Chen, Q. and Dalrymple, R. A., "Boussinesq-type equations with improved nonlinear performance", *Wave Motion*, **33**, 225-243, 2001.

Kim, D. H., "Turbulent flow and transport modeling by long waves and currents.", Diss. Texas A&M University, 2009.

Kim, D. H., "H2D morphodynamic model considering wave, current and sediment interaction." *Coastal Engineering*, **95**, 20-34, 2015.

Kirby, J. T., Shi, F., Tehranirad, B., Harris, J. C., and Grilli, S. T., "Dispersive tsunami waves in the ocean: Model equations and sensitivity to dispersion and Coriolis effects", *Ocean Modelling*, **62**, 39-55, 2012.

Lacy, J. R., Rubin, D. M., and Buscombe., D., "Currents, drag, and sediment transport induced by a tsunami.", *Journal of Geophysical Research: Oceans*, 117.C9, 2012.

Lee, J., Huang, Z., Kou, Z., and Xing, X., "The effect of tide level on the tsunami response of coastal harbors", *Coastal Engineering Proceedings*, **1**, currents.11. doi:http://dx.doi.org/10.9753/icce.v33.currents.11, 2012.

Li, L. and Huang Z., "Modeling the change of beach profile under tsunami waves: A comparison of selected sediment transport models", *Journal of Earthquake and Tsunami*, **7**, 2013.

Liu, P. L. F., Cho, Y. S., Briggs, M. J., Kanoglu, U., and Synolakis, C. E., "Runup of solitary waves on a circular island.", *Journal of Fluid Mechanics*, **302**, 259-285, 1995.

Long, W., Kirby J. T., and Shao Z., "A numerical scheme for morphological bed level calculations", *Coastal Engineering*, **55**, 167-180, 2008.

Lynett, P. and Liu P. L., "A numerical study of the run-up generated by three-dimensional landslides", *Journal of Geophysical Research*, **110**, C03006, 2005.

Lynett, P., and Liu, P., "Numerical simulation of complex tsunami behavior", *Computing in Science & Engineering*, **13**, 50-57, 2011.

Ma, G., Shi, F., and Kirby, J. T., 2012, "Shock-capturing non-hydrostatic model for fully dispersive surface wave processes", *Ocean Modelling*, **43**, 22-35.

NOAA, Crescent_City_pre_tsunami_0_5m.txt, ASCII Grid, NAD83 UTM zone 10, meters, MLLW Bathymetry Crescent City Harbor, California, NOAA NRT-6, November 1823, 2008.

NOAA, Crescent_City_posttsunami.txt, ASCII Grid, NAD83 UTM zone 10, meters, MLLW Bathymetry Crescent City Harbor, California, NOAA NRT3/4, March 1721, 2011.

National Geophysical Data Center (NGDC), "U.S. Coastal Relief Model - Northeast Atlantic", National Geophysical Data Center, NOAA, 1999.

National Geophysical Data Center (NGDC), "U.S. Coastal Relief Model - Central Pacific." National Geophysical Data Center, NOAA, 2003.

New York Times, "Satellite Photos of Japan, Before and After the Quake and Tsunami", http://www.nytimes.com/interactive/2011/03/13/world/asia/satellite-photos-japan-before-and-after-tsunami.html, 2011.

Nwogu, O., "An alternative form of the Boussinesq equations for nearshore wave propagation", *Journal of Waterway, Port, Coastal, and Ocean Engineering*, **119**, 618-638, 1993.

Pintado-Patiño, J. C., TorresFreyermuth, A., Puleo, J. A., and Pokrajac, D., "On the role of infiltration and exfiltration in swash zone boundary layer dynamics", *Journal of Geophysical Research: Oceans*, **120**, 6329-6350, 2015.

Pintado-Patiño, J. C., Puleo, J. A., Krafft, D., and Torres-Freyermuth, A., "Swash zone dynamics and sediment flux under dambreak driven forcing: an experimental study.", *in preparation.*

Rahman, S., Mano, A., and Udo, K., "Coupling of boussinesq and sediment transport model in a wave flume", *Journal of Japan Society of Civil Engineering*, **68**, 259-264, 2012.

Rubey, W. W.. "Settling velocity of gravel, sand, and silt particles", *American Journal of Science*, **148**, 325-338, 1933.

Ruffman, A., and Hann, V., "The Newfoundland tsunami of November 18, 1929: An examination of the twenty-eight deaths of the" South Coast Disaster"", *Newfoundland and Labrador Studies*, **21**, 2001.

Shi, F., Kirby, J. T., Harris, J. C., Geiman, J. D., and Grilli, S. T., "A high-order adaptive time-stepping TVD solver for Boussinesq modeling of breaking waves and coastal inundation", *Ocean Modelling*, **43-44**, 36-51, 2012.

Shi, F., Tehranirad, B., Kirby J. T., Harris, J. C., and Grilli, S. T., "FUNWAVE-TVD Fully Nonlinear Boussinesq Wave Model With TVD Solver Documentation And Users Manual (Version 2.1).", Technical report, No. CACR-11-04, Center for Applied Coastal Research, University of Delaware, 2011.

Shields, A., Ott, W., and Van Uchelen, J., "Application of similarity principles and turbulence research to bed-load movement", Soil Conservation Service, 1936.

Soulsby, Richard., "Dynamics of marine sands: a manual for practical applications.", Thomas Telford, 1997.

Sugawara, D., Goto, K. and Jaffe., B. E., "Numerical models of tsunami sediment transport - Current understanding and future directions", *Marine Geology*, **352**, 295-320, 2014.

Sumer, B. M., A. Kozakiewicz, J. Fredsoe, and R. Deigaard, "Velocity and Concentration Profiles in Sheet-Flow Layer of Movable Bed", J. *Hydraul. Eng.*, **122**(10), 549558, 1996.

Synolakis, C. E., Bernard, E. N., "Tsunami science before and beyond boxing day 2004", *Philosophical Transactions of the Royal Society A: Mathematical, Physical and Engineering Sciences*, **364**, 2231-2265, 2006.

Szczuciński, et al., "Sediment sources and sedimentation processes of 2011 Tohoku-oki tsunami deposits on the Sendai Plain, Japan, insights from diatoms, nannoliths and grain size distribution", *Sedimentary Geology*, **282**, 40-56, 2012.

Tanaka, H., Tinh, N. X., Umeda, M., Hirao, R., Pradjoko, E., Mano, A., and Udo, K., "Coastal and estuarine morphology changes induced by the 2011 Great East Japan Earthquake Tsunami", *Coastal Engineering Journal*, **54**, 2012.

Tappin, David R., Stephan T. Grilli, Harris, J.C., Geller, R. J., Masterlark, T., Kirby, J. T., Shi, F., Ma, G.,Thingbaijam, K. K., and Mai., P. M., "Did a submarine landslide contribute to the 2011 Tohoku tsunami?." *Marine Geology*, **357**, 344-361, 2014.

Tehranirad, B., Shi, F., Kirby, J. T., Harris, J. C., and Grilli, S. T., "Tsunami benchmark results for fully nonlinear Boussinesq wave model FUNWAVE-TVD. Version 1.0", Technical report, No. CACR-11-02, Center for Applied Coastal Research, University of Delaware, 2011.

Tehranirad, B., Banihashemi, S., Kirby, J. T., Callahan, J. A. and Shi, F., "Tsunami inundation mapping for Ocean City, MD NGDC DEM", Research Report No. CACR-14-04, Center for Applied Coastal Research, Department of Civil and Environmental Engineering, University of Delaware, 2014.

Tehranirad, B., Harris, J. C., Grilli, A. R., Grilli, S. T., Abadie, S., Kirby, J. T. and Shi, F., "Far-field tsunami hazard on the western European and US east coast from a large scale flank collapse of the Cumbre Vieja volcano, La Palma", *Pure and Applied Geophysics*, **172**, 3589-3616, doi:10.1007/s00024-015-1135- 5, 2015a.

Tehranirad, B., Kirby, J. T., Callahan, J. A. and Shi, F., "Tsunami inundation mapping for Atlantic City, NJ NGDC DEM", Research Report No. CACR-15-01, Center for Applied Coastal Research, Department of Civil and Environmental Engineering, University of Delaware, 2015b.

Tehranirad, B., Kirby, J. T., Callahan, J. A. and Shi, F., "Tsunami inundation mapping for the northern half of the State of New Jersey", Research Report No. CACR-15-02, Center for Applied Coastal Research, Department of Civil and Environmental Engineering, University of Delaware, 2015c.

Tehranirad, B., Kirby, J. T., Callahan, J. A. and Shi, F., "Tsunami inundation mapping for New York City", Research Report No. CACR-15-03, Center for Applied Coastal Research, Department of Civil and Environmental Engineering, University of Delaware, 2015d.

Tehranirad, B., Kirby, J. T., Callahan, J. A. and Shi, F., "Tsunami inundation mapping for Montauk, NY NGDC DEM", Research Report No. CACR-15-04, Center for Applied Coastal Research, Department of Civil and Environmental Engineering, University of Delaware, 2015e.

Tehranirad, B., Kirby, J. T., Callahan, J. A. and Shi, F., "Tsunami inundation mapping for Nantucket, MA NGDC DEM", Research Report No. CACR-15-05, Center for Applied Coastal Research, Department of Civil and Environmental Engineering, University of Delaware, 2015f.

Tehranirad, B., Kirby, J. T. and Shi, F., "Tsunami Inundation Mapping for Virginia Beach, VA NGDC DEM", Research Report No. CACR-15-11, Center for Applied Coastal Research, Department of Civil and Environmental Engineering, University of Delaware, 2015g.

Tehranirad, B., Kirby, J. T. and Shi, F., "Tsunami Inundation Mapping for Cape Hatteras, NC NGDC DEM", Research Report No. CACR-15-12, Center for Applied Coastal Research, Department of Civil and Environmental Engineering, University of Delaware, 2015h.

Tehranirad, B., Kirby, J. T. and Shi, F., "Tsunami Inundation Mapping for Myrtle Beach, SC NGDC DEM, Research Report No. CACR-15-13, Center for Applied Coastal Research, Department of Civil and Environmental Engineering, University of Delaware, 2015i.

Tehranirad, B., Kirby, J. T. and Shi, F., "Tsunami Inundation Mapping for Savannah, GA NGDC DEM", Research Report No. CACR-15-14, Center for Applied

Coastal Research, Department of Civil and Environmental Engineering, University of Delaware, 2015j.

ten Brink, U. S., "Vertical motions of the Puerto Rico Trench and Puerto Rico and their cause." *Journal of Geophysical Research: Solid Earth*, **110**, 2005.

ten Brink, U. S., Barkan, R., Andrews, B.D. and Chaytor, J.D., "Size distributions and failure initiation of submarine and subaerial landslides.", *Earth and Planetary Science Letters*, **287**, 31-42, 2009.

Titov, V. V., and Gonzalez, F. I. "Implementation and testing of the method of splitting tsunami (MOST) model.", US Department of Commerce, National Oceanic and Atmospheric Administration, Environmental Research Laboratories, Pacific Marine Environmental Laboratory, 1997.

Tonelli, M., and Petti, M., "Hybrid finite volumefinite difference scheme for 2DH improved Boussinesq equations.", *Coastal Engineering*, **56**, 609-620, 2009.

Udo, K., Sugawara, D., Tanaka, H., Imai, K., and Mano, A., "Impact of the 2011 Tohoku earthquake and tsunami on beach morphology along the northern Sendai coast", *Coastal Engineering Journal*, **54**, p.1250009, 2012.

van Rijn, L. C., "Sediment pick-up functions.", *Journal of Hydraulic Engineering*, **110**, 1494-1502, 1984.

Wang, "An ocean depth-correction method for reducing model errors in tsunami travel time: application to the 2010 Chile and 2011 Tohoku Tsunamis", *Journal of Tsunami Society International*, **34**(1), 2015.

Watanabe, A. "3-dimensional numerical model of beach evolution.", *Proc. Coastal Sediments (1987).*, ASCE, 801-817, 1987.

Wei, G., Kirby, J.T., Grilli, S.T., and Subramanya, R., "A fully nonlinear Boussinesq model for surface waves: Part I. Highly nonlinear unsteady waves", *Journal of Fluid Mechanics*, **3**(43), 216, 1995.

Wilson, K. C., "Friction of wave-induced sheet flow", *Coastal Engineering*, **12**, 371-379, 1989.

Wilson, R., Davenport, C., and Jaffe, B., "Sediment scour and deposition within harbors in California (USA), caused by the March 11, 2011 Tohoku-oki tsunami", *Sedimentary Geology*, **282**, 228-240, 2012.

Wilson, R. I., Admire, A. R., Borrero, J. C., Dengler, L. A., Legg, M. R., Lynett, P., and McCrink, T. P., "Observations and impacts from the 2010 Chilean and 2011 Japanese tsunamis in California (USA)" *Pure and Applied Geophysics*, **170**, 1127-1147, 2013.

Yamamoto, S., and Daiguji, H., "Higher-order-accurate upwind schemes for solving the compressible Euler and Navier-Stokes equations", *Computers & Fluids*, **22**, 259-270, 1993.

Yamamoto, S., Kano, S. and Daiguji, H, "An efficient CFD approach for simulating unsteady hypersonic shock shock interference flows", *Computers and Fluids*, **27**, 571-580, 1998.

Yeh, H., Robertson, I., and Preuss, J., "Development of design guidelines for structures that serve as tsunami vertical evacuation sites (p. 34)", Washington State Department of Natural Resources, Division of Geology and Earth Resources, 2005.